REPUBLIQUE ALGERIENNE DEMOCRATIQUE ET POPULAIRE
MINISTERE DE L'ENSEIGNEMENT SUPERIEUR ET DE LA RECHERCHE SCIENTIFIQUE

UNIVERSITE ABOU-BEKR BELKAID – TLEMCEN

THÈSE LMD

Présentée à :

FACULTE DES SCIENCES – DEPARTEMENT DE PHYSIQUE

Pour l'obtention du diplôme de :

DOCTORAT

Spécialité : *physique des gaz et des plasmas*

Par :

M. BENBAIER Kouider

Sur le thème

Modeling of a LIBS plasma emitted by organic components under Martian conditions with the aim of search for life in Mars

---

Soutenue publiquement le 21/06/2025 à Tlemcen devant le jury composé de :

M^{r}	CHIKHAOUI Abdelhak	Professeur	Université de Tlemcen	Président
M^{me}	BEDRANE Zeyneb	Professeur	Université de Tlemcen	Directrice de thèse
M^{r}	LIANI Bachir	Professeur	Université de Tlemcen	Examinateur
M^{r}	BELDJILALI Sid Ahmed	Professeur	USTO - MB	Examinateur
M^{r}	Gourari Djamel Eddine	Professeur	CU -- Naama	Examinateur

Laboratoire physique théorique
BP 119, 13000 Tlemcen - Algérie

Dedication

In memory of my mother

" اللهم ارحمها واغفر لها"

I dedicate this work to my father. I will never forget your sacrifices, your guidance, and your unwavering dedication to my education. May Allah Almighty preserve you and grant you health, a long life, and lasting happiness.

To my dear brother Mohamed El Amine and my dear sister Nour El Houda, who have always been examples of perseverance, courage, and generosity to me.

To my dear maternal aunt Fatima, my maternal cousins, and my late grandmother—may Allah have mercy on her and forgive her (اللهم ارحمها واغفر لها). I also extend my heartfelt gratitude to all members of my family, without exception.

To my dear friends, for all the moments we have shared.

Acknowledgments

First of all, I would like to thank the *Almighty and Merciful ALLAH*, who gave me the strength and patience to accomplish this modest work.

My sincere thanks go to Mrs. Zeyneb BEDRANE, my thesis supervisor, for sharing her brilliant insights, extensive knowledge, and experience in this field, while placing her trust in me and generously offering her expertise. I am also deeply grateful for her kindness, constant availability, and the many words of encouragement she provided throughout this work.

I would like to express my sincere gratitude to Mr. Noureddine Melikechi for his valuable advice, his trust, and his rigorous approach to work. It has been an honor to learn from him, both scientifically and personally. This thesis is the result of several years of collaboration with him.

I would also like to extend my sincere thanks to the members of the jury, beginning with Mr. Abdelhak Chikhaoui, Professor at the University of Tlemcen, who did me the honor of chairing the jury.

I express my sincere thanks to all the members of the jury of this thesis—Mr. Bachir Liani, Mr. Sid Ahmed Beldjilali, and Mr. Djamel Eddine Gourari for their availability and for having kindly agreed to review and evaluate this work.

I would also like to thank all the members of the Theoretical Laboratory.

Contents

List of Figures

List of Tables

Introduction

Throughout history, human beings have demonstrated an innate curiosity and desire to explore space. This began with observing the positions of stars and planets, as practiced by civilizations such as ancient Egypt and ancient Greece. The first human spaceflight occurred in 1961, when Soviet pilot Yuri A. Gagarin ventured beyond Earth's atmosphere. During the height of the Cold War, space exploration became a key area of competition between the United States of America (USA) and the Soviet Union (USSR). This rivalry ultimately propelled Neil Armstrong and Buzz Aldrin to the Moon during the Apollo 11 mission in 1969. One of the major goals of the mission was to understand the composition and nature of this mysterious satellite that orbits the Earth. The exploration of the solar system and the universe quickly became a field arousing the interest of the most curious individuals, who sought to discover new frontiers, learn about the mysteries of the cosmos, and unravel the secrets of our origins, including the possibility of finding life on other planets.

Over the centuries, humans have been captivated by the allure of Mars, the Red Planet. The first actual observations of Mars were made by C. Huygens between 1659 and 1672, which signaled the beginning of extensive observations of Mars in the 17th century. Huygens used the parallax of Mars to calculate the movement of Mars' rotation as well as to determine the separation between Earth and the Sun [1]. In the 18th century, W. Herschel continued the exploration by observing Mars' polar caps in 1777, determining the planet's axis of inclination, which revealed the existence of seasons, and discovering the planet's thin atmosphere. In 1877, A. Hall discovered the two natural satellites of Mars, Phobos and Deimos, using telescopes with improved spatial resolution [2]. Around the same time, G. Schiaparelli observed what he termed "canali" on the planet [3]. However, modern-day astronomers are particularly intrigued

by the Red Planet due to its proximity, making it accessible to probes and rovers. Additionally, unlike other planets in the Solar System, Mars likely experienced conditions similar to those on Earth in the past. It had a warmer and wetter climate billions of years ago, which may have created conditions suitable for life to emerge. There is evidence that liquid water once flowed on its surface, and the planet still has large amounts of water ice in its polar regions [4]. Furthermore, recent discoveries of methane on Mars suggest that there may still be some form of active geological or biological processes occurring on the planet [5]. These pieces of evidence often raise many questions. How does the presence of water, both in the past and present, affect the likelihood of life on Mars? What is the source of the methane detected on Mars, and could it be indicative of biological activity? Are there any organic molecules present on Mars that could be indicative of past or present life? What are the possibilities for microbial life existing in Martian underground aquifers or subsurface ice deposits?

Since the 1960s, Mars has been the most explored planet using human technology, with both Russian and American missions [6, 7]. Despite many failed attempts, the Americans managed to achieve their first successful flyby of the planet with the "Mariner 4 Mission" in 1965. The robots "Viking 1" and "Viking 2" were the first to explore the surface of Mars in 1976. In both of these missions, an orbiter and a lander were used. Mars Science Laboratory (MSL), the last rover of the twenty-first century and the largest to date, has as its main goal the placement and operation of a mobile science laboratory on the surface of Mars in order to assess the biological potential of the landing site, characterize the geology of the landing region, and investigate planetary processes that affect habitability [8]. The Mars Science Laboratory rover, commonly referred to as Curiosity, is a highly advanced six-wheeled robot that was commissioned by the United States' National Aeronautics and Space Administration (NASA) in 2012 [8], which allows it to carry out a wide range of experiments and studies on the surface of Mars. Equipped with a sophisticated robotic arm that features brushing, scooping, and drilling capabilities, Curiosity is capable of collecting and analyzing rock and soil samples from the Martian surface. In order to research the geology, climate, and atmospheric conditions of Mars, the rover has a number of scientific instruments, including a mass spectrometer, a gas chromatograph, and several cameras and sensors. The Chemical Camera (ChemCam)

is a remote sensing device that employs Laser-Induced Breakdown Spectroscopy (LIBS) to analyze the composition of rocks and surface sediments at remote distances. It is one of the most useful tools on board the Curiosity rover. The process involves directing a powerful laser beam onto the tops of rocks and soils, melting, vaporizing, and exciting the atoms inside the material that emit light as it cools. The spectrometers on ChemCam receive and analyze this light [9, 10]. It contributes significantly to our understanding of the planet's history, geology, and the potential presence of elements crucial to supporting life. Overall, the Laser-Induced Breakdown Spectroscopy (LIBS) technique employed by ChemCam is a powerful tool that allows for the analysis of elemental composition information on analysis spots with diameters varying at distances up to 7 meters [10]. Taking advantage of this achievement, NASA once more selected LIBS to be one of the analysis tools used by the SuperCam instrument, mounted on board the Perseverance rover, which landed on the surface of Mars in February 2021 [11].

The purpose of this PhD thesis is to develop and refine a comprehensive numerical model for simulating LIBS plasma generated by organic compounds under Martian conditions. This work analyzes LIBS spectra obtained from Martian samples and demonstrates how the model enables more accurate interpretation of plasma characteristics such as electron and ion temperatures, electron and ion number densities, and fluid velocity by incorporating the specific atmospheric and environmental parameters found on Mars and Earth. Additionally, the effect of lens-to-sample distance (LTSD) on plasma behavior is investigated. These findings are essential for optimizing LIBS applications in planetary exploration and enhancing our ability to detect and analyze potential organic traces of past or present life on Mars. To accomplish this objective, the research adopts a multidisciplinary approach that integrates theoretical modeling, laboratory experiments, and data analysis. The theoretical component focuses on developing a robust computational framework capable of simulating LIBS plasma dynamics and emission spectra under Martian environmental conditions. Laboratory experiments are conducted to validate the accuracy and reliability of the numerical model.

This thesis manuscript consists of three chapters. The purpose of the first chapter, *"Overview of Mars Exploration: Key Information and Characteristics"* is to provide a comprehensive introduction to the nature and features of the Red Planet. In this chapter, we explore various aspects of Mars, including its geological structure, surface composition, and atmospheric properties, establishing a solid foundation for understanding the planet's environment. Furthermore, the chapter introduces the Laser-Induced Breakdown Spectroscopy (LIBS) technique and its applications in Martian exploration, with a detailed discussion of the underlying processes. In particular, the LIBS instruments aboard the Curiosity and Perseverance rovers ChemCam and SuperCam are examined for their roles in identifying and characterizing Martian rocks and soils.

The second chapter, titled *"A Thermal Radiation-Hydrodynamics Framework for LIBS Plasma Simulation"* is dedicated to presenting the theoretical model developed and used in this thesis. The purpose of this chapter is to describe the simulated interaction of a pulsed laser with an organic target (graphite, in this case) in the presence of ambient gas, mimicking Martian environmental conditions. The laser parameters used in the model are the same as those of the ChemCam and SuperCam instruments [12–13]. The thermal radiation-hydrodynamics model of laser ablation and plasma formation incorporates several complex mechanisms, including laser heating, transport coefficients, shock wave generation, and radiative interactions within the plasma. To study these processes, a radiation-hydrodynamics (RHD) code, FLASH [14], was employed for the simulations. This code enabled the investigation of plasma dynamics during Laser-Induced Breakdown Spectroscopy (LIBS) under Martian conditions, providing insights into the thermal, hydrodynamic, and radiative behavior of the plasma.

The computational investigation aims to provide a comprehensive understanding of the interplay between laser ablation and plasma formation for different laser focusing conditions under Martian and Earth-like conditions. In this chapter, we employ a three-temperature (3T) Eulerian radiation model incorporating non-local thermodynamic equilibrium (NLTE) conditions. The fundamental principles and governing equations of the theoretical framework are presented, along with an explanation of how the FLASH code is used to simulate the interaction between laser pulses and the organic target, as well as the subsequent plasma formation.

By accurately representing environmental conditions involving both CO_2 and He, the model enhances our understanding of LIBS plasma characteristics relevant to Mars exploration.

The third chapter, titled *"Numerical Simulation of Graphite under Martian Conditions"* begins by presenting the foundation of our three-temperature (3T) radiation-hydrodynamics Eulerian model, which is used to simulate the interaction between a solid graphite target and laser radiation, leading to plasma formation. We employ Adaptive Mesh Refinement (AMR) to accurately capture the complex interactions among various physical and chemical processes within the LIBS plasma, while preserving realism under Martian ambient gas conditions.

This chapter serves as a pivotal component of the study, offering a detailed exposition of the results obtained from our carefully designed simulations using the FLASH platform. The primary focus is to unravel the complexities of graphite plasma behavior under Martian conditions. Our analysis explores key plasma characteristics, including electron and ion temperatures as indicators of thermal dynamics. Additionally, we examine electron and ion number densities to gain insight into plasma composition and spatial distribution. The dynamic motion of the plasma is analyzed through fluid velocity patterns, revealing the underlying mechanisms that govern plasma expansion and flow. The introduction of ambient CO_2 and He gases at pressures representative of both Martian (3–9 mbar) and Earth-like (up to 1000 mbar) conditions significantly influences plasma evolution.

Moreover, the study investigates the effects of laser irradiance and ambient pressure on LIBS plasma parameters, including the spatial evolution of the plasma size during both early and delayed stages. This comprehensive investigation deepens our understanding of the effect of lens-to-sample distance (LTSD) on these variables and their combined role in shaping plasma dynamics. The chapter concludes with a discussion of the limitations of the current modeling approach and suggests potential directions for future improvements.

In conclusion, this work reveals promising prospects—particularly for the search for life on Mars—through an extensive exploration of laser-induced breakdown spectroscopy (LIBS) plasma modeling under Martian and Earth-like environmental conditions. The seamless integration of experimental data, theoretical modeling, and computer simulations weaves together the core elements of our analysis, drawing meaningful parallels to the central challenge of

life detection on Mars. Through detailed simulations and careful analysis, we have gained a unique perspective on the complex interplay between the laser focusing system, plasma formation, and the Martian environment. This dual influence provides a foundation for optimizing LIBS analyses on Mars and other planetary bodies, uncovering critical insights essential for identifying potential biosignatures and indicators of life.

References

[1] Huygens, Systema Saturnium (1559); in *OEuvres Complètes de Christiaan Huygens*, Vol. 15 (La Haye: Martinus Nijhoff, 1925), 350.

[2] Mars Moons. https://solarsystem.nasa.gov/moons/mars-moons/in-depth/

[3] Robotic exploration of Mars, The Red Planet. https://exploration.esa.int/web/mars/-/44997-the-red-planet

[4] NASA Experiment Suggests Need to Dig Deep for Evidence of Life on Mars. https://www.nasa.gov/

[5] Yung YL, Chen P, et al. Methane on Mars and Habitability: Challenges and Responses. *Astrobiology*, Volume 18, Number 10, 2018.

[6] Huntress Jr, W.T., Moroz, V.I., Shevalev, I.L. Space Sci. Rev. 107, 541 (2003).

[7] Ulivi, P., Harland, D.M. *Robotic Exploration of the Solar System: Part 3: The Modern Era 1997-2009*. Springer Praxis Books, Berlin, 2012.

[8] Grotzinger, J.P., et al. Mars Science Laboratory Mission and Science Investigation. *Springerlink*, 25 July 2012.

[9] Wiens, R.C., et al. "The ChemCam instrument suite on the Mars Science Laboratory (MSL) rover: Body unit and combined system tests." In: *Space Science Reviews* (2012).

[10] Maurice, S., et al. "The ChemCam Instrument Suite on the Mars Science Laboratory (MSL) Rover: Science Objectives and Mast Unit Description." In: *Space Science Reviews* 170.1 (Sept. 15, 2012), pp. 95-166. ISSN: 00386308. doi: 10.1007/s11214-012-9912-2.

[11] Farley, K.A., Williford, K.H., Stack, K.M., et al. Mars 2020 Mission Overview. *Space Sci Rev*, 2020, 216, 142.

[12] Wiens, R.C., Maurice, S., Lasue, J., et al. “Pre-flight calibration and initial data processing for the ChemCam laser-induced breakdown spectroscopy instrument on the Mars Science Laboratory rover.” *Spectrochimica Acta Part B*, vol. 82, pp. 1-27, 2013.

[13] Maurice, S., Wiens, R.C., et al. "The SuperCam Instrument Suite on the Mars 2020 Rover: Science Objectives and Mast-Unit Description." *Space Sci. Rev.*, Volume 217, 12 April 2021.

[14] The Flash Center for Computational Science, *FLASH User's Guide Version-4.6.2*, University of Rochester, 2019.

Chapter 1

Overview of Mars exploration: key information and characteristics

The primary objective of this first chapter is to establish a foundation by introducing essential concepts pivotal to subsequent discussions and to frame the core ideas of this thesis. It begins by providing a comprehensive overview of Mars, highlighting its multifaceted nature. To lay a robust groundwork for the exploration ahead, the initial emphasis is on accumulating extensive knowledge about the Red Planet. This includes a detailed examination of the Martian surface in search of potential life signs. Although our understanding of biosignatures on Earth guides our search criteria, life on another planet may exhibit distinct chemical compositions, geological structures, and other characteristics. Advanced life detection technologies currently in development aim to define and identify life in its myriad forms. Concurrently, NASA missions actively seek potential biosignatures indicative of both current and past life on Mars. Understanding the distribution and properties of organic carbon molecules, as well as identifying the elemental building blocks of life (carbon, hydrogen, nitrogen, oxygen, sulfur, and phosphorus), could provide crucial insights into potential habitats for life's origin. Mars' atmosphere is primarily composed of carbon dioxide, and the discovery of carbonate minerals on its surface, believed to have formed through prolonged interactions between water and the atmosphere, strongly suggests the historical presence of water, potentially conducive to life. Drawing parallels from Earth's sedimentary rock formations that contain fossilized remains

offering valuable insights into past life forms, we acknowledge the significance of specific environmental conditions and geological formations in preserving such fossils. Chemical and isotopic signatures preserved in Martian sediments, particularly those from lakes and streams, offer critical clues about Mars' potential biological history over extended periods. The chapter then transitions to a detailed examination of the Chemical Camera (ChemCam) instrument aboard the Mars Science Laboratory (MSL) Curiosity rover. This instrument enables remote sensing of the chemical composition of rocks and minerals on Mars, particularly through its laser-induced breakdown spectrometer (LIBS) experimental setup.

1.1 The Red Planet Uncovered

Located fourth in the solar system, Mars is a terrestrial planet. It is sometimes referred to as the "red planet" because of its reddish hue, which is explained by the extensive dispersion of iron-rich rocks that have undergone oxidation (figure 1.1). Even though Mars is smaller than Earth, it has a radius that is only 0.53 times as large. It travels a 227.9 million-kilometer orbit, positioned about 1.5 times the distance between the sun and Earth. Mars is 0.107 times as massive as Earth, with a diameter that just barely exceeds half that of Earth (6,794 km) and a mass calculated to be 6.4185×10^{23} kg using gravity and density data [1]. Mars has a gravitational field that is just 0.38 times as strong as Earth's, making it relatively feeble. Notably, Mars' solar day is longer than Earth's, clocking in at 24 hours, 37 minutes, and 22 seconds. According to Williams [2], the Martian year is equivalent to 1 Earth year and 322 days. At 25.19°, Mars' axial tilt is exactly the same as Earth's, suggesting that the seasons on the two worlds are quite similar. Mars' eccentricity, however, causes its hemispheres to experience seasons with different lengths. Phobos and Deimos, two of Mars' natural satellites, were both found by A. Hall in 1877, a sign of how telescope technology has advanced and improved spatial resolution.

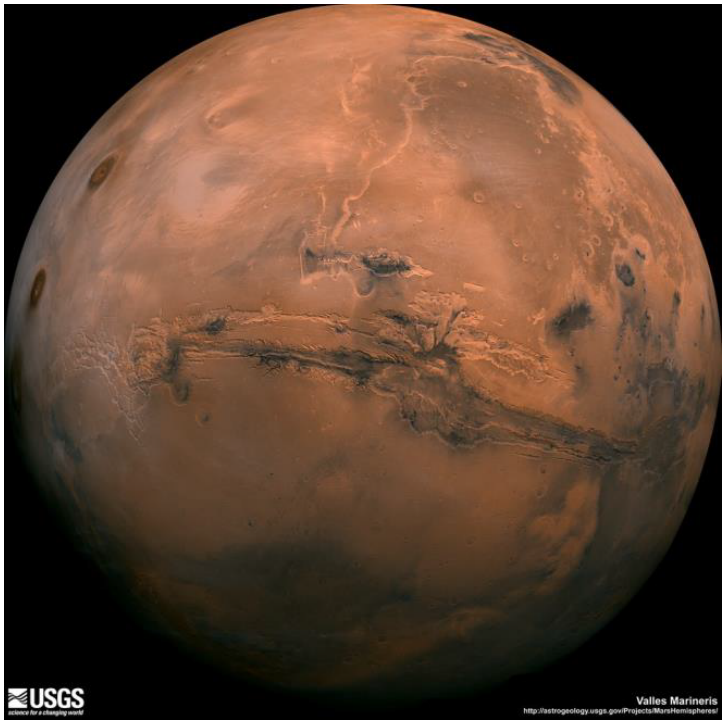

Figure 1.1: A picture of Mars that the Viking Orbiter probe took. The enormous canyon Valles Marineris, which spans more than 2000 km and descends as far as 8 km, can be seen in the image's center. The three volcanoes of Tharsis, whose heights range from 14.2 km to 18.2 km, may also be seen on the left [3].

1.1.1 Formation of the red planet

Our exploration of Mars' history commences in the shadows of ancient times, during an era when the solar system, as we now recognize it, was scarcely in existence—merely a fragment of its current age, around 10 billion years old, and only two-thirds of its present state. The materials destined to form the sun, Mars, Earth, and all living entities floated as gas and dust within the Orion Nebula, as depicted in figure 1.2. In an astonishingly brief span of just a few tens of millions of years, a mere blink on the vast cosmic timeline, the solar system manifested. Subsequent events would forever shape the destiny of the red planet. Approximately 4.52 billion years ago, the sun began radiating light within a disk of gas and dust. The temperature in this vicinity was so elevated that water and other volatile elements existed in a gaseous state. Only compounds with low volatility, such as silicon and magnesium oxides, along with metallic elements, remained solid. Dust particles collided and fused to form porous conglomerates roughly a meter in diameter. These entities, in turn, collided and merged, eventually becoming

kilometer-sized "planetesimals," the foundational components of future planets. Following a relatively calm "infancy," the sun entered a turbulent adolescent phase around 10 million years after its formation. Gases and volatile substances shifted direction for the first time since their origin, propelled outward toward the solar system's periphery due to the force of the solar wind, an intense stream of particles originating from the sun's corona. As matter dispersed, water vapor migrated to regions characterized by lower temperatures. At a distance of approximately 820 million kilometers from the sun (5.5 times the current Earth-Sun distance), water vapor condensed into ice particles. These ice particles combined with dust to shape a planet many times more massive than Earth's present mass. This massive body's gravitational pull attracted significant amounts of hydrogen, giving rise to Jupiter, a process taking less than 10 million years. Saturn, forming at twice the distance from the sun (roughly 1250 million kilometers), took twice as long to come into existence, with an orbital period twice that of Jupiter. Uranus and Neptune experienced analogous origins, consuming icy planetesimals at distances from the sun exceedingly even Saturn's by more than twofold [4].

Figure 1.2: Photo Representing the Exploration of the Orion Nebula: Insights into the Sun's Early Phases [4].

1.1.2 Evolution and growth of the red planet

The terrestrial planets (Mars, Mercury, Venus, and Earth) formed from a haphazard assembly of planetesimals. However, these planets now have an iron core surrounded by a rocky mantle that is less dense and topped by an exterior crust [5]. This differentiation process would have

been impossible unless the interiors of these early planets melted, undergoing a refinement process akin to that found in high-temperature industrial processes. Many planetary scientists first assumed that Mars, for example, went through this process over billions of years, necessitating the building of heat from radioactive element decay within the planet. The examination of Martian meteorites, on the other hand, suggested a significantly faster scenario. These meteorites, which contain iron (elements attracted to iron) and even core-like elements, did not contain the predicted amounts. This confirmed the theory that iron traveled predominantly from Mars' crust to its core during its accretion phase (figure 1.3), building the core in less than 50 million years, and maybe as soon as 20 million years [6]. In reality, the accretion process itself produced enough heat to purify components from the original mixture within planetesimals, similar to a blast furnace. Reactions at the center of a blast furnace produce iron and carbon dioxide. Similarly, interactions with iron oxides and graphite from carbonaceous chondrite meteorites produce metallic iron and carbon dioxide within a planet's magma. Molten iron falls toward the planet's core, accumulating heat in the process. 'Refractory' oxides, such as aluminum oxide and calcium oxide, on the other hand, rise to create a surface layer known as the 'primary crust.' Several variables, including initial size, cataclysmic cratering history, and interior heat loss, contribute to the different evolution of Mars and the other terrestrial planets. Mars was almost half the size of Venus and Earth at the conclusion of the accretion era over 4.45 billion years ago, and significantly less massive [8]. This discrepancy has a substantial impact on the energy stored in the planets. The larger the mass of a planet, the stronger the gravitational acceleration, resulting in more intense impacts during accretion. Furthermore, larger planets have more radioactive materials. Furthermore, larger planets retain more heat, resulting in denser, more opaque atmospheres. While Mercury and the Moon cooled quickly from their tiny sizes, Mars serves as a bridge between these smaller bodies and the larger Earth and Venus [9].

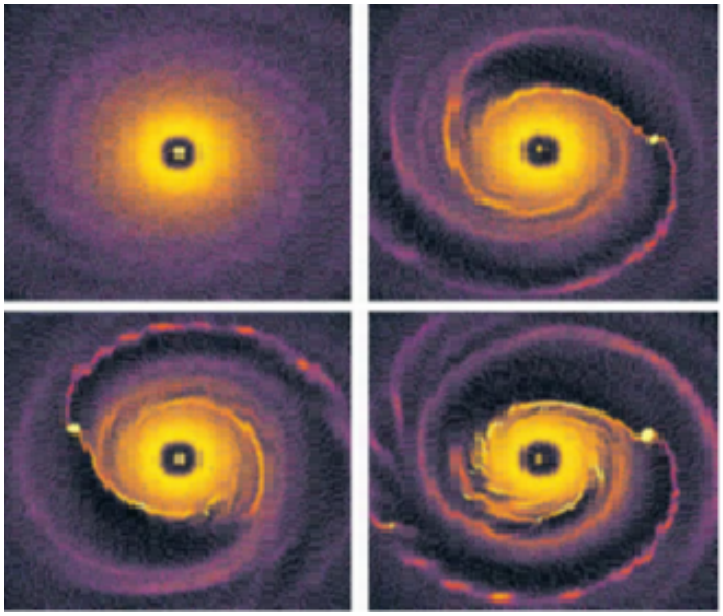

Figure 1.3: A computer simulation illustrates the process of planetary formation, and shows the role of the impacts of planetesimals liberating vast quantities of energy within terrestrial planets during the accretion phase of planet formation [7].

1.1.3 Martian surface: geologic and chemical exploration

There are several distinctive features on Mars that resemble those on Earth, including towering volcanoes, narrow gorges, and vast mountain ranges. Recent advancements in our understanding of Mars' surface geology have been driven by new data from rovers and orbiting satellites [10]. Analysis of the chemical composition of Martian soil and crust reveals that silicon, iron, aluminum, sulfur, magnesium, sodium, potassium, chlorine, titanium, chromium, manganese, and nickel are among the most abundant elements [11]. Geologists have utilized collected images to identify features providing evidence of Mars' watery past. Determining the absolute ages of Martian terrains involves accounting for Martian gravity, orbital distance from the Sun, and referencing lunar samples. This chronological framework has identified three distinct geological eras: the Noachian (spanning 4.6 to 3.7 billion years) [12], the Hesperian (spanning 3.7 to 3.2 billion years) [13], and the most recent Amazonian age [14]. Geological evidence indicates significant ice and liquid water activity on Mars during the Noachian period [15,16], which was widespread across the globe, refuting earlier beliefs that it was confined to the northern hemisphere [17,18,19]. Research also suggests the existence of a Martian Ocean that extended beyond impact crater lakes, covering a substantial portion of the planet's sur-

face during this early era [20,21]. Beyond surface studies, detailed analysis of Mars' chemical landscape has revealed significant hydrogen concentrations hidden beneath the polar regions, at depths less than a meter. This discovery, noted by [22,23], hints at potential ice reservoirs beneath the surface [24,25], adding to speculation about ancient climate conditions and dynamic geological processes. In conclusion, the primary objective of these advanced instruments is to investigate the chemical, isotopic, and mineralogical composition of the Martian surface, aiming to enhance our understanding of Martian evolution and potential habitability.

1.2 Martian atmosphere: key to life's potential

According to NASA's missions, the composition of Mars' atmosphere is dominated by carbon dioxide (CO_2), accounting for approximately 95.32%. Nitrogen (N_2) follows at 2.7%, with argon (Ar) comprising roughly 1.6%. Additionally, trace amounts of other gases have been detected, including water vapor (H_2O) 0.03%, oxygen (O_2) 0.13%, and carbon monoxide (CO) 0.07% [26]↓. On Mars, the average surface pressure is approximately 6 millibars, but it varies with seasons and topography [27]. Pressure also varies significantly with altitude, ranging from about 9 millibars in the deepest basins to approximately 1 millibar at the summit of Olympus Mons, Mars' tallest mountain [28], and can reach up to about 10 millibars in Hellas Planitia valley [29]. Over long geological epochs, numerous complex physical and chemical processes have influenced the evolution and depletion of Mars' atmosphere. Initially denser and more Earth-like, Mars' atmosphere gradually thinned, resulting in the dry desert-like conditions seen today. This intricate transformation has been shaped significantly by factors such as solar wind erosion, magnetic field variations, and volcanic activity [30].

1.2.1 Martian atmospheric climate and weather

Even though the environment on Mars is drastically different from what we are used to on Earth [31], it nonetheless bears a striking resemblance to our planet when compared to other celestial bodies. Mars experiences temperatures that are substantially colder than those on Earth because of its thin atmosphere and greater distance from the sun. Although the tenuous

Martian atmosphere is strong enough to withstand fierce winds and months-long dust storms that cover the entire planet [32], it produces only a weak greenhouse effect that very slightly raises surface temperatures above what they would be without an atmosphere [33]. As a result, large areas of Mars spend most of the year in temperatures below zero. The air pressure is so low that even when daytime readings at low latitudes briefly reach above freezing, water ice changes from solid to vapor without first liquefying [34]. In winter, Mars' temperature can drop to a freezing -125°C at the poles, but on average it stays at a chilly -60°C. At equatorial noon, Mars' temperature rises to a relatively comfortable 20°C (see figure 1.4), which is similar to Earth's. Notably, during the Martian summer at the equator, the planet's surface reaches its maximum known temperature of about 27°C [36].

Mars has four distinct seasons, although due to the Red Planet's eccentric orbit, their lengths vary more wildly than those on Earth. At the northern pole, seasonal fluctuations are particularly noticeable and are symbolized by cyclical waxing and waning [37]. In contrast to the generally stable conditions seen close to the southern pole, these yearly oscillations trigger dynamic patterns of winds, frost development, and cloud systems above the northern pole [38].

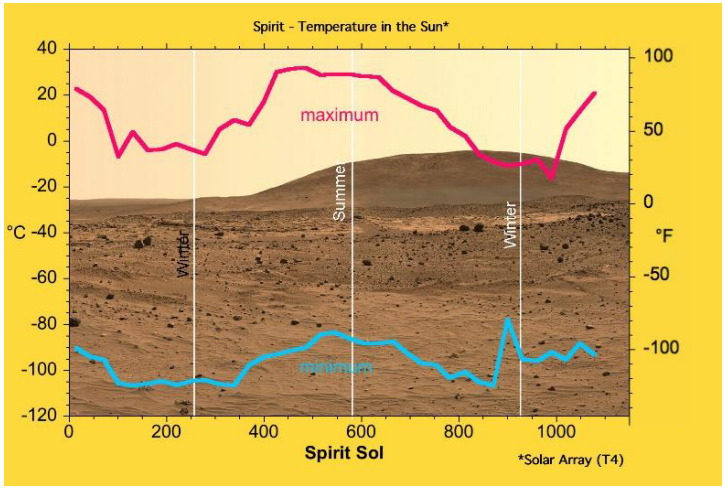

Figure 1.4: Depicting Summer and Winter Temperature Extremes on Spirit's Martian Solar Panels [35].

1.2.2 Investigating the Martian methane mystery

Methane plays a central role in the existence of life. On Earth, methane is produced by both biological and geological processes. Biological sources include microbes called methanogens that thrive in anaerobic environments. Geological sources include processes like serpentinization, which involves a reaction between water and certain minerals in Earth's mantle [39]. On Mars, the discovery of methane (CH_4) in the atmosphere in 2004, at quantities of several tenths of parts per billion (ppb), marked a turning point in the investigation of Mars (see figure 1.5). The Mars Express satellite in orbit facilitated this groundbreaking discovery [41]. The finding sparked intense interest and enthusiasm among scientists. The mystery surrounding Martian methane derives from its predicted susceptibility to rapid disintegration due to the relentless solar winds, leading to a forecasted lifespan of just a few centuries [42].

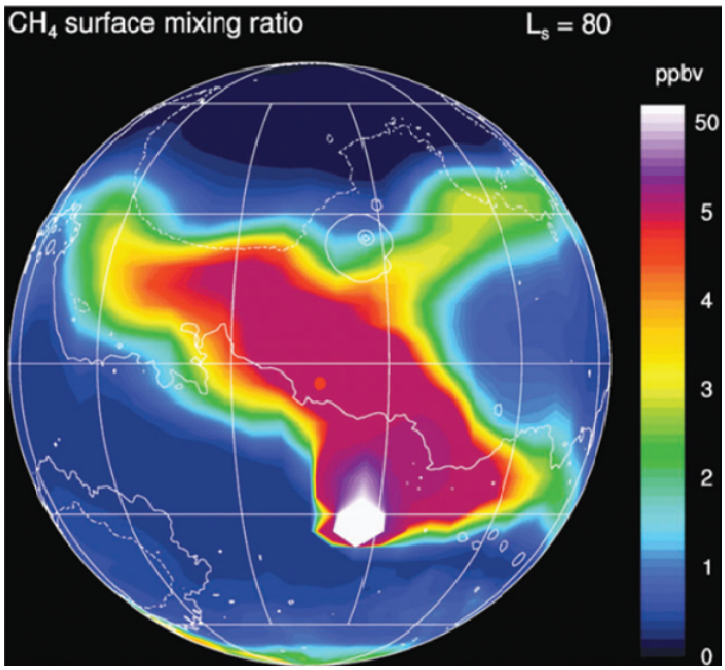

Figure 1.5: Illustrates a Simulation of methane CH_4 abundance [ppb] on the different regions of Mars at the Martz crater at Ls = 80° and a lifetime of 1 month [40].

The existence of methane on Mars suggests that it is continuously produced by an ongoing process. However, its comparatively lengthy lifetime allows for very uniform dispersion throughout the Martian atmosphere due to winds and diffusion. As a result, the observed differences in methane levels across the planet present a puzzling mystery [43]. These variations could represent regional sources of methane emissions or regional sinks that absorb it. Chem-

ically reactive Martian soil is one potential sink that could accelerate methane degradation. If these new sinks are active, an even larger source would be required to sustain the current levels of methane.

Our understanding of the underlying physical and chemical processes driving methane's persistence is seriously questioned by the discovery of the gas on Mars [44]. The two main hypotheses for the origin of Martian methane are the activities of methanogenic bacteria in the Martian soil and volcanic activity. Methane is emitted in huge amounts by Earth's volcanoes, which raises the possibility that it could be present on Mars if there has been recent intense volcanic activity. The absence of sulfur dioxide (SO_2) on Mars, however, challenges the volcanic explanation for Martian methane and supports the biological idea [45,46]. However, there are still other theories about Martian methane. One of these alternatives proposes that heat from deep magma causes reactions between underground moisture and minerals, producing methane but not sulfur dioxide (SO_2). It is estimated that these hydrological processes take place about 10 kilometers below the Martian surface [47]. This theory states that hydrogen is produced via subsurface water-rock interactions, which is then combined with carbon or carbon dioxide (CO_2) in crustal pores to produce methane. While a biogenic source for Martian methane is currently a tempting option, scientists are carefully striving to rule out all other plausible explanations before drawing a firm judgment. At this time, the situation is still obscure.

1.3 LIBS plasma technique and its applications in Martian exploration

The NASA Mars exploration program has seen significant advancements in instrumentation. In 2012, the Mars Science Laboratory (MSL) mission achieved the successful landing of the Curiosity rover in Gale crater on Mars. This mission aimed to investigate biosignature compounds and endure with the goal of comprehending Mars' geological evolution. Curiosity, depicted in figure 1.6, is a six-wheeled robotic rover equipped with a robotic arm capable of brushing, scooping, and drilling. Designed for traversing Mars' rugged terrain, the rover

houses a Rover Body and 80 kg of scientific instruments. Key instruments include the Sample Analysis at Mars (SAM) instrument, which includes a gas chromatograph-mass spectrometer and gas analyzer for detecting organic carbon in rocks, and the Chemistry and Mineralogy (CheMin) instrument, which employs X-ray diffraction to identify mineral types. In addition to its imaging capabilities with cameras such as MAHLI, MARDI, and Mastcam, Curiosity features an alpha-particle X-ray spectrometer (APXS) for analyzing rock and soil composition on-site. Further enhancing its scientific capabilities, Curiosity incorporates a weather station (REMS) for real-time environmental measurements, an active neutron spectrometer (DAN) to search for water in rocks and regolith, and a radiation assessment detector (RAD) for continuous monitoring of solar and cosmic radiation levels [48]. One of the most useful instruments onboard Curiosity is the Chemistry and Camera complex (ChemCam) [50], which carries out the first Laser-Induced Breakdown Spectroscopy (LIBS) experiment on the Martian surface. This advanced technology provides an active remote method to analyze the geochemistry of Martian rocks and soils at a submillimeter scale, at various distances from the rover's mast.

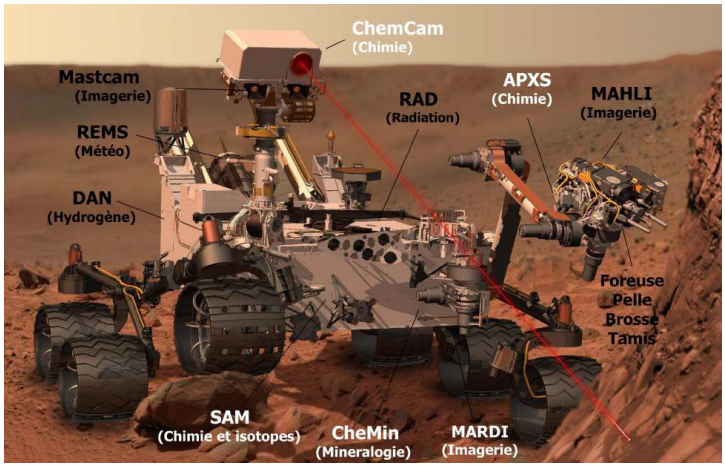

Figure 1.6: Schematic Representation of the NASA Curiosity Rover and Its Payload on the Martian Surface: Utilizing the ChemCam Instrument for Rock Ablation [49].

1.3.1 The foundation of LIBS technique

Laser-Induced Breakdown Spectroscopy (LIBS) is an analytical optical emission spectroscopy method that utilizes a pulsed laser source focused on samples, whether solid, liquid, gaseous, or biological [51]. The laser intensity ranges from several to tens of gigawatts per square centimeter, and the energy per pulse ranges from several to hundreds of millijoules, vaporizing

the sample surface depending on the application. The lengths of the laser pulses typically range from a few femtoseconds to a few nanoseconds. The emitted spectrum of the plasma generated is analyzed using a measurement chain. Within the plasma, excitation energies in the range of several to tens of electron volts (eV) enable a variety of processes for the ions, atoms, and molecules present (see figure 1.7) [53, 54]. These processes include excitation and de-excitation, ionization and inverse bremsstrahlung, dissociation and recombination, as well as the synthesis of molecules and the production of nanoparticles. The resultant light emitted from the LIBS plasma contains valuable information about the sample's composition and is analyzed using atomic emission spectroscopy.

The feasibility of achieving quantitative analysis through LIBS depends on several factors, including the specific characteristics of the laser used (wavelength, pulse duration, strength, and energy), properties of the ambient gas, and pressure effects on the target material's inherent properties [55, 56]. This analytical technique offers flexibility in its application, operating under two primary conditions: local thermal equilibrium (LTE) or non-local thermal equilibrium (NLTE). LIBS has proven to be invaluable for precise material processing, thanks to its unique attributes of high spatial and temporal coherence [57]. This laser-based technique excels in delivering unparalleled precision in energy deposition onto target materials, making it an optimal choice for a wide range of applications, especially in space exploration.

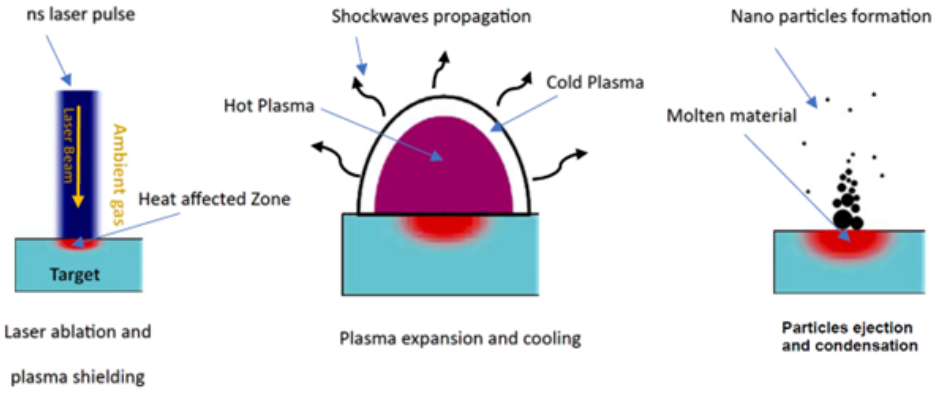

Figure 1.7: Overview of Laser Ablation Processes and Mechanisms (modified from [52]).

1.3.2 Principles of ChemCam spectroscopy

The Chemical Camera (ChemCam) instrument on the Curiosity rover provides a novel technique for analyzing rocks and soils on the surface of Mars. It utilizes a laboratory replica of the LIBS instrument. ChemCam incorporates Laser Induced Breakdown Spectroscopy (LIBS) along with high-resolution remote-micro-imager (RMI) observations. The telescope is used to capture the plasma light, and the device includes a spectrometer to analyze the light emitted by the plasma [58] (see experimental montage in figure 1.8). ChemCam utilizes a pulsed laser with 5 ns pulses and repetition rates ranging from 1 to 10 Hz, operating at a wavelength of 1067 nm. The beam quality, characterized by $M^2 < 3$, allows energies up to 14 mJ to reach the target surface [58].

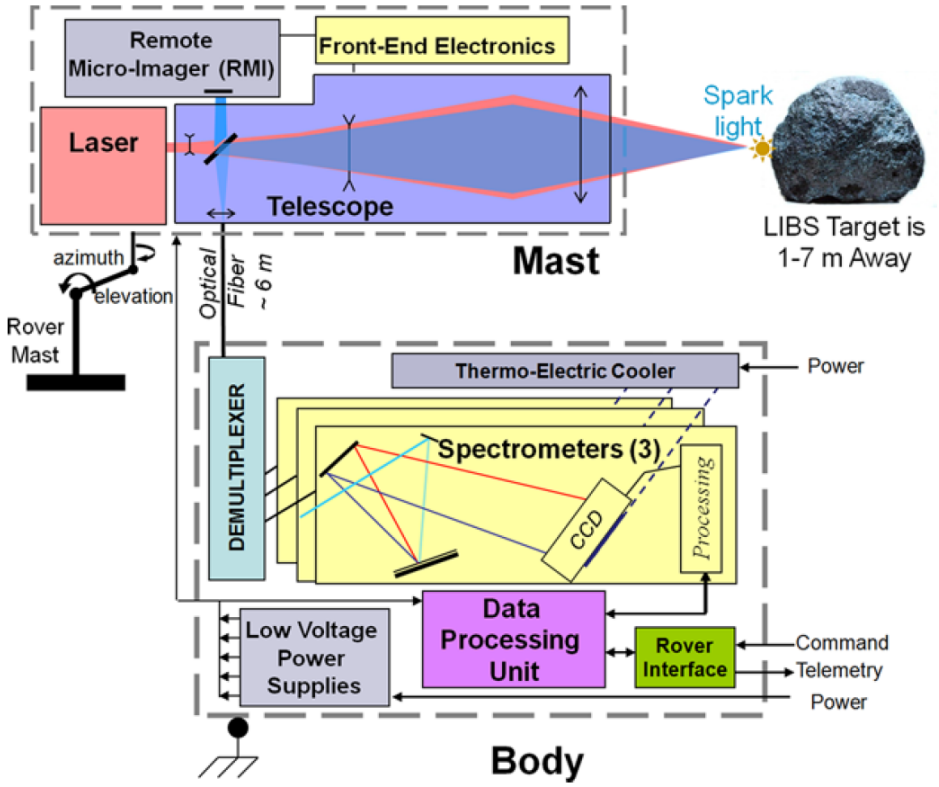

Figure 1.8: Schematic of the ChemCam device setup for LIBS calibration at distances ranging from 1 to 7 m [58].

The precise focusing of the infrared ChemCam laser onto Martian targets, typically situated 2 m to 7 m away, results in a spot diameter ranging from 350 μm (at 2 m) to 550 μm (at 7 m) [59]. This capability enables ChemCam to ablate rock and soil samples through

dust layers, generating plasma. As the plasma cools, electrons, ions, and molecules transition from their excited states, releasing energy in the form of light. This emitted light is captured and subjected to spectroscopic analysis. The ChemCam LIBS spectra encompass wavelengths from ultraviolet (UV) and violet-blue (VIO) to the remainder of the visible and near-infrared (VNIR) ranges [60]. Similar to other analytical methods, ChemCam LIBS techniques have limitations, such as physical and chemical matrix effects that can alter the emission peak intensities used to derive compositional information from samples [61]. Another factor that can influence spectral properties is the nature and thermal characteristics of the target, as well as the distance between the sample and the instrument [62].

Furthermore, ChemCam's record of success has paved the way for further advancements in LIBS technology for Mars exploration. Building on its achievements, two additional LIBS-equipped instruments have been deployed on missions to the Red Planet. SuperCam, a more advanced successor to ChemCam, is part of the scientific payload aboard the Perseverance rover [63]. While the fundamental principle of LIBS analysis remains consistent between ChemCam and SuperCam, there are notable differences in their specifications, including wavelength range, pulse duration, repetition rate, spot size, and spectral resolution. SuperCam builds upon the lessons learned from ChemCam's operations [64], with an enhanced focus on validating models across a broader range of compositions to deepen our understanding of the Martian environment. Looking ahead, LIBS capabilities are closely aligned with future mission goals. These include isotope and water compound classification, identification of rock types and mineral compositions, analysis of surface textures, and detailed characterization of both the Martian surface and subsurface, as well as atmospheric composition [65]. The information gathered through these instruments will be critical in addressing fundamental questions about the potential for life on planets beyond Earth.

References

[1] Barlow, N.G. (2008). *Mars: An Introduction to Its Interior, Surface, and Atmosphere*; Cambridge University Press: Cambridge, UK, p. 129. doi:10.1017/CBO9780511808317.

[2] Greeley, R., B. H. Foing, H. Y. McSween, G. Neukum, P. Pinet, M. van Kan, S. C. Werner, D. A. Williams and T. E. Zegers (2005). Erosion by flowing martian lava: New insights for Hecates Tholus from Mars Express and MER data. *J. Geophys. Res.* 110, E5, E05008. doi:10.1029/2004JE002376.

[3] Valles Marineris: The Grand Canyon of Mars [Online]. NASA. Available: https://science.nasa.gov/resource/valles-marineris-the-grand-canyon-of-mars/

[4] Izidoro, A. et al. (2014). Terrestrial planet formation in a protoplanetary disk with a local mass depletion: A successful scenario for the formation of Mars. *Astrophys. J.* 782:31 (20pp). doi:10.1088/0004-637X/782/1/31.

[5] Forget, F., Costard, F., Lognonné, P. (2006). *Planet Mars: Story of Another World*; Belin.

[6] Brasser, R. et al. (2017). The cool and distant formation of Mars. *Earth Planet. Sci. Lett.* 468, 85-93. doi:10.1016/j.epsl.2017.03.008.

[7] Armitage, P.J., Hansen, B.M.S. (1999). Nature No 402, 9 Dec.1999, p. 20.

[8] Hansen, B.M.S. (2009). Formation of the terrestrial planets from a narrow annulus. *Astrophys. J.* 703:1131-1140. doi:10.1088/0004-637X/703/2/1131.

[9] Baines, K.H. et al. (2007). Experiencing Venus: Clues to the origin, evolution, and chemistry of terrestrial planets via in-situ exploration of our sister world. In *Exploring Venus as a Terrestrial Planet*. Geophys. Monogr. 176, American Geophysical Union, Washington, DC, pp. 171-189.

[10] Clement, M.S. et al. (2021). The early instability scenario: Mars' mass explained by Jupiter's orbit. *Icarus* 367, 114585. doi:10.1016/j.icarus.2021.114585.

[11] McCauley, J.F., Carr, M.H., Cutts, J.A., et al. (1972). Preliminary Mariner 9 Report on the Geology of Mars. *Icarus* 17, 289. doi:10.1016/0019-1035(72)90003-6.

[12] Yoshizaki, T., McDonough, W.F. (2020). The composition of Mars. *Geochim. Cosmochim. Acta*. doi:10.1016/j.gca.2020.01.011.

[13] Hartmann, W. K., & Neukum, G. (2001). Cratering Chronology and the Evolution of Mars. In *Chronology and Evolution of Mars*, eds. R. Kallenbach, J. Geiss, & W. K. Hartmann, Space Sciences Series of ISSI, Dordrecht: Springer Netherlands, pp. 165–194. doi:10.1007/978-94-017-1035-0_6.

[14] Neukum, G., Jaumann, R., Hoffmann, H., et al. (2004). Recent and episodic volcanic and glacial activity on Mars revealed by the High Resolution Stereo Camera. *Nature* 432, 971. doi:10.1038/nature03231.

[14] Mangold, N., Gendrin, A., Gondet, B., LeMouelic, S., Quantin, C., Ansan, V., Bibring, J.-P., Langevin, Y., Masson, P., & Neukum, G. (2008). Spectral and geological study of the sulfate-rich region of West Candor Chasma, Mars. *Icarus*. DOI:10.1016/j.icarus.2007.10.021.

[15] Mellon, M.T., Feldman, W.C., Prettyman, T.H. (2003). The presence and stability of ground ice in the southern hemisphere of Mars. *Icarus* 169, 324-340. doi:10.1016/j.icarus.2003.10.022.

[16] Lewis, K.W., Aharonson, O. (2006). Stratigraphic analysis of the distributary fan in Eberswalde Crater using stereo imagery. *J. Geophys. Res. Planets* 111. doi:10.1029/2005JE002558.

[17] Bouley, S., Craddock, R.A. (2014). Age dates of valley network drainage basins and subbasins within Sabae and Arabia Terrae, Mars. *J. Geophys. Res. Planets* 119, 1302. doi:10.1002/2013JE004571.

[18] Ehlmann, B.L., Anderson, F.S., Andrews-Hanna, J., et al. (2016). The sustainability of habitability on terrestrial planets: Insights, questions, and needed measurements from Mars for understanding the evolution of Earth-like worlds. *J. Geophys. Res. Planets* 121, 1927. doi:10.1002/2016JE005134.

[19] Wilson, S.A., Grant, J.A., Howard, A.D., Buczkowski, D.L. (2018). The nature and origin of deposits in Uzboi Vallis on Mars. *J. Geophys. Res. Planets* 123, 1842. doi:10.1029/2017JE005508.

[20] Warren, A.O., Kite, E.S., Williams, J.-P., Horgan, B. (2019). Through the thick and thin: New constraints on Mars paleopressure history 3.8 – 4 Ga from small exhumed craters. *J. Geophys. Res. Planets* 124, 2793. doi:10.1029/2019JE006178.

[21] Wilson, S.A., Morgan, A.M., Howard, A.D., Grant, J.A. (2021). The global distribution of craters with alluvial fans and deltas on Mars. *Geophys. Res. Lett.* 48, e2020GL091653. doi:10.1029/2020GL091653.

[22] Dickeson, Z.I., Davis, J.M. (2020). Martian oceans. *Astron. Geophys.* 61, 3.11. doi:10.1093/astrogeo/ataa038.

[23] Diez, B. (2009). Détermination de la composition des surfaces planétaires par spectroscopie Gamma et Neutrons. Ph.D. thesis, Centre d'Etude Spatial des Rayonnement, Université Paul Sabatier, Toulouse, France.

[24] Sanin, A.B. et al. (2017). Hydrogen distribution in the lunar polar regions. *Icarus* 283, 20-30. doi:10.1016/j.icarus.2016.06.002.

[25] Sanin, A., Mitrofanov, I., Bakhtin, B., Litvak, M. (2020). Updated mapping of the hydrogen distribution in the lunar polar regions. *22nd EGU General Assembly*. doi:10.5194/egusphere-egu2020-8685.

[26] P. R. Mahaffy et al. (2013). "Abundance and Isotopic Composition of Gases in the Martian Atmosphere from the Curiosity Rover". *Science*. DOI: 10.1126/science.1237966.

[27] Ralph Kahn. (1985). "The evolution of CO2 on Mars". *Icarus*. DOI: 10.1016/0019-1035(85)90116-2.

[28] P. Wolkenberg et al. (2010). "The atmospheric temperatures over Olympus Mons on Mars: An atmospheric hot ring". *Icarus*. DOI: 10.1016/j.icarus.2009.11.005.

[29] Gerhard Wurm. (2019). "A challenge for martian lightning: Limits of collisional charging at low pressure". *Icarus*. DOI: 10.1016/j.icarus.2019.05.004.

[30] Chuanfei, Dong et al. (2018). "Modeling Martian Atmospheric Losses over Time: Implications for Exoplanetary Climate Evolution and Habitability". *The Astrophysical Journal Letters*. DOI: 10.3847/2041-8213/aac489.

[31] Peter L. Read at al. (2015). "The physics of Martian weather and climate: A review". *IOP Publishing*. DOI: 10.1088/0034-4885/78/12/125901.

[32] Ramstad, Robin, et al. (2017). "Global mars-solar wind coupling and ion escape." *Journal of Geophysical Research: Space Physics*. DOI: 10.1002/2017JA024306.

[33] Smith, David E et al. (2001). "Seasonal Variations of Snow Depth on Mars". *Science*. DOI: 10.1126/science.1066556.

[34] Sánchez-Cano, Beatriz, et al. "Spatial, seasonal, and solar cycle variations of the Martian Total Electron Content (TEC): Is the TEC a good tracer for atmospheric cycles?.',*Journal of Geophysical Research: Planets* 123.7 (2018): 1746-1759. DOI: .

[35] `https://mars.nasa.gov/mer/spotlight/20070612.html.`

[36] Mellon, M. T., W. C. Feldman, and T. H. Prettyman (2003), "The presence and stability of ground ice in the southern hemisphere of Mars", *Icarus*, 169, 324–340. DOI: 10.1016/j.icarus.2003.10.022.

[37] Banfield, Don, et al. "The atmosphere of Mars as observed by InSight." *Nature Geoscience* 13.3 (2020): 190-198. DOI: 10.1038/s41586-019-1096-4.

[38] Peter B. Buhler et al. (2017). "How the martian residual south polar cap develops quasi-circular and heart-shaped pits, troughs, and moats". *Icarus*. DOI: 10.1016/j.icarus.2017.01.012.

[39] Santiago Cadena, Francisco J. Cervantes, Luisa I. Falcón and José Q. García-Maldonado. "The Role of Microorganisms in the Methane Cycle". *Frontiers for Young Minds*. 2019. DOI: 10.3389/frym.2019.00133.

[40] Yuk Yung, Pin Chen, Kenneth H Nealson and Sushil Atreya. (2018). "Methane on Mars and Habitability: Challenges and Responses". *Astrobiology* 18(10). DOI: 10.1089/ast.2018.1917.

[41] P. Moulinier et al. (2003). "Mars Express spacecraft: design and development solutions for affordable planetary missions". *Acta Astronautica*. DOI: 10.1016/S0094-5765(02)00158-3.

[42] Vladimir A, Krasnopolsky et al. (2004). "Detection of methane in the martian atmosphere: evidence for life?". *Icarus*. DOI: 10.1016/j.icarus.2004.07.004.

[43] J.L. Grenfell et al. (2022). "Atmospheric processes affecting methane on Mars". *Icarus*. DOI: 10.1016/j.icarus.2022.114940.

[44] Korablev, O., Vandaele, A. C., Montmessin, F., et al. 2019. "No detection of methane on Mars from early ExoMars Trace Gas Orbiter observations", *Nature*, 568, 517. DOI: 10.1038/s41586-019-1096-4.

[45] Montmessin, F., Korablev, O. I., Trokhimovskiy, A., et al. 2021. "A Stringent Upper Limit of 20 Pptv for Methane on Mars and Constraints on Its Dispersion Outside Gale Crater", *Astronomy & Astrophysics*. DOI: 10.1051/0004-6361/202140389.

[46] P. Buford Price. (2010). "Microbial life in martian ice: A biotic origin of methane on Mars?". *Planetary and Space Science*. DOI: 10.1016/j.pss.2010.04.013.

[47] Oehler, Dorothy Z and Etiope, Giuseppe. (2017). "Methane Seepage on Mars: Where to Look and Why". *Astrobiology*. DOI: 10.1089/ast.2017.1657.

[48] Grotzinger, G., et al. (2012). Mars Science Laboratory Mission and Science Investigation. *Space Science Reviews*, 170(1-4), 5-56. DOI: 10.1007/s11214-012-9892-2.

[49] Cousin, A. (2012). LIBS (Laser-Induced Breakdown Spectroscopy) pour l'observation martienne.

[50] Maurice, S., Wiens, R. C., Saccoccio, M., Barraclough, B., Gasnault, O., Forni, O., ... Vaniman, D. (2012). The ChemCam Instrument Suite on the Mars Science Laboratory (MSL) Rover: Science Objectives and Mast Unit Description. *Space Science Reviews*, 170(1–4), 95–166. DOI: 10.1007/s11214-012-9912-2.

[51] Pascal Fichet, Denis Menut, Rene Brennetot, Evelyne Vors, Annie Rivoallan, Analysis by laser-induced breakdown spectroscopy of complex solids, liquids, and powders with an echelle spectrometer, *Appl. Opt.* 40(30) (2003) 6029–6035. DOI: 10.1364/AO.42.006029.

[52] Lagdish P. Singh and Surya N. Thakur. (2007). *Laser-Induced Breakdown Spectroscopy*. Book. Elsevier Science. DOI: 10.1016/B978-0-444-51734-0.X5001-7.

[53] L. Pietanza, G. Colonna, A.D. Giacomo, M. Capitelli. (2010). Kinetic processes for laser induced plasma diagnostic: a collisional-radiative model approach. *Spectrochimica Acta Part B Atomic Spectroscopy* 65(8):616. DOI: 10.1016/j.sab.2010.03.012.

[54] V. Morel, A. Bultel, B. Chéron. (2010). Modeling of thermal and chemical non-equilibrium in a laser-induced aluminum plasma by means of a collisional-radiative model. *Spectrochimica Acta Part B Atomic Spectroscopy*. DOI: 10.1016/j.sab.2010.08.002.

[55] Annemie Bogaerts and Zhaoyang Chen. (2005). Effect of laser parameters on laser ablation and laser-induced plasma formation: A numerical modeling investigation. *Spectrochimica Acta Part B Atomic Spectroscopy* 60(9):1280-1307. DOI: 10.1016/j.sab.2005.06.009.

[56] K. Zehra, et al. (2017). The effect of nature and pressure of ambient environment on laser-induced breakdown spectroscopy and ablation mechanisms of Si. *Laser Part. Beams* 35(3). DOI: 10.1017/S0263034617000477.

[57] F. Anabitarte, A. Cobo, and J. M. Lopez-Higuera. (2012). Laser-Induced Breakdown Spectroscopy: Fundamentals, Applications, and Challenges. *ISRN Spectroscopy*. DOI: 10.5402/2012/285240.

[58] S. Maurice, R. C. Wiens, M. Saccoccio, B. Barraclough, O. Gasnault, O. Forni, N. Mangold, D. Baratoux, S. Bender, G. Berger, J. Bernardin, M. Berthé, N. Bridges, D. Blaney, M. Bouyé, P. Caïs, B. Clark, S. Clegg, A. Cousin, D. Cremers, A. Cros, L. DeFlores, C. Derycke, B. Dingler, D. Vaniman. The ChemCam Instrument Suite on the Mars Science Laboratory (MSL) Rover: Science Objectives and Mast Unit Description. *Space Sci Rev* (2012) 170:95–166. DOI: 10.1007/s11214-012-9912-2.

[59] R.C. Wiens, S. Maurice, J. Lasue, O. Forni, R.B. Anderson, S. Clegg, S. Bender, D. Blaney, B.L. Barraclough, A. Cousin, et al. Pre-flight calibration and initial data processing for the ChemCam laser-induced breakdown spectroscopy instrument on the Mars Science Laboratory rover. *Spectrochim. Acta Part B* 2013, 82, 1–27. DOI: 10.1016/j.sab.2013.02.003.

[60] S. Maurice, S. Clegg, R.C. Wiens, O. Gasnault, W. Rapin, O. Forni, A. Cousin, et al. ChemCam activities and discoveries during the nominal mission of the Mars Science Laboratory in Gale crater, Mar. *J. Anal. At. Spectrom.* 2016. DOI: 10.1039/C5JA00417A.

[61] David M. Surmick, Leon Taleh, Noureddine Melikechi. Effects of Laser Beam Focusing Characteristics on Laser-Induced Breakdown Spectra. *Appl. Spectrosc.* 2021, Vol. 75(2) 127–136. DOI: 10.1177/0003702820961437.

[62] S. Schröder, K. Rammelkamp, D.S. Vogt, O. Gasnault, H.-W. Hübers. Contribution of a

martian atmosphere to laser-induced breakdown spectroscopy (LIBS) data and testing its emission characteristics for normalization applications. *Icarus* 2019, 325, 1–15. DOI: 10.1016/j.icarus.2019.01.018.

[63] S. Maurice, R.C. Wiens, P. Bernardi, P. Caïs. "The SuperCam Instrument Suite on the Mars 2020 Rover: Science Objectives and Mast-Unit Description". *Space Sci. Rev.* 2021, 217(3). DOI: 10.1007/s11214-021-00807-w.

[64] R.B. Anderson, O. Forni, A. Cousin, R.C. Wiens. "Post-landing Major Element Quantification Using SuperCam Laser-Induced Breakdown Spectroscopy". *Spectrochim. Acta B* 2021, 188, 106347. DOI: 10.1016/j.sab.2021.106347.

[65] T. Chen, T. Zhang, H. Li. "Applications of Laser-Induced Breakdown Spectroscopy (LIBS) Combined with Machine Learning in Geochemical and Environmental Resources Exploration". *TrAC Trends Anal. Chem.* 2020, 133, 116113. DOI: 10.1016/j.trac.2020.116113.

Chapter 2

A thermal radiation-hydrodynamics framework for LIBS plasma description

We will describe in this Chapter how we modelled the complex interaction of pulsed laser light with a solid target in the presence of surrounding gas. A portion of the energy given by laser radiation that is carefully focused onto a solid specimen is absorbed by it, leading to a temperature increase and possible phase changes. These alterations depend not only on the properties of the radiation but also on the particular material attributes that are present in the target. The processes by which matter absorbs pulsed laser energy are still not fully understood. As such, a thorough model that clarifies the complex ways in which laser radiation interacts with matter and forecasts the resulting interactions especially when surrounding gas is present has not yet been developed. The key mechanisms that are essential to our models include the following (refer to figure 2.1):

- Laser-target interaction: distinguished by the transfer of laser energy to the material, resulting in processes such as heating, melting, and evaporation or direct sublimation.
- In the presence of a gaseous environment, ablation induces the expulsion of mass, leading to the compression of the surrounding medium and the generation of shockwaves.
- Vapor produced above the target surface expanding and interacting with the ambient environment around it.

- Plasma is formed by absorbing laser radiation in the vapor, along with the plasma's self-absorption of radiation. This triggers the outward expansion of a plasma plume at supersonic speeds into the ambient gas. The plasma plume is characterized by distinct zones, comprising high-density hot and low-density cold plasma regions. The interaction between the plume and the surrounding medium acts to decelerate the plasma expansion.

Plasma formation is dependent on a number of variables, such as the laser's power, focal spot size, wavelength, composition of the target vapor, composition of the surrounding gas, and pressure. The expansion of high-pressure plasma compresses the nearby gas and creates a shock wave, which are the two main ways in which the hot, expanding plasma interacts with the surrounding gas. Thermal conduction, radiative transfer, and heating brought on by the shock wave all contribute to the transfer of energy to the surrounding gas during this expansion [1]. The ambient gas density, temperature, and pressure are all increased by this shock wave, and the shock wave edges are transparent to laser light. A portion of the energy that the plasma absorbs from the surrounding gas is reflected back to it, causing the plasma to cool over time.

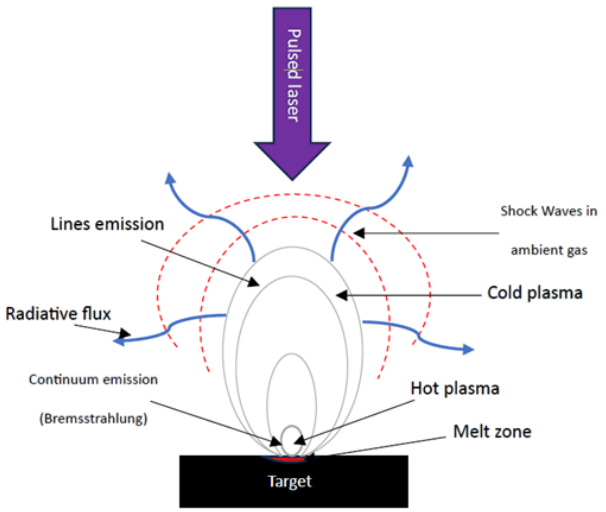

Figure 2.1: Illustrates a diagrammatic representation of the expansion of laser generated plasma in ambient gas.

The aim of this chapter was to formulate a comprehensive theoretical model that accounts for all the intricacies involved in the interaction between the laser and the target, culminating in the emission of plasma. This model accounts for the temporal evolution of the ablation

crater, the formation of the plasma plume, and its expansion under varying ambient gas pressures (both low and high), along with the propagation of shock waves under different laser focusing conditions (changing irradiance). Several models, all based on well-defined theories, have been put out to explain the interaction between a laser and a target. We used a stationary spatial mesh to enable fluid movement into and out of a cell in our simulation, which employed an Eulerian representation for plasma fluid description. The finite-volume Eulerian FLASH radiation-hydrodynamics code [2], which runs on a block-structured mesh using Adaptive Mesh Refinement (AMR) [3], was used in the simulation. When dealing with complicated fluid and dynamically moving mix zones, an Eulerian code reduces mesh entanglement [4], in contrast to Lagrangian algorithms where the mesh moves with the fluid. Conventionally, Lagrangian description of laser-induced plasma codes is used, in which cells move in a co-moving frame along with the fluid. This co-moving frame comes with difficulties, but it also makes hydrodynamic equations simpler and permits a non-uniform initial grid and high resolution of features such as discontinuities and shocks. Compression is particularly useful for implosion investigations since it usually increases resolution. But the Lagrangian frame poses challenges for multi-phase fluid simulation [5], especially when expanding to 2D and 3D dimensions because of increasingly complicated differential operators and possible mesh distortions from turbulence and shear, which can cause simulation failure [6–7]. The distinct advantages of FLASH, encompassing its robust spatial and temporal simulation capabilities, position it as a formidable tool for comprehensively studying LIBS plasma dynamics. This is particularly crucial given the intricate mixing regions and the influence of ambient gas.

2.1 Theoretical Framework of Radiation-Hydrodynamic Approach

The interaction between the laser and the target in the presence of ambient gas is modeled using a three-temperature approach (3T), accounting for electron, ion, and radiation temperatures. In this context, the term "three temperature" signifies that electrons and ions collectively behave as a single fluid (plasma) but are characterized by distinct temperatures ($T_{ele} \neq T_{ion}$).

The model allows for the emission and absorption of radiation, recognizing various physical processes that lead to deviations from thermal equilibrium among electrons, ions, and radiation [8,9]. These processes encompass the effects of shock and laser heating, transportation coefficients, slow equilibration timescales, as well as radiation absorption and emission.

2.1.1 Thermal hydrodynamic model

The Euler equations expressing conservation of mass, momentum, and total energy used to describe the evolution of a hydrodynamics 3T plasma are given by [10,11]:

$$\frac{\partial \rho}{\partial t} + \nabla \cdot (\rho \mathbf{v}) = 0 \tag{2.1}$$

$$\frac{\partial}{\partial t}(\rho \mathbf{v}) + \nabla \cdot (\rho \mathbf{v}\mathbf{v}) + \nabla P_{\text{tot}} = 0 \tag{2.2}$$

$$\frac{\partial}{\partial t}(\rho E_{\text{tot}}) + \nabla \cdot [(\rho E_{\text{tot}} + P_{\text{tot}})\mathbf{v}] = Q_{\text{las}} - \nabla \cdot \mathbf{q} \tag{2.3}$$

Where:

$$P_{\text{tot}} = P_{\text{ele}} + P_{\text{ion}} + P_{\text{rad}} \tag{2.4}$$

$$E_{\text{tot}} = e_{\text{int}} + \frac{1}{2}\mathbf{v} \cdot \mathbf{v} = e_{\text{ele}} + e_{\text{ion}} + e_{\text{rad}} + \frac{1}{2}\mathbf{v} \cdot \mathbf{v} \tag{2.5}$$

Here ρ is the plasma mass density, $\mathbf{v}$ is the fluid velocity, P_{tot} is the total pressure, P_{ele}, P_{ion}, and P_{rad} are the electron, the ion, and radiation pressure, respectively. E_{tot} is the total specific energy which includes the total internal energy e_{int} along with the specific kinetic energy; e_{ele}, e_{ion}, and e_{rad} the specific internal energy of the electrons, ions, and the radiation field respectively. Q_{las} is the energy source due to laser heating. $\mathbf{q}$ is the total heat flux which is the sum of the electron, the ion heat flux and the radiation flux:

$$\mathbf{q} = \mathbf{q}_{\text{ele}} + \mathbf{q}_{\text{ion}} + \mathbf{q}_{\text{rad}} \tag{2.6}$$

Since the plasma is assumed as reactive flows, a separate advection equation must be solved for each species [9]:

$$\frac{\partial(\rho X_i)}{\partial t} + \nabla \cdot (\rho X_i \mathbf{v}) = 0 \tag{2.7}$$

Where X_i is the mass fraction of i species, with the constraint that $\sum X_i = 1$, and the quantity represents the partial density of i fluid.

To address the non-equilibrium 3T plasma components ($T_{ele} \neq T_{ion} \neq T_{rad}$), we incorporate the non-conservative specific internal energy equations for electrons, ions, and the radiation field. These equations are:

$$\frac{\partial \rho e_{ion}}{\partial t} + \nabla \cdot (\rho e_{ion} \mathbf{v}) + P_{ion} \nabla \cdot \mathbf{v} = \rho \omega_{ei}(T_{ele} - T_{ion}) - \nabla \cdot \mathbf{q}_{ion} \tag{2.8}$$

$$\frac{\partial \rho e_{ele}}{\partial t} + \nabla \cdot (\rho e_{ele} \mathbf{v}) + P_{ele} \nabla \cdot \mathbf{v} = \rho \omega_{ei}(T_{ion} - T_{ele}) - \nabla \cdot \mathbf{q}_{ele} + Q_{abs} - Q_{emis} + Q_{las} \tag{2.9}$$

$$\frac{\partial \rho e_{rad}}{\partial t} + \nabla \cdot (\rho e_{rad} \mathbf{v}) + P_{rad} \nabla \cdot \mathbf{v} = -\nabla \cdot \mathbf{q}_{rad} - Q_{abs} + Q_{emis} \tag{2.10}$$

Here, Q_{las} represents the energy source due to laser heating, Q_{abs} represents the increase in electron internal energy due to the total absorption of radiation (heating term), Q_{emis} represents the decrease in electron internal energy due to the total emission of radiation (cooling term).

$\omega_{ei} = C_{v,e}\tau_{ei}$ is the electron-ion coupling term, where $C_{v,e}$ is the electron specific heat and τ_{ei} is the ion/electron equilibration time given by [12]:

$$\tau_{ei} = \frac{3k_B^{3/2}}{2^{7/2}\sqrt{2\pi}q_e^2} \cdot \frac{(m_i T_{ele} + m_e T_{ion})^{3/2}}{(m_e m_i)^{1/2} \bar{Z} n_i l n \Lambda_{ei}} \tag{2.11}$$

Where q_e is the electron charge, m_e is the electron mass, m_i is the ion mass, $\bar{Z}$ is the average ionization as computed by the equation of state (EOS), n_i is the ionic density, and $l_n\Lambda_{ei}$ is the Coulomb Logarithm associated with ion-electron collisions that corresponds to an integration over the impact parameter b as [13]:

$$\ln \Lambda_{ei} = \int \frac{db}{b} = \ln \frac{b_{\max}}{b_{\min}} \tag{2.12}$$

Where the expressions for b_{min} and b_{max} are given by the Spitzer model as:

$$b_{\min} = \max\left(\bar{Z}\frac{q_{\text{ele}}^2}{3k_B T_{\text{ele}}}, \left(\frac{1}{2}\left(\frac{\hbar^4}{3k_B T_{\text{ele}} m_e}\right)^{\frac{1}{2}}\right)\right) \quad and \quad b_{\max} = \left(\frac{k_B T_{\text{ele}}}{4\pi q_{\text{ele}}^2 n_e}\right)^{1/2} \tag{2.13}$$

Here $\hbar$ is the Planck's constant, n_e is the electron number density. The Broglie length λ_B is commonly utilized as the lower integration cut-off (b_{min}), with the upper cut-off (b_{max}) typically set to the Debye length λ_D despite some unresolved controversy on this matter as discussed by [14].

2.1.1.1 Electron and ion heat conduction

A thorough representation of electron and ion transport in collisional plasma hinges on kinetic principles, wherein the electron and ion distribution functions adhere to the Fokker-Planck equation [15, 16]. Nevertheless, the high computational cost associated with this kinetic description renders it impractical for integration into radiation-hydrodynamic codes such as FLASH. As an alternative, the diffusion equation is frequently derived by approximating the solution through a first-order linearized formulation centered on a Maxwellian electron and ion distribution function as [2]:

$$\rho \frac{\partial T_{ele}}{\partial t} = \nabla \cdot \mathbf{q}_{ele} \quad \text{with} \quad \mathbf{q}_{ele} = -K_{ele} \nabla T_{ele} \tag{2.14}$$

$$\rho \frac{\partial T_{ion}}{\partial t} = \nabla \cdot \mathbf{q}_{ion} \quad \text{with} \quad \mathbf{q}_{ion} = -K_{ion} \nabla T_{ion} \tag{2.15}$$

where K_{ele} and K_{ion} are, respectively, the thermal conductivities for electrons and ions, and they are determined using the Spitzer model [12, 17] as:

$$K_{ele} = (\frac{8}{\pi})^{3/2} \frac{k_B^{7/2}}{q_{ele}^4 \sqrt{m_e}} (\frac{1}{1+3.3/\bar{Z}}) \frac{T_{ele}^{5/2}}{\bar{Z} \ln \Lambda_{ei}} \tag{2.16}$$

$$K_{ion} = 3.28 \cdot (\frac{8}{\pi})^{3/2} \frac{k_B^{7/2}}{q_{ele}^4 \sqrt{m_i}} \frac{T_{ion}^{5/2}}{\bar{Z}^4 \ln \Lambda_{ii}} \tag{2.17}$$

Where $\ln \Lambda_{ii}$ is the Coulomb Logarithm associated with ion-ion collisions.

In the case where large values of $|\nabla \cdot \mathbf{T}_{ele}|$ and $|\nabla \cdot \mathbf{T}_{ion}|$ would give rise to unphysically large heat fluxes, this can be handled by the diffusion flux-limiter solver defined by [2]:

$$K_{lim_{ele(ion)}} = \frac{1}{\left[\left(\frac{1}{K_{ele(ion)}} \right)^n + \left(\left| \frac{\nabla T_{ele(ion)}}{\vec{q}_{max_{ele(ion)}}} \right| \right)^n \right]^{\frac{1}{n}}} \quad \text{with} \quad n = \begin{cases} \text{if flux limiter: } n = 0 \\ \text{harmonic flux limiter: } n = 1 \\ \text{Larsen flux limiter: } n = 2 \\ \text{minmax flux limiter: } n \to +\infty \end{cases} \tag{2.18}$$

Where $\vec{q}_{max_{ele}}$ and $\vec{q}_{max_{ion}}$ are the maximum heat flux in the free streaming limit for electron and ion respectively:

$$\vec{q}_{\max_{\text{ele(ion)}}} = \alpha_{e(i)} n_{e(i)} k_B T_{\text{ele(ion)}} \sqrt{\frac{k_B T_{\text{ele(ion)}}}{m_{e(i)}}} \tag{2.19}$$

α_e and α_i are, respectively, the conductivity flux-limiter coefficients for electrons and ions. For laser-produced plasma, these coefficients are significantly less than 1 [12]. It is important to highlight that the ad-hoc flux limiter mitigates the issue of excessive heat transport in regions with sharp temperature gradients. Nevertheless, it lacks the capability to simulate the behavior of non-thermal electrons and ions, which travel at elevated speeds and deposit energy ahead of the primary heat front. This phenomenon becomes notably pronounced, especially when dealing with high laser energy.

The ion number density of electrons and ions is determined by the following expressions as [2]:

$$n_i = N_A \frac{\rho}{\bar{A}}, \qquad n_e = N_A \bar{Z} \frac{\rho}{\bar{A}} \tag{2.20}$$

Where N_A is Avogadro's number and $\bar{A}$ is the average atomic mass.

2.1.1.2 Approaches to detecting and handling shock waves

When a short-pulsed laser is momentarily focused on a target, it can quickly start three processes: particle ejection, vaporization, and absorption of laser energy. Shock wave creation and expansion follow plasma ignition. Three waves are produced by laser absorption in the expanding vapor/plasma: laser-supported radiation (LSR), laser-supported detonation (LSD), and laser-supported combustion (LSC) [18]. In the majority of Laser-Induced Breakdown Spectroscopy (LIBS) plasma detonations, the shock structure is characterized by its thin nature. This thin shock structure implies that the transition from the pre-shock to the post-shock regions occurs over a relatively short distance. This phenomenon is particularly significant in the context of LIBS, where the laser-induced breakdown generates a rapidly expanding and highly dynamic plasma. The thin shock structure influences various aspects of the plasma dynamics, such as temperature gradients, pressure variations [19]. The most straightforward method to model shocks in the three-temperature (3T) plasma description involves recognizing that as the electron entropy s_{el} remains conserved across the shock, all the heating occurring in shocks is directed towards the ions. Following the solution of the Euler equations for total quantities, the electron entropy is determined through an advection equation as [2]:

$$\frac{\partial(\rho s_e)}{\partial t} + \nabla \cdot (\rho s_e \mathbf{v}) = 0 \tag{2.21}$$

Following its determination, the electron entropy serves as a crucial state variable in the equation of state EOS. Utilized in conjunction with the EOS, it calculates the internal energy of electrons $e_{ele} = EOS(\rho, s_e)$, facilitating the segregation of the updated total energy among various species. Notably, the present implementation of the entropy advection method faces compatibility issues with radiation treatment, thereby constraining its applicability primarily to Laser-Induced Breakdown Spectroscopy (LIBS) plasma simulations. A supplementary approach akin to the RAGE model [20] has been incorporated into the FLASH code. This alternative method effectively divides the overall energy variation resulting from hydrodynamic work and shock heating among ions, electrons, and radiation, proportionally based on their

respective partial pressures. This stands in contrast to the entropy advection approach, which accurately distributes energy but is constrained by its inherent limitations. The adoption of this alternative technique contributes to a nuanced understanding of energy dynamics within the system, addressing specific constraints associated with other methods.

2.1.1.3 Viscosity effect

The Reynolds number (*Re*) is a dimensionless parameter that gauges the equilibrium between inertial and viscous forces within a fluid flow, expressed mathematically as follows [21]:

$$Re = \frac{uL}{\nu} \tag{2.22}$$

Where u is the velocity of the fluid, L is the size of the flow, and ν represents the kinematic viscosity of the fluid. This numerical number, which indicates whether inertial or viscous factors dominate the flow, offers important insights into the flow regime. Higher Reynolds numbers are indicative of turbulent flow, which is caused by an abundance of inertial forces; lower Reynolds numbers are caused by an abundance of viscous forces, which is indicative of laminar flow [22]. A key component of fluid dynamics, the Reynolds number affects the general behavior and properties of fluid flow in a variety of systems. The dynamic viscosity (μ_{ion}) of ionized plasma, generated in the absence of magnetic fields, adheres to the Spitzer model [17]:

$$\mu_{ion}[\mathrm{g}\cdot\mathrm{cm}^{-1}\cdot\mathrm{s}^{-1}] = 2.21\times10^{-15}\frac{A_{ion}^{1/2}T_{ion}^{5/2}}{\bar{Z}^4\rho\ln\Lambda_{ii}} \tag{2.23}$$

Here A_{ion} is the average atomic number for ion, $\bar{Z}$ is the average ionization state for ion, and $\ln\Lambda_{ii}$ is the ion-ion Coulomb logarithm. The kinematic viscosity is also computed as:

$$\nu_{ion}[\mathrm{cm}^2\cdot\mathrm{s}^{-1}] = \frac{\mu_{ion}}{\rho} \tag{2.24}$$

Where ρ is the plasma density. These expressions contribute to understanding the dynamic and kinematic characteristics of ionized plasma, crucial for comprehending its behavior in laser-induced material interactions. In conclusion, a physical system described by the Euler

equations is considered non-viscous when the Reynolds number (Re) is much greater than 1 ($Re \gg 1$). In contrast, a viscous flow is typically associated with a Reynolds number much less than 1 ($Re \ll 1$).

2.1.2 Radiation transfer approach

At elevated temperatures in Laser-Induced Breakdown Spectroscopy (LIBS) plasma, radiative heat transfer tends to dominate over electron-thermal conduction. Incorporating effective radiation models is crucial to accurately account for these energy losses in various LIBS applications [23]. Photons, fundamental quanta exhibiting dual characteristics of both waves and particles, play a pivotal role in conveying electromagnetic radiation across a broad spectrum of energies and frequencies, from radio waves to gamma rays [24]. Radiation, in its various forms, propagates through space via wave-particle entities known as photons. Differentiating features of photons are indicated by their wavelength (λ) and frequency (ν), which are connected by the formula $\lambda = \frac{c}{\nu}$, where c is the speed of light. A photon's energy is expressed as $E = h\nu$, where h stands for Planck's constant. Additionally, a vector representing the energy flux in the electromagnetic field can be used to determine a photon's direction. A radiation field is represented in detail by a distribution function, $f(\mathbf{r}, v, \Omega, t)\, dv\, dr\, d\Omega$, where each element represents a large number of photons in a spatial volume, dr, that is centered at point $\mathbf{r}$. This description is complete, including a time component, t, and a direction component represented by the solid angle $d\Omega$ around the unit vector Ω, which gives the orientation of photon motion. The distribution function provides a detailed insight into the behavior of photons in the frequency range of v to $v + dv$ by quantifying their number in this defined space. Such detailed considerations contribute to a comprehensive analysis of the radiation field's dynamics. Each photon carries energy equal to hv and travels with a velocity c. The spectral radiation intensity is determined by this fundamental relationship [25]:

$$I_\nu(\mathbf{r}, \Omega, t)\, dv\, d\Omega = h\nu c\, f(\mathbf{r}, \nu, \Omega, t)\, dv\, d\Omega \tag{2.25}$$

All of the physical characteristics ($\mathbf{r}$ the position, dr the volume, and time t) that were

discussed in the previous paragraph are included in the spectral radiation intensity. It is noteworthy that the direction of this radiation intensity is perpendicular to both the unit vector Ω and an area at point $\mathbf{r}$. From the center, the solid angle beneath which this area element dA (see figure 2.2) is visible is expressed as follows:

$$d\Omega = \frac{dA}{R^2} = \sin\theta \, d\theta \, d\phi \tag{2.26}$$

In the context of spherical coordinates, the expression for an elemental area on the sphere is given by:

$$dA = R^2 \sin\theta \, d\theta \, d\phi \quad \text{such that} \quad 0 \leq \theta \leq \pi \quad \text{and} \quad 0 \leq \phi \leq 2\pi \tag{2.27}$$

For the complete sphere, the solid angle Ω_A is given by the following expression:

$$\Omega = \int_A d\Omega_A = \int_0^{\pi} \int_0^{2\pi} \sin^2\theta \, d\theta \, d\phi = 2\pi \left[-\cos\theta\right]_0^{\pi} = 4\pi \tag{2.28}$$

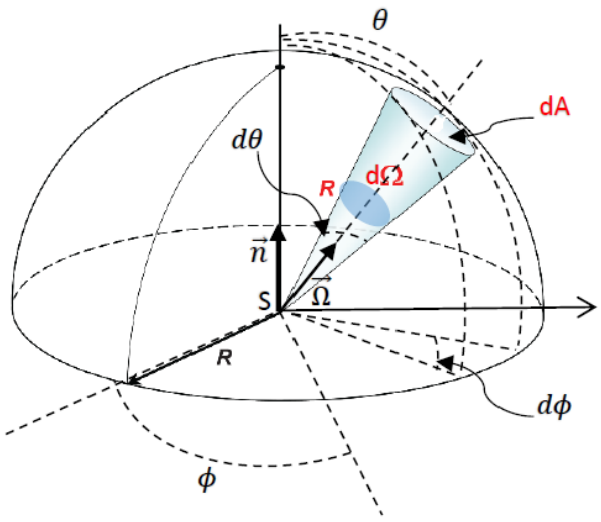

Figure 2.2: Definition and Visualization of the Solid Angle in Spherical Coordinates

2.1.2.1 Radiation transfer equation: A comprehensive overview

Compared to ions and electrons, photons equilibrate more slowly, which frequently leads to longer mean free pathways. When a ray of light traverses a volume, as shown in figure 2.3,

the output intensity at a thickness increment dz is $I_\nu + dI_\nu$. The volume's absorption coefficient κ_ν characterizes the decrease in output intensity due to absorption within the volume. Furthermore, any emitted light along the ray's propagation direction contributes to an increase in output intensity, quantified by the volume's emission coefficient η_ν. An essential tool for tracking changes in photon distribution over time and space is the radiation transport equation. In the context of simulations, the FLASH code, in particular, utilizes the specific intensity, denoted as I_ν, to comprehensively model photon behavior. This equation is a fundamental component in elucidating the intricate dynamics of radiation within the simulated environment, as expressed in the following equation [26]:

$$\frac{1}{c}\frac{\partial I_\nu}{\partial t} + \Omega \cdot \nabla I_\nu = \eta_\nu - \rho\chi_\nu I_\nu = -\kappa_\nu(I_\nu - S_\nu) \qquad \text{with} \qquad \kappa_\nu = \rho\chi_\nu \tag{2.29}$$

Where χ_ν is the opacity (in units of cm^2/g), ρ is the total mass density, ν is the frequency, and $S_\nu = \eta_\nu/\kappa_\nu$ is the source function.

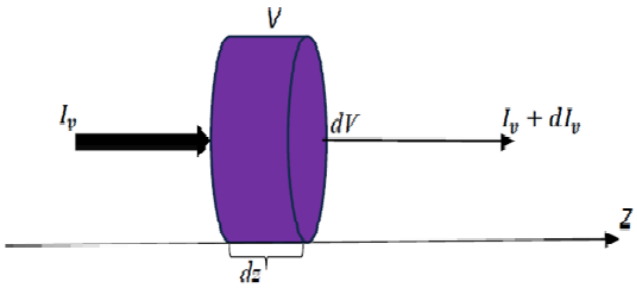

Figure 2.3: Light's Intensity Modification while Traveling through a Volume V with Cross-Sectional Area dV

The overarching challenge of the radiative transport equation lies in determining its solution. An alternative approach for an approximate solution to the transfer equation has been introduced, such as the method of spherical harmonics [27, 28]. This method shares similarities with the moment's method, except that the moments with the solid angle are selected to capitalize on the orthogonality of the spherical harmonic's basis [29]. The moments method, also referred to as the diffusion approximation [30], computes successive moments of the ra-

diation transport equation considering the solid angle. Another technique is the method of discrete ordinates [31], employing a discrete representation of the directional variation of radiative intensity, resulting in a system of n simultaneous partial differential equations (PDE). This method is versatile, allowing for application to any order and accuracy, and has gained extensive use in addressing radiation transport challenges within the LIBS plasma field. Finally, the radiation transport equation can be tackled using statistical methods, employing sampling techniques in the Monte Carlo method [32]. Nevertheless, this method is subject to an unavoidable statistical error if the number of samples is insufficient. The transport equation is intricately linked within FLASH to the electron internal energy through a set of interrelated variables and parameters. This coupling is vital for accurately representing the dynamic interplay between the transport of energy carried by photons and its impact on the internal energy of electrons.

$$\frac{\partial u_{\text{ele}}}{\partial t} = \int_0^{\infty} \int_0^{4\pi} (\alpha_\nu I_\nu - \eta_\nu)\, d\nu\, d\Omega \tag{2.30}$$

Where $u_{\text{ele}} = \rho \cdot e_{\text{ele}}$ represents the electron internal energy, and e_{ele} is the internal electron energy.

2.1.2.2 Multigroup radiation diffusion approach

In the context of the approximate methods employed to solve the radiation transport equation, an additional consideration involves addressing the frequency dependence of radiation intensity. Two prominent approaches are often adopted: one entails iterating over all frequencies, while the other samples the photon energy range using the multigroup diffusion (MGD) approach. The latter method, MGD, is utilized in the FLASH code. The approximation in MGD involves categorizing the energy of photons into discrete groups, facilitating a more manageable computational approach. The total radiation flux, absorption (Q_{abs}), and emission (Q_{emis}) terms in equations (2.9) and (2.10) account for contributions from each energy group. The absorption term (Q_{abs}) quantifies the increase in electron internal energy resulting from the

total absorption of radiation and is expressed as [2]:

$$Q_{\text{abs}} = \sum_{g=1}^{N_g} Q_{\text{abs},g} \qquad \text{with} \qquad Q_{\text{abs},g} = -c\sigma_{a,g}u_{\text{rad},g} \tag{2.31}$$

The term Q_{emis} denotes the reduction in electron internal energy resulting from the overall emission of radiation. It is assumed that the plasma emits radiation according to a Planck spectrum, and the emission opacity varies across different energy groups:

$$Q_{\text{emis}} = \sum_{g=1}^{N_g} Q_{\text{emis},g} \quad \text{with} \quad Q_{\text{emis},g} = \sigma_{e,g}\frac{a_r T_{ele}^4}{15\pi^4}\left[P(x_g+1) - P(x_g)\right] \tag{2.32}$$

$$P(x) = \int_0^x \frac{x'^3}{e^{x'}-1}dx' \qquad \text{with} \qquad x = \frac{h\nu}{k_B T_{ele}} \tag{2.33}$$

$\sigma_{e,g}$ is the emission opacity for group g, a_r is the radiation constant, and $P(x)$ is the Planck integral. In the FLASH code, the frequency spectrum is divided into N_g groups, where g is defined by the frequency range from ν_g to ν_{g+1}, using the multi-group diffusion (MGD) solver. The evolution of radiation energy density for each group, $u_{\text{rad},g}$, is described by the following partial differential equations as [2]:

$$\frac{1}{c}\frac{\partial u_{\text{rad},g}}{\partial t} - \nabla\cdot\left(\frac{1}{3}\sigma_{t,g}\nabla u_{\text{rad},g}\right) + \sigma_{a,g}u_{\text{rad},g} = \sigma_{e,g}\frac{aT_{ele}^4}{15\pi^4}\left[P(x_g+1) - P(x_g)\right] \tag{2.34}$$

The total specific radiation energy density is related to $u_{\text{rad},g}$ through:

$$u_{\text{rad}} = \rho u_{\text{rad}} = \sum_{g=1}^{N_g} u_{\text{rad},g} \tag{2.35}$$

The electron internal energy must be updated to account for the emission and absorption coefficients for each group g through the following equation:

$$\frac{\partial u_{\text{ele},g}}{\partial t} = \sum_g \left(\sigma_{a,g}u_{\text{rad},g} - \sigma_{e,g}\frac{aT_{ele}^4}{15\pi^4}\left[P(x_g+1) - P(x_g)\right]\right) \tag{2.36}$$

Where $\sigma_{t,g}$ is the transport opacity for group g. In the following section, we will review how the

multigroup mean opacities $\sigma_{a,g}$, $\sigma_{e,g}$, and $\sigma_{t,g}$ necessary to solve the radiation transport equation, are calculated. The multigroup radiation diffusion and electron internal energy equations are partial differential equations (PDE) that we address at each time level n using an implicit treatment. This approach involves discretizing the equations in time to iteratively update the solution at each time step. The specific form of discretization allows for a robust numerical solution that captures the dynamic behavior of the system accurately.

$$\frac{1}{c}\cdot\frac{u_{\mathrm{rad},g}^{n+1}-u_{\mathrm{rad},g}^{n}}{\Delta t}-\nabla\cdot\left(\mathbf{D}_{\mathrm{rad},g}^{n}\nabla u_{\mathrm{rad},g}^{n+1}\right)+\sigma_{a,g}^{n}u_{\mathrm{rad},g}^{n+1}=\sigma_{e,g}^{n}\frac{a(T_{ele}^{n})}{15\pi^{4}}\left[P(x_{g+1}^{n})-P(x_{g}^{n})\right] \quad (2.37)$$

$$\frac{u_{\mathrm{ele},g}^{n+1}-u_{\mathrm{ele},g}^{n}}{\Delta t}=\sum_{g}\left\{\sigma_{a,g}^{n}u_{\mathrm{rad},g}^{n+1}-\sigma_{e,g}^{n}\frac{a(T_{ele}^{n})}{15\pi^{4}}\left[P(x_{g+1}^{n})-P(x_{g}^{n})\right]\right\} \quad (2.38)$$

Where Δt is the time step length. These equations are solved at each time step. $\mathbf{D}_{\mathrm{rad},g}^{n}$ represents the diffusion coefficient, and the flux limiter constrains the radiation flux in each group to the free streaming limit. The maximum radiation flux is determined by the following expression as [2]:

$$q_{\mathrm{rad,max}}=\gamma_{\mathrm{rad}}cu_{\mathrm{rad},g}^{n} \quad (2.39)$$

The coefficient γ_{rad} is set to one for the most experiment, which is what is physically most realistic. In general, the MGD method proves valuable for simulating the behavior of radiation in dynamic environments, enabling the consideration of emission and absorption coefficients for each frequency group. This approach strikes a balance between accuracy and computational efficiency, making it well-suited for studying complex radiative processes.

2.2 Plasma spectrum modeling

During the initial stages of Laser-Induced Breakdown Spectroscopy (LIBS) plasma, the prevalent electron population arises from the ionization processes induced by inverse Bremsstrahlung and multiphoton absorption. This instigates the formation of a time-dependent continuum radiation spectrum, which can endure for several hundreds of nanoseconds. As the plasma boundary expands along the laser beam direction, both particle temperature and number density experience a decline. Following the cessation of the laser pulse, the plasma undergoes

cooling as the power source is terminated, and processes such as de-excitation and recombination become predominant. Consequently, during the relaxation phase of the plasma, the emission spectrum is characterized by distinct spectral lines originating from charged ions and neutral atoms [33]. The interpretation of most LIBS spectra necessitates an analysis to discern the non-local thermodynamic equilibrium (NLTE) conditions of the plasma, leading to the development of various diagnostic approaches based on plasma models. Among these, radiation transfer equations represent one of the most prevalent methods [34, 35]. The determination of the intensity of a spectral emission at a specific frequency involves solving the radiation transport equation, as outlined in the preceding section (2.29). The radiation transport equation is expressed in the following form:

$$\left[\frac{1}{c}\frac{\partial}{\partial t} + \Omega \cdot \nabla\right] I_\nu(\mathbf{r},\mathbf{v},\Omega,t) = \eta_\nu(\mathbf{r},\Omega,\mathbf{v},t) - \alpha_\nu(\mathbf{r},\Omega,\mathbf{v},t) I_\nu(\mathbf{r},\mathbf{v},\Omega,t) \tag{2.40}$$

In a one-dimensional planar geometry, considering an intensity I_ν at a frequency ν emanating orthogonally from a radiating plasma medium:

$$\left[\frac{1}{c}\frac{\partial}{\partial t} + \frac{\partial}{\partial z}\right] I_\nu(z,\Omega,\nu,t) = \eta_\nu(z,\Omega,\nu,t) - \alpha_\nu(z,\Omega,\nu,t) I_\nu(z,\Omega,\nu,t) \tag{2.41}$$

In numerous LIBS plasmas, it is commonly assumed that the temporal variation of radiation intensity is relatively smaller than its spatial variation, leading to the neglect of the time dependence of the radiation field. In the case of time independence, the transfer equation takes the following form:

$$\frac{dI_\nu(z,\nu,\Omega)}{dz} = \eta_\nu(z,\Omega,\nu) - \alpha_\nu(z,\Omega,\nu) I_\nu(z,\Omega,\nu) \tag{2.42}$$

Boundary conditions for typical LIBS plasmas can be defined such that there is no incoming radiation from the outermost boundary. Additionally, for the symmetry condition about the center, the derivative of the specific intensity at the center is assumed to be zero. The absorption coefficient κ_ν and emission coefficient η_ν can be expressed in relation to absorption cross sections [36], denoted as $\alpha^{ff}(\nu)$ for free-free transitions, $\alpha^{bf}(\nu)$ for bound-free transitions, and $\alpha^{bb}(\nu)$ for bound-bound transitions, as indicated in reference [36].

The line shape function, denoted as $L(\Gamma, \Delta\nu)$, is described by the Voigt line profile, as presented in [49]:

$$L_V(\Gamma, \Delta\nu) = \frac{H(\Gamma, \Delta\nu, \Delta\nu_D)}{(\pi^{1/2}\Delta\nu_D)} \tag{2.43}$$

The Voigt function, denoted as $H(\Gamma, \Delta\nu, \Delta\nu_D)$. In this expression, $\Delta\nu$ represents the photon frequency shift from the line center and $\Delta\nu_D$ is the Doppler shift. Γ accounts for the damping factor arising from natural, Doppler (thermal), and collisional broadening:

$$\Gamma = \Gamma_{\text{nat}} + \Gamma_{\text{Dop}} + \Gamma_{\text{Col}} \tag{2.44}$$

The transport equation (2.41) can be expressed as a function of the optical depth τ_ν and the source function, denoted as $S_\nu = \frac{\eta_\nu}{\kappa_\nu}$:

$$\frac{dI_\nu(z,\nu)}{d\tau_\nu(z,\nu)} = I_\nu(z,\nu) - S_\nu(z,\nu) \tag{2.45}$$

The optical depth is a measure of the number of mean-free paths a photon at frequency ν travels along the line-of-sight from 0 to z. Defined as a dimensionless quantity, it encapsulates the absorption coefficient of the material integrated over the line of sight from the outer surface. The optical depth is expressed as [37]:

$$\tau_\nu(z,\nu) = \int_0^z \kappa_\nu dz' \tag{2.46}$$

The optical thickness of the plasma plays a key role in shaping the observed spectral features and is a fundamental parameter in the study of radiative transfer within the plasma. It determines the extent to which photons are absorbed and scattered as they traverse the material. When the optical depth is less than unity, the plasma is described as optically thin. Conversely, when the optical depth exceeds unity, the plasma is considered optically thick. In the absence of external illumination, the radiation spectrum's intensity within a plasma is obtained by solving the equation (2.45). The resulting solution is articulated as [38]:

$$I_\nu = S_\nu(1 - e^{-\tau_\nu}) \tag{2.47}$$

For plasma optically thin ($\tau_\nu \ll 1$), all emitted photons exit the plasma without being reabsorbed. Under the additional assumptions of plasma homogeneity and independence of the emission coefficient with respect to z, the intensity is given as follows:

$$I_\nu = S_\nu \tau_\nu \tag{2.48}$$

In the case of an optically thick plasma ($\tau_\nu \gg 1$), the radiation emitted by a plasma slice can undergo reabsorption by neighboring slices, resulting in changes to the overall spectrum radiance of the global plasma. Under these conditions, the intensity expression is modified to:

$$I_\nu = S_\nu \tag{2.49}$$

In conclusion, the radiation emitted by both LTE and NLTE plasmas, corresponding to the change in electron kinetic energy, is distributed continuously across all frequencies for continuum radiation. Unlike line radiation, which exhibits intensity concentration at a line-center frequency [39], continuum radiation displays a broad frequency distribution. The analysis of continuum radiation proves invaluable for identifying impurity ions within a Laser-Induced Breakdown Spectroscopy (LIBS) plasma. This strategy capitalizes on the efficiency of heavier elements in generating Bremsstrahlung (free-free) and recombination (bound-free) radiation, especially at elevated temperatures with multiple ionization stages. The evaluation of the continuum radiation ratio emerges as a critical temperature diagnostic tool for high-temperature plasmas, offering insights into the thermal characteristics of the system. Additionally, line emission spectrum measurements provide complementary information, facilitating the extraction of essential plasma parameters, notably the electron temperature [40]. This multifaceted approach, combining continuum radiation and line emission spectrum analysis, contributes to a comprehensive understanding of the intricate plasma dynamics and material composition under various conditions.

2.3 Impact of laser focusing conditions and target material on LIBS plasma behavior

The formation and evolution of plasma in laser-induced breakdown spectroscopy (LIBS) depend on a wide range of factors. Chief among these are the intrinsic properties of the target material and the characteristics of the incident laser pulse. Parameters such as irradiance, wavelength, and focal spot size exert significant influence on the process [41]. These factors critically affect the laser-induced ablation mechanism, governing the efficiency of material removal and vapor generation, which may be ionized to varying degrees. The term "target" is used here in a broader sense to encompass both the sample and its surrounding environment, including the ambient gas.

In particular, during plasma expansion, the composition and pressure of the ambient gas play a crucial role. Previous studies have extensively examined the complex interactions between the laser and the target, yielding valuable insights into these phenomena [42, 43]. Moreover, detailed records have been compiled regarding the melting and evaporation dynamics at metal surfaces under laser irradiation [44]. A key finding from these investigations is the importance of thermal conductivity in facilitating efficient vaporization of the target material—regardless of whether it is in a solid, liquid, or gaseous state—especially during expansion into a vacuum [45]. Notably, whether the plasma plume develops in a vacuum or within an ambient gas, it typically exhibits supersonic expansion perpendicular to the target surface.

However, a critical process in the LIBS technique lies in the configuration of the focusing optics. One essential parameter in this context is the lens-to-sample distance (LTSD), as emphasized in reference [46]. LTSD directly influences the spot size of the laser beam, and even slight variations in the beam waist radius can cause substantial changes in both the laser fluence $F_{\text{las}} = \frac{E_{\text{las}}}{\pi r^2}$ and the irradiance incident on the target. The plasma behavior differs markedly depending on the spot size. When a small-diameter beam is used, the laser energy induces a more spherical plasma expansion, resulting in a relatively uniform distribution of the ablated material in all directions. Conversely, with a larger-diameter beam, the wider focal spot minimizes transverse expansion, causing the plasma to undergo a primarily longitudinal expansion

along the direction normal to the target surface, as illustrated in Figure 2.4. This variation in expansion geometry significantly affects the density of the material in the laser path. Specifically, a larger beam diameter results in a denser plasma along the laser axis. This increased density leads to a stronger screening effect, predominantly due to inverse Bremsstrahlung absorption, which enhances the efficiency of laser energy deposition and redistribution within the plasma [47, 48].

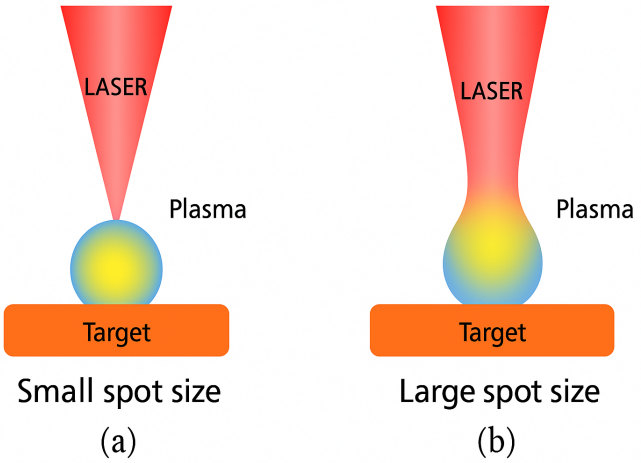

Figure 2.4: Persistent Impact of the spot size diameters on plasma formation.

The aim of this chapter was to formulate a comprehensive theoretical model that accounts for all the intricacies involved in the interaction between the laser and the target, culminating in the emission of plasma. This model accounts for the temporal evolution of the ablation crater, the formation of the plasma plume, and its expansion under varying ambient gas pressures (both low and high), along with the propagation of shock waves under different laser focusing conditions (changing irradiance).

On the other hand, detailed compositional analysis may benefit from the use of larger laser spot sizes to minimize the effects of sample heterogeneity. To overcome the spatial limitations imposed by smaller spot sizes, techniques such as laser beam scanning or sample translation can be employed. However, these methods must carefully account for potential oscillations or artifacts caused by overlapping laser pulses. It is important to recognize that various factors such as the laser beam profile, pulse duration, and the physical and chemical properties of the target material influence laser–matter interactions. Consequently, careful selection of the laser spot size is critical in laser-based analyses to achieve optimal results while minimizing

undesirable effects [49].

In general, LIBS plasma is often described using the local thermodynamic equilibrium (LTE) model due to the dominance of electron-driven processes, particularly at later delay times. However, because of the plasma's spatial inhomogeneity and rapid temporal evolution at early times especially during the initial laser–material interaction in the presence of ambient gas—a non-local thermodynamic equilibrium (NLTE) model provides a more accurate description.

References

[1] J. F. Ready, "Effect of High Power Laser Radiation," Academic Press, New York (1971).

[2] The Flash Center for Computational Science, FLASH User's Guide Version-4.6.2, University of Rochester, 2019.

[3] MacNeice P., Olson K. M., Mobarry C., De Fainchtein R. and Packer c., PARAMESH: A parallel adaptive mesh refinement community toolkit, Computer Physics Communications, 2000, 126, 330.

[4] Takahiro Yamada and Fumio Kikuchi. "An arbitrary Lagrangian-Eulerian finite element method for incompressible hyperelasticity". Computer Methods in Applied Mechanics and Engineering Volume 102, Issue 2, January 1993, Pages 149-177. DOI: 10.1016/0045-7825(93)90106-8.

[5] Alexandre Caboussat. " Numerical Simulation of Two-Phase Free Surface Flows ", Arch. Comput. Meth. Engng. Vol. 12, 2, 165-224 (2005).

[6] Roman Yurchak, Experimental and numerical study of accretion-ejection mechanisms in laboratory astrophysics HAL Id: tel-01338614 https://theses.hal.science/tel-01338614, 28 Jun 2016.

[7] Benson, D. (1992). "Computational methods in Lagrangian and Eulerian hydrocodes". In: Computer Methods in Applied Mechanics and Engineering.

[8] Tzeferacos P., Fatenejad M., Flocke N., Graziani C., Gregori G., Lamb D. Q., Lee D., Meinecke J., Scopatz A., and Weide K., FLASH MHD simulations of experiments that study shock generated magnetic fields, High Energy Density Phys., 2015, 17(Part A), 24.

[9] Gray Radiation Hydrodynamics with the FLASH Code for Astrophysical Applications, E. Chatzopoulos and K. Weide 2019 ApJ 876 148.

[10] Mihalas D. and Mihalas B. W., Foundations of radiation hydrodynamics, Oxford University Press, New York, 1984, ISBN 0-19-503437-6.

[11] Castor J. I., Radiation Hydrodynamics, Cambridge University Press, 2004, ISBN: 9780511536182.

[12] Atzeni S. and Meyer-Ter-Vehn J., The Physics of Inertial Fusion: Beam Plasma Interaction, Hydrodynamics, Hot Dense Matter, International Series of Monographs on Physics, Oxford University Press, 2004, ISBN 9780198562641.

[13] Brysk H., Campbell P.M., Hammerling P., Thermal conduction in laser fusion, Plasma Phys., 1974, 17, 473.

[14] Mulser, P et al. (2014). "Revision of the Coulomb logarithm in the ideal plasma". Phys. Plasmas 21, 042103. https://doi.org/10.1063/1.4870501.

[15] F. CHEN, Introduction to Plasma Physics and Controlled Fusion. Plenum Press, New York, 1984.

[16] J.L. DELCROIX AND A. BERS, Physique des Plasmas. InterEditions, Paris, V. 2 (1994).

[17] Spitzer L., Physics of Fully Ionized Gases, Interscience Publishers, New York, 1962, ISBN: 13-978-0486449821.

[18] J. F. Ready, "Effect of High Power Laser Radiation," Academic Press, New York (1971).

[19] Alexander Miloshevsky, Sivanandan S. Harilal, Gennady Miloshevsky, and Ahmed Hassanein. (2014). "Dynamics of plasma expansion and shockwave formation in femtosecond laser-ablated aluminum plumes in Argon gas at 0.5 and 1 atmosphere". Physics of Plasmas. DOI:10.1063/1.4873701.

[20] Gittings, M., et al. 2008, Computational Science and Discovery, 1, 015005.

[21] Vaclav Uruba. "On Reynolds number physical interpretation". AIP Conference Proceedings 2000(1):020019. DOI:10.1063/1.5049926.

[22] Bill Rehm, Arash Haghshenas, Amir Saman Paknejad and Jerome Jacob Schubert. "Situational problems in MPD". Managed Pressure Drilling (pp.39-80). DOI:10.1016/B978-1-933762-24-1.50008-5.

[23] Zel'dovich, Y.B. and Y.P. Raizer, *Physics of Shock Waves and High-Temperature Hydrodynamic Phenomena* (Dover Books on Physics). 2012, Meneola, New York: Dover Publications, Inc. ISBN: 048613508X, 9780486135083.

[24] Credit: NASA's Imagine the Universe: https://imagine.gsfc.nasa.gov/science/toolbox/emspectrum2.html.

[25] Miloš Stanić. *HUNTSVILLE, ALABAMA*. 2013. "Effects of Plasma Jet Parameters, Ionization, Thermal Conduction, and Radiation Stagnation Conditions of an Imploding Plasma Liner".

[26] Yuri Ralchenko, Hyuh-Kyung Chung, Howard A. Scott, and Stephanie B. Hansen. 2016. "Modern Methods in Collisional-Radiative Modeling of Plasmas". *Springer Series on Atomic, Optical and Plasma Physics* 90. DOI: 10.1007/978-3-319-27514-7.

[27] Jeans, J.H. The equations of radiative transfer of energy. *Monthly Notices Royal Astronomical Society*, 28–36 (1917).

[28] Barichello, L. & C. Siewert (1998). "On the equivalence between the discrete ordinates and the spherical harmonics methods in radiative transfer". In: *Nuclear science and engineering*, pp. 79–84.

[29] Garcia, R. & C. Siewert (1986). "A generalized spherical harmonics solution for radiative transfer models that include polarization effects". In: *Journal of Quantitative Spectroscopy and Radiative Transfer*.

[30] Pomraning, C.T. (1973) *The Equations of Radiation Hydrodynamics*. Oxford: Pergamon.

[31] Chandrasekhar, S (1960). *Radiative transfer*. Dover Publications. DOI: https://ui.adsabs.harvard.edu/abs/1960ratr.book.

[32] Whitney, B.A. (2011). "Monte Carlo Radiative Transfer". *Bulletin of the Astronomical Society of India*, Vol. 39, p. 101-127 (2011). Bibliographic Code: 2011BASI...39..101W.

[33] A.F. Nikiforov, V.G. Novikov, V.B. Uvarov, *Quantum-Statistical Models of Hot Dense Matter: Methods for Computation Opacity and Equation of State*, Birkhauser Verlag, Basel, Boston, Berlin, 2005.

[34] Ya.B Zel'dovich, Yu.P. Raizer, *Physics of shock waves and high temperature hydrodynamics phenomena*, Academic Press, New York, 1967.

[35] J. Richter, *Plasma diagnostics*, in: W. Lochte-Holtgreven (Ed.), North-Holland Publishing, Amsterdam, 1968.

[36] J.J. Macfarlane, *IONMIX - a code for computing the equation of state and radiative properties of LTE and non-LTE plasmas*, Comput. Phys. Commun. 56, 259-278 (1989).

[37] MacFarlane, I. Golovkin, P. Wang, P. Woodruff, N. Pereyra, *SPECT3D – a multidimensional collisional-radiative code for generating diagnostic signatures based on hydrodynamics and PIC simulation output*, High Energy Density Phys. 3 (1–2) (2007) 181–190.

[38] G. Perez-Callejo, J.S. Wark, S.J. Rose. (2019). *Radiation transfer in cylindrical, toroidal and hemi-ellipsoidal plasmas*. Journal of Quantitative Spectroscopy and Radiative Transfer, Volume 235, p. 24-30. DOI: 10.1016/j.jqsrt.2019.06.008.

[39] F. Barbato, D. Scarpellini, A. Malizia, P. Gaudio, M. Richetta, L. Antonelli. (2015). *X-ray High-Resolution Spectroscopy for Laser-Produced Plasma*. Physics Procedia. DOI: 10.1016/j.phpro.2015.02.015.

[40] Hyun-Kyung Chung, Mau H. Chen, Yuri Ralchenko, Richard W. Lee. (2008). *FLYCHK At NIST : The Population Kinetics Modeling Capability*. URL: http://nlte.nist.gov/fly.

[41] Hyun-Kyung Chung, Mau H. Chen, Yuri Ralchenko, Richard W. Lee. (2008). *FLYCHK At NIST: The Population Kinetics Modeling Capability*. URL: http://nlte.nist.gov/fly.

[42] R.E. Russo, X.L. Mao, C. Liu, J. Gonzalez. (2004). *Laser assisted plasma spectrochemistry: laser ablation*. J. Anal. Atom. Spectrom. 19: 1084–1089.

[43] C. Gray-Morgan. (1975). *Report on Progress in Physics*. Rep. Prog. Phys. 38: 621.

[44] X.Y. Chen, Z.G. Liu. (1999). *Interaction between laser beam and target in pulsed laser deposition: laser fluence and ambient gas effects*. Appl. Phys. A 69(Suppl 1): S523–S525. DOI: 10.1007/s003390051460.

[45] J. F. Ready. (1971). *Effect of High-Power Laser Radiation*. Academic Press, New York.

[46] Yongsheng Ling, Yu Wang, Wenbao Jia, et al. (2023). *A novel method for correcting the effect of the lens-to-sample distance change on the signal intensity in laser-induced breakdown spectroscopy*. Anal. Methods 15(5). DOI: 10.1039/D3AY00280B.

[47] S. S. Harilal. (2007). *Influence of spot size on propagation dynamics of laser-produced tin plasma*. J. Appl. Phys. 102(12): 123306. DOI: 10.1063/1.2822450.

[48] Xingwen Li, Wenfu Wei, Jian Wu, Shenli Jia. (2013). *The influence of spot size on the expansion dynamics of nanosecond-laser-produced copper plasmas in atmosphere*. J. Appl. Phys. 113(24): 243301. DOI: 10.1063/1.4812580.

[49] Selen Unaldi, Alexandre Rondepierre. (2020). *Beam size dependency of a laser-induced plasma in confined regime: Shortening of the plasma release. Influence on pressure and thermal loading*. Opt. Laser Technol. 135: 106689. DOI: 10.1016/j.optlastec.2020.106689.

Chapter 3

Numerical simulation of LIBS Graphite plasma under Martian conditions: results and discussion

odeling laser-induced breakdown spectroscopy (LIBS) plasma experiments under both LTE and NLTE conditions using radiation-hydrodynamic codes involves considering diverse physical phenomena, including the hydrodynamic evolution of the plasma, thermal heat conduction, radiation transport in the diffusion limit, and laser energy deposition. In our thesis, we specifically investigate the complex interplay between laser-induced plasma dynamics and the ambient gas environment designed to replicate Mars' conditions, encompassing its chemical composition and pressure [1]. To achieve a comprehensive simulation, we employ the multi-physics radiation-hydrodynamics code FLASH [2], which utilizes an Eulerian representation with a fixed spatial mesh to facilitate plasma movement into and out of cells. FLASH also integrates adaptive mesh refinement (AMR) capabilities. We complement this with the IONMIX code, which generates non-local thermodynamic equilibrium (NLTE) data for equations of state (EOS) and opacity, thereby enhancing simulation accuracy. This comprehensive approach allows us to faithfully represent the intricate interactions among various physical processes within LIBS plasma, maintaining realism in environmental conditions. FLASH is recognized as a versatile multi-physics simulation code applicable to a wide range of physical

systems, including experiments involving laser-induced plasma and extending to astrophysical phenomena [3]. Numerous studies have used FLASH to validate simulation processes related to laser-produced plasmas [4].

Within the FLASH framework, the laser beam is discretized into rays that traverse the target, and the modeling of laser energy deposition during propagation uses geometrical optics, a topic to be discussed in detail in the following section. This energy is absorbed through inverse Bremsstrahlung by electrons, transferring it to ions and initiating plasma generation. The modular structure of FLASH enables users to selectively simulate specific physics problems tailored to their research goals, highlighting its adaptability as a powerful tool for addressing challenges in LIBS plasma modeling and numerical simulation. In the next section, we will provide a comprehensive description of the Adaptive Mesh Refinement (AMR) grid used in our study, along with an overview of the results obtained from simulating graphite LIBS plasma under Martian conditions using the FLASH code.

3.1 Ray-tracing in the geometric optics approximation to model laser energy deposition

The laser beam is composed of multiple rays, and their paths are traced within the domain, influenced by the local refractive index of each cell. The calculation of laser power deposited in a cell involves the consideration of inverse Bremsstrahlung power, reliant on the local electron temperature and electron number density gradients within the cell. The laser beam's energy deposition is determined using the laser ray trace approximation, applicable to both planar and cylindrical geometries. Within the geometric optics approximation, the trajectory of a laser wave is characterized as the movement of a ray with unit mass through the potential field, as articulated in reference [5]:

$$V(r) = \frac{c}{2}\eta(r)^2 \tag{3.1}$$

Where, η represents the index of refraction of the medium, which is presumed to vary over spatial scales much greater than the wavelength of the laser wave. The function $\eta(r)$ is treated

as constant during the time it takes for the ray to traverse the cell domain, indicating a frozen medium. However, it is permitted to vary from one time step to the next. In the context of non-relativistic unmagnetized plasma, the refractive index is expressed as:

$$\eta(r) = \sqrt{1 - \frac{\omega_p^2(r)}{\omega^2}} = \sqrt{1 - \frac{n_e(r)}{n_c}} \tag{3.2}$$

$$n_c = \left(\frac{m_e}{4\pi}\right)\left(\frac{\omega}{q_{ele}}\right)^2 \tag{3.3}$$

Here, $\omega_p(r)$ denotes the plasma frequency at the specific location r, ω represents the laser frequency, $n_e(r)$ stands for the electron number density at the given location r, and n_c is the critical density at which the laser frequency equals the plasma frequency. Within the framework of geometrical optics approximation, the equation of the ray is derived through the linearization of the eikonal equation, as detailed in reference [6]:

$$\frac{d^2r}{dt^2} = -\frac{c}{2}\nabla\left(\frac{n_e(r)}{n_c}\right) \tag{3.4}$$

The Taylor expansion provides the electron number density and electron temperature in the vicinity of a specific location as follows [5]:

$$n_{e0} = \langle n_e \rangle + \langle \nabla n_e \rangle \cdot (\mathbf{r}_0 - \langle \mathbf{r} \rangle) + \mathscr{O}(\varepsilon^2) \tag{3.5}$$

$$T_{ele0} = \langle T_{ele} \rangle + \langle \nabla T_{ele} \rangle \cdot (\mathbf{r}_0 - \langle \mathbf{r} \rangle) + \mathscr{O}(\varepsilon^2) \tag{3.6}$$

Here $\langle\rangle$ denotes a zone average, symbolizing the center of the cell. The ray equation of motion, as indicated in Eq. (3.4), is then expressed as:

$$\frac{d^2\mathbf{r}}{dt^2} = -\left(\frac{c^2}{2}\right)\langle n_e(\mathbf{r})\rangle n_c \tag{3.7}$$

This illustrates that in cases where n_e exhibits linearity within a cell, the rays trace a parabolic trajectory through the cell (refer to figure 3.1). For a separable 2nd order ordinary differential equation (ODE), we can formulate the following expressions for ray velocity and position as

functions of time:

$$\mathbf{V}(t) = \mathbf{V}_0 - \left(\frac{c^2}{2}\right) n_c \langle n_e \rangle \mathbf{t} \tag{3.8}$$

$$\mathbf{r}(t) = \mathbf{r}_0 + \mathbf{V}_0 t - \left(\frac{c^2}{4}\right) n_c \langle n_e \rangle t^2 \tag{3.9}$$

Where $\mathbf{r}_0$, $\mathbf{V}_0$ are the initial position and velocity of the ray, respectively.

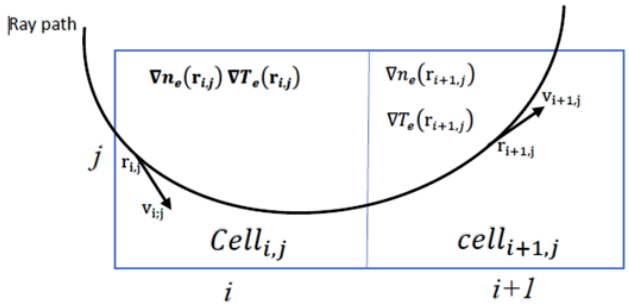

Figure 3.1: Illustration of the Laser Ray Trajectory in Two Simulation Cells in 2D Using the Kaiser Algorithm.

The electron number density is not generally continuous. The Kaiser algorithm [5] addresses this issue by implementing Snell's law at the interfaces between cells, as described by the following equations:

$$\eta \sin\theta = \eta' \sin\theta' \tag{3.10}$$

$$\sqrt{1 - \frac{n_e}{n_c}} \sin\theta = \sqrt{1 - \frac{n'_e}{n_c}} \eta' \sin\theta' \tag{3.11}$$

3.1.1 Power deposition by inverse Bremsstrahlung

As rays inherently represent spatial curves, they lack information regarding radiation intensity or spatial extent transverse to their direction. Their characteristics are solely determined by their frequency, velocity, and power, with the latter two attributes typically exhibiting spatial dependence. The power (P) of an electromagnetic wave undergoes depletion through the inverse Bremsstrahlung (ib) process. The rate of this power loss is dictated by a 1st order

ordinary differential equation (ODE) as [7]:

$$\frac{dP}{dt} = -\nu_{ib}(t)P \tag{3.12}$$

As a ray traverses through a cell, its power (energy) diminishes over time:

$$P(\Delta t) = P_0 \exp\left[-\int_0^{\Delta t} \nu_{ib}(\mathbf{r}(t))dt\right] \tag{3.13}$$

The position $\mathbf{r}(t)$, at time Δt is provided by Here $\langle\rangle$ denotes a zone average, symbolizing the center of the cell. The ray equation of motion, as indicated in Eq. (3.2), is then expressed as: as:

$$\mathbf{r}(\Delta t) = \mathbf{r}_0 + \mathbf{V}_0\Delta t - \frac{c^2}{4n_c\langle n_e\rangle}\Delta t^2 \tag{3.14}$$

The inverse Bremsstrahlung frequency factor ν_{ib} (representing the rate of energy loss), is expressed by the formula:

$$\nu_{ib} = \frac{n_e}{n_c}\nu_{ei} \qquad \text{with} \qquad n_e \leq n_c \tag{3.15}$$

Where ν_{ei}, the electron-ion collision frequency, is given by the following expression:

$$\nu_{ei} = \frac{4}{3}\sqrt{\frac{2\pi}{m_e}}\frac{n_e\bar{Z}q_{ele}^4\ln\Lambda_{ei}}{(k_BT_{ele})^{3/2}} \tag{3.16}$$

Here, $\bar{Z}$ is the average ionization number of the plasma, and $\ln\Lambda_{ei}$ is the Coulomb logarithm representing the natural logarithm of the Debye number and is taken as [7]:

$$\ln\Lambda_{ei} = \ln\left[\frac{3}{2\bar{Z}q_{ele}^3}\sqrt{\frac{k_B^3T_{ele}^3}{\pi n_e}}\right] \tag{3.17}$$

The inverse Bremsstrahlung frequency is contingent upon the electron temperature and the electron number density, both of which vary with position. Given that the position undergoes changes over time, this frequency inherently becomes a function of time as well:

$$\nu_{ib}(\mathbf{r}) = \nu_{ib}(t) = \frac{4}{3}\sqrt{\frac{2\pi}{m_e}}\frac{\bar{Z}q_{ele}^4}{n_ck_B^{3/2}}\frac{n_e[\mathbf{r}(t)]^2\ln\Lambda_{ei}[\mathbf{r}(t)]}{T_{ele}[\mathbf{r}(t)]^{\frac{3}{2}}} \tag{3.18}$$

The laser beam encodes detailed information about its shape and orientation in the Flash code. By giving the lens and target's coordinates, orientation is defined. The size and shapes of the lens and target cross-sectional areas, as well as the cross-sectional ray power distribution law, define the form of the laser (see figure 3.2).

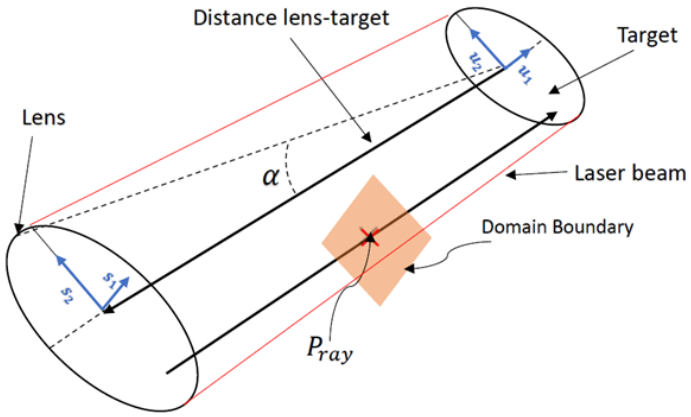

Figure 3.2: Illustrates the Laser Beam Shape and the Process of Setting Up Rays Between the Beam's Lens and Target Area.

The power distribution of the rays inside the beam at launch is explained by the beam cross-section power function. In contrast, ray tracing with the randomization of ray parameters, including position and direction, is a common practice in Lagrangian hydrodynamic programs. This approach aims to achieve uniform irradiation within simulated cells of varied sizes in the ablation region, primarily to mitigate laser imprint [8].

3.2 Describing material properties: EOS and Opacity explanations

As discussed in the preceding section, the utilization of a ray-tracing approach for laser energy deposition through collisional absorption offers a simplified representation of laser plasma interaction (LPI). However, inherent uncertainties arise due to the description of material properties related to the target and surrounding gas, including the equation of state (EOS), opacity, and radiative transfer properties [9]. It must be underlined that certain kinetic processes are inevitably missed when using a fluid description. The fluid approach offers an averaged and

macroscopic picture of plasma dynamics, ignoring minute details related to collisions and interactions between individual particles [10]. Although fluid descriptions are typically conceptually straightforward and computationally efficient, their inherent simplicity makes it more difficult for the model to represent finer-scale phenomena. When examining scenarios with complicated particle dynamics in Laser-Induced Breakdown Spectroscopy (LIBS) plasma, especially in non-equilibrium settings or with fast temporal shifts, some kinetic processes are excluded more than others.

Accurately quantifying both the equation of state and opacity necessitates a meticulous understanding of the atomic-level population distributions of particles within a plasma. In our current study, we employ a collisional-radiative (CR) non-LTE model, chosen for its versatility in computing both opacity coefficients and the equation of state. Notably, this model exhibits robust performance across a broad spectrum of temperatures, demonstrating equal efficacy at low and high-temperature regimes. The determination of the number density of the i-fold ionized ion n_i is governed by the non-LTE rate equation in steady-state, expressed as follows:

$$n_{i+1}n_e^2\alpha_{i+1} + n_{i+1}n_e\beta_{i+1} + n_{i+1}n_eD_{i+1} - n_in_eC_i = 0 \tag{3.19}$$

where α_{i+1}, β_{i+1}, and D_{i+1} represent the coefficients corresponding to collisional recombination, radiative recombination, and dielectronic recombination, respectively. Collisional recombination is a 3-body process involving two electrons and an ion. The electronic collisional ionization coefficient is denoted by C_i. The electron density is represented by n_e, while the ion density for the specific element in the mixture is $n_m = \sum n_i$, where the ion densities are determined by the steady-state solution of equation (3.19):

$$\frac{n_{i+1}}{n_i} = \frac{C_i}{n_e\alpha_{i+1} + \beta_{i+1} + D_{i+1}} \tag{3.20}$$

The above equations together with the consistency condition $n_m = \sum n_i$ are solved to obtain all n_i values and the average degree of ionization for each chemical species. All the coefficients for collisional recombination, radiative recombination, dielectronic recombination, and the electronic collisional ionization formula are detailed in [11].

3.3 Grid description

In order to solve the differential equations for radiation transmission and hydrodynamics numerically, the simulation domain must be spatially discretized. One typical framework used in laser-induced plasma (LIP) is a Lagrangian mesh [12], in which cells move with the fluid. Hydrodynamic equations are made simpler with this co-moving frame, allowing for a non-uniform initial grid and good feature resolution, including discontinuities and shocks. It is especially useful for implosion studies since the compression frequently improves resolution. However, difficulties with the Lagrangian frame [13] in multi-phase fluid simulations occur, particularly when extending to 2D and 3D dimensions, because of potentially problematic mesh distortions from shear and turbulence, which can result in simulation failures [14]. On the other hand, within the framework of an Eulerian grid description [15], a fixed mesh offers the advantage of accommodating multi-phase flow and handling arbitrarily large deformations, particularly in 2D and 3D dimensions. However, there are issues with Eulerian grids since they can deform, particularly when there are intricate flows or free surface boundaries present. This could lead to inaccurate simulation results. This strategy was underutilized until higher-order techniques that effectively addressed and overcome these constraints emerged, despite its intrinsic diffusivity. While the Arbitrary Lagrangian-Eulerian (ALE) method [16, 17] is commonly utilized to tackle challenges associated with Eulerian grids, its application introduces increased simulation complexity. Despite its effectiveness in handling moving boundaries and large deformations, the added intricacy necessitates careful consideration of computational resources and implementation intricacies for accurate and efficient results. The Adaptive Mesh Refinement (AMR) technique [18] has emerged as a pivotal strategy to address the limitations associated with Eulerian grids. Unlike fixed grids, which maintain a uniform resolution throughout the entire computational domain, AMR introduces a dynamic and flexible approach to grid generation. The key innovation lies in the adaptive adjustment of grid resolution based on the evolving features of the simulated phenomenon. In regions where intricate details or rapid changes occur, the AMR algorithm selectively refines the grid, allocating more computational resources to those specific areas. Conversely, in regions where the flow is relatively smooth or less complex, the grid can be coarsened, thereby optimizing computa-

tional efficiency [19]. This dynamic adaptation allows FLASH to more accurately represent the underlying physics while simultaneously mitigating the computational cost associated with uniformly high resolutions, unlike Lagrangian code[20].

3.3.1 The structure of the grid

Adaptive mesh refinement (AMR) computational grid is a complex architecture made up of many blocks with different physical cell sizes. A tree data structure establishes the complex hierarchical connections between these components. The largest cells are found in the root blocks, which are at the top of the tree. When the hierarchy descends, the children or progeny blocks inherit smaller cells, which are referred to as refined (see figure 3.3(a)). As referenced [21], this hierarchical structure enables the AMR grid to dynamically modify its resolution, concentrating on more granular information in certain places where refinement is critical. Currently, block-structured AMR in the FLASH code is implemented by default using the PARAMESH (Parallel Adaptive Mesh Refinement) package [22]. The base spatial grid unit in this AMR method is made up of a block of simulation cells surrounded by several layers of guard cells (see figure 3.3(a)). The mesh construction process is refined and derefined by PARAMESH, which is responsible for introducing data into guard cells from nearby blocks or, if the physical domain is bounded, from an external border. This block structure guarantees that calculations within a block stay independent of the remainder of the simulation for localized FLASH concerns, such as hydrodynamic dynamics and radiation diffusion. The guard cells provide all necessary information, especially for spatial derivatives (nguard). The type of solver being used has a significant impact on how many guard cells are required. The PARAMESH AMR simulation grid comprises diverse blocks, each with varying cell sizes (see Figure 3.3(b)). Each block encompasses $n_{xb} \times n_{yb} \times n_{zb}$ interior cells and a set of guard cells, forming a hierarchical arrangement through a tree data structure (see figure 3.3(c)).

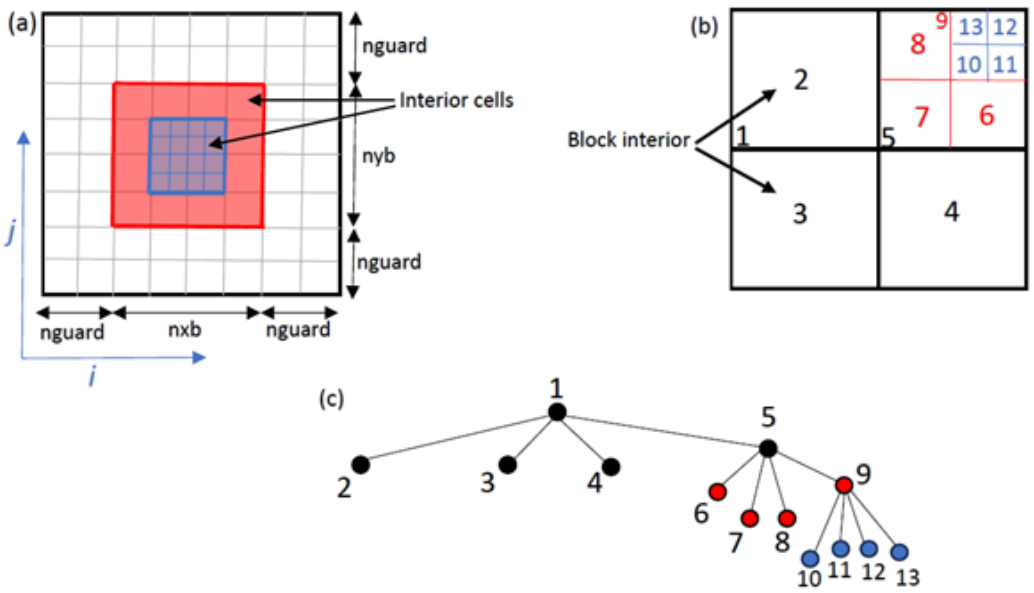

Figure 3.3: (a) Visualizing a 2D single block showing interior cells (nbx=nby=4) bounded by the guard cells (nguard=2), (b) The interior block structure of AMR grid (c) the tree data structure of AMR grid.

3.3.2 Dynamic resolution in simulation grid (refinement/derefinement operation)

The PARAMESH AMR grid's refinement/derefinement process is essential for dynamically modifying grid resolution in response to changing features in simulated phenomena. Certain factors, like as density or temperature, might start the refinement process. To capture emergent plasma features in that location, for example, mesh refinement is triggered by a change in density. Refinement levels of $l_{\text{ref\_max}}$ result in $2^{l\text{ref\_max}-\text{ref\_min}}$ with $1 \leq l_{\text{ref\_min}} \leq l_{\text{ref\_max}}$ (see figure 3.4). Changes in the mesh resolution are determined by criteria that are applied to every physical variable in the simulation and are checked at every time step. A refinement criterion derived from the one-dimensional error estimator E_i on a uniform mesh is utilized by PARAMESH in FLASH. The following is the expression of the estimator, which is a modified second derivative normalized by the average gradient over one computing cell as [23]:

$$E_i = \frac{|u_{i+2} - 2u_i + u_{i-2}|}{|u_{i+2} - u_i| + |u_i - u_{i-2}| + \varepsilon(|u_{i+2}| + 2|u_i| + |u_{i-2}|)} \tag{3.21}$$

Where u_i (temperature or density) represents the refinement test value in the i-th cell, and

ε is the latter factor. This factor is weighted by a small constant to allow the filtering out of oscillations with high spatial frequency. In the context of multiple dimensions, the preceding expression can be extended by applying the Euclidean norm to both the first and second-order derivatives. This entails considering the magnitude of the vector composed of the derivatives in each dimension as:

$$E_{i_x i_y i_z} = \left[\frac{\left(\sum_{pq} \left(\frac{\partial^2 u}{\partial x_p \partial x_q} \right)^2 \right)}{\left(\sum_{pq} \left[\frac{1}{2\Delta x_q} \left(\left| \frac{\partial u}{\partial x_p} \right|^2_{i_q+1} + \left| \frac{\partial u}{\partial x_p} \right|^2_{i_q-1} \right) + \varepsilon \left| \frac{\bar{u}_{pq}}{\Delta x_p \Delta x_q} \right| \right] \right)^2} \right]^{\frac{1}{2}} \tag{3.22}$$

Here, the indices i_x, i_y, and i_z denote the coordinates of the i-th cell, Δx_q represents the cell size in the q direction, and $|\bar{u}_{pq}|$ is the local average value of $|u|$ over several neighboring cells in the p and q directions.

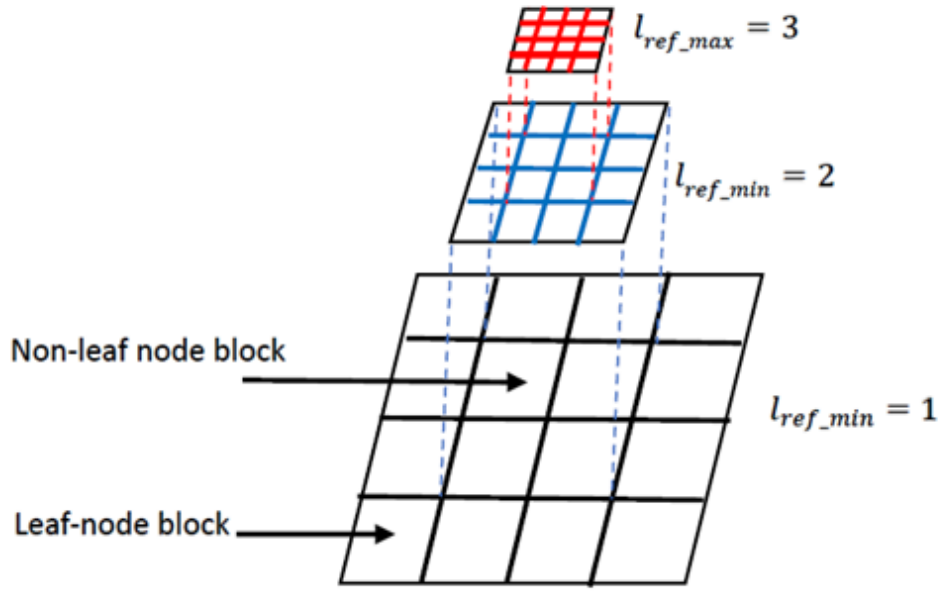

Figure 3.4: Illustration of Refinement Levels in a 2D Block, where Leaf-Node Blocks Store the Solution and Non-Leaf Node Blocks Store the Correction.

Furthermore, by computing tested quantity gradients, the AMR grid is refined and derefined. AMR also guarantees conservation of flux at refinement jumps. Assumed and communicated to their parent cells are the fluxes of mass, momentum, internal and total energy, and

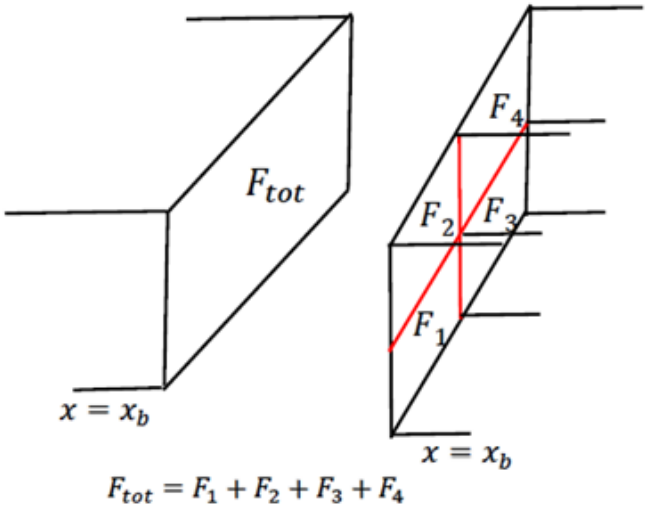

Figure 3.5: Demonstrating Flux Conservation Across a Refinement Jump, where the Fluxes in Fine Cells are Summed and Replace the Coarse Cell Flux (F_{total}).

species density in the fine cells across boundary cell faces (see figure 3.5).

3.4 Setting up the simulation: numerical computation and discussion

As is well known, rock samples collected from the surface of Mars are rich in graphite [77], while the Martian atmosphere is predominantly composed of carbon dioxide (CO_2), which constitutes approximately 96% of its composition [24], along with trace amounts of helium (He), around 0.0002%. In this distinct Martian environment, the physical and chemical properties of the plasma differ significantly from those on Earth. The unique combination of graphite-rich rocks and the predominance of CO_2, along with trace amounts of He in the Martian atmosphere, imparts distinctive characteristics to the plasma, resulting in notable variations in its behavior and composition compared to Earth's conditions. Specifically, under Martian conditions, the plasma exhibits heightened brightness and more intense spectral lines, leading to a higher acquired signal compared to ambient or vacuum conditions [25]. Our simulation setup, taking into account Martian environmental conditions, involves the laser ablation of a

graphite target, resulting in plasma formation in the presence of ambient CO_2 and He gases. This comprehensive approach considers the intricate dynamics arising from the simultaneous processes of plasma formation and the generation of shock waves. To precisely capture the interplay between these phenomena, we have employed a 3T plasma Eulerian radiation description model, incorporating a Non-LTE (Non-Local Thermodynamic Equilibrium) approach, as detailed in section 2.1. The FLASH code is equipped with a diverse range of directionally split and unsplit methods designed for solving the system of Euler equations governing radiation-hydrodynamics (RHD). This system of equations (equations (2.1), (2.2), (2.3)) constitutes a mixed hyperbolic-parabolic system. Initially, all the terms on the right-hand side of the equations are separated from the solution of the non-ideal single fluid hydrodynamics. This separation is managed using the single-step, time-marching algorithm of the unsplit staggered mesh (USM) [26, 27], specifically tailored for Cartesian coordinates. Subsequently, the right-hand terms of equations (equations (2.8), (2.9), (2.10)) are individually separated, and each term is treated independently. The first term on the right-hand side (equations (2.8), (2.9)) accounts for the exchange of energy between electrons and ions through collisions, and it is addressed by solving the system as outlined in [28]:

$$\frac{\partial e_{\text{ion}}}{\partial t} = \frac{C_{v,\text{ei}}}{\tau_{ei}}(T_{\text{ele}} - T_{\text{ion}}) \tag{3.23}$$

$$\frac{\partial e_{\text{ele}}}{\partial t} = \frac{C_{v,\text{ei}}}{\tau_{ei}}(T_{\text{ion}} - T_{\text{ele}}) \tag{3.24}$$

The subsequent term on the right-hand side of equations ((3.23)) and ((3.24)) accounts for electron thermal conduction and the parabolic terms. These components are resolved implicitly through the utilization of the HYPRE library [29], enabling the retention of larger time steps. The residual terms on the right-hand side of equations ((2.9)) and ((2.10)) pertain to radiation transport, with the HYPRE library being employed to compute radiation diffusion.

The equations governing radiative transfer (equation (2.29)) and electron internal energy (equation (2.30)) are managed through the multi-group diffusion (MGD) approximation [30] within FLASH. In this approach, the frequency space is discretized into N groups, denoted

by g, each defined within the frequency range from ν_g to ν_{g+1}. In our simulation, a total of 25 frequency groups are utilized, and the overall quantities of interest are expressed as summations over each group. The second and third terms on the left-hand side of equation (2.34) denote the radiation diffusion flux for each group g ($\nabla \cdot \mathbf{q}_{\mathrm{rad},g}$) and the absorption source term for each group g ($Q_{\mathrm{abs},g}$), respectively. Conversely, the right-hand side of equation (2.34) signifies the emission source term for each group g ($Q_{\mathrm{emis},g}$). The final term in equation (2.34) represents the laser heating source (Q_{las}), computed through an inverse Bremsstrahlung model (refer to section 3.1.2). The energy deposited by the laser beam was determined using the laser ray-trace algorithm for both (X-Y) planar and (R-z) cylindrical geometries. FLASH boasts extensive laser modeling capabilities, accommodating various laser configurations. In our simulation, a specific laser ray-tracing model property in the FLASH Code was utilized, enabling a 2D Cartesian laser beam to emulate a 3D cylindrical beam.

The interaction between the laser and the graphite target in the presence of CO_2 and He was simulated using FLASH, an Adaptive Mesh Refinement (AMR) code, on a 2D Cartesian grid over a duration of 5 ns. The visualization of these simulations was facilitated by the software VisIt [31]. We employed four levels of refinement, resulting in a total of 33,280 cells and achieving an equivalent resolution of approximately 39 μm per cell, as shown in figure 3.6. The boundary conditions are set to be reflective on the left side of the y-axis, while the remaining boundaries are set to outflow (zero gradient), as illustrated in figure 3.6.

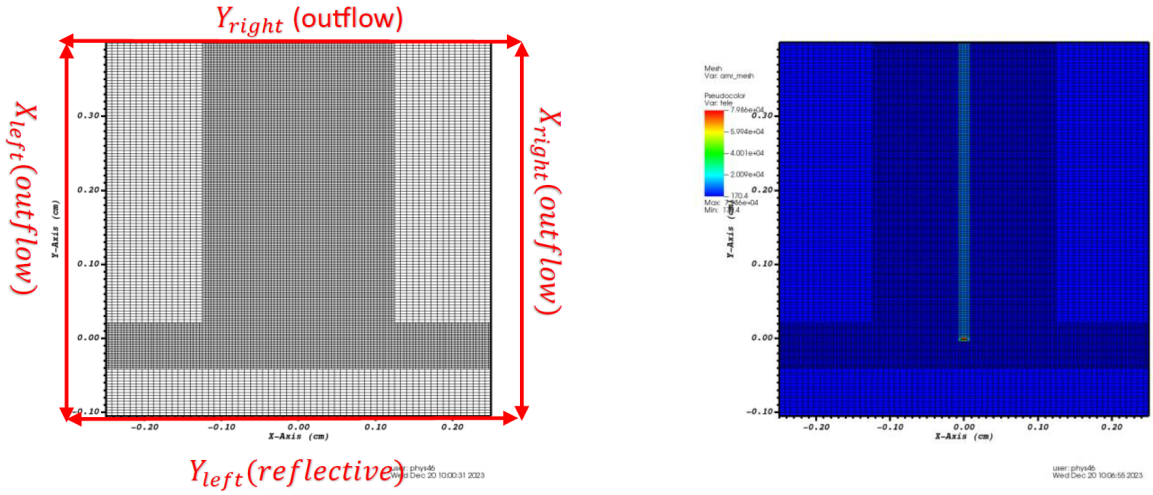

Figure 3.6: Illustration of the evolution of a 2D Cartesian AMR grid during a simulation at $t = 5$ ns (33,280 Cells) depicting the interaction between the laser and the graphite target in the presence of CO_2 and He gases, by utilizing the visualization software VisIt.

For both the target material (Graphite) and the surrounding ambient gases (CO_2 and He) under Non-Local Thermodynamic Equilibrium (NLTE) conditions, we utilized the IONMIX4 program to generate tabulated data that could be incorporated into the FLASH code. The IONMIX code is designed to compute the steady-state ionization and excitation populations for a mixture of up to 10 distinct atomic species. This includes the calculation of radiative absorption, emission, and scattering coefficients at numerous photon energies (approximately several hundred). These coefficients are then integrated over selected energy intervals to derive the multi-group Planck and Rosseland mean opacities [25].

Table 3.1: Electronic configuration and the ionization energy for helium (He)

Ion	**Electronic Configuration**	**Ground Level**	**Ionized Level**	**Ionization Energy (eV)**
He	$1s^2$	$^1S_0$	$1s^2S_{1/2}$	24.5873890
He^+	$1s$	$^2S_{1/2}$		54.41776552

A temperature grid spanning 0.01 to 50 eV, an ion density grid ranging from 10^{12} to 10^{25} ion/cm^3, and an energy grid from 1 to 6 eV were employed in calculating the equations of state (EOS) and opacity data, respectively. Ionization potential energies for the excited levels of helium (Table 3.1), carbon (Table 3.2) and oxygen (Table 3.3) were obtained from the National Institute of Science and Technology (NIST)[32]. These values were used by IONMIX4 to generate data for graphite, carbon dioxide (CO_2), and helium (He). The populations

Table 3.2: Electronic configuration and the ionization energy for carbon (C)

Ion	Electronic Configuration	Ground Level	Ionized Level	Ionization Energy (eV)
C	$1s^2 2s^2 2p^2$	$^3P_0$	$2s^2 2p\ ^2P^0_{1/2}$	11.2602880
C^+	$1s^2 2s^2 2p$	$^2P^2_{1/2}$	$2s^2\ ^1S_0$	24.383143
C^{2+}	$1s^2 2s^2$	$^1S_0$	$2s\ ^2S_{1/2}$	47.88778
C^{3+}	$1s^2 2s$	$^2S_{1/2}$	$1s^2\ ^1S_0$	64.49352
C^{4+}	$1s^2$	$^1S_0$	$1s\ ^2S_{1/2}$	392.09056
C^{5+}	$1s$	$^2S_{1/2}$		489.99320779

Table 3.3: Electronic configuration and the ionization energy for oxygen (O)

Ion	Electronic Configuration	Ground Level	Ionized Level	Ionization Energy (eV)
O	$1s^2 2s^2 2p^4$	$^3P_2$	$2p^3\ ^4S^0_{3/2}$	13.618055
O^+	$1s^2 2s^2 2p^3$	$^4S^0_{3/2}$	$2p^2\ ^3P_0$	35.12112
O^{2+}	$1s^2 2s^2 2p^2$	$^3P_0$	$2s^2 2p\ ^2P^0_{1/2}$	54.93554
O^{3+}	$1s^2 2s^2 2p$	$^2P^0_{1/2}$	$2s^2\ ^1S_0$	77.41350
O^{4+}	$1s^2 2s^2$	$^1S_0$	$2s\ ^2S_{1/2}$	113.8990
O^{5+}	$1s^2 2s$	$^2S_{1/2}$	$1s^2\ ^1S_0$	138.1189
O^{6+}	$1s^2$	$^1S_0$	$1s\ ^2S_{1/2}$	739.32697
O^{7+}	$1s$	$^2S_{1/2}$		871.4099138

of atomic energy levels were computed using a collisional-radiative non-local thermodynamic equilibrium (CR-NLTE) model (refer to Section 3.2).

The LIBS graphite plasma simulation in the presence of CO_2 and He evolves over a duration from 0 ns to 1000 ns, using the unsplit time-marching method of the USM algorithm, which is an extension of the corner transport upwind (CTU) approach [33]. The simulation utilizes a variable time step, ranging from 1 fs to 0.1 ns, determined by changes in electron and ion temperatures, radiation energy density, and limits imposed by the Courant Friedrichs Lewy (CFL) condition. A CFL number of 0.1 is maintained throughout the run. Spatial reconstruction is performed using the Piecewise Parabolic Method (PPM) [34] and a monotonized central (MC) limiter, while Godunov fluxes are recovered with an HLLC (Harten, Lax & van Leer-Contact) Riemann solver [35,36]. Implicit solvers for electron and ion thermal conduction employ a conjugate gradient method (CG) [37] preconditioned with algebraic multigrid (AMG), as implemented in the HYPER library [38]. For visualizing our data, we employed the multi-code analysis tool "yt-project" [39], an open-source Python code. This tool encompasses a data management layer for transporting and tracking simulation outputs, a plotting layer, and a

parallel analysis layer capable of handling both mesh-based and particle-based data. Additionally, "yt" offers various interfaces and has been extended to collaborate with diverse simulation methods and codes, including the FLASH code. figure 3.7 provides a thorough understanding of the software integration landscape by revealing the complex interactions between FLASH and several programs and libraries through a precise schematic portrayal. This graphic functions as a road map, showing the dynamic relationships and exchanges that FLASH has with the surrounding computing environment. To gain a thorough understanding of our simulation configuration, including specific code and FLASH parameters.

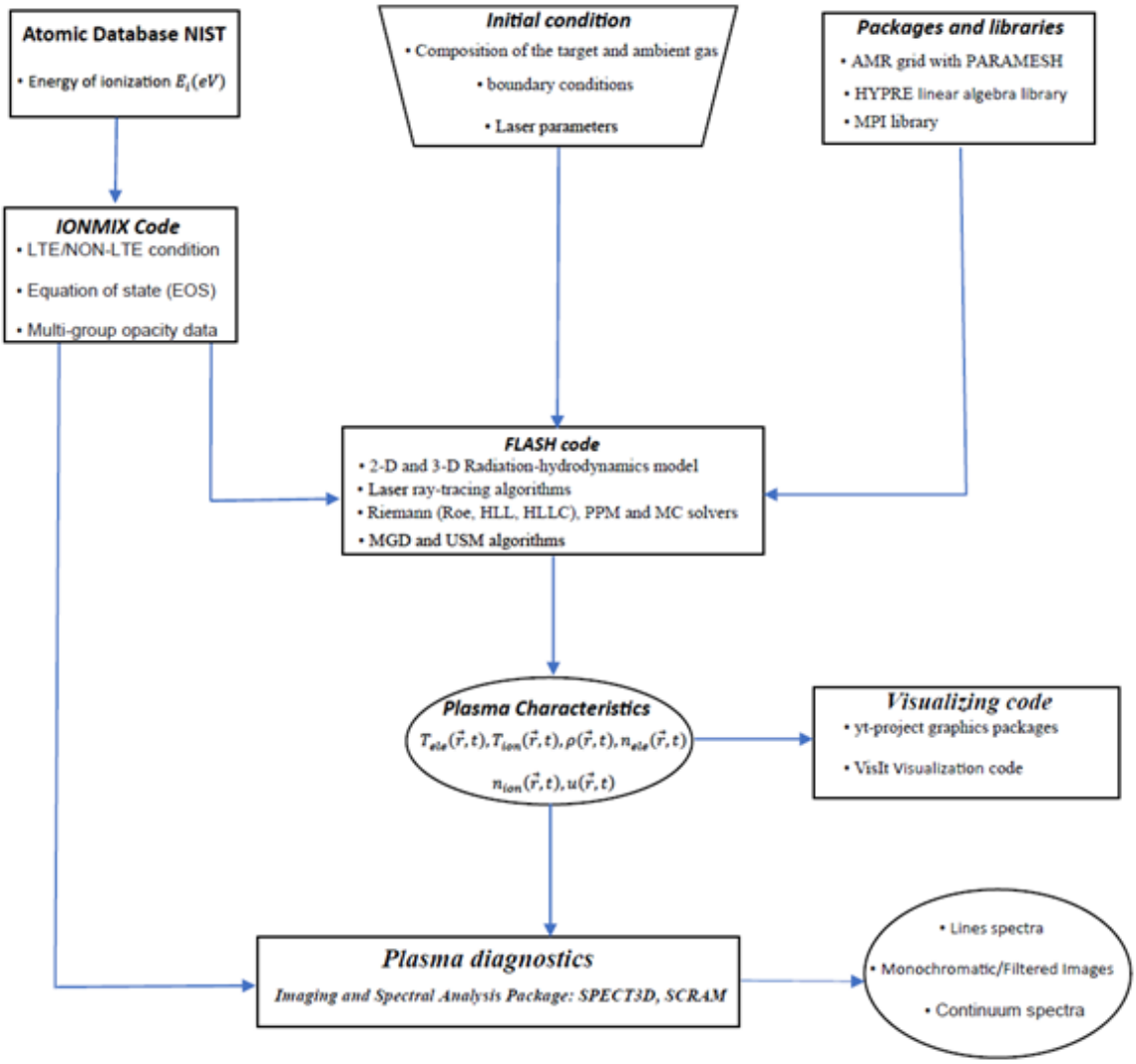

Figure 3.7: Presents a detailed flow diagram that illustrates the movement and integration of data between the FLASH simulation framework and various associated codes and software packages.

3.5 Simulation framework and design

In an attempt to gain a deeper understanding of the characteristics of ChemCam and SuperCam LIBS, numerical simulations have been employed as a complementary approach to the conventional method of replicating experimental conditions on Mars within an Earth-based laboratory [40,41]. Unlike comparative studies conducted in laboratories, numerical simulations offer distinct advantages. These benefits include the flexibility to easily modify laser parameters such as wavelength, pulse, energy, spot size, profile shape, and ambient gas pressures.

However, their limitations stem from the challenge of accurately determining numerous factors related to chemical, physical, optical, and environmental gas properties, which influence the development of the plasma plume and spectral regions. Consequently, the spectra observed in Earth-based laboratories and those generated through simulations can be regarded as complementary to each other.. Ewusi-Annan et al [42] employed a 1-D Lagrangian hydrodynamic model to simulate the laser-induced breakdown spectra of graphite and synthetic shergottite glass in an environment resembling Mars. They presented their findings under a local thermodynamic equilibrium (LTE) approach for the emission spectra. Examined the properties of LIBS (Laser-Induced Breakdown Spectroscopy) plasma under Martian atmospheric conditions through a stationary model, which utilized a one-dimensional approach to depict the plasma divided into two zones along the line of sight [43]. Their simulations, grounded in the principles of local thermal equilibrium, were conducted employing radiative transfer methods.

Typically, characterizations of LIBS plasma rely on the premise of local thermodynamic equilibrium (LTE), favored for its straightforward depiction of plasma. However, the appropriateness of the LTE assumption is contingent on specific experimental conditions and is only applicable at certain times following the initiation of the plasma. Alberti et al. [44] employed a non-equilibrium model to study the dynamics of plasma kernels generated by lasers. They conducted simulations of laser-induced plasma using nanosecond pulses, encompassing a variety of ambient conditions and laser properties. Notably, their simulations successfully predicted the axial and radial dimensions of the plasma. More crucially, they accurately replicated the

propagation of both forward and backward plasma waves, as observed in experimental settings involving air [45] and Argon [46].

In this study, we numerically investigate the influence of lens-to-sample distance (LTSD) and laser irradiance on key plasma parameters, including electron and ion temperatures, electron and ion number densities, and fluid velocity. Additionally, we examine the evolution of plasma dynamics and spatial extent under different ambient gas environments specifically carbon dioxide (CO_2) and helium (He) at pressures of 6 mbar (representative of Martian conditions) and 1000 mbar (Earth-like conditions), with an initial background temperature of approximately 290.11 K (17 °C).

3.5.1 Laser ablation target structure in presence of ambient gas

To simulate the ablation of a graphite target and the formation of plasma in the presence of ambient CO_2 gas, we employed the multi-material capabilities of the FLASH code, as described in the numerical and computational framework presented in Section 2.1.1. The simulation features a flat, homogeneous solid graphite target with a thickness of 0.12 cm and a radius of 0.3 cm, both initially having a mass density of $\rho = 2.23$ g/cm^3. The initial temperature of the graphite is denoted as $T_{\mathrm{G}} = 17^{\circ}\mathrm{C} = 290.11$ K, and the ambient CO_2 and He gases are initialized at $T_{\mathrm{CO_2}} = T_{\mathrm{He}} = 17^{\circ}\mathrm{C} = 290.11$ K.

We additionally explore the effect of varying focusing conditions by considering three distinct cases in which the focal point of the laser beam is positioned at, above, and below the target surface, respectively. This variation along the Z-axis modifies the radial distribution of the focused laser beam, thereby significantly influencing the spot size and energy density at the target surface. These three configurations are illustrated in Figure 3.8, highlighting the impact of focal positioning on plasma formation and expansion dynamics.

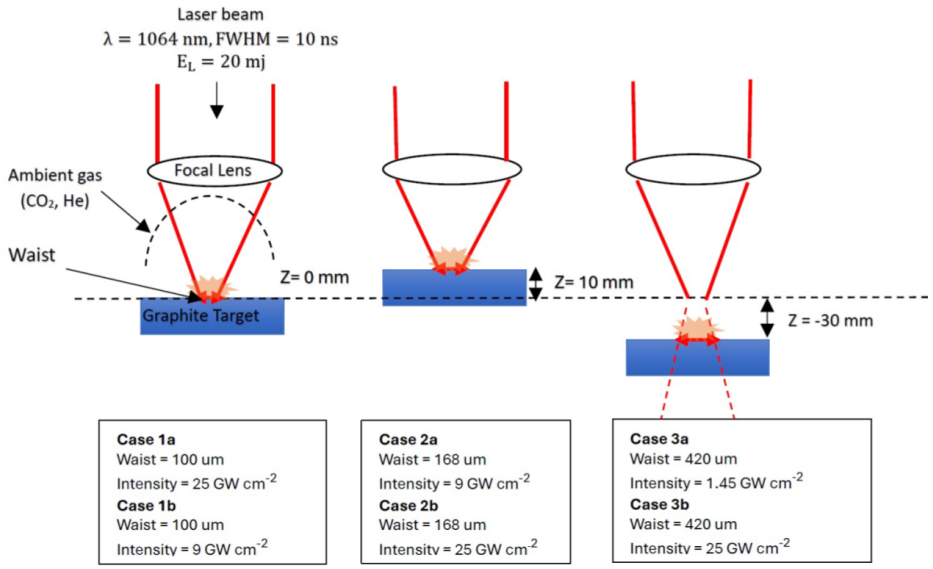

Figure 3.8: Illustrates the temporal evolution of the top-hat laser beam power profile over time.

In the first case, the laser beam was tightly focused, producing a minimum beam waist of 100 µm at the target surface. This configuration yielded an on-target irradiance of 25 GW cm^{-2} (Case 1a), a condition typically associated with maximum LIBS signal intensity. For comparison, a lower irradiance of 9 GW cm^{-2} was also considered (Case 1b). In the second case, the laser was focused slightly above the target surface, resulting in an increased spot size of 168 µm and a corresponding irradiance of 9 GW cm^{-2} (Case 2a), with a secondary condition at 25 GW cm^{-2} (Case 2b). In the third configuration, the laser was significantly defocused, leading to a spot size of 420 µm and a reduced irradiance of 1.45 GW cm^{-2}. To assess the influence of spot size at constant irradiance, this case was also evaluated at 25 GW cm^{-2} (Case 3b). Each configuration was simulated under ambient CO_2 and He environments at pressures of 3, 6, 9, and 1000 mbar to examine the effects of different atmospheric conditions. The initial temperatures of both the graphite target and the surrounding gases were set to approximately (17 °C).

3.5.1.1 Laser beam design

In our simulation model, a single laser beam—represented by 8192 rays per time step—is used to irradiate a flat graphite target within a two-dimensional (X–Y) Cartesian geometry. The laser is focused along the Y-axis and enters the computational domain at the origin (0, 0),

illuminating the target from above. It has a wavelength of 1064 nm, and its temporal profile follows an ideal Gaussian-shaped pulse with a full width at half maximum (FWHM) of 10 ns. The laser energy incident on the sample surface, denoted as E_{las}, is set between 15 and 20 mJ [47].

The maximum power (energy) of the laser pulse follows a Gaussian function, as expressed by [48]:

$$P(t) = P_{max} \exp\left(-\left(\frac{t-\tau}{\tau}\right)^2\right) \tag{3.25}$$

Where P_{max} is the maximum laser power, τ is the full width at half maximum of the Gaussian laser pulse (FWHM). A representative figure 3.9 shows the Gaussian distribution of laser power as a function of time.

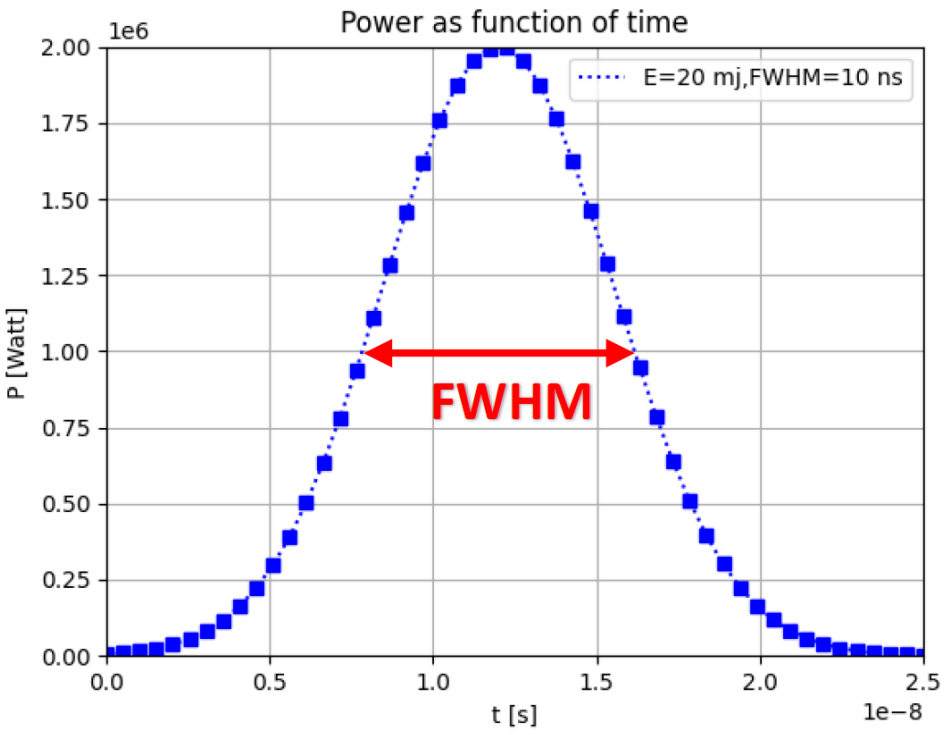

Figure 3.9: Illustrating the temporal evolution of the ideal Gaussian laser power profile.

The spatial profile of the laser irradiance was assumed to be a ideal-Gaussian of exponent 1 with an e2-folding radius; its expression is given by [49, 50]:

$$I(r) = I_0 \exp\left(-2\left(\frac{r}{\omega_0}\right)^n\right) \tag{3.26}$$

Where I_0 is the laser irradiance at $r = 0$, n is the Gaussian exponent, selected to be 1 in our simulation, r is the radial coordinate, and ω_0 is the e^2-folding Gaussian radius of the laser, which is set between approximately $100\,\mu$m and $420\,\mu$m.

The intensity profile of this laser beam is modeled using a specific property of the laser ray-tracing model in FLASH. This feature allows for a 2D Cartesian laser beam to effectively emulate a 3D cylindrical beam. To investigate the effect of Lens-to-Sample Distance (LTSD) on plasma behavior, a laser beam composed of 8192 rays heats the graphite target from above in the presence of CO_2 and He ambient gases. The spatial profile of the laser intensity is assumed to follow an ideal Gaussian distribution with an exponent $n = 1$. In our simulations, the laser beam is circular on the target surface, with a focused spot size diameter of $2w_0 = 100\,\mu$m (beam waist) located at $z = 0\,$mm. This configuration results in an on-target intensity of approximately $I \approx 25\,\text{GW/cm}^2$. The beam radius at the target, $w(z)$, varies as a function of the longitudinal position along the Z-axis and is given by [51]:

$$w(z) = w_0\sqrt{1 + \left(\frac{z}{z_R}\right)^2} \tag{3.27}$$

Where w_0 is the beam waist and z_R is the Rayleigh range. We selected two distinct target positions from the focal point for our simulation. At $z = 10\,$mm, the spot size diameter was $D = 168\,\mu$m, resulting in an on-target intensity of $I \approx 9\,\text{GW/cm}^2$. At $z = -30\,$mm, the spot size diameter was $D = 420\,\mu$m, corresponding to an intensity of $I \approx 1.45\,\text{GW/cm}^2$.

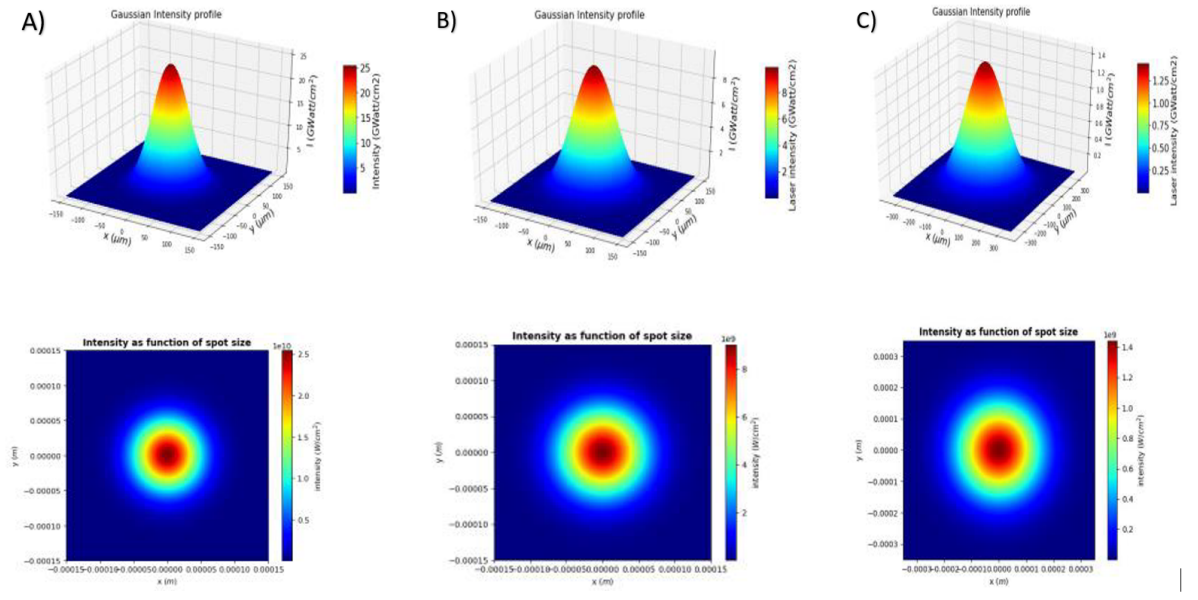

Figure 3.10: Illustrating the Gaussian laser intensity profile and the variation of laser intensity with spot size for 25 GW/cm^2 (A), 9 GW/cm^2 (B), and 1.45 GW/cm^2 (C).

Figure 3.10 presents a detailed visualization of the Gaussian laser intensity distribution as a function of different spot sizes. It clearly illustrates the inverse relationship between spot size and laser intensity smaller spot sizes correspond to higher intensities. This relationship highlights the critical influence of spot size on the concentration of laser energy delivered to the target.

3.5.1.2 Target design

Our simulation involves a single laser beam represented by 8192 rays used to heat flat graphite targets. The upper surface of the graphite target undergoes ablation due to the laser beam, with intensities ranging from $I = 1.45$ GW/cm^2 for a spot size diameter of $D = 420$ μm, to $I = 25$ GW/cm^2 for a diameter of $D = 100$ μm. This interaction leads to the formation of a plasma plume expanding into both CO_2 and He ambient gases. Simultaneously, a shock front develops and propagates through the plasma, eventually breaking out after a certain time.

The computational domain in the 2D Cartesian (X–Y) geometry was designed to mimic the distance between the laser source (e.g., ChemCam telescope) and the target on Mars, approximately 2 m as described in [52]. The domain is defined as follows: at $z = 0$ mm, it spans $[-0.3\text{ cm}, 0.3\text{ cm}] \times [-0.12\text{ cm}, 0.6\text{ cm}]$; at $z = 10$ mm, it spans $[-0.3\text{ cm}, 0.3\text{ cm}] \times [0.88\text{ cm}, 1.6\text{ cm}]$; and at $z = -30$ mm, it spans $[-0.3\text{ cm}, 0.3\text{ cm}] \times [-3.12\text{ cm}, -2.5\text{ cm}]$.

We employed five levels of adaptive mesh refinement (AMR) using blocks of 8×8 cells, yielding an effective spatial resolution of $39\,\mu$m per cell. Plasma properties including electron and ion temperatures, number densities, and fluid velocity were simulated for both flat and spherical graphite targets over time durations ranging from 5 ns to 1000 ns.

The simulations employ the unsplit staggered mesh (USM) scheme with a Courant number of 0.1. The time step used in the simulations ranges from 1 fs to 0.1 ns. Reconstruction is performed using a monotonized central (MC) limiter, while Godunov fluxes are computed using an HLLC Riemann solver, which accurately handles contact surfaces and shock waves. The effect of lens-to-sample distance (LTSD) on plasma characteristics is examined under varying pressure conditions in CO_2 and He atmospheres. Laser irradiation of the flat graphite target induces surface ablation, leading to the formation of a plasma plume that expands into the surrounding gas. Simultaneously, a shock front develops within the plasma and propagates outward, ultimately breaking through the ambient medium after a brief delay. The large spatial extent of the atmosphere in our simulation is chosen to replicate the distance between the laser source (focal lens) and the target on Mars, which is 200 mm, as reported in [51].

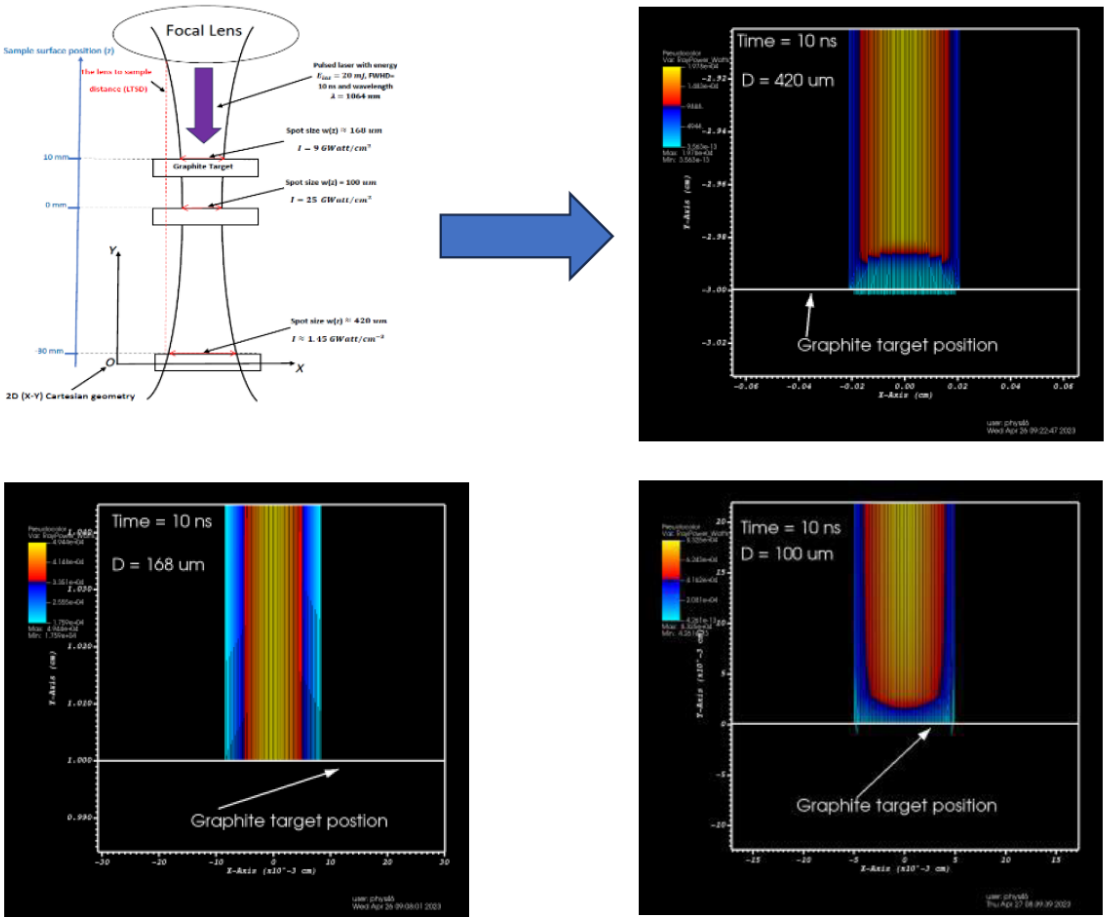

Figure 3.11: Schematic of the focusing conditions at different lens-to-sample distances (LTSDs). The laser beam is simulated for a flat graphite target using 8192 rays per time step. The corresponding spot size diameters are: $D = 420$ μm for LTSD = -30 mm, $D = 168$ μm for LTSD = 10 mm, and $D = 50$ μm for LTSD = 0 mm, respectively.

Figure 3.11 illustrates a schematic of the laser intensity distributions at different lens-to-sample distance (LTSD) positions. In the Cartesian (X–Y) geometry mesh:

- At $z = 0$ mm, the region where $Y \leq 0.0$ cm is occupied by the flat graphite target, which has a thickness of 1.2 mm and a radius of 3 mm. The region where $Y > 0.0$ cm is assumed to be filled with the ambient gas, CO_2.
- At $z = 10$ mm, the region where $Y \leq 1.0$ cm is occupied by the graphite target, while the region where $Y > 1.0$ cm is considered to be filled with CO_2.
- At $z = -30$ mm, the region where $Y \leq -3.0$ cm is occupied by the graphite target, and the region where $Y > -3.0$ cm is assumed to contain the ambient gas CO_2.

For a small LTSD, the intensity of the laser radiation is greater than that for a large LTSD. The LTSD significantly influences the laser spot size on the target surface: a smaller LTSD results in a smaller spot size, concentrating the laser energy over a smaller area and thereby increasing the laser intensity. Conversely, a larger LTSD leads to a larger spot size, spreading the laser energy over a wider area and thus reducing its intensity. Therefore, smaller LTSD values lead to higher local laser intensities compared to larger LTSD values.

3.6 Results and discussion

3.6.1 Effects of Varying LTSD on Plasma Characteristics

We systematically explore various lens-to-sample distances (LTSDs) under two distinct ambient pressure conditions, encompassing both low and high pressures. For the low-pressure scenarios, the ambient carbon dioxide (CO_2) gas is tested at three different values—Mars-like conditions of P = 3, 6 and 9 mbars, respectively. Conversely, under Earth-like conditions, the CO_2 gas is examined at a single pressure of P = 1000 mbar. This comprehensive approach enables us to investigate the combined effects of LTSD and ambient pressure on various plasma characteristics, including electron and ion temperatures, electron and ion number densities, and fluid velocity. The simulations are conducted in an environment designed to mimic Martian atmospheric conditions, providing valuable insights into plasma behavior under these settings.

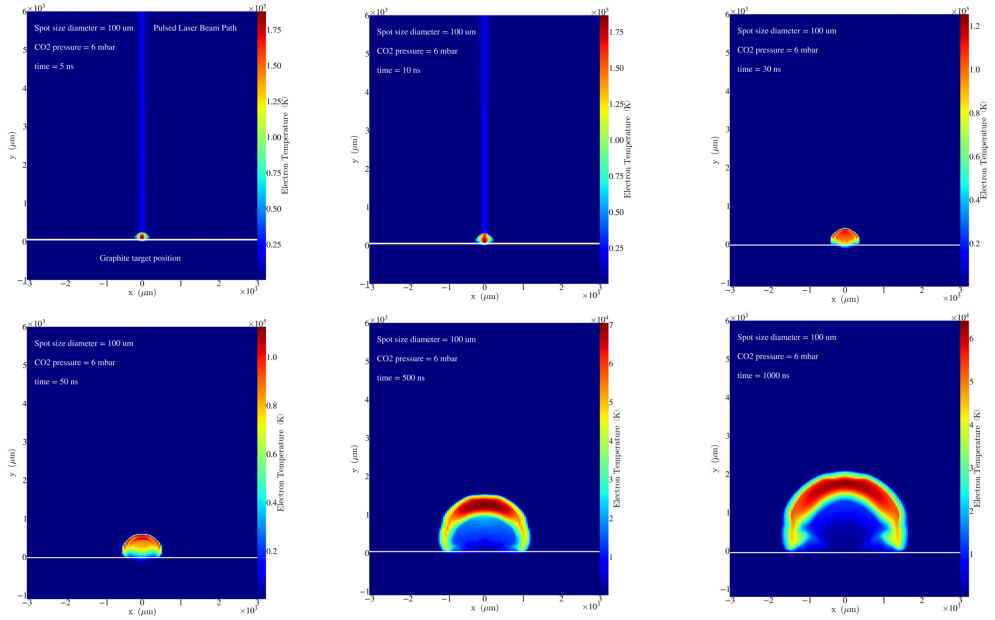

Figure 3.12: Plasma electron temperature distribution and plume expansion evolution at 5 ns, 10 ns, 30 ns, 100 ns, 500 ns, and 1000 ns simulation time for a spot size diameter of 100 μm under 6 mbar CO_2 pressure.

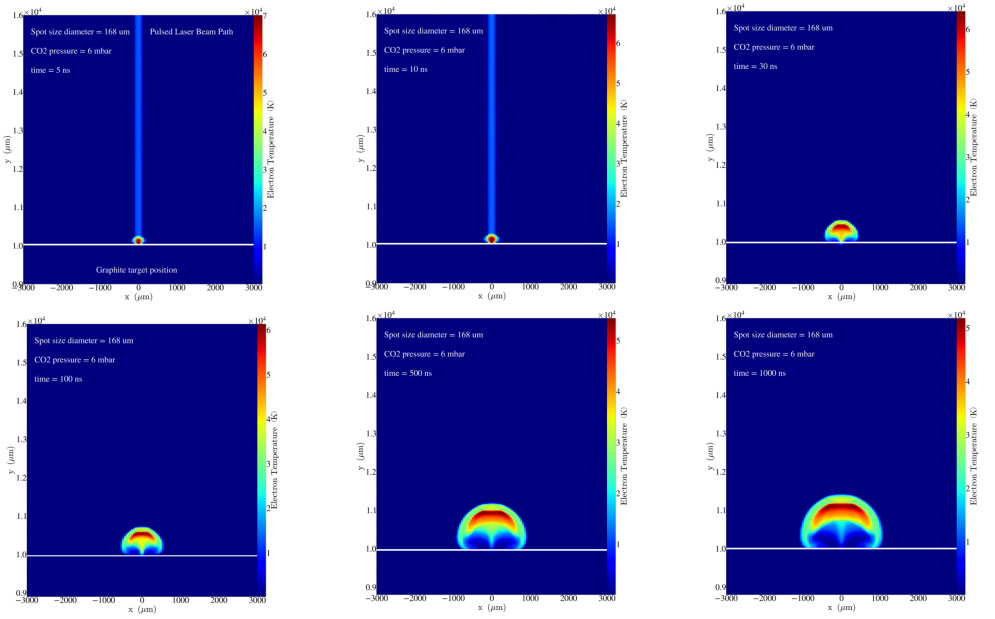

Figure 3.13: Plasma electron temperature distribution and plume expansion evolution at 5 ns, 10 ns, 30 ns, 100 ns, 500 ns, and 1000 ns simulation time for a spot size diameter of 168 μm under 6 mbar CO_2 pressure.

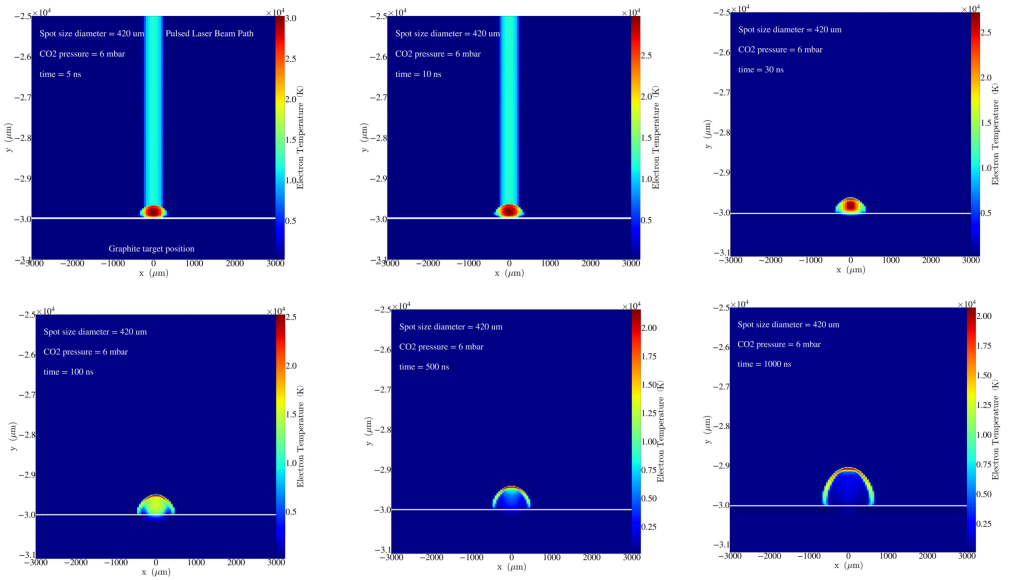

Figure 3.14: Plasma electron temperature distribution and plume expansion evolution at 5 ns, 10 ns, 30 ns, 100 ns, 500 ns, and 1000 ns simulation time for a spot size diameter of 420 µm under 6 mbar CO_2 pressure.

Figures 3.12, 3.13, and 3.14 illustrate the interaction of the pulsed laser with the flat solid graphite target, showing the evolution of the electron temperature field and plume formation at different stages of plasma evolution. The results cover both the active laser phase (5 to 10 ns) and the post-laser phase (30 to 1000 ns), under a CO_2 ambient pressure of 6 mbar (Mars-like conditions), with focal spot sizes of 100 µm (irradiance $I = 25$ GW/cm^2), 168 µm ($I = 9$ GW/cm^2), and 420 µm ($I = 1.45$ GW/cm^2).

Our results show that both the electron temperature and its spatial plume extent are influenced by the Lens-to-Sample Distance (LTSD) and the ambient gas pressure. Contrary to expectations, the simulations indicate that the electron temperature decreases with increasing LTSD. This behavior is driven by the laser beam's focusing characteristics: a larger LTSD results in a less concentrated laser beam on the target (i.e., reduced laser irradiance), leading to lower energy absorption by the target material and, consequently, lower electron temperatures within the plasma. These findings are consistent with the experimental results reported by Harilal et al.[58] in their measurements of the temperature in laser-produced carbon plasma.

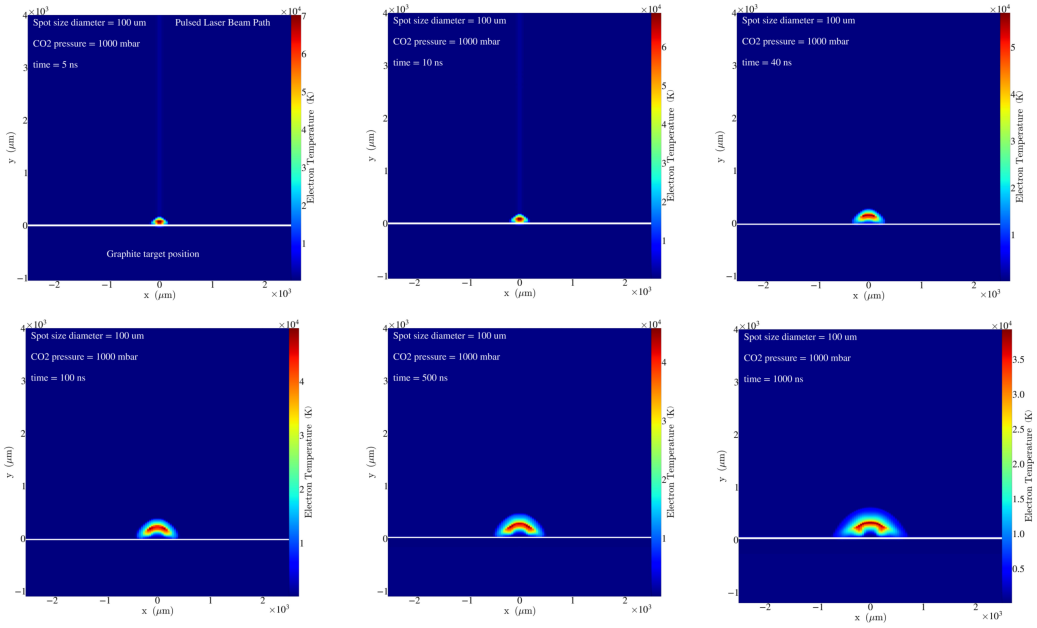

Figure 3.15: Plasma electron temperature distribution and plume expansion evolution at 5 ns, 10 ns, 30 ns, 100 ns, 500 ns, and 1000 ns simulation time for a spot size diameter of 100 μm under 1000 mbar CO_2 pressure.

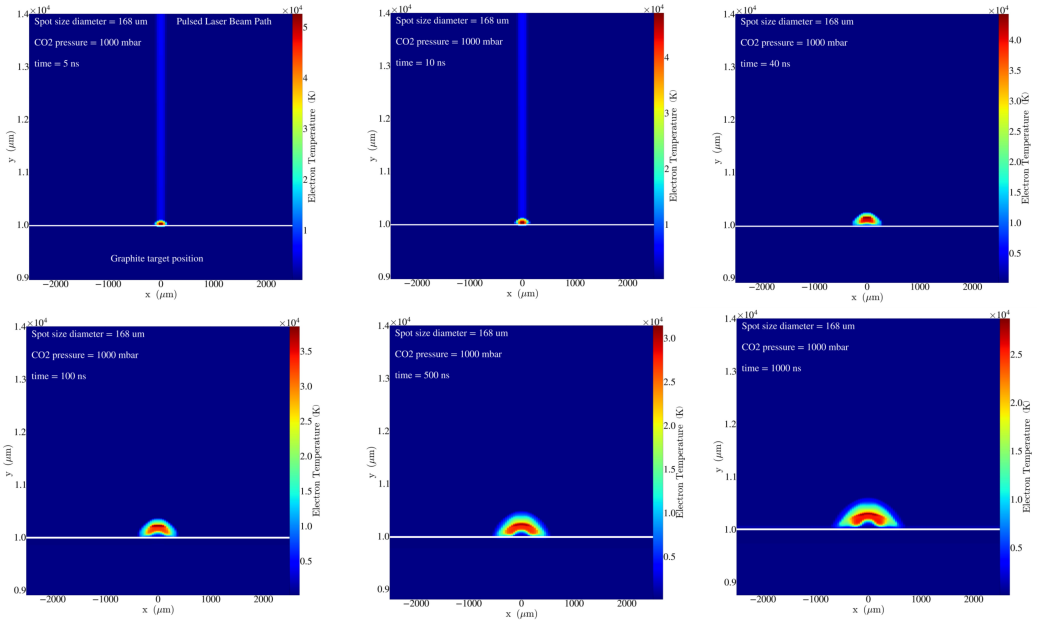

Figure 3.16: Plasma electron temperature distribution and plume expansion evolution at 5 ns, 10 ns, 30 ns, 100 ns, 500 ns, and 1000 ns simulation time for a spot size diameter of 168 μm under 1000 mbar CO_2 pressure.

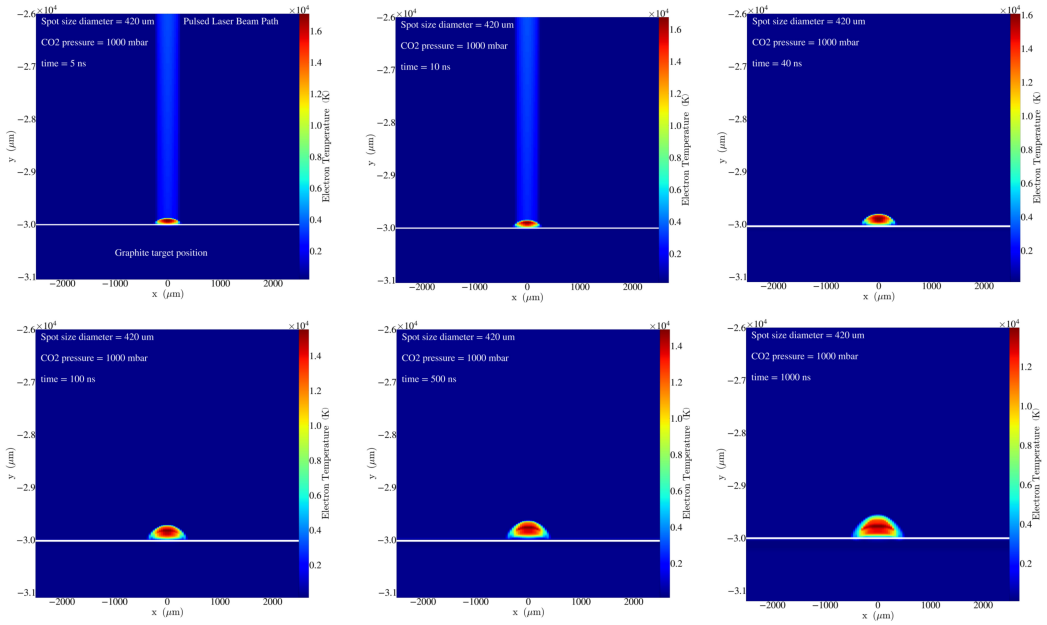

Figure 3.17: Plasma electron temperature distribution and plume expansion evolution at 5 ns, 10 ns, 30 ns, 100 ns, 500 ns, and 1000 ns simulation time for a spot size diameter of 420 µm under 1000 mbar CO_2 pressure.

Figures 3.15, 3.16, and 3.17 illustrate the interaction of the pulsed laser with the flat solid graphite target, showing the evolution of the electron temperature field and plume formation at different stages of plasma evolution. The results cover both the active laser phase (5 to 10 ns) and the post-laser phase (30 to 1000 ns), under a CO_2 high pressure of 1000 mbar(Earth-like conditions), with focal spot sizes of 100 µm (irradiance $I = 25$ GW/cm^2), 168 µm ($I = 9$ GW/cm^2), and 420 µm ($I = 1.45$ GW/cm^2).

Both the electron temperature and its spatial distribution are influenced by gas pressure and laser irradiance. Throughout all simulation durations, the temperature increases with higher laser irradiance. However, under high-pressure conditions, the electron temperature decreases. These findings are consistent with experimental observations reported by J. S. Cowpe et al. [53], who measured the electron temperature in laser-generated silicon plasma.

In our approach, we also account for the interaction between the plasma and the ambient gas, which significantly influences the expansion of the plasma plume and, consequently, affects its temperature and density [54]. Additionally, the discrepancies in temperature values reported in [42, 43] may be attributed to their neglect of plasma emission and reabsorption in their two-temperature model, as well as their assumption of local thermal equilibrium (LTE). It is noteworthy that the equation of state (EOS) model not only determines the plasma pressure at a given density and temperature but also governs heat conduction efficiency by defining the mean ionization fraction and specific heat [4, 55]. Our results reveal distinct zones of electron and ion temperatures compared to previous approaches, which can be attributed to several factors [42]. These include the interaction between the forming plasma and the surrounding medium considered in our simulation, as well as the implementation of CR-NLTE (collisional-radiative non-local thermodynamic equilibrium) conditions [56]. Notably, the electron temperature is significantly higher than the ion temperature for all laser irradiance levels and both low and high pressure conditions considered in our study. This behavior is due to the greater energy imparted to the target material by the more intense laser beam. When a laser with higher irradiance is used, it delivers more energy to the target surface over a shorter duration, resulting in rapid heating and vaporization. This, in turn, leads to the formation of a plasma plume with higher kinetic energy. Experimental observations have confirmed this phenomenon [57], showing the presence of a shock front associated with plasma initiation, dynamics, and expansion into the CO_2 ambient gas.

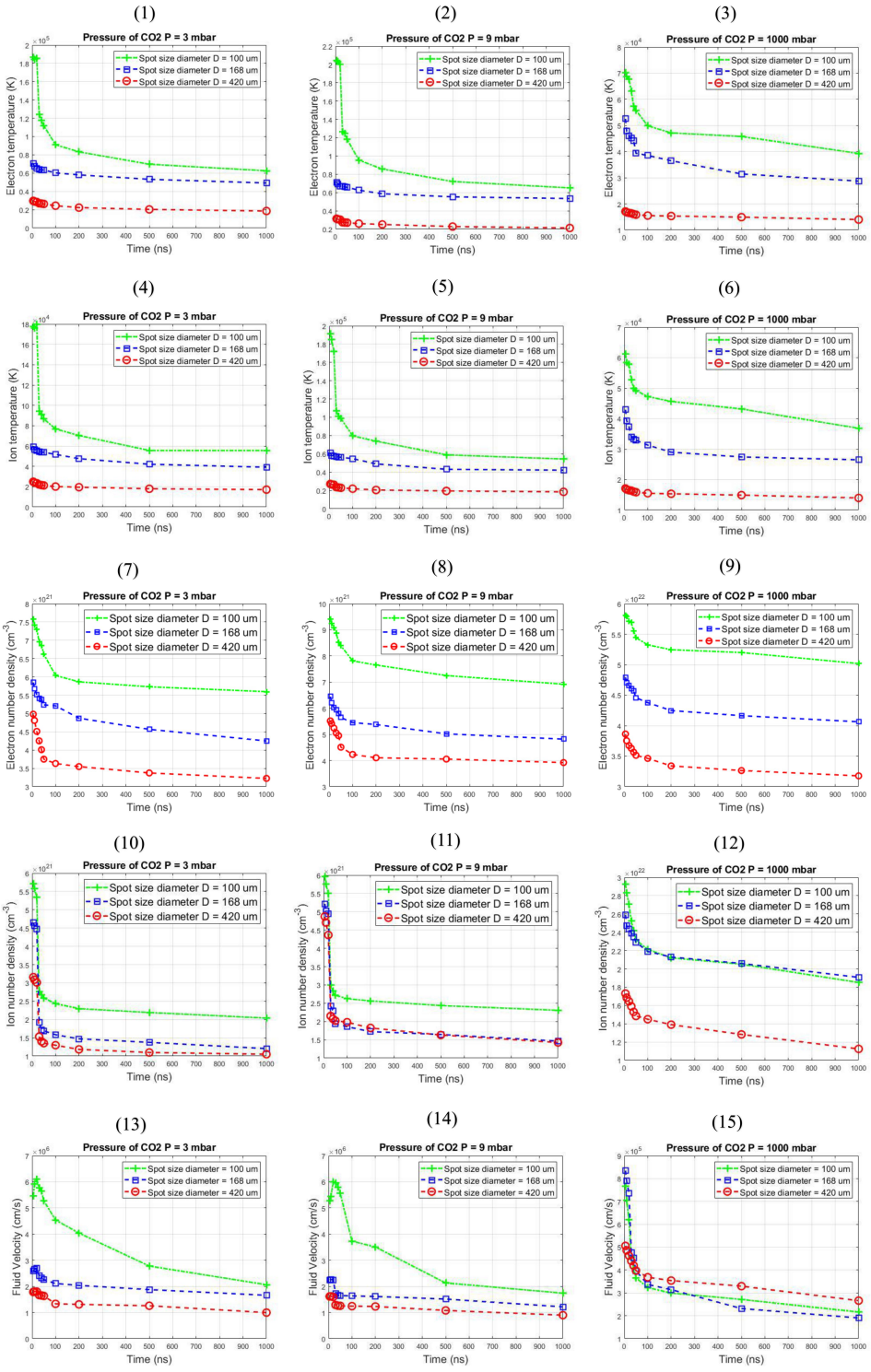

Figure 3.18: Variation of the electron temperature (1st row), ion temperature (2nd row), electron density (3rd row), ion density (4th row), and fluid velocity (5th row) with time, calculated for different focusing diameters: 100 µm (green line), 168 µm (blue line), and 420 µm (red line) for three CO_2 pressures: 3 mbar (1st column), 9 mbar (2nd column), and 1000 mbar (3rd column). Subpanels (1–15) represent individual cases.

Figure 3.18 shows the electron and ion temperatures, electron and ion number densities, and fluid velocity of the simulated graphite plasma for different spot sizes (100 μm, 168 μm, and 420 μm) under varying carbon dioxide pressures of 3 to 9 mbar on Mars and 1000 mbar on Earth. The evolution of the simulated plasma was monitored at intervals of 5 ns, from 10 to 50 ns in 10 ns steps, and then at 100 ns, 200 ns, 500 ns, and 1000 ns. Each column details the results for a specific CO_2 pressure (3, 9, and 1000 mbar) across different laser irradiances: 25 GW/cm^2 for a spot size of 100 μm, 9 GW/cm^2 for a spot size of 168 μm, and 1.45 GW/cm^2 for a spot size of 420 μm.

Figure 3.18 (subpanels 1–6) presents the variation of electron and ion temperature distributions as a function of laser spot size and ambient CO_2 pressure. For a given spot size, both electron and ion temperatures show a slight increase at low pressure (a few mbar), whereas at higher pressure ($\geq$ 1000 *mbar*), a pronounced decrease in temperature is observed across all simulation times. This reduction is attributed to plasma confinement by the dense ambient gas, which impedes the motion of plasma particles [59]. For a spot size of 100 μm, the peak electron temperature during the laser-active phase (5–10 ns) ranges from 186,676.8 K at 3 mbar to 204,475.8 K at 9 mbar and drops to 70,230.6 K at 1000 mbar. Similarly, the peak ion temperature at 5 ns varies from 177,396.9 K at 3 mbar to 191,592.0 K and 61,210.7 K at 9 and 1000 mbar, respectively. Following laser cessation (> 20 ns), both electron and ion temperatures exhibit an exponential decay, governed by plasma cooling dynamics [60].

The observed temperature variation with pressure depends not only on spot size but also on the duration of plasma evolution. Notably, the temperature values obtained in this study exceed those reported in prior works [61, 62]. This discrepancy arises from our model's inclusion of graphite plasma–CO_2 mixing under NLTE conditions. At elevated pressures, CO_2 molecules adhere to the target surface, increasing collision rates and facilitating energy transfer into plasma species, thereby elevating electron and ion temperatures as well as radiative emissions [63, 64].

Furthermore, the simulations reveal that enhanced ionization states of carbon and oxygen improve the plasma's ability to emit and absorb radiation, leading to the formation of localized temperature peaks. Analysis of the temperature and ionization distributions indicates a

direct correlation between high ionization regions and elevated plasma temperatures [65, 66], underscoring the critical role of ionization dynamics in shaping the thermal behavior of the plasma.

Figure 3.18 (subpanels 7–12) presents the evolution of electron and ion number densities over time intervals ranging from 5 ns to 1000 ns. The results indicate that ambient gas pressure exerts a greater influence on electron and ion densities than the laser spot size. Electron number density peaks during laser activation (5–10 ns). At low pressures (3–9 mbar), it increases modestly from approximately 7.57×10^{21} cm^{-3} at 3 mbar to 9.42×10^{21} cm^{-3} at 9 mbar. At high pressure (1000 mbar), a pronounced rise to 5.8×10^{22} cm^{-3} is observed for a 100 µm spot size.

Larger spot sizes (168 µm and 420 µm) result in reduced electron densities across all pressures, with respective decreases of 0.77 and 0.65-fold at 3 mbar, 0.68 and 0.58-fold at 9 mbar, and 0.82 and 0.66-fold at 1000 mbar. For ion densities at 5 ns and a 100 µm spot size, values are approximately 5.71×10^{21} cm^{-3} at 3 mbar, 5.96×10^{21} cm^{-3} at 9 mbar, and 2.93×10^{22} cm^{-3} at 1000 mbar. Similar reductions are observed for larger spot sizes, with ion density decreasing by 0.81, 0.88, and 0.89-fold (168 µm) and by 0.55, 0.82, and 0.67-fold (420 µm) for 3, 9, and 1000 mbar, respectively.

At low Martian pressures, ion density is less sensitive to pressure variations compared to electron density [67]. In contrast, under Earth's atmospheric pressure, both electron and ion densities significantly increase due to enhanced plasma ionization [68]. Following laser deactivation at 20 ns, electron density undergoes a marked exponential decrease as free electrons rapidly diminish. The decline continues throughout the simulation, reaching minimum values at 500 ns and 1000 ns.

Figure 3.18 (subpanels 13–15) illustrates the variation of plasma fluid velocity across different laser spot sizes (100 µm, 168 µm, and 420 µm) and CO_2 pressures ranging from 3 to 9 mbar and 1000 mbar, with measurements taken from 5 ns to 1000 ns. A clear correlation between fluid velocity and spot size is observed during the initial laser activation period (5–10 ns), where smaller spot sizes lead to higher plasma velocities due to enhanced laser irradiance and more efficient energy coupling.

At an ambient pressure of 3 mbar and 10 ns, the plasma expansion velocity peaks, increasing from approximately 1.8×10^6 cm/s for a 420 µm spot to 2.69×10^6 cm/s and 6.1×10^6 cm/s for 168 µm and 100 µm spots, respectively. Raising the ambient pressure to 9 mbar further enhances velocities by factors of 1.40 (168 µm) and 3.76 (100 µm), consistent with experimental observations of aluminum plasmas at low ambient pressures [69, 70]. This behavior arises from increased energy transfer and higher ionization efficiency in plasmas with smaller focal spots.

At high ambient pressure (1000 mbar), plasma velocities decrease significantly to approximately 0.14, 0.30, and 0.27 (normalized units) for 100 µm, 168 µm, and 420 µm spot sizes, respectively. The confining effect of the surrounding gas restricts plasma expansion and reduces flow speed. Following laser deactivation (≥ 20 *ns*), the fluid velocity exhibits a quasi-exponential decay, gradually approaching minimal values at later time intervals (500–1000 ns).

3.6.2 Effect of ambiant gases: He vs CO2

Especially in plasma formation, the ambient gas composition plays a crucial role. This section examines the influence of ambient gas composition on the evolution of graphite plasma under NLTE conditions. Simulations were performed using helium (He) and carbon dioxide (CO_2) at identical pressure conditions.

Figures 3.19, 3.20, and 3.21 compare the plasma electron temperature field and spatial distribution at multiple stages of plasma evolution in the presence of He gas, at pressures of 6 mbar (Mars-like) and 1000 mbar (Earth-like). The simulations were conducted for two laser spot sizes: 100 µm with a laser irradiance of 25 GW cm^{-2}, and 420 µm with a laser irradiance of 1.5 GW cm^{-2}. Plasma evolution was recorded at several simulation times: 5 ns and 10 ns during laser pulse activation, and at 20–50 ns (in 10 ns increments), as well as at 100 ns, 200 ns, 500 ns, and 1000 ns after laser pulse deactivation.

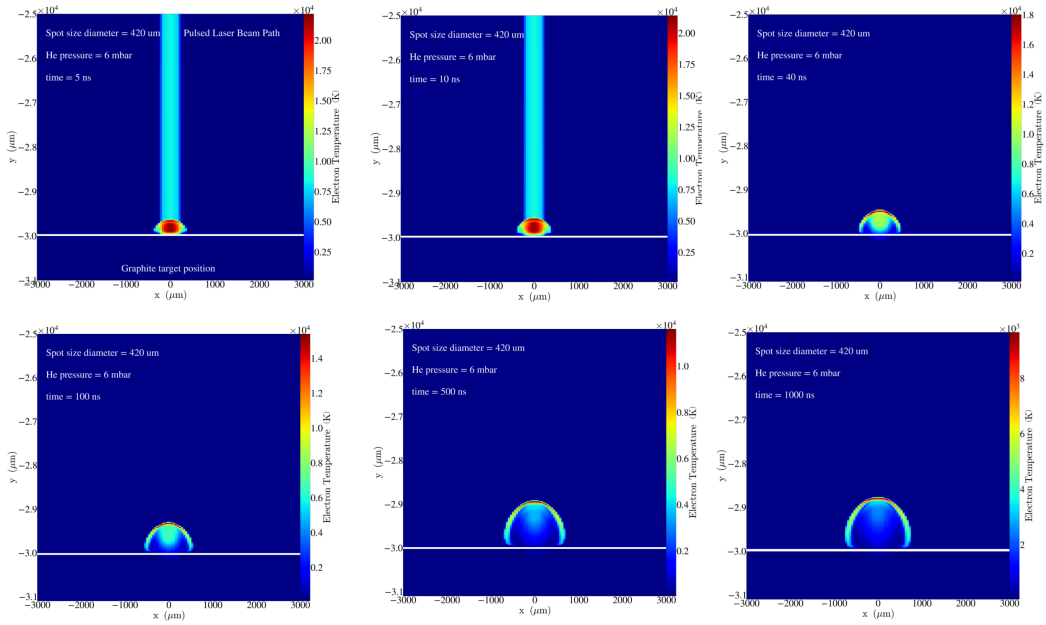

Figure 3.19: Plasma electron temperature distribution and plume expansion evolution at 5 ns, 10 ns, 40 ns, 100 ns, 500 ns, and 1000 ns simulation time for a spot size diameter of 420 µm under 6 mbar He pressure.

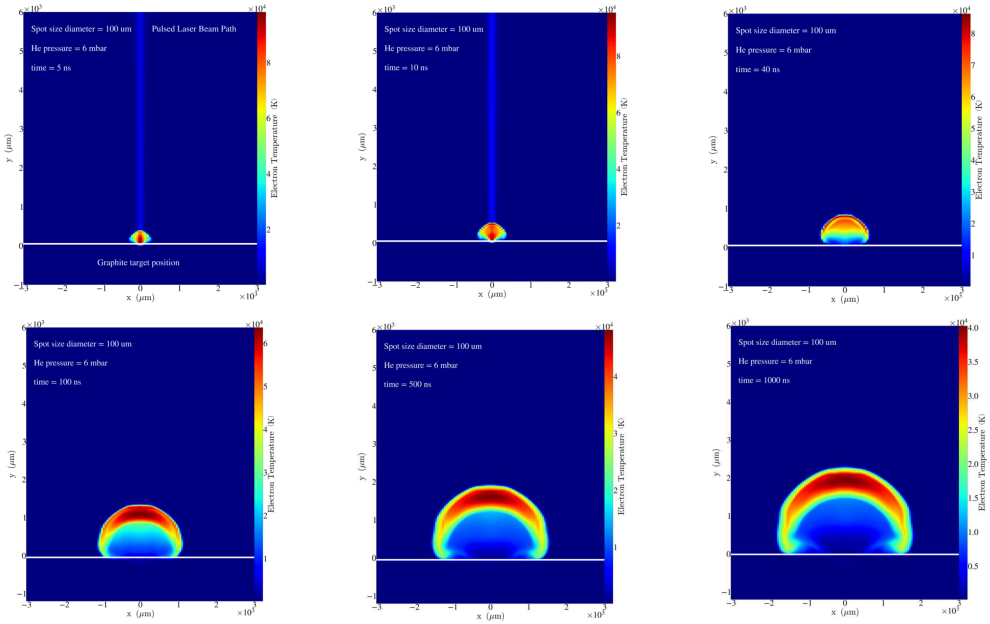

Figure 3.20: Plasma electron temperature distribution and plume expansion evolution at 5 ns, 10 ns, 40 ns, 100 ns, 500 ns, and 1000 ns simulation time for a spot size diameter of 100 µm under 6 mbar He pressure.

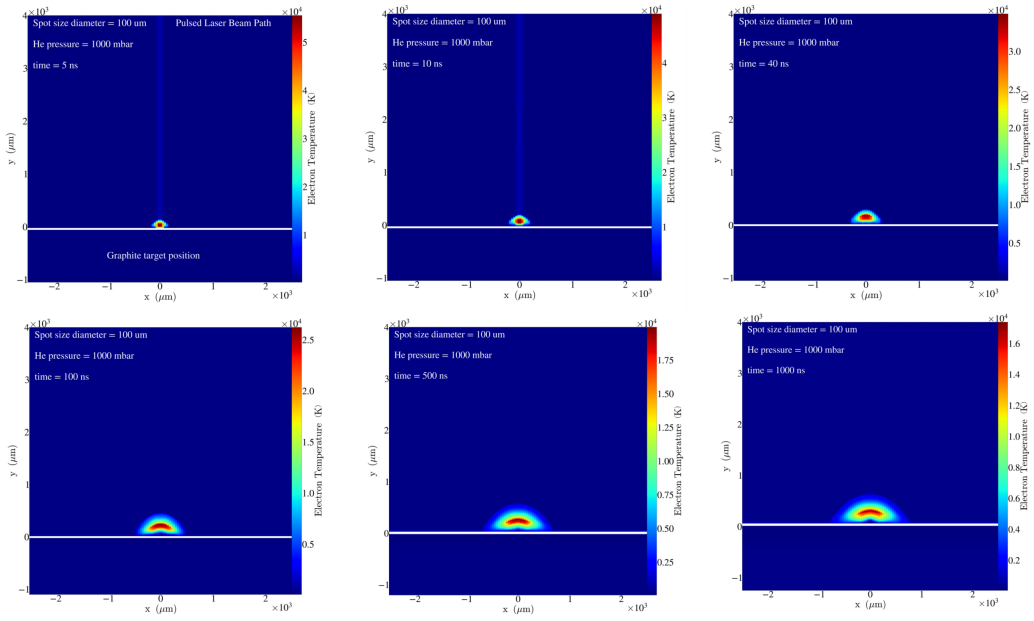

Figure 3.21: Plasma electron temperature distribution and plume expansion evolution at 5 ns, 10 ns, 40 ns, 100 ns, 500 ns, and 1000 ns simulation time for a spot size diameter of 100 µm under 1000 mbar He pressure.

Figure 3.22 (subpanels 1–6) illustrates how the ambient gas composition (He vs. CO_2) influences electron and ion temperature dynamics at two pressures—6 mbar and 1000 mbar—over time delays ranging from 5 ns to 1000 ns, with laser spot sizes of 100 µm and 420 µm. Across all time points, CO_2 consistently results in higher temperatures than He due to its higher molecular mass, larger collision cross-section, and superior ability to confine heat within the plasma. These properties enable CO_2 molecules to transfer energy more effectively and slow plasma expansion, thereby maintaining elevated temperatures for a longer duration.

Both electron and ion temperatures peak during the laser pulse (5–10 ns). At 6 mbar, electron temperatures range from 187,821.6 K (CO_2) and 98,153 K (He) with a 100 µm spot to 30,260 K (CO_2) and 22,181.3 K (He) with a 420 µm spot. At 1000 mbar, the electron temperature reduction factors are 1.5 for CO_2 and 1.8 for He at a 100 µm spot size. Ion temperatures show similar trends: at 6 mbar, they range from 185,120.7 K (CO_2) and 96,335.4 K (He) for a 100 µm spot, down to 25,897.3 K (CO_2) and 20,538 K (He) for a 420 µm spot.

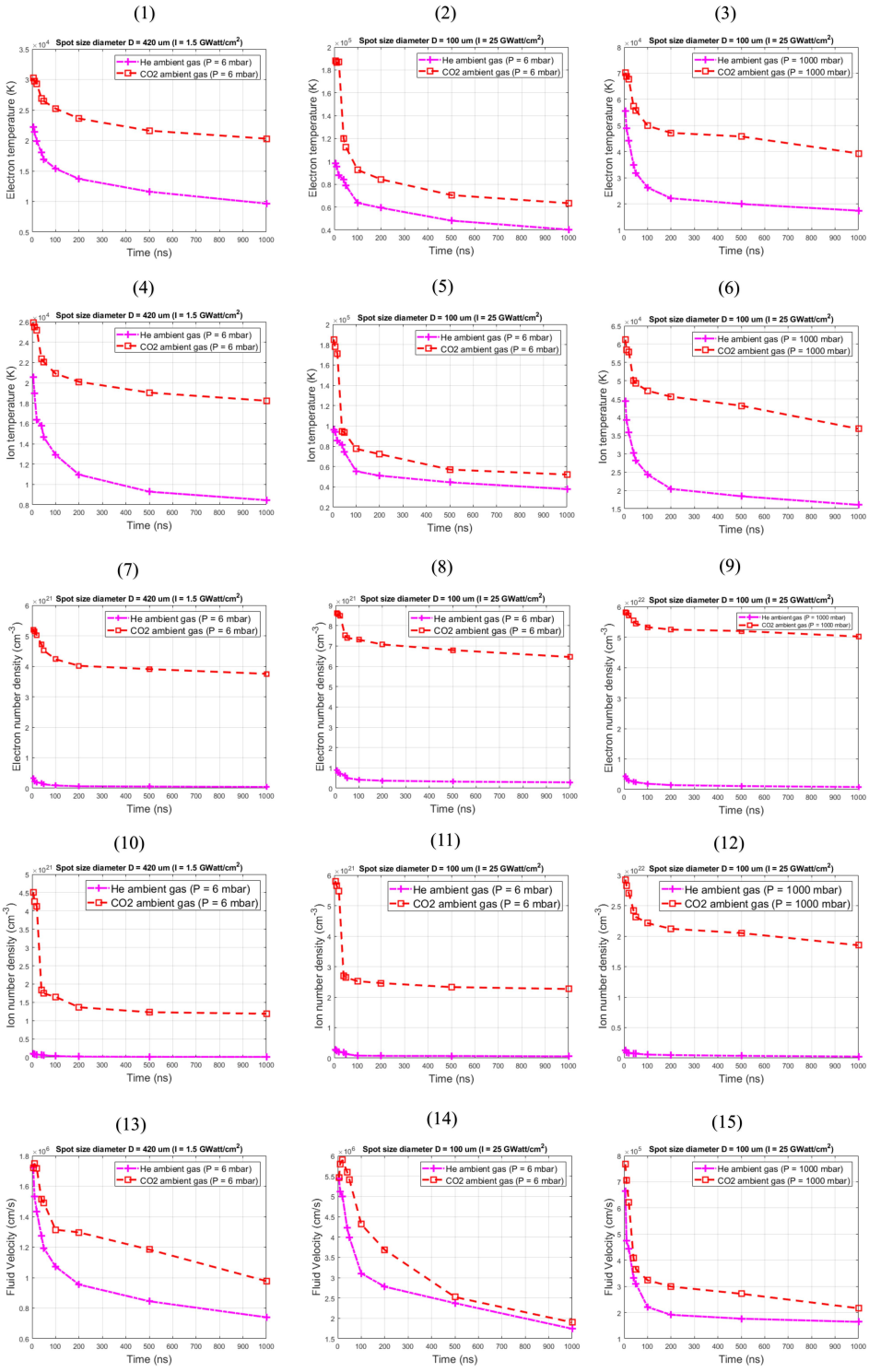

Figure 3.22: Variation of the electron temperature (1st row), ion temperature (2nd row), electron number density (3rd row), ion number density (4th row), and fluid velocity (5th row) with time and spot sizes (100 μm and 420 μm). Calculations are performed for different ambient gas compositions: He (magenta line) and CO_2 (red line) under two pressures, 6 mbar (1st and 2nd columns) and 1000 mbar (3rd column). Subpanels (1–15) represent individual cases.

At 1000 mbar, both electron and ion temperatures are approximately two times lower in He than in CO_2, primarily due to CO_2 higher density (under equal pressure), greater mass, and higher ionization potential [71]. The thermal properties of CO_2, along with the internal energy modes of its diatomic molecules, further enhance this effect [72]. Following the laser pulse, at an early delay time of 20 ns, both electron and ion temperatures decay exponentially, reaching minimum values at delay times of 500 ns and 1000 ns, driven by plasma expansion and the cooling effect of the background gas.

At both low (6 mbar) and high (1000 mbar) pressures, electron and ion number densities are consistently higher in a CO_2 atmosphere than in a He atmosphere, as shown in figure 3.22, subpanels (7–12). This behavior is primarily due to the greater mass density and higher ionization potential of CO_2 relative to He [73]. It is also evident that a degree of mixing occurs between the ablated graphite material and the surrounding CO_2 or He atmosphere. The electron and ion number densities peak at 5 ns, reaching 9.2×10^{20} cm^{-3} and 2.7×10^{20} cm^{-3}, respectively, in He, and 8.6×10^{21} cm^{-3} and 5.8×10^{21} cm^{-3}, respectively, in CO_2, for a laser spot size of 100 µm at 6 mbar. For a spot size of 420 µm, both electron and ion number densities decrease by factors of approximately 3 and 2 in He and CO_2, respectively.

At 1000 mbar, the electron and ion number densities increase by roughly a factor of 5 compared to those at 6 mbar. This increase is attributed to enhanced collisional interactions with the background gas and a reduced mean free path [74]. After 10 ns, both densities exhibit an exponential decline over time due to plasma expansion, cooling effects of the background gas, and confinement dynamics.

In our simulation, the dynamic behavior of fluid motion within the plasma was thoroughly analyzed, enabling us to characterize the evolution of fluid velocity patterns under different ambient gases (He and CO_2), as illustrated in figure 3.22, subpanels (13–15). These velocity profiles provide key insights into plasma expansion dynamics. Overall, the fluid velocity is lower in a He atmosphere compared to CO_2, particularly during the initial phase (5–10 ns). This difference arises from the greater density of ambient species in CO_2, which more effectively slows the expansion of the plasma plume [75].

At 10 ns, the maximum fluid velocity for both laser spot sizes (100 μm and 420 μm) increases slightly from 5.4×10^6 cm/s and 1.7×10^6 cm/s under low-pressure He to 5.8×10^6 cm/s and 1.75×10^6 cm/s under low-pressure CO_2. After the laser pulse (> 10 ns), the fluid velocity undergoes a quasi-exponential decay, reaching minimum values at delay times of 500 ns and 1000 ns due to plasma cooling and interaction with the background gas. At high background pressure (1000 mbar), the overall fluid velocity decreases by approximately a factor of 7, as a result of enhanced plasma confinement effects.

3.6.3 Effect of Focusing Diameter for Fixed Laser Irradiance

In planetary LIBS applications, maintaining constant irradiance is uncommon, as laser irradiance often varies due to changes in standoff distance, atmospheric conditions, and target surface irregularities. In this study, we examine the case of constant irradiance to isolate the specific influence of focusing diameter on plasma formation and dynamics. By controlling irradiance, we are able to assess how variations in spot size affect energy deposition and plasma behavior, particularly in a CO_2 rich environment such as that on Mars. The interaction between the laser beam waist and the resulting plasma plume—impacting energy absorption, confinement, and expansion provides valuable insights for optimizing LIBS measurements under planetary conditions.

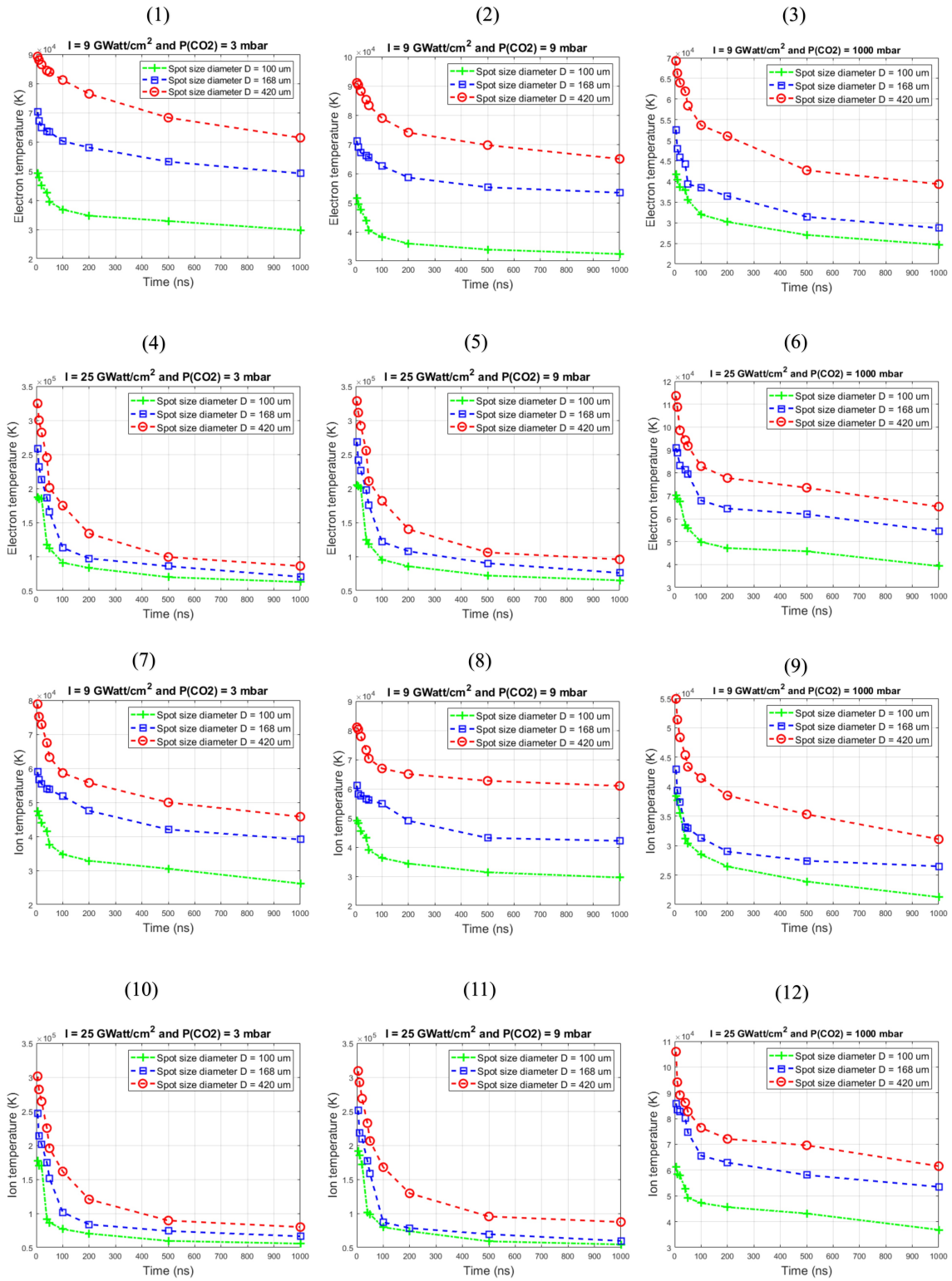

Figure 3.23: Variation of the electron temperature (first and second rows) and ion temperature (third and fourth rows) with time and laser irradiances 9 GW cm^{-2} (first and third rows) and 25 GW cm^{-2} (second and fourth rows). Calculated for different focusing diameters: 100 μm (green line), 168 μm (blue line), and 420 μm (red line) under three CO_2 pressures: 3 mbar (first column), 9 mbar (second column), and 1000 mbar (third column). Subpanels 1–12 represent individual cases.

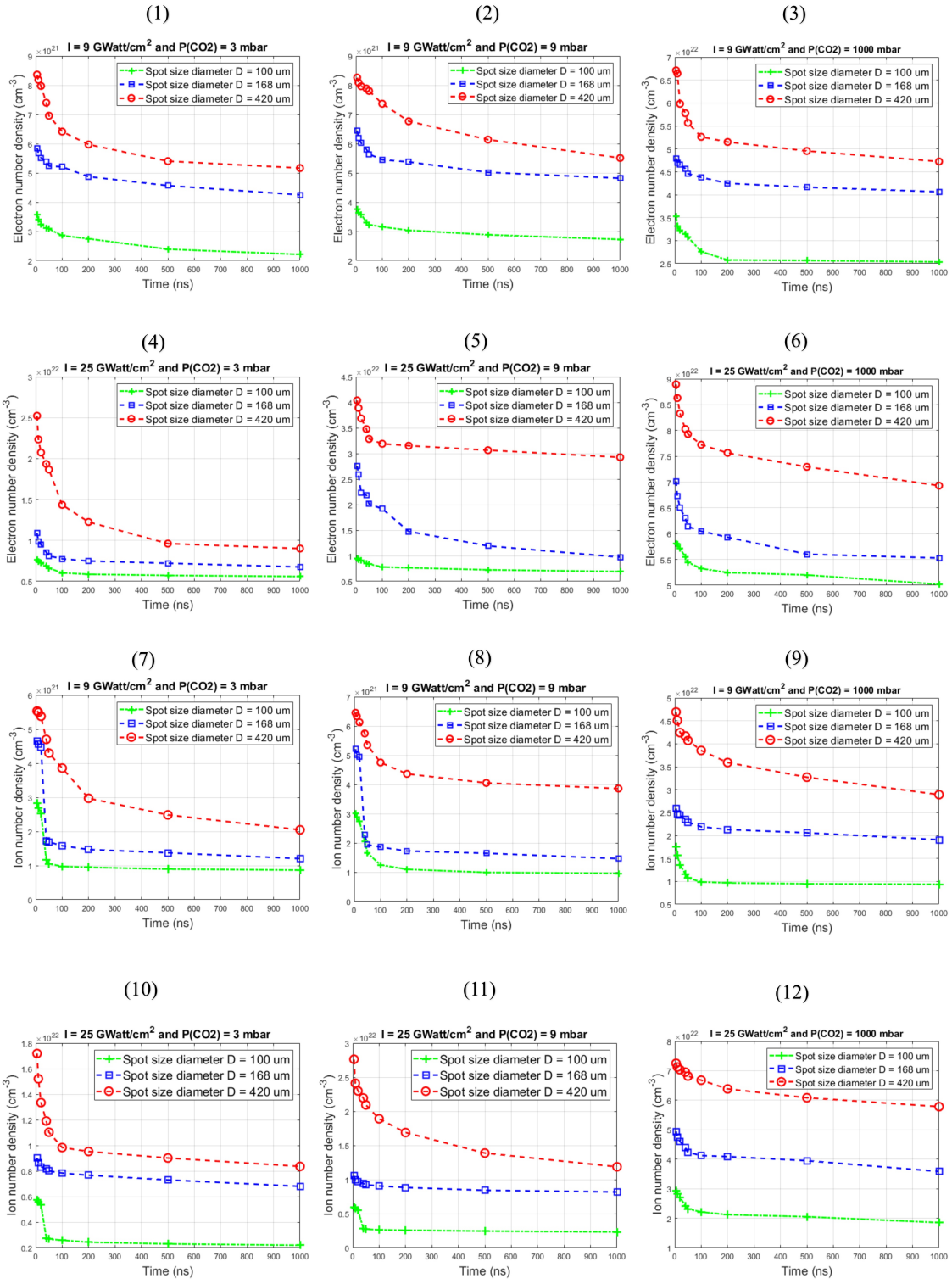

Figure 3.24: Variation of the electron number density (first and second rows) and ion number density (third and fourth rows) with time and laser irradiances 9 GW cm^{-2} (first and third rows) and 25 GW cm^{-2} (second and fourth rows). Calculated for different focusing diameters: 100 μm (green line), 168 μm (blue line), and 420 μm (red line) under three CO_2 pressures: 3 mbar (first column), 9 mbar (second column), and 1000 mbar (third column). Subpanels 1–12 represent individual cases.

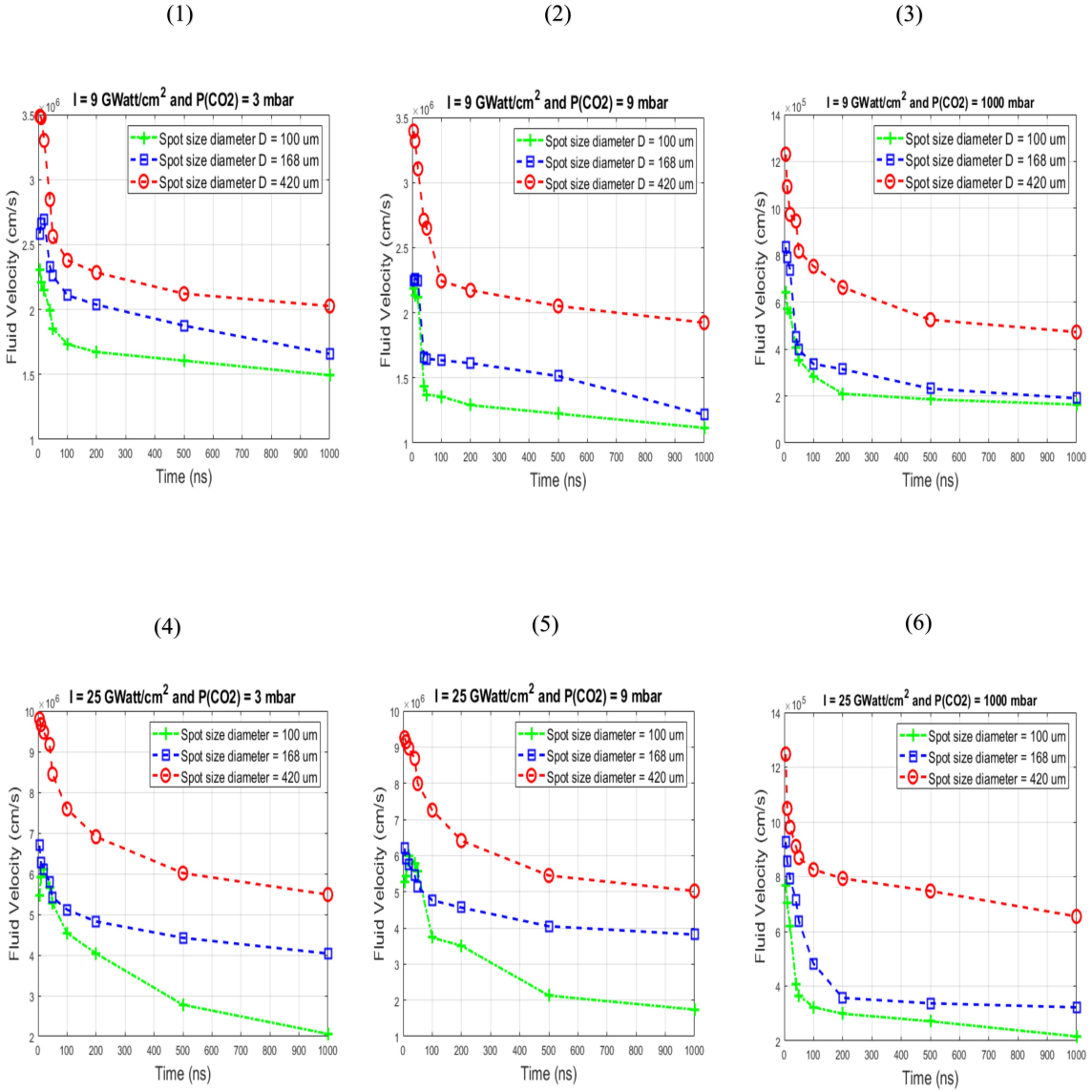

Figure 3.25: Variation of the fluid velocity (fifth and sixth rows) with time and laser irradiances 9 GW cm^{-2} (fifth row) and 25 GW cm^{-2} (sixth row). Calculated for different focusing diameters: 100 μm (green line), 168 μm (blue line), and 420 μm (red line) under three CO_2 pressures: 3 mbar (first column), 9 mbar (second column), and 1000 mbar (third column). Subpanels 1–6 represent individual cases.

The plasma parameters generated by a nanosecond laser on a graphite target are strongly influenced by laser irradiance and focusing diameter. An increase in focusing diameter enhances energy transfer to the target, promoting plasma expansion in the direction of the incident laser due to additional heating effects from the nanosecond pulse [76, 77]. Figures 3.23 to 3.25 illustrate the variations in electron and ion temperatures, number densities, and fluid velocity distributions under laser irradiances of 25 and 9 GW·cm^{-2}, across different focusing diameters

(100, 168, and 420 μm), and under both low and high CO_2 pressures over a simulation time span of 5 to 1000 ns.

At both irradiance levels of 9 and 25 GW·cm^{-2}, electron and ion temperatures rise notably with increasing spot size, as depicted in Figure 3.23 (subpanels 1–12). For 9 GW·cm^{-2} at low ambient pressures (3–9 mbar) during the laser-active period (5–10 ns), temperatures increase from approximately 5.0×10^4 K (electrons) and 4.7×10^5 K (ions) for a 100 μm spot size to 9.0×10^5 K and 8.0×10^5 K, respectively, for a 420 μm spot. At 25 GW·cm^{-2}, initial temperatures for a 100 μm spot size reach 1.87×10^5 K (electrons) and 1.86×10^5 K (ions), increasing by factors of approximately 1.4 and 1.7 for larger spot sizes.

Under high-pressure conditions (1000 mbar), both temperatures decrease by factors of approximately 3.7 and 3.9 across all spot sizes. The observed rise in temperature with increased irradiance and spot size is attributed to enhanced energy absorption by electrons and ions through laser-photon interactions [78]. After the laser pulse terminates (20 ns), both temperatures exhibit a rapid exponential decay, with significant cooling observed at 500 and 1000 ns.

Figure 3.24 (subpanels 1–12) presents the temporal evolution of electron and ion number densities in the plasma plume. At constant laser irradiance, increasing the spot size results in substantial growth in both electron and ion densities, particularly during the laser-active period (5–10 ns). For an irradiance of 9 GW·cm^{-2} at 5 ns, maximum electron and ion densities increase from approximately 4×10^{21} cm^{-3} and 3×10^{21} cm^{-3} (100 μm spot size) to 8×10^{22} cm^{-3} and 6×10^{22} cm^{-3} (420 μm spot size), respectively. At 25 GW·cm^{-2}, a 100 μm spot size yields densities of about 8×10^{21} cm^{-3} (electrons) and 6×10^{21} cm^{-3} (ions), which increase by factors of 2.9 and 4.2 with larger spot sizes.

Under high-pressure conditions (1000 mbar), number densities across all spot sizes are further enhanced—by approximately one order of magnitude for electrons and up to 15-fold for ions. This increase is attributed to more effective laser energy absorption and intensified ionization and recombination processes within the graphite target [79]. As the simulation advances, both densities decrease exponentially, reaching minimum values at later times (500–1000 ns).

Figure 3.25 (subpanels 1–6) illustrates the variation of fluid velocity as a function of laser irradiance and spot size. During the active laser phase (5–10 ns), a strong positive correlation is observed between spot size and fluid velocity. At 9 GW·cm^{-2} and low pressure, velocity increases from 2.3×10^6 to 3.5×10^6 cm·s^{-1} for spot sizes of 100, 168, and 420 μm, respectively. When the irradiance is increased to 25 GW·cm^{-2}, the fluid velocity reaches 5.4×10^6 cm·s^{-1} for a 100 μm spot and increases further by factors of 1.24 and 1.82 for larger spots.

These increases are attributed to more effective energy coupling at larger spot sizes, which enhances the acceleration of plasma species. At high ambient pressure (1000 mbar), fluid velocities at 10 ns are reduced by approximately a factor of 4 at 9 GW·cm^{-2} and a factor of 6 at 25 GW·cm^{-2}, across all spot sizes, due to increased resistance from the surrounding gas. Following the termination of the laser pulse (20 ns), the fluid velocity declines quasi-exponentially, approaching minimum values at 500–1000 ns as the plasma undergoes thermal equilibration with the ambient environment.

In contrast, pressure variations primarily influence the quantitative characteristics of plasma density. Changes in the laser focal spot size, on the other hand, indirectly affect plume morphology and expansion dynamics particularly under low-pressure conditions such as those encountered in the Martian atmosphere, and especially during the laser pulse duration. At high pressures, the effects are more evident in the spatial distribution and initial energy profile of the plasma. Increased ambient pressure confines the plasma and resists the motion of plasma species, leading to reductions in key parameters such as electron and ion temperatures and fluid velocity. This confinement also causes notable changes in electron and ion number densities. These findings are highly relevant for in situ LIBS elemental analysis on Mars, where both focusing conditions and the composition of the surrounding gas critically influence the resulting LIBS signal.

3.6.4 Model limitations

To enhance our approach, this simulation focuses on carefully analyzing the various physical, chemical, optical, and environmental factors that influence plasma properties and the resulting spectral features in LIBS, with particular attention to ChemCam and SuperCam LIBS

spectra. Initially, we investigate laser-induced plasma formation at both early and delayed times ($t = 5$ ns to 1000 ns) in our simulations, taking into account the interaction between the expanding plasma plume and the surrounding ambient gases (He and CO_2). However, it is important to acknowledge that our simulations are subject to certain limitations, such as the use of a single laser pulse (the matrix effect)[80] and the relatively short simulation duration for plasma evolution (up to 1 μs). This limitation poses a challenge when comparing to real LIBS instruments, where integration times typically exceed 1 ms, allowing the plasma to evolve over significantly longer periods.

Moreover, experimental studies [81] have shown that molecular species persist in the graphite plasma beyond a delay time of 1 μs, indicating that the emission intensities of atomic lines can be influenced by ongoing molecular formation throughout the plasma lifetime. In addition, the effectiveness of the hydrodynamic radiation model diminishes at extended simulation times due to a substantial increase in the Knudsen number (Kn), which represents the ratio of the species' mean free path to the characteristic plasma length scale. Addressing this issue requires considering alternative approaches, such as the direct simulation Monte Carlo (DSMC) method, which offers a more accurate representation of plume expansion, particularly at longer delay times [82].

Furthermore, the use of a finer Eulerian grid in targeted regions of the simulation domain can improve accuracy, especially when modeling the interaction between plasma formation and the ambient gas. It is also important to note that chemical reactions are not included in this study; thus, molecular band emissions are not modeled. Nevertheless, the role of molecular formation becomes increasingly significant at longer times (> 1 μs) [83].

References

[1] Cousin A., Forni O., Maurice S., Gasnault O., Fabre C., Sautter V., Wiens R., Mazoyer J., Laser induced breakdown spectroscopy library for the martian environment, Spectrochim. Acta B At. Spectrosc., 2011, 66 (1112), 805–814.

[2] B. Fryxell, K. Olson, P. Ricker, F. X. Timmes, M. Zingale, D. Q. Lamb, P. MacNeice, R. Rosner, and H. Tufo, FLASH: An adaptive mesh hydrodynamics code for modelling astrophysical thermos nuclear flashes. Astrophys. J. Suppl. Ser., vol. 131, 273–334 (2000).

[3] D. R. Farley, K. Shigemori, and H. Azechi, "Laser-produced blast wave and numerical simulation using the flash code," Laser and Particle Beams, vol. 23, pp. 513–519, 2005.

[4] C. Orban, M. Fatenejad, S. Chawla, S. Wilks, and D. Q. Lamb, "A radiation hydrodynamics code comparison for laser-produced plasmas: Flash versus hydra and the results of validation experiments," arXiv:1201.5885 [physics.data-an], 2013.

[5] Kaiser T.B., Laser ray tracing and power deposition on an unstructured three-dimensional grid, Phys. Rev. E, 2000, 61, 895–905.

[6] Stavroudis, O. (1972). The Optics of Rays, Wavefronts, and Caustics, p. 324.

[7] The Flash Center for Computational Science, FLASH User's Guide Version-4.6.2, University of Rochester, 2019.

[8] Nathan Daniel Masters, T B Kaiser, Robert W Anderson and D. C. Eder. (2010). "Laser ray tracing in a parallel arbitrary Lagrangian-Eulerian adaptive mesh refinement hydrocode". Journal of Physics Conference Series 244(3):032022. DOI:10.1088/1742-6596/244/3/032022.

[9] A.F. Nikiforov, V.G. Novikov, V.B. Uvarov, *Quantum-Statistical Models of Hot Dense Matter: Methods for Computation Opacity and Equation of State* (Birkhauser Verlag, Basel, Boston, Berlin, 2005).

[10] Lucia Daniela Pietanza, Olivier Guaitella, Vincenzo Aquilanti, Iole Armenise et al., "Advances in non-equilibrium CO2 plasma kinetics: a theoretical and experimental review," *The European Physical Journal D* **75**(9), DOI:10.1140/epjd/s10053-021-00226-0 (2021).

[11] J.J. Macfarlane, "IONMIX - a code for computing the equation of state and radiative properties of LTE and non-LTE plasmas," *Comput. Phys. Commun.* **56**, 259-278 (1989).

[12] H. Schamel, "Lagrangian fluid description with simple applications in compressible plasma and gas dynamics". Physics Reports 392(5):279-319. 9-319. DOI:10.1016/j.physrep.2003.12.00 2004.

[13] Alexandre Caboussat, "Numerical Simulation of Two-Phase Free Surface Flows". Archives of Computational Methods in Engineering 12(2):165-224. DOI :10.1007/BF03044518, 2005.

[14] D. Benson, "Computational methods in Lagrangian and Eulerian hydrocodes". In: Computer Methods in Applied Mechanics and Engineering, 1992.

[15] Minna Palmroth et al., "Vlasov methods in space physics and astrophysics". Living Reviews in Computational Astrophysics. https://doi.org/10.1007/s41115-018-0003-2, 2018.

[16] Takahiro Yamada, Fumio Kikuchi, "An arbitrary Lagrangian-Eulerian finite element method for incompressible hyperelasticity". Computer Methods in Applied Mechanics and Engineering. https://doi.org/10.1016/0045-7825(93)90106-8,1993.

[17] M. Kucharik, Ph. D. Thesis, Czech Technical University in Prague 27, 1273 (2006).

[18] M. J. Berger & J. Oliger, "Adaptive mesh refinement for hyperbolic partial differential equations". In: Journal of Computational Physics 53.3, pp. 484–512, 1984.

[19] M. Gittings et al., "The RAGE radiation hydrodynamic code," Comput. Sci. Discovery 1,015005 (2008).

[20] J.J. MacFarlane et al., Journal of Quantitative Spectroscopy & Radiative Transfer 99 (2006) 381–397.

[21] D. DeZeeuw & K. G. Powell, JCP, 104, 56, 1993.

[22] P. MacNeice & K. Olson, "PARAMESH: A parallel adaptive mesh refinement community toolkit". In: Computer Physics Communications October, 2000.

[23] R. Löhner, "An adaptive finite element scheme for transient problems in CFD". In: Computer Methods in Applied Mechanics and Engineering, 1987.

[24] Andrew Steele, Francis M Mccubbin, Marc Fries and D.C. Golden, "Graphite in the Martian meteorite Allan Hills 84001". American Mineralogist 97(7):1256-1259. DOI:10.2138/am.2012 2012.

[25] A. Cousin et al., Spectrochimica Acta Part B 66 (2011) 805–814.

[26] D. Lee and A. E. Deane, "An unsplit staggered mesh scheme for multidimensional magnetohydrodynamics", J. Comput. Phys., 2009, 228, 952.

[27] D. Lee, "A solution accurate, efficient and stable unsplit staggered mesh scheme for three dimensional magnetohydrodynamics", J. Comput. Phys., 2013, 243, 269.

[28] P. Tzeferacos et al., "FLASH MHD simulations of experiments that study shock-generated magnetic fields". High Energy Density Physics 17:24-31. DOI:10.1016/j.hedp.2014.11.003, 2015.

[29] The HYPRE library is available at: https://computing.llnl.gov/projects/hypre-scalable-li software.

[30] M. M. Marinak et al., APS Meeting Abstracts 2009, 8100P.

[31] VisIt an open-source interactive parallel visualization and graphical analysis tool for viewing scientific data. visit.llnl.gov/.

[32] A. Kramida, Yu. Ralchenko, J. Reader, NIST ASD Team, "NIST Atomic Spectra Database (ver. 5.9)", [Online]. Available: https://www.nist.gov/pml/atomic-spectra-database. [2021, October 30].

[33] P. Colella, "J. Comput. Phys. 87, 171 (1990)".

[34] R. LeVeque, "Finite Volume Methods for Hyperbolic Problems", Cambridge University Press, 2002, ISBN: 9780511791253.

[35] S. Li, "An HLLC Riemann solver for magneto-hydrodynamics", J. Comput. Phys., 2005, 203, 344.

[36] E. F. Toro, "Riemann Solvers and Numerical Methods for Fluid Dynamics", Springer Science & Business Media, 2009, ISBN: 978-3-540-49834-6.

[37] Jing Ye, Chengcai Shen, Jun Lin and Zhixing Mei, "An efficient parallel semi-implicit solver for anisotropic thermal conduction in the solar corona". Astronomy and Computing 30:100341. DOI:10.1016/j.ascom.2019.100341.

[38] P. Tzeferacos, A. Rigby, A. Bott, A. R. Bell, "Numerical modeling of laser-driven experiments aiming to demonstrate magnetic field amplification via turbulent dynamo". Physics of Plasmas 24(4). DOI:10.1063/1.4978628, 2017.

[39] M.J. Turk et al., "yt: A multi-code analysis toolkit for astrophysical Simulation data", The Astrophysical Journal Supplement Series, 2011, 192:9 (16pp), available at:http://yt.enzotools.org/.

[40] Colao, F., Fantoni, R., Lazic, V., & Paolini, A. (2004). LIBS application for analyses of Martian crust analogues: search for the optimal experimental parameters in air and CO_2 atmosphere. Appl. Phys. A, **79**(1), 143–152.

[41] Capitelli, M., Casavola, A., Colonna, G., & Giacomo, A. D. (2004). Laser-induced plasma expansion: theoretical and experimental aspects. Spectrochim. Acta B At. Spectrosc., **59**(3), 271–289.

[42] Ewusi-Annan, E., Surmick, D. M., Melikechi, N., & Wiens, R. C. (2018). Simulated laser-induced breakdown spectra of graphite and synthetic shergottite glass under Martian conditions. Spectrochimica Acta Part B, **148**, 31–43.

[43] Hansen, P. B., Schroder, S., Kubitza, S., Rammelkamp, K., Vogt, D. S., & Hubers, H.-W. (2021). Modeling of time-resolved LIBS spectra obtained in Martian atmospheric conditions with a stationary plasma approach. Spectrochimica Acta Part B: Atomic Spectroscopy, **178**, 106115.

[44] Alberti, A., Munafo, A., Koll, M., Nishihara, M., Pantano, C., Freund, J. B., & Panesi, M. (2020). Laser-induced nonequilibrium plasma kernel dynamics. J. Phys. D: Appl. Phys., **53**, 025201 (18pp).

[45] Glumac, N. G., & Elliott, G. S. (2007). The effect of ambient pressure on laser-induced plasmas in air. Opt. Lasers Eng., **45**, 27–35.

[46] Tsuda, N., & Yamada, J. (1996). Observation of forward breakdown mechanism in high-pressure argon plasma produced by irradiation by an excimer laser. J. Appl. Phys., **81**, 96.

[47] Maurice S. et al., The ChemCam instrument suite on the Mars science laboratory (MSL) rover: science objectives and mast unit description, Space Science Reviews 170(1-4). DOI: 10.1007/s11214-012-9912-2.

[48] Sizyuk, V., Hassanein, A., & Sizyuk, T. (2006). Three-dimensional simulation of laser produced plasma for extreme ultraviolet lithography applications. Journal of Applied Physics. DOI: 10.1063/1.2365717.

[49] Davies J. R., Bahr R. E., Barnak D. H., Betti R., Bonino M. J., Campbell E. M., Hansen E. C., Harding D. R., Peebles J. L., Sefkow A. B., Seka W., Chang P.-Y., Geissel M. and Harvey-Thompson A. J., Laser entrance window transmission and reflection measurements for preheating in magnetized liner inertial fusion, Physics of Plasmas, 2018, 25, 062704.

[50] Surmick D. M., Taleh L., and Melikech N., Effects of laser beam focusing characteristics on laser-induced breakdown spectra, *Applied Spectroscopy*, 2021, **75**(2), 127–136. DOI: 10.1177/0003702820961437.

[51] Gillen-Christandl K., Gillen Glen D., Piotrowicz M. J. and Saffman M., Comparison of Gaussian and super Gaussian laser beams for addressing atomic qubits, Appl. Phys. B, 2016, 122, 131.

[52] Sylvestre Maurice, Samuel Clegg, Roger C. Wiens, and Olivier Gasnault. 2016. ChemCam Activities and Discoveries during the Nominal Mission of Mars Science Laboratory in Gale crater, Mars. *Journal of Analytical Atomic Spectrometry* 31(4): DOI: 10.1039/C5JA00417A.

[53] Cowpe J. S., Pilkington R. D., Astin J. S., and Hill A. E., The effect of ambient pressure on laser-induced silicon plasma temperature, density and morphology, J. Phys. D: Appl. Phys., 2009, 42, 165202; doi:10.1088/0022-3727/42/16/165202.

[54] Sharma A.K., Thareja R.K., Plume dynamics of laser-produced aluminum plasma in ambient nitrogen, Applied Surface Science, 2005, 243, 68–75. DOI: 10.1016/j.apsusc.2004.09.093.

[55] Heltemes T.A. and Moses G. A., BADGER v1.0: A Fortran equation of state library, Computer Physics Communications, 2012, 183, 2629. DOI: 10.1016/j.cpc.2012.07.010.

[56] chen2023 Chen, Z., Chen, Z., Jiang, W., Guo, L., & Zhang, Y. (2023). Line intensity calculation of laser-induced breakdown spectroscopy during plasma expansion in nonlocal thermodynamic equilibrium. *Optics Letters*, 48. DOI:10.1364/OL.488250.

[57] Itina T.E., Hermann J., Delaporte P., Sentis M., 2003. Laser-generated plasma plume expansion: combined continuous-microscopic modeling, Physical Review E 66(6 Pt 2):066406. DOI:10.1103/PhysRevE.66.066406.

[58] Harilal S.S., Bindhu C.V., Issac R.C., Nampoori V.P.N., Vallabhan C.P.G. "Electron Density and Temperature Measurements in a Laser Produced Carbon Plasma." J. Appl. Phys. 1997. 82: 2140.

[59] Le H.C., Zeitoun D.E., Parisse J.D. "Modeling of Gas Dynamics for a Laser-Generated Plasma: Propagation into Low-Pressure Gases." Phys. Rev. E 2000. 62: 4152; doi: 10.1103/PhysRevE.62.4152.

[60] Dawood M.S., Margot J. "Effect of Ambient Gas Pressure and Nature on the Temporal Evolution of Aluminum Laser-Induced Plasmas." AIP Adv. 2014. 4: 037111; doi: 10.1063/1.4869076.

[61] Stetzler J., Tang S., Chinni R.C. "Plasma Temperature and Electron Density Determination Using Laser-Induced Breakdown Spectroscopy (LIBS) in Earth and Mars Atmospheres." Atoms 2020. 8(3): 50; doi: 10.3390/atoms8030050.

[62] Hansen P.B., Schroder S., Kubitza S., Rammelkamp K., Vogt D.S., et al. "Modeling of Time-Resolved LIBS Spectra Obtained in Martian Atmospheric Conditions with a Stationary Plasma Approach." Spectrochim. Acta Part B: At. Spectrosc. 2021. 178: 106.

[63] Szilagyi J., Parchamy H., Masnavi M., Richardson M. "Spectral Irradiance of Singly and Doubly Ionized Zinc in Low-Intensity Laser-Plasma Ultraviolet Light Sources." J. Appl. Phys. 2017. 121: 033303; doi: 10.1063/1.4973848.

[64] Sharma A.K., Thareja R.K. "Plume Dynamics of Laser-Produced Aluminum Plasma in Ambient Nitrogen." Appl. Surf. Sci. 2005. 243: 68–75; doi: 10.1016/j.apsusc.2004.09.093.

[65] Masnavi M., Parchamy H. "Calculation of the Extreme-Ultraviolet Radiation Conversion Efficiency for a Laser-Produced Tin Plasma Source." Phys. Open. 2019. 1: 100003; doi: 10.1016/j.physo.2019.100003.

[66] Parchamy H., Szilagyi J., Masnavi M., Richardson M. "Quantitative Analysis of Vacuum-Ultraviolet Radiation from Nanosecond Laser-Zinc Interaction." Opt. Laser Technol. 2018. 103: 1–7; doi: 10.1016/j.optlastec.2018.01.006.

[67] Chen Z., Bleiner D., Bogaerts A. "Effect of Ambient Pressure on Laser Ablation and Plume Expansion Dynamics: A Numerical Simulation." J. Appl. Phys. 2006. 99(6): 063304.

[68] Hermann J., Lorusso A., Perrone A., Strafella F., et al. "Simulation of Emission Spectra from Nonuniform Reactive Laser-Induced Plasmas." Phys. Rev. E Stat. Nonlinear Soft Matter Phys. 2015. 92: 5.

[69] Itina T. E., Hermann J., Delaporte P., Sentis M. "Laser-Generated Plasma Plume Expansion: Combined Continuous-Microscopic Modeling." Phys. Rev. E 2002. 66: 066406.

[70] Harilal S. S., Bindhu C. V., Tillack M. S., Najmabadi F., et al. "Internal Structure and Expansion Dynamics of Laser Ablation Plumes into Ambient Gases." J. Appl. Phys. 2003. 93: 2380; doi: 10.1063/1.1544070.

[71] Bashir, S., Farid, N., Mahmood, K., Rafique, M. S. "Influence of Ambient Gas and its Pressure on the Laser-induced Breakdown Spectroscopy and the Surface Morphology of Laser Ablated Cd." Appl. Phys. A 2012. 107: 203. DOI: 10.1007/s00339-011-6730-4.

[72] Iida, Y. "Effects of Atmosphere on Laser Vaporization and Excitation Processes of Solid Samples." Spectrosc. Acta B 1990. 45: 1353. DOI: 10.1016/0584-8547(90)80188-O.

[73] Dawood, M. S., Margot, J. "Effect of Ambient Gas Pressure and Nature on the Temporal Evolution of Aluminum Laser Induced Plasmas." AIP Advances 2014. 4: 037111. DOI: 10.1063/1.4869076.

[74] Irimiciuc, S. A., Hodoroaba, B. C., Bulaic, G., Gurlui, S. "Multiple Structure Formation and Molecule Dynamics in Transient Plasmas Generated by Laser Ablation of Graphite." Spectrochim. Acta Part B: Atomic Spectrosc. 2020. DOI: 10.1016/j.sab.2020.105774.

[75] Harilal, S. S., O'Shay, B., Tao, Y., Tillack, M. S. "Ambient Gas Effects on the Dynamics of Laser-Produced Tin Plume Expansion." J. Appl. Phys. 2006. 99: 083303. DOI: 10.1063/1.2188084.

[76] Li, X., Wei, W., Wu, J., Jia, S., Qiu, A. "The Influence of Spot Size on the Expansion Dynamics of Nanosecond-Laser-Produced Copper Plasmas in Atmosphere." *J. Appl. Phys.* 2013. **113**: 243304.

[77] Martan, J., Kunes, J., Semmar, N. "Experimental Mathematical Model of Nanosecond Laser Interaction with Material." *Appl. Surf. Sci.* 2006. **253**(7): 3525–3532. DOI: 10.1016/j.apsusc.2006.07.059.

[78] Ready, J. F. *Effect of High Power Laser Radiation*. New York: Academic Press, 1971.

[79] Pietanza, L., Colonna, G., Di Giacomo, A., Capitelli, M. "Kinetic Processes for Laser Induced Plasma Diagnostic: A Collisional-Radiative Model Approach." *Spectrochim. Acta, Part B*. 2010. **65**(8): 616–626.

[80] Anderson, R. B., Morris, R. V., Clegg, S. M., Bell, J. F., et al. "The Influence of Multivariate Analysis Methods and Target Grain Size on the Accuracy of Remote Quantitative Chemical Analysis of Rocks Using Laser Induced Breakdown Spectroscopy". Icarus. 2011. 215(2): 608–627.

[81] S. Acquaviva, M.L.D. Giorgi, High-resolution investigations of C2 and CN optical emissions in laser-induced plasmas during graphite ablation, J. Phys. B Atomic Mol. Phys. 35 (4) (2002) 795.

[82] M. Skocic, S. Bukvic, Laser induced plasma expansion and existence of local thermodynamic equilibrium, Spectrochim. Acta B At. Spectrosc. 125 (2016) 103–110.

[83] M. Dong, J. Lu, S. Yao, Z. Zhong, J. Li, J. Li, W. Lu, Experimental study on the characteristics of molecular emission spectroscopy for the analysis of solid materials containing C and N, Opt. Express 19 (18) (2011) 17021–17029.

General conclusion and outlook

Humans are naturally born curious and are driven to unravel a myriad of perplexing questions: How was the universe formed? What are the origins of life? Could life potentially thrive on other planets? These unanswered inquiries serve as a catalyst for mankind's relentless pursuit of knowledge. Mars, a planet with an atmosphere that potentially holds water in liquid or solid form beneath its surface, presents a compelling question: Can it, or has it ever, supported life? This captivating inquiry has been the driving force for scientists for nearly half a century. Significant strides in scientific exploration have unfolded since the commencement of the American rover Curiosity's mission to Mars in 2012, a historic endeavor that equipped a rover with tools for analyzing carbon isotopes on the Martian surface for the first time. Curiosity has successfully identified organic molecules in Martian sediments, including fossil fuels and muds. Concurrently, other missions have meticulously gathered data on isotopic signatures within the Martian atmosphere, while scientists have scrutinized the ratios present in Martian meteorites discovered on Earth. NASA has also disclosed compelling findings regarding the seasonal dynamics of methane in Mars' atmosphere. Terrestrial methane production involves bacteria consuming carbon dioxide (CO_2) and emitting methane (CH_4). Despite methane's relatively short lifespan of about 300 years, planetologists theorize continuous Martian methane production by the planet, persisting to this day. Notably, methane levels on Mars exhibit intriguing seasonal fluctuations, surging in summer and waning in winter. Drawing parallels with Earth, where various life forms go dormant in cold conditions and reawaken in warmth, this pattern hints at the potential for biological activity on the Red Planet. In 2020, NASA's Perseverance rover was assigned the crucial task of identifying optimal sample types to collect, aiming to confirm the source of the carbon signature and definitively ascertain its biological or

non-biological origin.

This thesis has enabled us to simulate LIBS (Laser-Induced Breakdown Spectroscopy) plasmas emanating from organic components in Mars environment using a theoretical model. This model comprehensively incorporates all the processes involved in the interaction of the ChemCam laser with the target, leading to plasma formation. Currently, there is no model available that can accurately forecast the characteristics of an ablation plume generated by a specific laser on a particular material within a given environment. Laser ablation is a multi-faceted process encompassing various physical phenomena, often occurring in non-local thermodynamic equilibrium (NLTE). The thermal parameters, optical properties, and phase diagrams of materials subjected to such intense irradiation conditions are inadequately understood and pose challenges for measurement. Consequently, despite considerable progress in understanding the expansion dynamics of laser-induced plasma, every application of LIBS demands extensive experimental and numerical simulation studies. Additionally, we have presented a three-temperature (3T) radiation-hydrodynamics model for LIBS graphite plasma under Martian environmental conditions.

This includes an Eulerian description with a non-equilibrium (non-local thermodynamic equilibrium, NLTE) approach for modeling the temporal evolution of the ablation crater and the plasma plume formation and expansion under various laser irradiance levels and different carbon dioxide (CO_2) pressure conditions, representative of the low Martian environmental temperature ($-63\,^{\circ}$C). The model employs two-dimensional (X–Y) Cartesian and (R–Z) cylindrical grids. It assumes that electrons and ions move together as a single fluid, but with different temperatures ($T_e \neq T_i$), and that the plasma can both emit and absorb radiation. The model also accounts for the mixing between the plasma and the ambient CO_2 gas, which leads to shock wave formation. These shock waves gradually expand in the shape of a spherical bubble and eventually trigger an acceleration of the breakout shock front at later stages. We also present simulation results of graphite plasma characteristics, including electron and ion temperatures, electron and ion number densities, and fluid velocity, for various laser spot diameters ($D = 550$ μm, $I = 1$ GW/cm^2 and $D = 300$ μm, $I = 4$ GW/cm^2), and for different CO_2 pressures ($P = 3$, 6, and 9 mbar), considering both flat and spherical graphite solid tar-

gets. The plasma simulations were conducted at various delay times ($t = 100$ ns, 500 ns, and 1000 ns), using the FLASH simulation code.

In planetary LIBS applications, constant irradiance is a rare scenario, as laser irradiance typically varies due to factors such as changes in distance, atmospheric conditions, and target surface irregularities. To provide a more comprehensive analysis of LIBS under Martian conditions, we investigated the effect of lens-to-sample distance (LTSD) on plasma parameters and spatial distribution during both the laser pulse activation phase (5–10 ns) and after laser deactivation ($t > 20$ ns). These parameters reach their maximum values at the focal point ($z = 0$ mm, spot size $= 100\ \mu$m), in comparison to other positions away from the focal plane at $+10$ mm (spot size $= 168\ \mu$m) and -30 mm (spot size $= 420\ \mu$m). The focal point, representing the optimal focusing position, corresponds to the highest laser intensity. This concentrated energy deposition enhances electron heating, excitation, and ionization processes within the plasma. Consequently, plasma parameters such as electron and ion temperatures, electron and ion number densities, and fluid velocity exhibit significantly higher values at this location. During the initial phase of laser interaction with the graphite target, a marked increase in plasma characteristics is observed. However, following laser deactivation, the plasma undergoes rapid exponential cooling, resulting in a gradual decline of plasma parameters toward minimum values at later delay times.

We further extended this investigation of graphite LIBS plasma to include both He and CO_2 ambient gases, under both low-pressure ($\sim$ mbar) and high-pressure (> 1000 mbar) conditions. Increasing the environmental pressure in CO_2 compared to He results in higher electron and ion densities and lower plasma temperatures. Under these high-pressure CO_2 conditions, the plasma exhibits enhanced confinement, which significantly alters the intensity and shape of the spectral peaks, thereby influencing the accuracy of plasma composition analysis.

In conclusion, our observations reveal clear trends in the graphite plasma: electron and ion temperatures, electron and ion densities, and fluid velocity increase with higher laser irradiance, due to the enhanced energy deposition and corresponding excitation and ionization processes. Plasma behavior under varying pressure conditions further modulates its dynamics and characteristics. At low ambient pressures (a few mbar of CO_2 or He), electron and ion

temperatures and ion density exhibit only moderate increases. However, pressure has a more pronounced effect on fluid velocity and electron density due to more frequent electron–ion collisions. As neutral particle density increases with pressure, the rate of electron–ion collisions and ionization processes also intensifies, leading to elevated electron densities. Moreover, the plasma plume becomes more confined at higher pressures as plasma particles encounter increased resistance from the denser ambient gas.

This combined influence of focusing and pressure provides a foundation for optimizing LIBS analyses on Mars by adjusting focal parameters to account for the unique atmospheric conditions, thereby improving the accuracy and consistency of spectral measurements. In our future studies, it would be valuable to enhance the current model to simulate LIBS plasmas generated from complex materials, such as synthetic shergottite glass, under Martian-like conditions, including aqueous environments and multi-pulse LIBS with cavity effects at extended delay times (up to 1 μs). This expansion is essential for achieving a comprehensive understanding of plasma interactions with Martian materials, given the planet's distinct environmental factors such as temperature, atmospheric composition, and radiation environment. Incorporating data from SuperCam aboard the *Perseverance* rover, which provides in-situ compositional information about Mars, will be pivotal in refining and validating the model.

List of Publications and Presentations

Refereed Journals/Manuscripts

1. K. Benbaier, Z. Bedrane, and A. Abdelmalek. 3T Eulerian-radiation description of graphite laser induced plasma under Martian conditions, *Rev. Mex. Fis.*, 2025, **71**(1), 011501; doi:10.31349/RevMexFis.71.011501.

2. K. Benbaier, Z. Bedrane, A. Abdelmalek, and N. Melikechi. Focusing Effects on Laser-Induced Plasma Parameters: Applications to a Graphite Target Under Martian Atmospheric Conditions, *Appl. Spectrosc.*, 2025, **in press**; doi:10.1177/00037028241307675.

Conferences National/International

1. K. Benbaier, B. Liani, and Z. Bedrane, Effect of Electric and Magnetic Field on the Transport Coefficients of a Non-Equilibrium Gas by the Monte Carlo Method, *1st National Conference of Theoretical Physics (CNPT-21)*, Ouargla, Algeria, 28–29 June 2021.

2. K. Benbaier, B. Liani, and Z. Bedrane, Effect of Electric and Magnetic Field on the Transport Coefficients of a Weakly Ionized Gas, *1st International Conference on Computational & Applied Physics (ICCAP-2021)*, Ghardaïa, Algeria, 27–28 December 2021.

3. K. Benbaier, Z. Bedrane, and A. Abdelmalek, LIBS spectroscopy: a tool for detecting environmental pollution, *International Conference on Environment and Advanced Natural Sciences (ICEANS)*, Oum El Bouaghi, Algeria, 6–7 November 2022.

4. K. Benbaier, LIBS: a tool for detecting environmental pollution by heavy metals, *International Conference on Materials Science and Engineering and their Impact on the Environment (ICMSE-21)*, El Oued, Algeria, 21–22 December 2022.

3T Eulerian-radiation description of graphite laser induced plasma under Martian conditions

K. Benbaier, A. Abdelmalek and Z. Bedrane
Theoretical Physics Laboratory, Physics Dpt., Sciences Faculty, Tlemcen University, Algeria.

Received 30 April 2024; accepted 5 July 2024

We report the results of a simulation of the laser-induced breakdown spectra of graphite in an atmosphere similar to that of Mars using a non-equilibrium 3T-Eurlian fluid model. In our approach the atomic energy level populations were calculated using a collisional-radiative (CR) NLTE-model taking into account the mixing between the plasma and the ambiant gas. The simulation was performed with the FLASH radiation-hydrodynamics code. We have investigate the effects of laser irradiance and ambient CO_2 pressure on the plasma parameters namely the electron and ion temperatures and the electron and ion densities and the temporal variation of the fluid velocity with the laser irradiance at constant pressure which indicate the presence of a shock front associated with the plasma initiation, dynamics, and expansion into the ambient gas.

Keywords: 3T-Eurlian model; NLTE; LIBS; mars; plasma physics.

DOI: https://doi.org/10.31349/RevMexFis.71.011501

1. Introduction

For centuries, the planet Mars has exerted a kind of fascination on humans. But if astronomers today are so interested in the Red Planet, it is primarily because of its relative proximity makes it reachable to their probes and other rovers. Moreover, unlike the other planets of the Solar System, Mars undoubtedly experienced in the past conditions quite similar to those prevailing on Earth which could have allowed the appearance of life - which remains to be confirmed [1].

Nasa Space missions steadily advanced our knowledge of the planet. The main scientific goal of the Nasa's Exploration Program studies is to understand the formation and early evolution of Mars as a planet, the history of geological processes that have shaped Mars through time, the potential for Mars to have hosted life, and the future exploration of Mars by humans [1].

Laser Induced Breakdown Spectroscopy (LIBS) has made it possible to analyze numerous geological samples on the surface of the Martian soil since 2012 thanks to the ChemCam instrument installed on board the Curiosity rover, the largest and most capable rover ever sent to Mars and which has already carried out more than a million laser shots. ChemCam is based on the technique of spectroscopic analysis induced by laser ablation. A powerful laser fires on a target, which causes the volatilization of the material and the appearance of a plasma whose fluorescence is analyzed [2]. Building on this success, LIBS was once again chosen by NASA to be one of the analysis tools implemented by the SuperCam instrument, installed on board the Perseverance rover, which reached the Martian soil in February 2021 [3].

In an effort to better understand ChemCam LIBS spectra numerical simulations in an approach complementary to that based on mimicking the experimental conditions on Mars in an Earth-based laboratory [4] has been performed [5–9]. Ewusi-Annan *et al*. [8] reported the results of a simulation of the laser-induced breakdown spectra of graphite and synthetic shergottite glass in an atmosphere similar to that of Mars using a 1-D, Lagrangian hydrodynamic model and a local thermodynamic equilibrium (LTE) approach for the emission spectra.

Hansen *et al*. [9] investigated the characteristics of the LIBS plasma in Martian atmospheric conditions using stationary modeling of the LIBS plasma using a one-dimensional model of the plasma divided into two zones along the line of sight. Their simulations were based on local thermal equilibrium and carried out using radiative transfer.

Most approaches for characterizing the LIBS plasma are based on the assumption of local thermodynamic equilibrium (LTE) due to the simplicity of the description of the plasma in LTE although the validity of this assumption can only be considered under certain experimental conditions at specific time intervals after plasma initiation [9, 10].

In a recent work, Alberti *et al*. [11] used a non-equilibrium model for laser generated plasmas to investigate plasma kernel dynamics. Laser-induced plasma simulations were performed for nanosecond length pulses for a range of ambient conditions and laser characteristics, and were able to correctly predict the axial and radial sizes of the plasma and, more importantly, to reproduce the propagation of the forward and backward plasma waves observed in experiments in air [12] and Argon [13].

In this paper, we present a novel simulation to model the problem of laser-induced breakdown spectroscopy under Martian conditions . This includes a three temperature (3T) Eurlian radiation description with NLTE (non-local thermodynamic equilibrium) approach for the emission spectra. To model the laser target interaction in the presence of an ambient gas, the usual two temperature (2T) model [14] treatment of plasma is not sufficient since there are a number of physical processes that cause a deviation from electron-

ion radiation thermal equilibrium, or which are critically affected, such as laser heating, transport coefficients, shock waves generation, diffusion effect of radiation, radiation absorption, emission from the plasma and slow equilibration timescales. In order to include these effects, we have considered a 3T plasma model. The simulation was performed with the FLASH radiation-hydrodynamics code [15] which is a finite-volume Eulerian code that operates on a block-structured mesh using Adaptive Mesh Refinement (AMR) [16].

The term "three-temperature" (or "3T") denotes the approximation that electrons and ions move together as a single fluid but with two different temperatures, and that this fluid can emit or absorb radiation. In the 3T simulations presented throughout this paper each cell has an electron temperature, an ion temperature, and radiation energy densities in a number of photon energy bins [17]. In our approach the atomic energy level populations were calculated using a collisional-radiative (CR) NLTE-model [18]. The plasma simulations were allowed to evolve for different times utilizing the second-order unsplit time marching method of USM algorithm [19], an extension of the corner transport upwind (CTU) approach [20] reconstruction was done utilizing the piecewise monotonized central (MC) limiter. The upwind fluxes were computed with a Harten-Laxvan Leer Contact (HLLC) Riemann solver [21]. Implicit solvers for radiation and electron thermal conduction was carried out using a conjugate gradient method (PCG), preconditioned with algebraic multi-grid (AMG), as implemented in the HYPRE library [22].

2. Modeling approach

2.1. Hydrodynamics and plasma radiation simulation

The Euler equations expressing conservation of mass, momentum, and total energy used to describe the evolution of a hydrodynamics 3T plasma are given by [23, 24]:

$$\frac{\partial \rho}{\partial t} + \nabla.(\rho \overrightarrow{v}) = 0, \tag{1}$$

$$\frac{\partial}{\partial t}(\rho \overrightarrow{v}) + \nabla.(\rho \overrightarrow{v}\,\overrightarrow{v}) + \nabla P_{\rm tot} = 0, \tag{2}$$

$$\frac{\partial}{\partial t}(\rho \overrightarrow{v}) + \nabla.[(\rho E_{\rm tot} + P_{\rm tot})\overrightarrow{v}] = Q_{\rm las} - \nabla.\overrightarrow{q}, \tag{3}$$

where

$$P_{\rm tot} = P_{\rm ele} + P_{\rm ion} + P_{\rm rad}, \tag{4}$$

$$E_{\rm tot} = e_{\rm ele} + e_{\rm ion} + e_{\rm rad} + \frac{1}{2}\overrightarrow{v}\,\overrightarrow{v}. \tag{5}$$

Here ρ is the plasma mass density, $\overrightarrow{v}$ is the fluid velocity, $P_{\rm tot}$ is the total pressure, $P_{\rm ele}$, $P_{\rm ion}$ and $P_{\rm rad}$ are the electron, the ion and the radiation pressure, respectively. $E_{\rm tot}$ is the total specific energy which includes the specific internal energies of the electron $e_{\rm ele}$, ions $e_{\rm ion}$ and the radiation field $e_{\rm rad}$ along with the specific kinetic energy. $Q_{\rm las}$ is the energy source due to laser heating. $\overrightarrow{q}$ is the total heat flux which is the sum of the electron, the ion heat flux and the radiation flux:

$$\overrightarrow{q} = \overrightarrow{q}_{\rm ele} + \overrightarrow{q}_{\rm ion} + \overrightarrow{q}_{\rm rad}, \tag{6}$$

$$\overrightarrow{q}_{\rm ele} = -K_{\rm ele}\nabla.T_{\rm ele}, \tag{7}$$

$$\overrightarrow{q}_{\rm ion} = -K_{\rm ion}\nabla.T_{\rm ion}, \tag{8}$$

where $K_{\rm ele}$ and $K_{\rm ion}$ are respectively the electron and the ion thermal conductivity which are determined using the Spitzer model [25, 26]. In cases where a large values of $|\nabla.T_{\rm ele}|$ and $|\nabla.T_{\rm ion}|$ would give rise to unphysically large heat fluxes, this can be handled by the diffusion flux-limiter solver. The maximum flux-limit used for electron $\overrightarrow{q}_{\max_{\rm ele}}$, ion $\overrightarrow{q}_{\max_{\rm ion}}$ thermal conductions, respectively are defined as [15]:

$$\overrightarrow{q}_{\max_{\rm ele(ion)}} = \alpha_{\rm e(i)} n_{\rm e(i)} k_{\rm B} T_{\rm ele(ion)} \sqrt{\frac{k_{\rm B} T_{\rm ele(ion)}}{m_{\rm e(i)}}}, \tag{9}$$

where $k_{\rm B}$ is the Boltzmann constant, $m_{\rm i}$ is the average mass of an ion, $m_{\rm e}$ is the mass of electron, $n_{\rm e}$ is the electron density, $n_{\rm i}$ is the ion density. $\alpha_{\rm e}$ and $\alpha_{\rm e}$ are respectively the electron and the ion conductivity flux-limiter coefficient. This coefficients are much less than 1 [26].

Since the plasma is assumed to have multi-temperatures, additional equations must be evolved to describe the change in specific internal energies of the ions, electrons, and radiations field:

$$\frac{\partial \rho e_{\rm ion}}{\partial t} + \nabla.(\rho e_{\rm ion}\overrightarrow{v}) + P_{\rm ion}\nabla.\overrightarrow{v} = \rho\omega_{\rm ei}(T_{\rm ele} - T_{\rm ion}) - \nabla.\overrightarrow{q}_{\rm ion}, \tag{10}$$

$$\frac{\partial \rho e_{\rm elec}}{\partial t} + \nabla.(\rho e_{\rm elec}\overrightarrow{v}) + P_{\rm ele}\nabla.\overrightarrow{v} = \rho\omega_{\rm ei}(T_{\rm ion} - T_{\rm ele}) - \nabla.\overrightarrow{q}_{\rm ele} + Q_{\rm abs} - Q_{\rm emis} + Q_{\rm las}, \tag{11}$$

$$\frac{\partial \rho e_{\rm rad}}{\partial t} + \nabla.(\rho e_{\rm rad}\overrightarrow{v}) + P_{\rm rad}\nabla.\overrightarrow{v} = -\nabla.\overrightarrow{q}_{\rm rad} - Q_{\rm abs} + Q_{\rm emis}, \tag{12}$$

where $e_{\rm ion}$ is the ion specific internal energy, $e_{\rm ele}$ is the electron specific internal energy, $e_{\rm rad}$ is the radiation specific internal energy. $Q_{\rm las}$ is represents the energy source due to laser heating. $Q_{\rm abs}$ represents the increase in electron internal energy due to the total absorption of radiation, $Q_{\rm emis}$ represents the decrease in electron internal energy due to the total emission of radiation.

Where $\omega_{\rm ei} = C_{v,e}/\tau_{\rm ei}$ is the electron-ion coupling term, where $C_{v,e}$ is the electron specific heat and $\tau_{\rm ei}$ is the ion/electron equilibration time given by [26]:

$$\tau_{\rm ei} = \frac{3k_{\rm B}^{3/2}}{8\sqrt{2\pi}q_{\rm e}^4}.\frac{(m_{\rm i}T_{\rm ele} + m_{\rm e}T_{\rm ion})^{3/2}}{(m_{\rm e}m_{\rm i})^{1/2}\overline{Z}n_{\rm i}\ln\Lambda_{\rm ei}}, \tag{13}$$

where $\overline{Z}$ is the average ionization, $n_{\rm i}$ the ionic density, $q_{\rm e}$ the electron charge and $\ln \Lambda_{\rm ei}$ is the Coulomb Logarithm associated to the ion-electron collisions [27].

FLASH code already provides a variety of directionally split and unsplit methods for solving the system of Euler equations of hydrodynamics (HD). The system of Eqs. (1), (2), (3) is a mixed hyperbolic-parabolic system. First, all the terms on the right-hand side of the equations are split off from the solution of the non- ideal single-fluid hydrodynamics. The latter is handled using the single step, time marching algorithm of the unsplit staggered mesh (USM) [19, 31] for cartesian coordinates. The right-hand terms of Eqs. (10), (11), (12) is in turn split off and each term is handled separately. The first term on the right-hand side Eqs. (10), (11) represents the exchange of energy between electrons and ions through collisions, and it is handled by solving the system as [15]:

$$\frac{\partial e_{\rm ion}}{\partial t} = \frac{C_{v,\rm elec}}{\tau_{\rm ei}}(T_{\rm ele} - T_{\rm ion}), \tag{14}$$

$$\frac{\partial e_{\rm ele}}{\partial t} = \frac{C_{v,\rm elec}}{\tau_{\rm ei}}(T_{\rm ion} - T_{\rm ele}). \tag{15}$$

The second term on the right-hand side of Eqs. (14) and (15) represents the electron thermal conduction and the parabolic terms, which are solved implicitly using the HYPRE library [22], to retain large time steps.

The remaining terms on the right-hand of Eqs. (11) and (12) describe radiation transport. The HYPRE library was used to calculate the radiation diffusion.

FLASH code includes radiative transfer through the following equation:

$$\frac{1}{c}\frac{\partial I}{\partial t} + \widehat{\Omega}.\nabla I + \rho\kappa I = \eta, \tag{16}$$

where $I(x, \widehat{\Omega}, \nu, t)$ is the specific radiation intensity at position x in the direction $\widehat{\Omega}$, c is the speed of the light, ρ is the mass density $\kappa(x, \nu, t)$ is the opacity or absorption coefficient, $\eta(x, \nu, t)$ is the emissivity, ν is the frequency. This equation is coupled within FLASH to the electron internal energy through:

$$\frac{\partial u_{\rm ele}}{\partial t} = \int_O^\infty d\nu \int_{4\pi} d\widehat{\Omega}(\rho\kappa I - \eta), \tag{17}$$

where $u_{\rm ele} = \rho.e_{\rm ele}$ represent the electron internal energy density, $e_{\rm ele}$ is the internal electron energy, and ρ the total mass density.

The radiative transfer Eq. (16), and the electron internal energy Eq. (17) equations are handled using multi-group diffusion (MGD) approximation [32]. FLASH divided the frequency space into N groups, where g is defined by the frequency range from ν_g to ν_{g+1}. For our Simulation the number of frequency groups used is 25, and the total quantities of interest can be defined as summations over each group:

$$Q_{\rm emis} = \sum_{g=1}^{N_g} Q_{\rm emis,g}, \tag{18}$$

$$Q_{\rm abs} = \sum_{g=1}^{N_g} Q_{\rm abs,g}, \tag{19}$$

$$Q_{\rm rad} = \sum_{g=1}^{N_g} Q_{\rm rad,g}, \tag{20}$$

$$u_{\rm rad} = \sum_{g=1}^{N_g} u_{\rm rard,g}, \tag{21}$$

where $u_{\rm rad} = \rho e_{\rm rad}$ is the radiation energy density, where $e_{\rm rad}$ is the internal radiation energy.

The total energy density is given by:

$$\begin{aligned}\varepsilon &= \rho.E_{\rm tot} = \rho.E_{\rm internal} + \rho.E_{\rm kinetic} \\ &= \rho.(e_{\rm ele} + e_{\rm ion} + e_{\rm rad}) + \frac{1}{2}\rho.\overrightarrow{v}\overrightarrow{v}.\end{aligned} \tag{22}$$

Then we solve the following system of equations, assuming that the plasma emitted a radiation in a Planck spectrum with an emission opacity given by:

$$\begin{aligned}\frac{1}{c}\frac{\partial u_{\rm rad}}{\partial t} - \nabla.\left(\frac{1}{3\sigma_{\rm t,g}}\nabla u_{\rm rad}\right) + \sigma_{\rm a,g}u_{\rm rad} \\ = \sigma_{\rm e,g}aT_{\rm ele}^4\frac{15}{\pi^4}\left[P(x_{\rm g+1}) - P(x_{\rm g})\right],\end{aligned} \tag{23}$$

$$\begin{aligned}\frac{\partial u_{\rm ele}}{\partial t} = \sum_{\rm g}\Bigg(\sigma_{\rm a,g}u_{\rm rad} - \sigma_{\rm e,g}aT_{\rm ele}^4 \\ \times \frac{15}{\pi^4}\left[P(x_{\rm g+1}) - P(x_{\rm g})\right]\Bigg),\end{aligned} \tag{24}$$

where $u_{\rm rad}$ is the radiation energy density, $\sigma_{\rm t,g}$ is the transport opacity for group g, $\sigma_{\rm a,g}$ is the absorption opacity for group g, $\sigma_{\rm e,g}$ is the emission opacity for group g, a is the radiation constant, and $P(x)$ is the Planck integral. The argument to the Planck integral is $x = h\nu/kT$ where h is the Planck's constant. The second and third terms on the left-hand side of equation Eq. (23) represent $\nabla Q_{\rm rad,g}$ and $Q_{\rm abs,g}$, respectively. While the right-hand side of Eq. (23) represent $Q_{\rm emis,g}$.

The last term of Eq. (11) represents the laser heating $Q_{\rm las,g}$, which is computed using an inverse Bremsstrahlung model (described in Appendix A). The energy deposited by the laser beam was calculated using the laser ray-trace algorithm for planar and cylindrical geometries. This algorithm was used by FLASH to calculates the paths of each rays using the geometric optics approach [33]. Beams are the collection of a number of rays whose paths are traced through the simulation domain based on the local index of refraction of each cell. The power of the laser deposited in a cell is assumed to be due to the inverse Bremsstrahlung power, which depends on the electron temperature gradient and the electron number

density gradient. The ion number density $n_{\rm i}$ and the electron number density $n_{\rm e}$ of our work were obtained from the following equations [15]:

$$n_{\rm i} = N_{\rm A}\frac{\rho}{\overline{A}}, \tag{25}$$

$$n_{\rm e} = N_{\rm A}\overline{Z}\frac{\rho}{\overline{A}}, \tag{26}$$

where $N_{\rm A}$ is the Avogadro number, $\overline{A}$ is the average atomic mass, $\overline{Z}$ is the average ionization level, and ρ is the mass density.

2.2. Simulation code

The software used in our work is the FLASH Code [28]. It is a multi-physics, multi-dimensional radiation-hydrodynamic, and magneto-hydrodynamic (MHD) open-source code capable of handling different physics problems like plasma emission phenomena. Flash has also extensive high energy density plasmas (HEDP) capabilities for simulating laser-driven plasma experiments [29], and a variety of partial differential equations (PDE) solver employed in the numerical modeling. By a range of algorithms FLASH include adaptive mesh refinement capabilities (AMR) [30]. This means that the grid includes individual blocks which can be divided into smaller blocks (children blocks), providing a better resolution in desired regions of the domain. The refinement can be triggered by a chosen variables, such as density or temperature. In our simulation we used 4 refinement variables: density, electron temperature, ion temperature and pressure. Unlike Lagrangian hydrodynamics code [8] where the mesh moves with the fluid, FLASH code utilizes an Eulerian representation of the fluid, where the stationary spatial mesh allows fluid to move into and out of a cell, this gives FLASH the feature of avoiding mesh entanglement, to handed multi-complex fluid. HEDP capabilities includes range of algorithms: three temperatures (electron, ion, and radiation) state-of-the art radiation-hydrodynamics solver, including the thermal conduction, multi-group radiation diffusion, tabulated equations-of states, and laser ray-tracing model. The laser ray-tracing model is in 1D, 2D, and 3D Cartesian coordinates and in 2D cylindrical coordinate.

2.3. Equations of State (EOS) and opacities

The equations of state (EOS) for the target (Graphite) and ambient gas (CO_2) were used in the computation for the electrons, ions and radiation pressures ($P_{\rm ele}$, $P_{\rm ion}$, $P_{\rm rad}$), the electron and ion specific heats ($C_{v,{\rm ele}}$, $C_{v,{\rm ion}}$), electron, ion and radiation internal energies ($e_{\rm ele}$, $e_{\rm ion}$, $e_{\rm rad}$) and electron-ion coupling term ($\omega_{\rm ei}$) from the plasma temperature and ion density grid. To compute tabulated EOS for NLTE plasma we used the program IONMIX4 [18]. The IONMIX4 code was also used to calculate tabulated emissivity and opacity for NLTE used by FLASH code.

The IONMIX code computes the steady-state ionization and excitation populations for a mixture of up to 10 different atomic species. The radiative absorption, emission, and scattering coefficients are calculated at a large number ($\sim$ several hundred) of photon energies, and integrated over selected energy intervals to determine the multi-group Planck and Rosseland mean opacities. The code also calculates the thermodynamic properties of the plasma, such as the specific energy, average charge state, pressure, and heat capacity [18].

A temperature grid spanning 0.01-50 eV, ion density grid in the range of 10^{12}-10^{25} ion/cm^3 and an energy grid from 1 to 6 eV were used in the calculation of the EOS and opacity data respectively. The ionization potential energies of the excited levels for carbon (C^{+1}, C^{+2}, C^{+3}, C^{+4}, C^{+5}, C^{+6}) and oxygen (O^{+1}, O^{+2}, O^{+3}, O^{+4}, O^{+5}, O^{+6}, O^{+7}, O^{+8}) were driven from the National Institute of Science and Technology (NIST) [34] and used by IONMIX4 to generate data for the Graphite and Carbon dioxide (CO_2). The populations of atomic energy levels were calculated using a collisional-radiatif non-local thermodynamic equilibrium (CR-NLTE) model [18] (described in Appendix B). It should be noted that in our simulation, the emission from molecules has not been considered. Experimental evidence [35] confirms the presence of molecules in the graphite plasma beyond a delay time of 1 μs. This suggests that the emission line intensities of atomic species could be influenced by molecular formation throughout the plasma's duration. Notably, our simulation accounts for a duration of only up to 1000 ns.

2.4. Design simulation setup

In order to simulate the ablation of the Graphite target and the plasma formation in presence of an ambient gas (CO_2), we took advantage of support for multi-materials in the FLASH Code. In our Simulation we have considered a 0.1 cm thick and 0.5 cm radius flat solid graphite ($\rho = 2.23$ g/cm^3) target irradiated by 1064 nm, 5 ns temporal "top-hat" shaped laser pulse (Fig. 1) with laser energy on the target $E_{\rm las} = 15$ mJ [36].

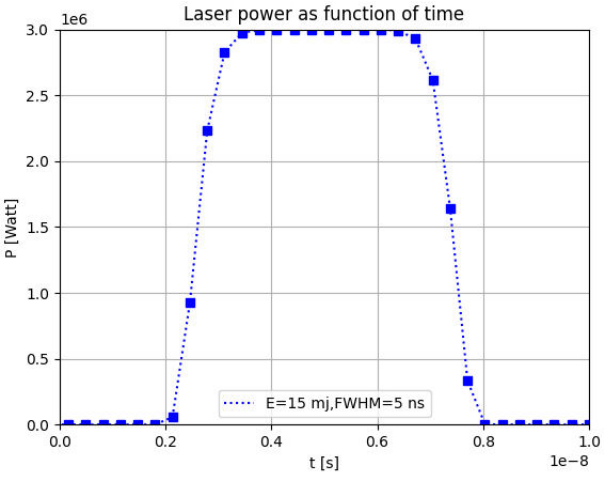

FIGURE 1. Top hat laser beam profile as function of time.

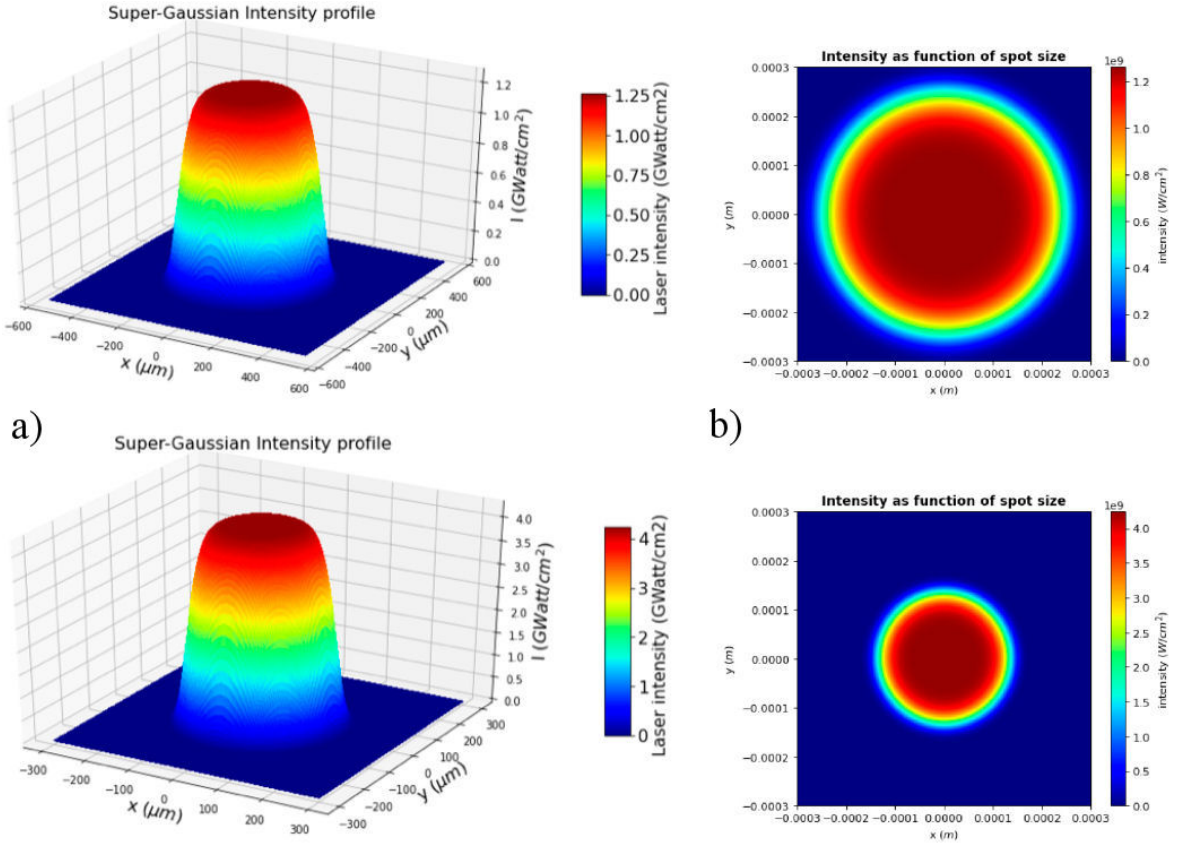

FIGURE 2. Super-Gaussian laser intensity profile a) and the laser intensity as function of the spot size b) are given for 1 GW/cm^2 (1$^{\rm st}$ row) and for 4 GW/cm^2 (2$^{\rm nd}$ row).

The spatial profile of the laser intensity was assumed to be a super-Gaussian of exponent 4 an e^2-folding radius, its expression is given by [37–39]:

$$I(r) = I_0 \mathrm{e}^{-2\left[(\frac{r}{\omega_0})^2\right]^n} \tag{27}$$

where I_0 is the laser intensity, n is the super Gaussian exponent selected to be 4 in our simulation, r is the radius, and ω_0 is the e^2-folding Gaussian radius for our laser set to 150 μm, 225 μm, respectively. Initially, the region of $y \geqslant 0.9$ cm occupied by the target (target thick = 1 mm, and target radius = 5 mm), and the region of $y < 0.9$ cm is assumed to be occupied by the ambient gas (CO_2) with different pressures (3 mbars, 6 mbars et 9 mbars). The large spatial extent of the atmosphere is chosen to mimic the distance between the laser source (ChemCam telescope), and the target on Mars which varies between 1 m (spot size diameter $D = 300$ μm) and 7 m (spot size diameter $D = 550$ μm) (Fig. 2).

In our simulation we used one of laser ray-tracing model proprieties in the FLASH Code, this allows to 2D Cartesian laser beam to emulate a 3D cylindrical beam. The plasma simulations are allowed to evolve for 100 ns, 500 ns and 1000 ns respectively, utilizing the unsplit staggered mesh (USM) scheme, a currant number of 0.1 the time step used in the simulation varied from 1 fs to 0.1 ns. We used 4 levels of refinement and blocks of 8 $\times$ 8 cells, obtaining an equivalent resolution of approximately 78 μm per cell. The reconstruction is carried out with a monotonized central (MC) limiter [40], whereas the Godunov fluxes are recovered with an HLLC Riemann solver [21, 41], which restores contact surface and cut wave. The boundary conditions were set to outflow for all axis.

For visualizing our data we have used the multi-code analysis tool "yt-project" [42], an open-source code written in Python which consists on data management layer for transporting and tracking simulation out-puts, plotting layer, parallel analysis layer for handling mesh-based and particle-based data as well as several interfaces, "yt" has been extended to work with several different simulation methods and simulation codes including FLASH code.

3. Results and discussion

3.1. Electron temperature

To calculate the electron and ion temperatures, we consider, in our simulation model, a single laser beam with 4096 rays illuminating a flat solid graphite target (radius = 0.05 cm, thickness=0.05 cm) in 2D-Cartesian geometry ($x - y$). The laser is focused on the y-axis, and enters $x \in [-0.5; 0.5\,\mathrm{cm}] \times y \in [-1; 1\,\mathrm{cm}]$ computational domain at a 0° angle, the ambient gas is supposed to be CO_2 (Fig. 3). The boundary conditions are set to outflow for all axes. We

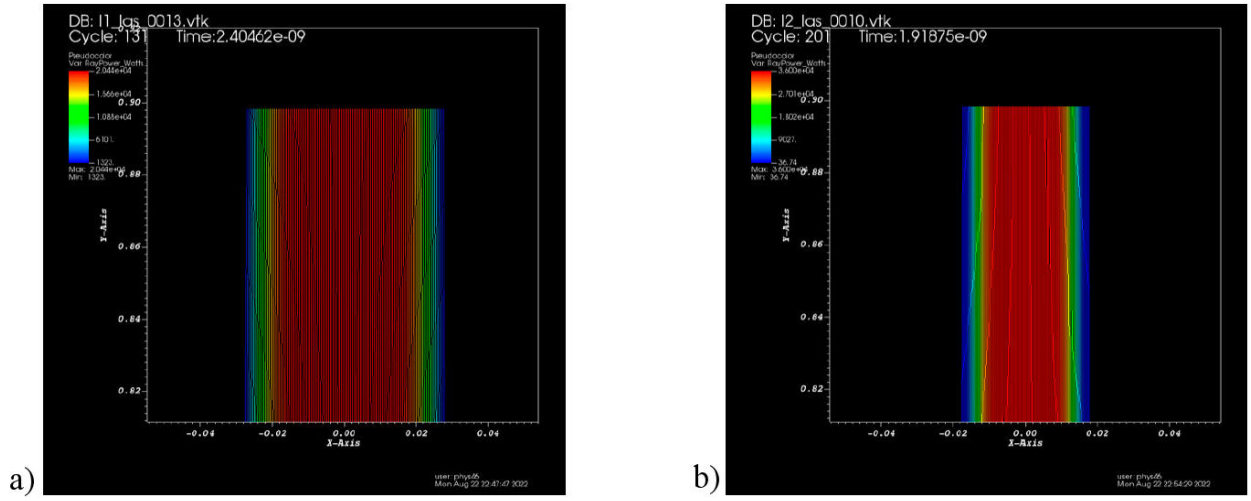

FIGURE 3. Laser beam simulated using 4096 rays per time step in 2D-Cartesian geometry $(x-y)$ a) for 1 GW/cm^2 and b) for 4 GW/cm^2.

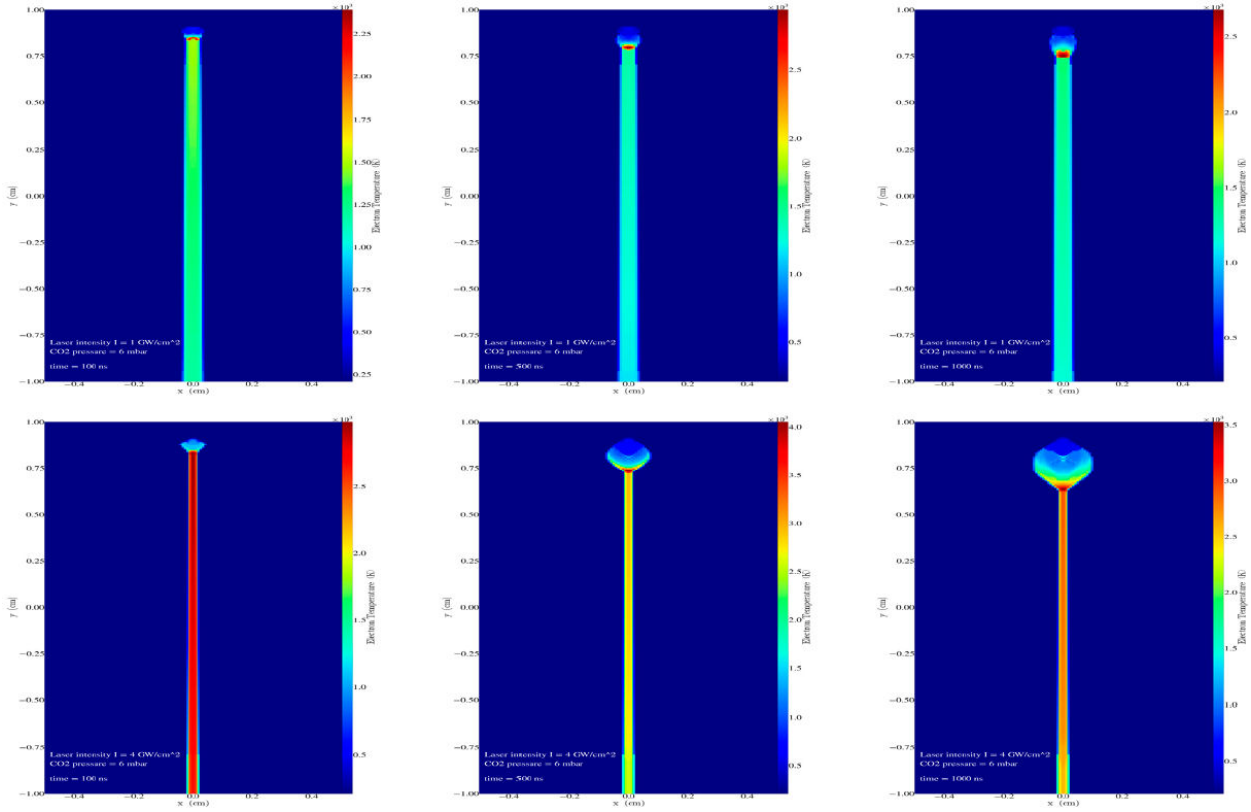

FIGURE 4. Electron temperature calculated at 6 mbars $C0_2$ ambient gas pressure, for 1 GW/cm^2, (1$^{\text{st}}$ row), 4 GW/cm^2 (2$^{\text{nd}}$ row) laser irradiance and for 3 time steps: 100 ns (1$^{\text{st}}$ column), 500 ns (2$^{\text{nd}}$ column) and 1000 ns (3$^{\text{rd}}$ column).

used 4 levels of refinement and blocks of 8×8 cells, obtaining an equivalent resolution of approximately 78 μm per cell.

Figure Fig. 4 shows the electron temperature for carbon dioxide pressure of 6 mbars and two laser irradiances 1 GW/cm^2 and 4 GW/cm^2 and three simulation times 100, 500 and 1000 ns. Each row in the figure shows the result obtained using one laser irradiance at 3 time steps. Each column shows the results for the same time for the two laser irradiances.

Both the electron and its spatial extent distribution are affected by the ambient gas pressure and the laser irradiance. At all simulation times the temperature increases with growing laser irradiance as obtained experimentally by Harilal *et al.* [43] when measuring the temperature in a laser produced carbon plasma. Figure 5 shows the influence of the laser irradiance on the maximum magnitude of the electron temperature for a constant pressure. The blue line correspond to 1 GW/cm^2 and the red line to 4 GW/cm^2.

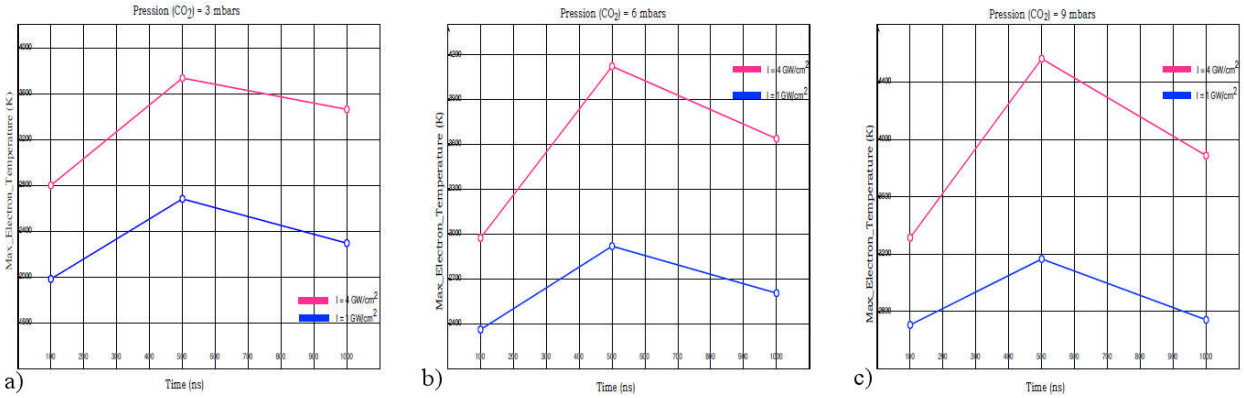

FIGURE 5. Influence of the laser irradiance (1 GW/cm^2 blue line, 4 GW/cm^2 red line) on the electron temperature for a constant pressure : a) 3 mbars, b) 6 mbars and c) 9 mbars.

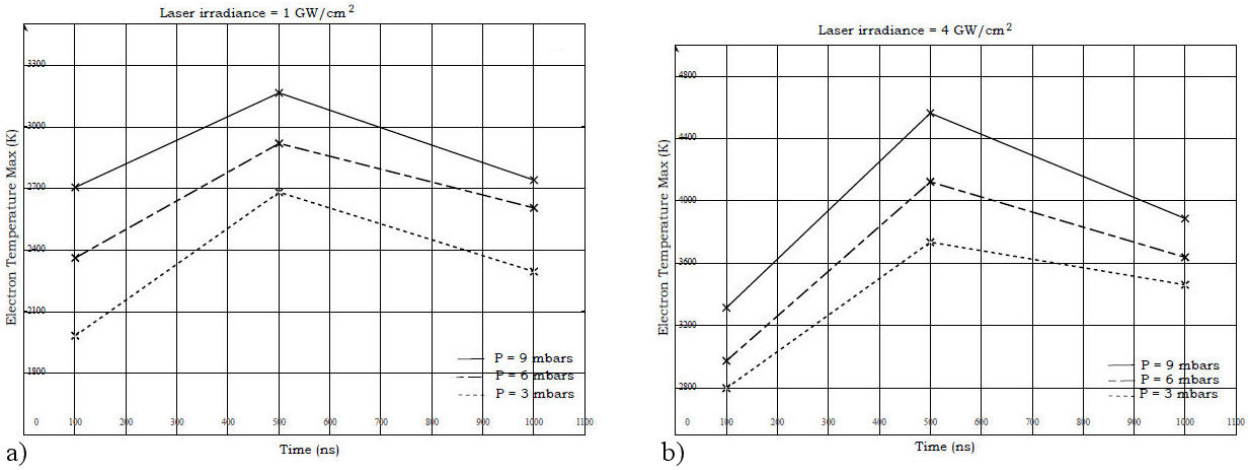

FIGURE 6. Variation of the electron temperature with the pressure (3 mbars dotted line, 6 mbars broken line and 9 mbars full line) at constant laser irradiance [a): 1 GW/cm^2, b) 4 GW/cm^2].

For a constant pressure, the magnitude of the temperature increases with laser irradiance at all time steps reaching a peak temperature at 500ns: increasing from 2681.2 K to 3735.4 K at 3 mbars, 2919.2 K to 4122.3 K at 6 mbars and 3165.4 K to 4563.0 K at 9 mbars when the laser irradiance increases fron 1 GW/cm^2 to 4 GW/cm^2 respectively, which represents an average increase of 1.4 of the magnitude of the electron temperature. We can notice that the spatial extent distribution is also affected and increases with growing laser irradiance.

Figure 6 shows the variation of the temperature with pressure which dependent on the laser irradiance and the time of observation.

At constant laser irradiance, the electron temperature increases slightly with growing ambiant pressure. At 4 GW/cm^2, the peak temperature at 500 ns varied from 3735.4 K at 3 mbars to 4122.3 K and 4563.0 K at 6 and 9 mbars, respectively. for the other time steps the augmentation is not very important ($\sim$175 K at 100 ns and $\sim$100 K at 1000 ns)

Overall, pressure effect on the electron temperature is marginal compared to the effect of laser irradiance.

What should be noted is that the temperature values we found are lower by a factor of 10 compared to those found by [8, 9]. The reason is that we considered in our simulation the real conditions on the planet Mars namely an average temperature of $-63°$ (initial temperature for graphite and CO_2) whereas experiments, carried out in Earth-based laboratory mimicking the experimental conditions on Mars, are carried out at room temperature [4, 6] or 0° which dramatically overestimates the temperature values [45]. Adding to this, we considered in our approach, the mixing between the plasma and the ambient gas which play an important role in the plasma plume expansion and affect the temperature and the density number of the plasma [46]. Moreover, the possible cause for the over-predicted values obtained by [8, 9] could be due to neglecting plasma emission and re-absorption in their 2T model and assuming the LTE. It is important to note that the EOS model controls not only the pressure of the plasma, given a density and temperature, but also affects the efficiency of heat conduction by determining the mean ionization fraction, as well as the specific heat [17, 44].

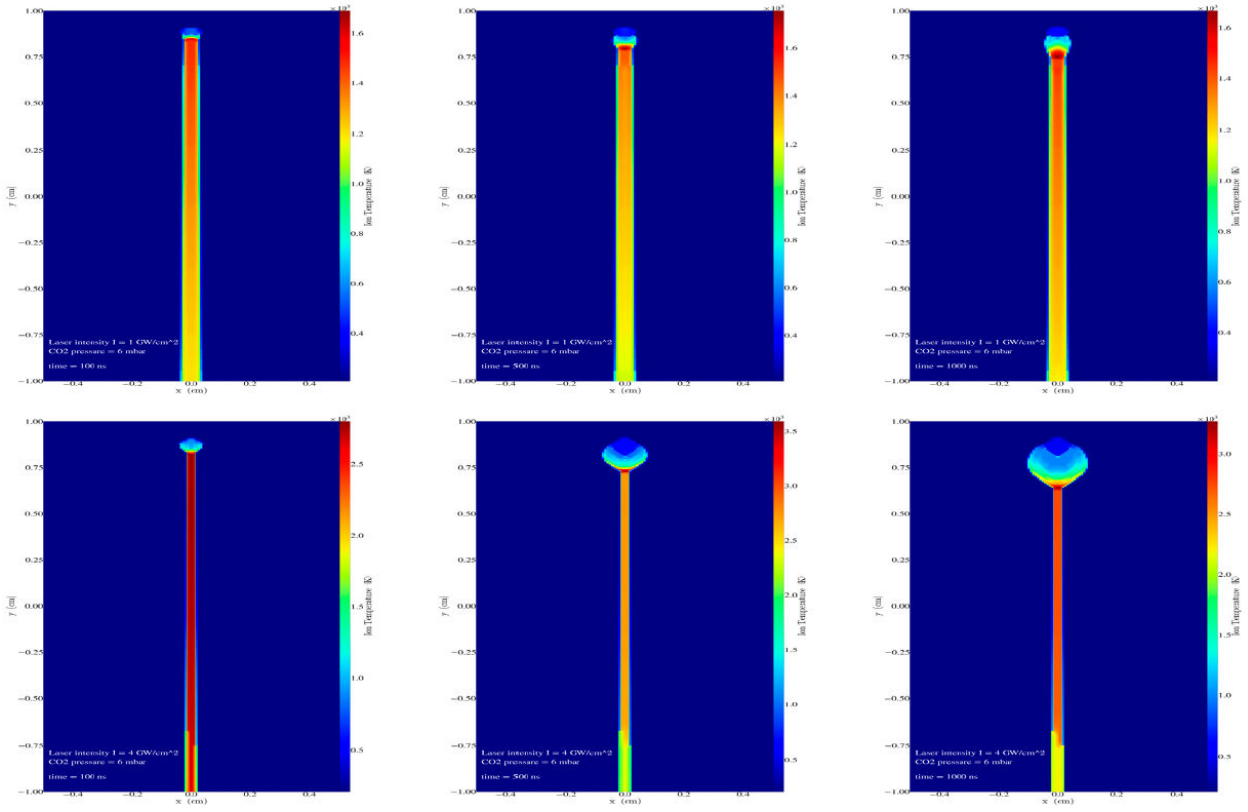

FIGURE 7. Ion temperature calculated at 6 mbars CO_2 ambient gas pressure, for 1 GW/cm^2, (1st row), 4 GW/cm^2 (2nd row) laser irradiance and for 3 time steps: 100 ns (1st column), 500 ns (2nd column) and 1000 ns (3rd column).

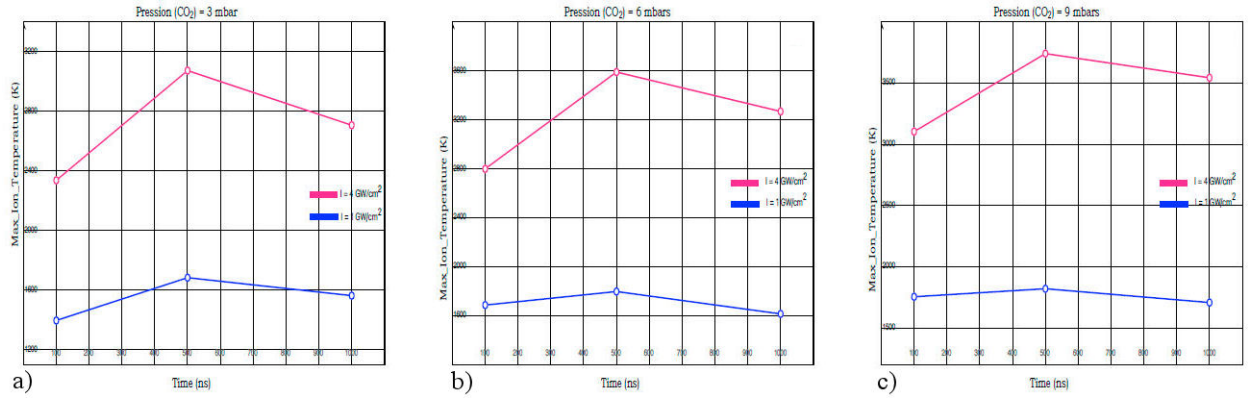

FIGURE 8. Influence of the laser irradiance (1 GW/cm^2 blue line, 4 GW/cm^2 red line) on the ion temperature for a constant pressure: a) 3 mbars, b) 6 mbars and c) 9 mbars.

3.2. Ion temperature

Figure 7 shows the electron temperature for carbon dioxide pressure of 6 mbars and two laser irradiances 1 GW/cm^2 and 4 GW/cm^2 and three simulation times 100, 500 and 1000 ns. Each row in the figure shows the result obtained using one laser irradiance at 3 time steps. Each column shows the results for the same time for the two laser irradiances.

Figure 8 shows the influence of the laser irradiance on the maximum magnitude of the ion temperature for a constant pressure. The blue line correspond to 1 GW/cm^2 and the red line to 4 GW/cm^2.

At 1 GW/cm^2 the ion temperature increases very slightly with time for the three pressures considered. At 6 mbars, for example, its varied from 1687.2 K at 100 ns to 1797.9 K and 1615.2 K at 500, 1000 ns, respectively. The evolution become more noticeable when the laser irradiance grows to 4 GW/cm^2 and even the magnitude grows significantly and reach a peak for 500 ns increasing from 1684.1 K to 3074.1 K at 3 mbars, 1797.9 K to 3591.2 K at 6 mbars and 1820.7 K to 3741.9 K at 9 mbars. The effect of the variation of the pressure on the ion temperature is not very important as shown in Fig. 9.

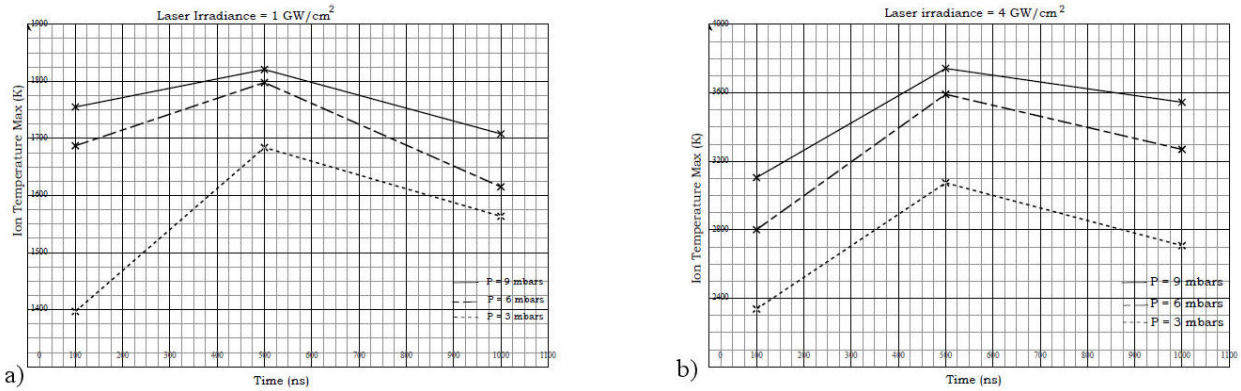

FIGURE 9. Variation of the ion temperature with the pressure (3 mbars dotted line, 6 mbars broken line and 9 mbars full line) at constant laser irradiance [a): 1 GW/cm^2, b) 4 GW/cm^2].

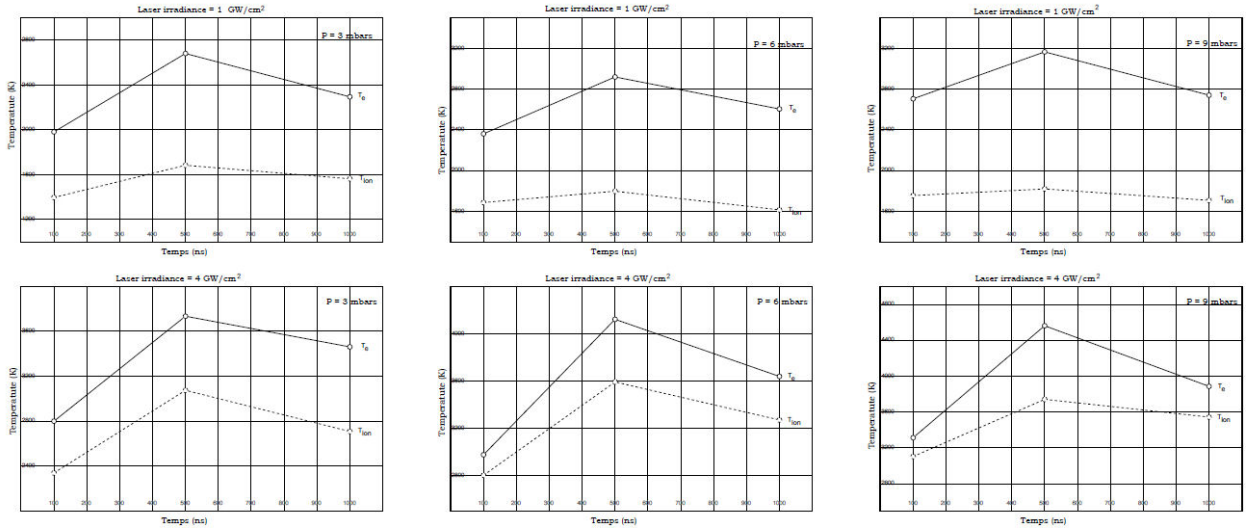

FIGURE 10. Comparison between electron temperature (full line) and the ion temperature (dotted line) for 3 dioxide carbon pressures: 3 mbars (1$^{\rm st}$ column), 6 mbars (2$^{\rm nd}$ column) and 9 mbars (3$^{\rm rd}$ column) at constant laser irradiance [1 GW/cm^2 (1$^{\rm st}$ row), 4 GW/cm^2 (2$^{\rm nd}$ row)].

3.3. Electron and ion number density

In this part, we consider, in our simulation model, a single laser beam with 4096 rays illuminating a spherical graphite target (radius = 0.05 cm, thickness = 0.05 cm) in 2D-cylindrical ($R-Z$) geometry. The laser is focused on the z-axis, and enters $R \in [0; 1.0\,\mathrm{cm}] \times Z \in [-0.4; 0.8\,\mathrm{cm}]$ computational domain at a 45° angle, the ambient gas is supposed to be CO_2 (Fig. 11). The boundary Conditions are set reflective for z-axis, whereas the remaining boundaries are set to outflow (zero gradient). We utilize 5 levels of refinement and blocks of 8×8 cells obtaining an equivalent resolution of 39 μm/cell.

Figures 12 and 13 show the electron and the ion density, respectively, for carbon dioxide pressure of 6 mbars and two laser irradiances 1 GW/cm^2 and 4 GW/cm^2 and three simulation times 100, 500 and 1000 ns. Each row in the figure shows the result obtained using one laser irradiance at 3 time steps. Each column shows the results for the same time for the two laser irradiances.

For all, the number density and the spatial extent of the corresponding profiles increase when the time step is increasing and with growing the laser irradiance. The peak of density for both electrons and ions is reached at 1000 ns.

3.4. Fluid velocity

Figure 14 shows time variation of the fluid velocity with the laser irradiance at constant pressure (6 mbar). For all simulations, the radial location of the shock front increases with laser irradiance, at the tree simulation times 100 ns, 500 ns and 1000 ns. The fluid velocity increases from 1.26×10^6 cm/s ($I = 1$ GW/cm^2) to 1.42×10^6 cm/s ($I = 4$ GW/cm^2) at $t = 100$ ns and from 7.55×10^5 cm/s ($I = 1$ GW/cm^2) to 8.32×10^5 cm/s ($I = 4$ GW/cm^2) at $t = 500$ ns and from 5.08×10^5 cm/s ($I = 1$ GW/cm^2) to 6.0×10^5 cm/s ($I = 4$ GW/cm^2) at $t = 1000$ ns. This phenomenon occurs due to the higher energy imparted to the target material by the more intense laser beam. When a laser, with higher irradiance, is employed, it delivers a greater amount of energy to the target

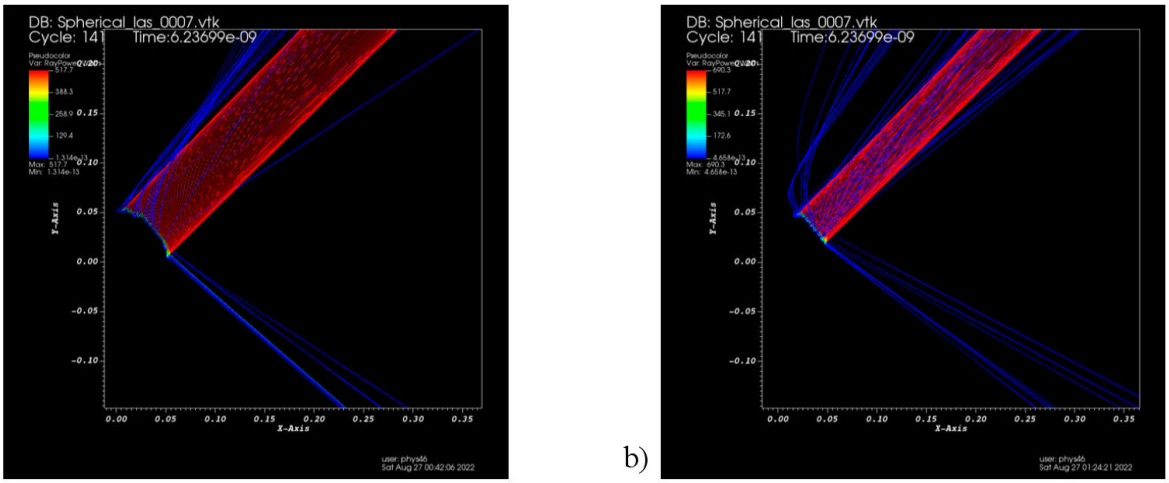

FIGURE 11. Laser beam simulated using 4096 rays per time step in 2D-cylindrical ($R-Z$) a) geometry for 1 GW/cm^2 and b) for 4 GW/cm^2.

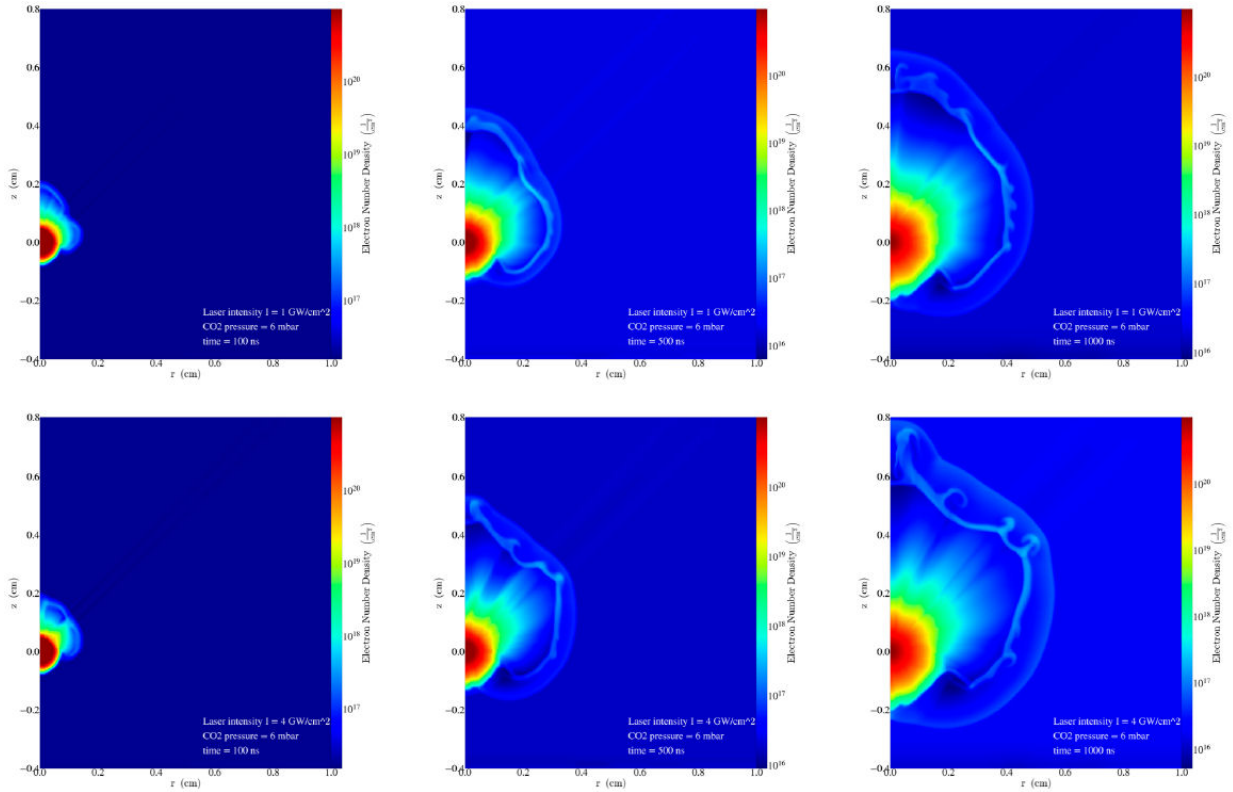

FIGURE 12. Electron density calculated at 6 mbars CO_2 ambient gas pressure, for 1 GW/cm^2, (1$^{\text{st}}$ row), 4 GW/cm^2 (2$^{\text{nd}}$ row) laser irradiance and for 3 time steps: 100 ns (1$^{\text{st}}$ column), 500 ns (2$^{\text{nd}}$ column) and 1000 ns (3$^{\text{rd}}$ column).

surface in a shorter period. Consequently, rapid heating and vaporization of the target material occur, leading to the formation of a plasma plume with higher kinetic energy. This phenomenon has been observed experimentally [47], and indicate the presence of a shock front associated with the plasma initiation, dynamics, and expansion into the ambient gas. As the plasma propagates a shock region of highly compressed gas is formed between the background gas and expanding plasma. Interaction of laser with the target results in the formation of plasma which is a strong source of UV radiation. In presence of an ambient gas this radiation interacts with it and results in an increase in the density in a very narrow region which propagates in the ambient atmosphere with speed more than that of the local ion sound speed [46]. laser interactions with solid density targets can be treated as a hydrodynamic problem with the laser rays acting as a source of energy on the grid. This laser energy is absorbed by electrons at a rate specified by the inverse bremsstrahlung approximation, after which this energy can be transferred to ions.

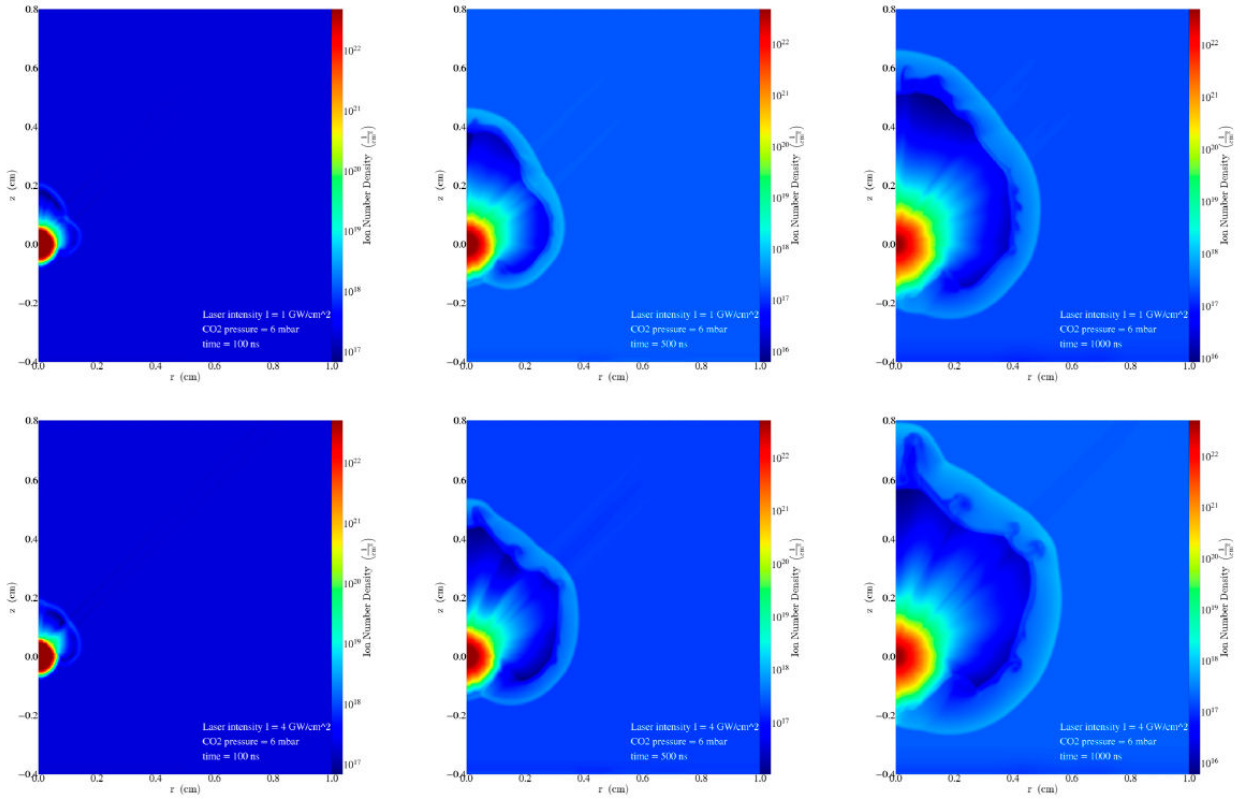

FIGURE 13. Ion density calculated at 6 mbars $C0_2$ ambient gas pressure, for 1 GW/cm^2, (1$^{\text{st}}$ row), 4 /cm^2 (2$^{\text{nd}}$ row) laser irradiance and for 3 time steps: 100 ns (1$^{\text{st}}$ column), 500 ns (2$^{\text{nd}}$ column) and 1000 ns (3$^{\text{rd}}$ column).

4. Limitation

The limitations of our approach, as highlighted in this study, primarily stem from our challenge to accurately determine the wide range of physical, chemical, optical, and environmental factors affecting plasma properties and the formation of spectral lines in Laser-Induced Breakdown Spectroscopy (LIBS). Initially, we simulate delay times of 100 ns, 500 ns, and 1000 ns; however, it is crucial to emphasize the importance of simulating early times (t = 10 ns), to understand the plasma formation dynamics when the pulsed laser interacts with the target is pivotal. Furthermore, the application of the hydrodynamics radiation model becomes unreliable during extended simulation periods, as the Knudsen Number (KN), which represents the ratio of species mean free path to plasma length, significantly increases. To address this challenge, alternative methodologies such as the direct simulation Monte Carlo approach can provide a more accurate depiction of plume expansion, particularly noticeable at prolonged delay times [48]. Additionally, employing a finer Eulerian grid in specific regions of the domain can yield more precise simulations, especially when considering the mixing between plasma formation and ambient gas. It is important to note that chemical reactions are not accounted for in this work, hence molecular band emissions are not considered. Molecular formation becomes particularly relevant at longer times [49].

5. Conclusion

This paper has provided detailed validation of a non-equilibrium model for laser-induced breakdown plasmas under Martian atmosphere conditions. Non-equilibrium effects were described using a 3T-Eurlian fluid model in the approximation that electrons and ions move together as a single fluid but with two different temperatures, and that this fluid can emit or absorb radiation. In our approach the atomic energy level populations were calculated using a collisional-radiative (CR) NLTE-model taking into account the mixing between the plasma and the ambiant gas. The simulation was performed with the FLASH radiation-hydrodynamics code which is a finite-volume Eulerian code that operates on a block-structured mesh using Adaptive Mesh Refinement (AMR). The plasma simulations were allowed to evolve for different times utilizing the second-order unsplit time marching method of USM algorithm.

We have investigated the effects of laser irradiance and ambient pressure on the plasma parameters namely the electron and ion temperatures and the electron and ion densities. We have also shown the temporal variation of the fluid velocity with the laser irradiance at constant pressure which indicated the presence of a shock front associated with the plasma initiation, dynamics, and expansion into the ambient gas.

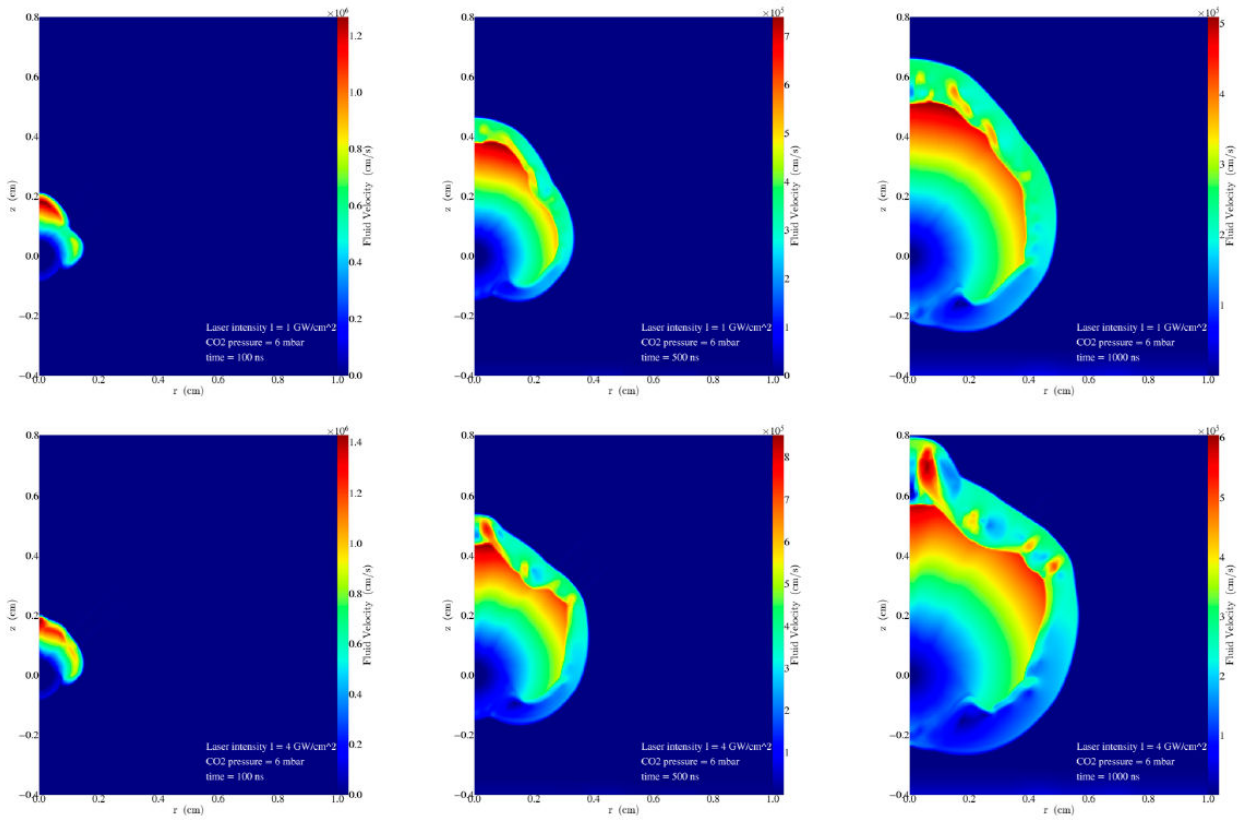

FIGURE 14. Fluid velocity calculated at 6 mbars $C0_2$ ambient gas pressure, for 1 GW/cm^2, (1$^{\rm st}$ row), 4 /cm^2 (2$^{\rm nd}$ row) laser irradiance and for 3 time steps: 100 ns (1$^{\rm st}$ column), 500 ns (2$^{\rm nd}$ column) and 1000 ns (3$^{\rm rd}$ column).

Appendix

A. Inverse Bremsstrahlung model used to calculate $Q_{\rm las}$

A.1 Ray-tracing in the geometric optics approximation to model laser energy deposition [33]

The laser beam is made of a number of rays whose paths are traced through the domain based on the local refractive index of each cell. The term represent the deposition of energy by laser heating. The laser power deposited in a cell is calculated based on the inverse Bremsstrahlung power in the cell and depends on the local electron number density gradient and local electron temperature gradient. The energy deposited by the laser beam was calculated using the laser ray trace approximation for planar and cylindrical geometries. In this approximation, the equation of motion of ray is given by:

$$\frac{d^2x}{dt^2} = \nabla\left(\frac{c}{2}\eta^2\right), \tag{A.1}$$

where the index of refraction η is given by:

$$\eta^2 = 1 - \frac{\omega_{\rm p}^2}{\omega^2} = 1 - \frac{n_{\rm e}}{n_{\rm c}}, \tag{A.2}$$

$$n_{\rm c} = \left(\frac{m_{\rm e}}{4\pi}\right)\left(\frac{\omega}{e}\right)^2, \tag{A.3}$$

where $\omega_{\rm p}$ is the plasma frequency, ω is the laser frequency, c is the speed of light in vacuum and $n_{\rm c}$ is the critical density at which the laser frequency and the plasma frequency are equal. The quantities $n_{\rm e}$, $m_{\rm e}$ and e are the density, the mass and the charge of the electron, respectively. Combing Eq. (A.1) with Eq. (A.2) we obtain the final from of the ray equation of motion:

$$\frac{d^2x}{dt^2} = \nabla\left(\frac{c^2}{2}\frac{n_{\rm e}}{n_{\rm c}}\right). \tag{A.4}$$

The electron number density is given by:

$$n_{\rm e}(\overrightarrow{x}) = \langle n_{\rm e}\rangle + \left\langle \overrightarrow{\nabla} n_{\rm e}\right\rangle .(\overrightarrow{x} - \langle\widehat{x}\rangle) + O(\varepsilon^2), \tag{A.5}$$

where $\langle\rangle$ denotes a zone average. The ray equation of motion Eq. (3) becomes:

$$\frac{d^2x}{dt^2} = -\left(\frac{c^2}{2}\right)\frac{\langle n_{\rm e}\rangle}{n_{\rm c}}. \tag{A.6}$$

This shows that when $n_{\rm e}$ is linear within a cell, the rays follow a parabolic trajectory through the cell. The electron number density will not be continuous in general. The Kaiser algorithm fixes this by applying Snell's law at the cell inter-

faces as the following equations :

$$\eta \sin\theta = \eta' \sin\theta', \tag{A.7}$$

$$\sqrt{1-\frac{n_{\rm e}}{n_{\rm c}}}\sin\theta = \sqrt{1-\frac{n'_{\rm e}}{n_{\rm c}}}\sin\theta', \tag{A.8}$$

where unprimed (primed) quantities denote values before (after) the transition, and θ is the angle between the ray velocity and the interface normal. This, rays can reflect or refract off of cell interface.

A.2 Power deposition by inverse Bremssrahlung [33]

Because rays are simply curves in space, they carry no information about radiation intensity or special extent transverse to their direction. Their state is completely defined by their frequency, velocity, and power, the latter two attributes of which are, in general, spatially dependent. The power P of an electromagnetic wave is depleted by the inverse Bremsstrahlung (*ib*) process.

The rate of power loss is governed by the 1^{st} order ordinary differential equation (ODE):

$$\frac{dP}{dt} = -\nu_{ib}(t)P. \tag{A.9}$$

As a ray travels through a cell, its power (energy) decreases with time:

$$P(\Delta t) = P_0 \exp - \left(\int_0^{\Delta t} \nu_{ib}(\overrightarrow{x}(t))dt \right). \tag{A.10}$$

The inverse Bremsstrahlung frequency factor ν_{ib} (the rate of energy loss) is given by the formula:

$$\nu_{ib} = \frac{n_{\rm e}}{n_{\rm c}}\nu_{ei}, \tag{A.11}$$

where ν_{ei} is the electron-ion collision frequency, given by :

$$\nu_{ei} = \frac{4}{3}\sqrt{\frac{2\pi}{m_e}}\frac{n_e \overline{Z} e^4 \ln\Lambda_{ei}}{(k_{\rm B}T_e)^{3/2}}. \tag{A.12}$$

Here $\overline{Z}$ is the average ionization number of the plasma, m_e, e and T_e are the mass, the charge and the temperature oh the electron respectively, $K_{\rm B}$ is the Boltzmann constant. The Coulomb logarithm $\ln\Lambda_{ei}$ is the natural logarithm of the Debye number and is taken here as:

$$\ln\Lambda_{ei} = \ln\left[\frac{3}{2\overline{Z}e^3}\sqrt{\frac{K_{\rm B}^3 T_e^3}{\pi n_e}}\right]. \tag{A.13}$$

The inverse Bremsstrahlung frequency depends thus on the electron temperature and the electron number density, both of which are functions of the position, and since the position changes with time, it's ultimately also a function of time:

$$\nu_{ib}(t) = \frac{4}{3}\sqrt{\frac{2\pi}{m_e}}\frac{\overline{Z}e^4}{n_c K_{\rm B}^{3/2}}\frac{n_e(x(t))^2 \ln\Lambda_{ei}(x(t))}{T_e(x(t))^{3/2}}. \tag{A.14}$$

B. CR NLTE - Model

To describe the population of the atomic levels, we utilized a collisional-radiative (CR) NLTE-model, which is equally applicable for low, and high temperature ranges. The number density of i-fold ionized ion n_i is given by NLTE rate equation (steady state):

$$n_{i+1}n_e^2\alpha_{i+1} + n_{i+1}n_e\beta_{i+1} + n_{i+1}n_e D_{i+1} - n_i n_e C_i = 0, \tag{B.1}$$

where α_{i+1}, β_{i+1} and D_{i+1} are the coefficients for collisional recombination, radiative and dielectronic recombination respectively. Collisional recombination is 3-body process involving two electrons and an ion. C_i denotes the electronic collisional ionization coefficient. The electron density is denoted by n_e and the ion density for the element under consideration in the mixture is $n_m = \sum_i n_i$.

The steady state solution of Eq. (B.1) gives the ion densities as:

$$\frac{n_{i+1}}{n_i} = \frac{C_i}{n_e\alpha_{i+1} + \beta_{i+1} + D_{i+1}}. \tag{B.2}$$

The above equations together with the consistency condition $n_m = \sum_i n_i$ is solved to obtain all n_i and the average degree of ionization.

All the coefficients for collisional recombination, radiative, dielectronic recombination and the electronic collisional ionization formula are described in Ref. [18].

Acknowledgments

One of the authors Pr Z. Bedrane gratefully acknowledges the DGRSDT, Algerian Ministry of Higher Education and Research, under Project PRFU code B00L02UN130120220002.

1. Mars exploration program, Curiosity Rover Mission Overview. https://mars.nasa.gov/msl/mission/overview/.

2. C. Fabre and B. Bousquet, *De ChemCam á SuperCam: l'apport de la LIBS pour le spatial, Photoniques* **103 2020**, https://doi.org/10.1051/photon/202010338.

3. K.A. Farley **et al**. Mars 2020 Mission Overview, *Space Sci Rev*, **216** (2020) 142, https://doi.org/10.1007/s11214-020-00762-y.

4. F. Colao, R. Fantoni, V. Lazic, and A. Paolini, LIBS applica-

tion for analyses of Martian crust analogues:search for the optimal experimental parameters in air and CO_2 atmosphere, *Appl. Phys. A*, **79** (2004) 143, https://doi.org/10.1007/s00339-003-2262-x.

5. M. Capitelli, A. Casavola, G. Colonna and A.D. Giacomo, Laser-induced plasma ex- pansion: theoretical and experimental aspects, *Spectrochim. Acta B At. Spectrosc.*, **59** (2004) 271, https://doi.org/10.1016/j.sab.2003.12.017.
6. A. Cousin *et al*., Laser induced breakdown spectroscopy library for the martian environment, *Spectrochim. Acta B At. Spectrosc.*, *66* (2011) 805, https://doi.org/10.1016/j.sab.2011.10.004.
7. J. Colgan *et al*., Theoretical modeling and analysis of the emission spectra of a ChemCam standard: basalt BIR-1A, *Spectrochim. Acta B At. Spectrosc. 110* (2015) 20, https://doi.org/10.1016/j.sab.2015.05.005.
8. E. Ewusi-Annan, D. M. Surmick, N. Melikechi and R.C. Wiens, Simulated laser-induced breakdown spectra of graphite and synthetic shergottite glass under Martian conditions, *Spectrochimica Acta Part B, 148* (2018) 31, https://doi.org/10.1016/j.sab.2018.06.006.
9. P. B. Hansen, S. Schröder, S. Kubitza, K. Rammelkamp, D. S. Vogt, and H.-W. Hübers, Modeling of time-resolved LIBS spectra obtained in Martian atmospheric conditions with a stationary plasma approach, *Spectrochimica Acta Part B: Atomic Spectroscopy, 178* (2021) 106115, https://doi.org/10.1016/j.sab.2021.106115.
10. G. Cristoforetti *et al*., Local thermodynamic equilibrium in laser-induced breakdown spectroscopy: beyond the McWhirter criterion, *Spectrochim. Acta - Part B At. Spectrosc.*, **65** (2010) 86, https://doi.org/10.1016/j.sab.2009.11.005.
11. A. Alberti *et al*., Laser-induced non-equilibrium plasma kernel dynamics, *J. Phys. D: Appl. Phys.*, **53** (2020) 025201, https://doi.org/10.1088/1361-6463/ab492a.
12. N. G. Glumac and G. S. Elliott, The effect of ambient pressure on laser-induced plasmas in air, *Opt. Lasers Eng.*, **45** (2007) 27, https://doi.org/10.1016/j.optlaseng.2006.04.002.
13. N. Tsuda and J. Yamada, Observation of forward breakdown mechanism in high-pressure argon plasma produced by irradiation by an excimer laser, *J. Appl. Phys.*, **81** (1996) 96, https://doi.org/10.1063/1.364200.
14. J. Macfarlane, I. Golovkin, and P. Woodruff, HELIOS-CR - A 1-D radiation-magnetohydrodynamics code with inline atomic kinetics modeling, *J. Quant. Spectrosc. Radiat. Transf.*, **99** (2006) 381, https://doi.org/10.1016/j.jqsrt.2005.05.031.
15. The Flash Center for Computational Science, *FLASH User's Guide Version-4.6.2*, University of Rochester, (2019). https://flash.rochester.edu/site/flashcode/user_support/.
16. P. MacNeice, K. M. Olson, C. Mobarry, R. De Fainchtein and C. Packer, PARAMESH: A parallel adaptive mesh refinement community toolkit, *Computer Physics Communications 126* (2000) 330, https://doi.org/10.1016/S0010-4655(99)00501-9.
17. C. Orban, Fatenejad M., Chawla S., Wilks S. and Lamb D., A Radiation-Hydrodynamics Code Comparison for Laser-Produced Plasmas: FLASH versus HYDRA and the Results of Validation Experiments, *LLNL-JRNL:Physics.plasm-ph*, **7** (2013) 636375, https://doi.org/10.48550/arXiv.1306.1584.
18. J.J. MacFarlane, IONMIX-a code for computing the equation of state and radiative properties of LTE and non-LTE plasmas, *Comput. Phys. Comm.*, **56** (1989) 259, https://doi.org/10.1016/0010-4655(89)90023-4.
19. D. Lee, A solution accurate, efficient and stable unsplit staggered mesh scheme for three dimensional magnetohydrodynamics, *J. Comput. Phys.*, **243** (2013) 269, https://doi.org/10.1016/j.jcp.2013.02.049.
20. P. Colella, Multidimensional upwind methods for hyperbolic conservation laws, *J. Comput. Phys.* **87** (1990) 171, https://doi.org/10.1016/0021-9991(90)90233-Q.
21. S. Li, An HLLC Riemann solver for magneto-hydrodynamics, *J. Comput. Phys.*, **203** (2005) 344, https://doi.org/10.1016/j.jcp.2004.08.020.
22. The HYPRE library is available at: https://computing.llnl.gov/projects/hypre-scalable-linear-solvers-multigrid-methods/software.
23. D. Mihalas and B. W. Mihalas, Foundations of radiation hydrodynamics, *Oxford University Press*, New York, (1984) ISBN 0-19-503437-6.
24. J. I. Castor, Radiation Hydrodynamics, *Cambridge University Press*, (2004). ISBN: 9780511536182.
25. L. Spitzer, Physics of Fully Ionized Gases, *Interscience Publishers*, New York, (1962) ISNB: 3-978-0486449821.
26. S. Atzeni and J. Meyer-Ter-Vehn, The Physics of Inertial Fusion: Beam Plasma Interaction, Hydrodynamics, Hot Dense Matter, *International Series of Monographs on Physics, Oxford University Press*, (2004) ISBN 9780198562641.
27. H. Brysk, P.M. Campbell, and P. Hammerling, Thermal conduction in laser fusion, *Plasma Phys.*, **17** (1974) 473, https://doi.org/10.1088/0032-1028/17/6/007.
28. The Flash Center for Computational Science, available online https://flash.rochester.edu/
29. P. Tzeferacos *et al*., FLASH MHD simulations of experiments that study shock-generated magnetic fields, *High Energy Density Phys.*, **17** (2015) 24, https://doi.org/10.1016/j.hedp.2014.11.003.
30. B. Fryxell *et al*., FLASH: An adaptive mesh hydrodynamics code for modeling astrophysical thermonuclear flashes, *The Astrophysical Journal Supplement Series*, **131** (2000) 273, https://doi.org/10.1086/317361.
31. D. Lee and A. E. Deane, An unsplit staggered mesh scheme for multidimensional magnetohydrodynamics, *J. Comput. Phys.*, **228** (2009) 952, https://doi.org/10.1016/j.jcp.2008.08.026.
32. M. M. Marinak *et al*., NP8.00100: New capabilities in HYDRA for simulations of inertial confinement fusion targets, in 51st Annual Meeting of the APS Division of Plasma Physics (American Physical Society, 2009), **Vol. 54** p. 15. Site: https://meetings.aps.org/Meeting/DPP09/Content/1617.

33. T.B. Kaiser, Laser ray tracing and power deposition on an unstructured three- dimensional grid, *Phys. Rev. E*, **61** (2000) 895, https://doi.org/10.1103/PhysRevE.61.895.

34. A. Kramida, Yu. Ralchenko, and J. Reader, NIST ASD Team, NIST Atomic Spectra Database (ver. 5.9), [Online]. Available: https://www.nist.gov/pml/atomic-spectra-database.

35. S. Acquaviva and M. L. D. Giorgi, High-resolution investigations of C_2 and CN optical emissions in laser-induced plasmas during graphite ablation, *J. Phys. B Atomic Mol. Phys.*, **35** (2002) 795, https://doi.org/10.1088/0953-4075/35/4/304.

36. S. Maurice *et al.*, The ChemCam instrument suite on the Mars science laboratory (MSL) rover: science objectives and mast unit description, *Space Sci. Rev.*, **170** (2012) 95, https://doi.org/10.1007/s11214-012-9912-2.

37. J. R. Davies *et al*., Laser entrance window transmission and reflection measurements for preheating in magnetized liner inertial fusion, *Physics of Plasmas*, **25** (2018) 062704, https://doi.org/10.1063/1.5030107.

38. A. J. Harvey-Thompson *et al*., Diagnosing laser-preheated magnetized plasmas relevant to magnetized liner inertial fusion, *Physics of Plasmas*, **22** (2015) 122708, https://doi.org/10.1063/1.4938047.

39. K. Gillen-Christandl, D. Gillen Glen, M. J. Piotrowicz and M. Saffman, Comparison of Gaussian and super Gaussian laser beams for addressing atomic qubits, *Appl. Phys. B*, **122** (2016) 131, https://doi.org/10.1007/s00340-016-6407-y.

40. R. J. LeVeque, Finite Volume Methods for Hyperbolic Problems, *Cambridge University Press*, (2002) ISBN: 9780511791253.

41. E.F. Toro, Riemann Solvers and Numerical Methods for Fluid Dynamics, *Springer Science & Business Media*, (2009) ISBN: 978-3-540-49834-6.

42. M. J. Turk, A multi-code analysis toolkit for astrophysical Simulation data, *The Astrophysical Journal Supplement Series*, **192** (2011) 16, https://doi.org/10.1088/0067-0049/192/1/9.

43. S.S. Harilal, C.V. Bindhu, R.C. Issac, V. P. N. Nampoori, and C. P. G. Vallabhan, Electron density and temperature measurements in a laser produced carbon plasma, *J. Appl. Phys.*, **82** (1997) 2140, https://doi.org/10.1063/1.366276.

44. T.A. Heltemes and G.A. Moses, BADGER v1.0: A Fortran equation of state library, *Computer Physics Communications* **183** (2012) 2629, https://doi.org/10.1016/j.cpc.2012.07.010.

45. Z. Chen, Z. Chen, W. Jiang, L. Guo, and Y. Zhang, Line intensity calculation of laser-induced breakdown spectroscopy during plasma expansion in nonlocal thermodynamic equilibrium, *Opt. Lett.* **48** (2023) 3227, https://doi.org/10.1364/OL.488250.

46. A.K. Sharma and R.K. Thareja, Plume dynamics of laser-produced aluminum plasma in ambient nitrogen, *Applied Surface Science* **243** (2005) 68, https://doi.org/10.1016/j.apsusc.2004.09.093.

47. T.E. Itina, J. Hermann, P. Delaporte, and M. Sentis, Laser-generated plasma plume expansion: combined continuous-microscopic modeling, *Phys. Rev. E 66* (2002) 066406, https://doi.org/10.1103/PhysRevE.66.066406.

48. M. Skocic and S. Bukvic, Laser induced plasma expansion and existence of local thermodynamic equilibrium, *Spectrochim. Acta B At. Spectrosc.* **125** (2016) 103, https://doi.org/10.1016/j.sab.2016.09.011.

49. M. Dong, J. Lu, S. Yao, Z. Zhong, J. Li and W. Lu, Experimental study on the characteristics of molecular emission spectroscopy for the analysis of solid materials containing c and n, *Opt. Express* **18** (2011) 17021, https://doi.org/10.1364/OE.19.017021.

Submitted Paper

Applied Spectroscopy

www.s-a-s.org

Applied Spectroscopy
1–18

DOI: 10.1177/00037028241307675
journals.sagepub.com/home/asp
Sage

Focusing Effects on Laser-Induced Plasma Parameters: Applications to a Graphite Target Under Martian Atmospheric Conditions

Kouider Benbaier[1], Ahmed Abdelmalek[1], Zeyneb Bedrane[1] and Noureddine Melikechi[2]

Abstract

Under various atmospheric conditions, laser-induced breakdown spectroscopy (LIBS) is a powerful technique for elemental analysis, including in Earth- and Mars-like environments. However, understanding the plasma behavior and its dependence on ambient pressure and laser parameters remains a challenge. In this study, a numerical model based on a three-temperature Eulerian radiation framework under non-local thermodynamic equilibrium conditions is employed to investigate the interaction of a nanosecond laser pulse with a graphite target under helium (He) and carbon dioxide (CO_2 atmospheres. The aim is to provide insights into the effects of focusing conditions and ambient pressure (3 to 9 mbar and 1000 mbar) on plasma parameters relevant to both Earth- and Mars-like settings. Our results show that increased ambient pressure significantly enhances electron and ion densities, while the focusing conditions influence the temperature and fluid velocity of plasma species, as well as the spatial distribution and intensity of the plasma, ultimately affecting its diagnostic potential. These findings are critical for optimizing LIBS applications in planetary exploration and contribute to improving quantitative analyses under varying atmospheric compositions.

Keywords

Laser-induced breakdown spectroscopy plasma, LIBS plasma, non-local thermodynamic equilibrium, NLTE approach, focusing conditions, ambient gas, plasma parameters

Date received: 16 August 2024; accepted: 18 November 2024

Introduction

Laser-induced breakdown spectroscopy (LIBS) is an analytical technique shown to provide multi-elemental information on solid, liquid, and gas, with minimal or no sample preparation.[1,2] In recent years, this technique has gained significant interest in numerous areas, including applications in medicine,[3–7] food and environmental science,[8–10] isotope discrimination,[11,12] and remote sensing of extraterrestrial samples.[13] LIBS is a form of atomic emission spectroscopy that analyzes the emission spectra obtained from a plasma produced by the evaporation and excitation of the target material. It requires selecting a laser that operates at a wavelength that can be absorbed by the sample and focusing it so that its energy density is above the breakdown threshold energy of the material. This process depends on the optical focusing conditions of the laser beam as well as the environment in which the plasma expands and emits radiation while decaying.[14]

Laser-induced breakdown spectroscopy (LIBS) measurements are typically performed using nanosecond-long laser pulses with a reasonably good Gaussian profile and energies ranging from about 10 to 100 mJ. Several research groups have noted that the analysis of LIBS spectra depends critically on the spatial characteristics of the laser beam at the interaction region. Wang et al.[15] reported that the focusing conditions of the laser beam impact the spectra and, in particular, the quantitative analysis of the sample investigated. Recently, we reported that the atomic and ionic emissions of

[1]Theoretical Physics Laboratory, Physics Department, Sciences Faculty, Tlemcen University, Tlemcen, Algeria
[2]Department of Physics & Applied Physics, Kennedy College of Sciences, University of Massachusetts Lowell, Lowell, Massachusetts, USA

Corresponding Author:
Zeyneb Bedrane, Theoretical Physics Laboratory, Physics Department, Sciences Faculty, Tlemcen University, B.P. 119, Tlemcen, 13000, Algeria.
Email: zeynebbedrane@gmail.com

aluminum, copper, and steel samples behave differently under different focusing conditions in both ambient Earth and simulated Martian atmospheres.[16] In addition to the focusing conditions, the environment in which the LIBS spectra are acquired, such as changes in pressure and environmental species, can affect the evolution of the plasma.[17]

Stand-off analysis of geological samples using LIBS has attracted tremendous interest, particularly since the successful operations of the ChemCam and SuperCam instruments on board NASA's Curiosity and Perseverance rovers.[18,19] Recently, we reported on the effects of the distance from a laser source to a sample on the LIBS spectra acquired by Curiosity. In Melikechi et al.,[20] Mezzacappa et al.,[21] and Lasue et al.,[22] the authors have shown that carefully selected emission lines from Martian dust can be used as a proxy spectroscopic standard to evaluate and correct for distance effects. More recently, we used an extensive Mars database to analyze the distance effects on the quantification of multiple elements and observed trends that reflect changes in laser beam properties that influence plasma temperature.[23]

To obtain a better understanding of the effects of laser parameters and atmospheric pressures on LIBS spectra collected by ChemCam, we simulated the laser-induced breakdown spectra of graphite and synthetic shergottite glass in a Mars atmosphere using a 1D Lagrangian hydrodynamic model, a spherical geometry description of laser ablation and plume expansion, and a local thermodynamic equilibrium (LTE) assumption.[24] More recently, Liang et al.[25] investigated the effects of different focusing conditions and laser energies on the LIBS-integrated plasma images. They reported that when the focal point is above the sample surface, the laser beam strongly interacts with the ambient air and produces a weaker plasma. Wang et al.[26] reported that the distance from the focusing lens to the target greatly affects the spectral intensities. Using a 1D stationary model, Hansen et al.[27] reported the characteristics of LIBS plasma measured under Martian atmospheric conditions.

Although fluid models relying on LTE have produced satisfactory outcomes, this approach is valid only when the plasma is assumed to be in a near-equilibrium state, and plasma populations are characterized by Boltzmann and Saha distributions with a single temperature.[28,29] To explore the spatiotemporal evolution of LIBS plasmas, some research groups have used a non-LTE approach and successfully predicted the dimensions and propagation patterns of plasma waves observed in several experiments conducted in various gases.[30,31]

In this work, we have used a non-LTE (NLTE) model based on a three-temperature Eulerian radiation approach to simulate the physical characteristics of LIBS plasmas of homogeneous graphite targets assumed to be under either Martian carbon dioxide (CO_2) or helium (He) atmospheric conditions. The three-temperature approach was adopted because the two-temperature model falls short of describing adequately the complexity of the plasma formation process.[32] The plasmas were simulated for single laser pulse excitation and different focusing conditions. We have investigated the effects of waist sizes and irradiances of the laser on electron and ion temperatures and densities, and fluid velocities under 6–9 mbar of CO_2 (pressure on Mars) ambient atmospheres, as well as changes to these parameters in a He ambient atmosphere. We have considered the mixing between the plasma and each of the two ambient gases, CO_2 and He, as well as the propagation of the shock waves under different focusing conditions. As this study was limited to a single-pulse excitation, cavity effects that follow ablation were not considered.

Hydrodynamics and Plasma Radiation Theoretical Model

The Euler equations expressing conservation of mass, momentum, and total energy used to describe the evolution of a hydrodynamics 3T plasma are given by Mihalas and Mihalas[33] and Castor:[34]

$$\frac{\partial \rho}{\partial t} + \nabla \cdot (\rho \mathbf{v}) = 0 \tag{1}$$

$$\frac{\partial}{\partial t}(\rho \mathbf{v}) + \nabla \cdot (\rho \mathbf{v}\mathbf{v}) + \nabla P_{\text{tot}} = 0 \tag{2}$$

$$\frac{\partial}{\partial t}(\rho E_{\text{tot}}) + \nabla \cdot \left[(\rho E_{\text{tot}} + P_{\text{tot}})\mathbf{v}\right] = Q_{\text{las}} - \nabla \cdot \mathbf{q} \tag{3}$$

ρ is the plasma mass density, $\mathbf{v}$ is the fluid velocity, P_{tot} is the total pressure, P_{ele}, P_{ion}, and P_{rad} are the electron, the ion, and the radiation pressure, respectively. E_{tot} is the total specific energy, which includes the specific internal energies of the electron e_{ele}, ions e_{ion}, and the radiation field e_{rad} along with the specific kinetic energy. Q_{las} is the energy source due to laser heating. $\mathbf{q}$ is the total heat flux, which is the sum of the electron, the ion heat flux, and the radiation flux. Since the plasma is assumed to have multi-temperatures, additional equations must be evolved to describe the change in specific internal energies of the ions, electrons, and radiations field:

$$\begin{aligned}\frac{\partial \rho e_{\text{ion}}}{\partial t} + \nabla \cdot (\rho e_{\text{ion}} \mathbf{v}) + P_{\text{ion}} \nabla \cdot \mathbf{v} \\ = \rho \omega_{\text{ei}}(T_{\text{ele}} - T_{\text{ion}}) - \nabla \cdot \mathbf{q}_{\text{ion}}\end{aligned} \tag{4}$$

$$\begin{aligned}\frac{\partial \rho e_{\text{ele}}}{\partial t} + \nabla \cdot (\rho e_{\text{ele}} \mathbf{v}) + P_{\text{ele}} \nabla \cdot \mathbf{v} \\ = \rho \omega_{\text{ei}}(T_{\text{ion}} - T_{\text{ele}}) - \nabla \cdot \mathbf{q}_{\text{ele}} + Q_{\text{abs}} - Q_{\text{emis}} + Q_{\text{las}}\end{aligned} \tag{5}$$

$$\begin{aligned}\frac{\partial \rho e_{\text{rad}}}{\partial t} + \nabla \cdot (\rho e_{\text{rad}} \mathbf{v}) + P_{\text{rad}} \nabla \cdot \mathbf{v} \\ = -\nabla \cdot \mathbf{q}_{\text{rad}} - Q_{\text{abs}} + Q_{\text{emis}}\end{aligned} \tag{6}$$

e_{ion} is the ion specific internal energy, e_{ele} is the electron specific internal energy, e_{rad} is the radiation specific internal

energy. Q_{las} represents the energy source due to laser heating. Q_{abs} represents the increase in electron internal energy due to the total absorption of radiation, and Q_{emis} represents the decrease in electron internal energy due to the total emission of radiation. We solve the following system of equations, assuming that the plasma emitted radiation in a Planck spectrum with an emission opacity given by:

$$\frac{1}{c}\frac{\partial u_{rad}}{\partial t} - \nabla \cdot \left(\frac{1}{3\sigma_{t,g}} \nabla u_{rad}\right) + \sigma_{a,g} u_{rad} = \sigma_{e,g} a T_{ele}^4 \frac{15}{\pi^4}\left[P(x_{g+1}) - P(x_g)\right] \quad (7)$$

$$\frac{\partial u_{ele}}{\partial t} = \sum_g \left\{ \sigma_{a,g} u_{rad} - \sigma_{e,g} a T_{ele}^4 \frac{15}{\pi^4}\left[P(x_{g+1}) - P(x_g)\right] \right\} \quad (8)$$

where u_{rad} is the radiation energy density, $\sigma_{t,g}$ is the transport opacity for group g, $\sigma_{a,g}$ is the absorption opacity for group g, $\sigma_{e,g}$ is the emission opacity for group g, a is the radiation constant, and $P(x)$ is the Planck integral.[34]

Simulation Approach

The Eulerian approach is commonly employed for LIBS plasma simulations,[35,36] where the simulations track temporal changes at fixed spatial positions. To establish a comprehensive kinetic model that encompasses several physical phenomena within LIBS, we used a collisional-radiative NLTE model based on a three-temperature Eulerian radiation approach. This model was employed to perform simulations of LIBS plasma parameters, specifically for a solid, flat graphite target irradiated under CO_2 and He atmospheric conditions at Martian pressures. The interaction between the laser and the target in the presence of ambient gas is crucial for accurately simulating the complex nature of plasma formation.

The simulations were performed using the FLASH radiation-hydrodynamics code,[37] which is characterized by a block-structured mesh with adaptive mesh refinement. In this approach, we treat electrons and ions as a cohesive fluid with distinct temperatures while considering radiation emission and absorption.[38] Plasma simulations were conducted over relatively long-time ranges (ns) using the second-order unsplit time marching method, utilizing the unsplit staggered mesh solver algorithm.[39] Upwind fluxes were computed with the Harten–Lax–van Leer Contact Riemann solver.[40] To enhance the precision of the simulation, we employed Cartesian (x–y) geometry, which accounted for plasma plume expansions in both horizontal and vertical directions. The laser beam was designed to emulate a three-dimensional cylindrical shape using the Kaiser algorithm.[41] The boundary conditions are set to be reflective on the left side of the y-axis, while the remaining boundaries are set to outflow (zero gradient). To visualize the plasma characteristics data, we utilized the multi-code analysis tool yt-project.[42] This open-source Python-based software provides a robust data management layer, facilitating the organization and tracking of simulation results, including those generated by the FLASH code.

The equations of state (EOS) for the graphite target and the CO_2 ambient gas were incorporated into the computation for various plasma parameters, including electron and ion pressures, specific heats, and internal energies. We computed the electron–ion coupling term based on the plasma temperature and ion density grid. To derive the EOS and emissivity for NLTE plasma, we used the program IONMIX4,[43] which provided inputs for the FLASH code. FLASH is an open-source, multi-physics software designed to handle complex physical phenomena, including radiation-hydrodynamics and magneto-hydrodynamics in multiple dimensions. It is particularly adept at simulating laser-driven plasma experiments.[44] Unlike Lagrangian hydrodynamics approaches, FLASH employs a stationary spatial mesh that allows fluid movement into and out of cells, thereby avoiding mesh entanglement and facilitating the simulation of complex multi-component fluids.

For the calculations of EOS and opacity data, we used a temperature grid spanning 0.01–100 eV, an ion density grid ranging from 10^{11} to 10^{25} ions cm^{-3}, and an energy grid from 1 to 6 eV. The ionization potential energies of the excited levels for carbon and oxygen were obtained from the National Institute of Standards and Technology.[45] These data were essential for generating information related to graphite and CO_2 and He. The populations of atomic energy levels were also computed using a collisional-radiative NLTE model.[43] Figure 1 presents a detailed workflow diagram that illustrates the interactions between FLASH and the various programs and libraries mentioned above through a precise schematic representation. This graphic serves as a roadmap, highlighting the dynamic relationships and exchanges between FLASH and its surrounding computing environment.

Simulations of electron and ion temperatures, densities, and fluid velocities were performed under focusing and atmospheric pressure conditions similar to those encountered by ChemCam,[46] as reported by Ewusi-Annan et al.[24] and Schröeder et al.[47] We considered a flat solid, homogeneous graphite target, 0.12 cm thick and 0.3 cm in radius, with a density of 2.23 g cm^{-3}, irradiated by 1064 nm, 10 ns long laser pulses, which were assumed to have a Gaussian spatial profile.

The laser beam is directed perpendicularly to the graphite target surface along the z-axis, resulting in plasma formation at the point of interaction. To account for different focusing conditions, we investigated three cases where the focal point of the laser beam is set at, above, and below the target surface, respectively. This variation in the z-axis position alters the radial structure of the focused laser and significantly affects the laser spot size and energy density at the target. The three scenarios are illustrated in Figure 2, demonstrating

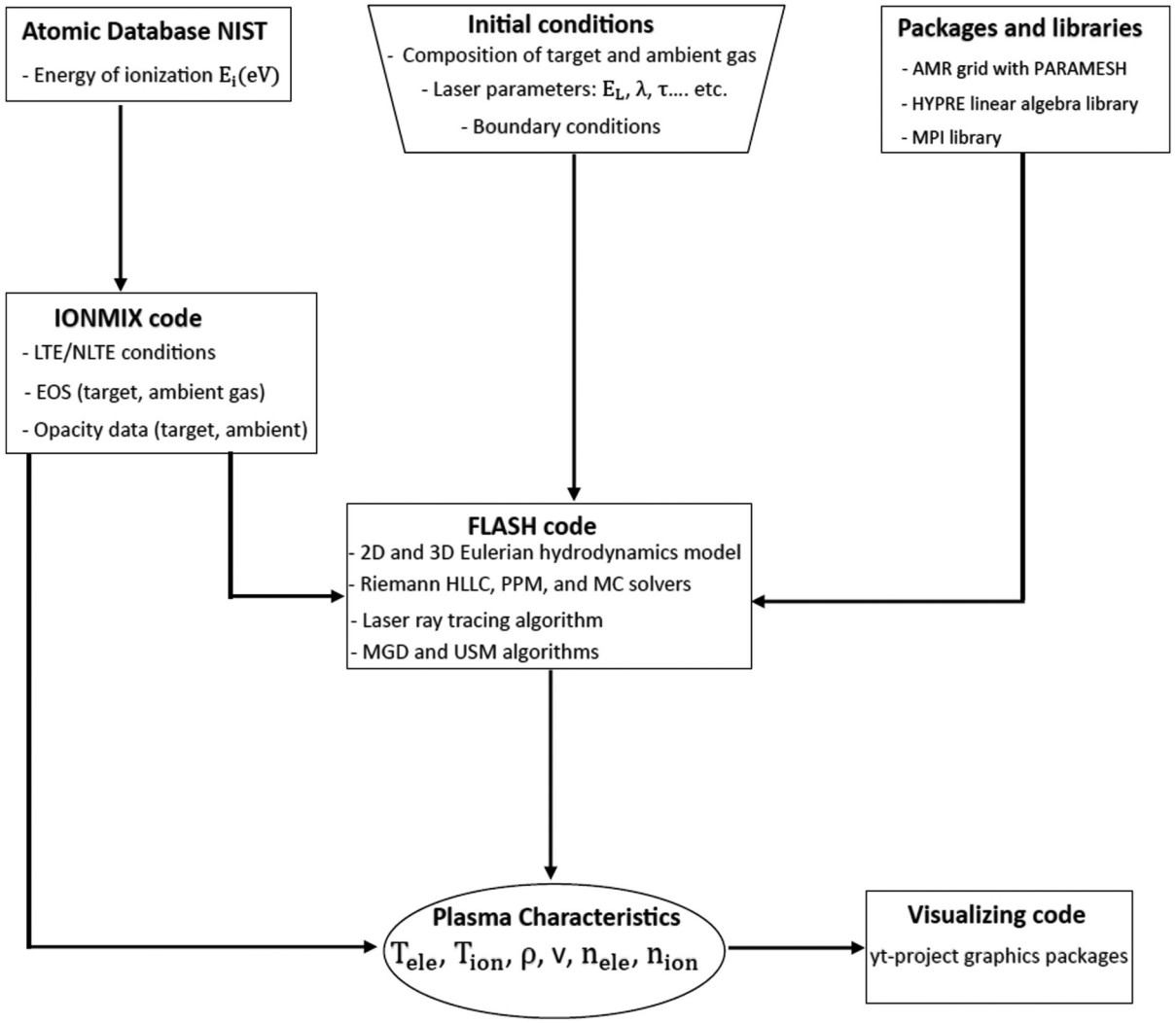

Figure 1. Presents a detailed flow diagram that illustrates the movement and integration of data between the FLASH simulation framework and various associated codes and software packages.

how the z-axis focal position influences plasma formation and expansion.

Different experimental conditions were considered for the laser spot size and intensity. In the first case, the waist of the laser beam was minimal at the surface of the target (100 μm), yielding an on-target irradiance of 25 GW cm^{-2} (Case 1a), which typically produces maximum LIBS signal intensity. The irradiance was varied to 9 GW cm^{-2} for comparison (Case 1b). In the second case, we simulated the scenario where the laser beam was focused slightly off the surface of the target, resulting in a spot size of 168 μm and an on-target irradiance of 9 GW cm^{-2} (Case 2a), with a corresponding adjustment to 25 GW cm^{-2} (Case 2b). Lastly, we simulated a defocused laser beam, producing a spot size of 420 μm and an on-target irradiance of 1.45 GW cm^{-2}. For this case, the irradiance was also varied to 25 GW cm^{-2} (Case 3b) to analyze the effect of spot diameter on the plasma properties at a fixed laser irradiance. For each case, we conducted simulations at CO_2 and He pressures of 3, 6, 9, and 1000 mbar to investigate the influence of different atmospheric conditions.

The plasma simulations were evolved for various time increments, including 5 ns, 10–50 ns in 10 ns increments, 100 ns, 200 ns, 500 ns, and 1000 ns, with time steps of 0.1 ns. The initial temperatures of the graphite and the ambient gas were set at 17 °C, significantly lower than the plasma temperature, and thus had no effect on the simulation results.

An essential simulation used for validation of the model experimentally verified for LIBS plasmas confirmed by Orban et al.[38] A numerical modeling of laser-produced plasma experiments and expansion of shock waves in ambient gas confirmed by Tzeferacos et al.[44,48] The radial and longitudinal dependence of the plasma expansion electron and

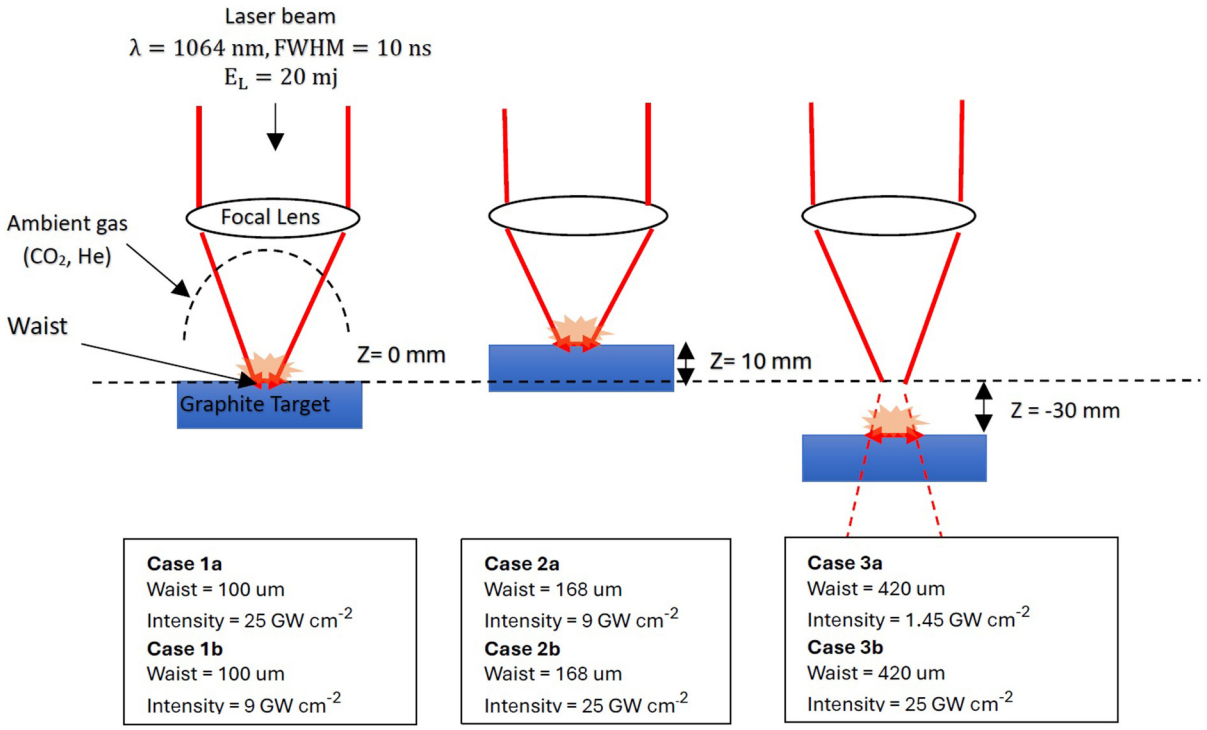

Figure 2. Simulation design for different z-axis focal positions and experimental cases.

ion temperatures, electron and ion densities, and flow velocity trend are experimentally verified in Fu et al.,[49] and confirmed by using the same model of our calculations. It is shown that plasma evolution significantly depends on the laser spot size and this makes it clearer that radiation is the main factor contributing to the energy redistribution.

Typically, the majority of models cited in the aforementioned references begin describing plasma evolution from the onset of the laser pulse interaction with the target material. In contrast, our work presents a model of laser-induced plasma that captures the entire process, from the initial laser–target interaction to the subsequent plasma plume formation and its expansion into the surrounding ambient gas over time. Once the pulsed laser turns off, the interaction with the target material ceases, and a NLTE state is established.

Results and Discussion

A single Gaussian-shaped laser pulse was used for the simulation. The plasma characteristics were determined for a solid, flat graphite target, with varying distances between the focusing lens and the target, resulting in different laser spot sizes (100, 168, and 420 μm). The distance between the focusing lens and the target was adjusted to simulate different gases (CO_2 and He) under varying pressures: 3, 6, and 9 mbar on Mars, and 1000 mbar on Earth. During the initial nanoseconds of the laser pulse, the plasma expands uninhibitedly, encountering minimal counterpressure from the ambient gas. Consequently, the plasma plume remains low, and the inverse bremsstrahlung effect is minimal. This indicates that the sample surface can receive the majority of the laser energy, producing a sizable amount of ablated mass.[50] While the lower ambient gas pressure allows for greater laser energy absorption by the sample, it also results in elevated electron and ion temperatures in the plasma. In contrast, higher ambient gas pressures enhance plasma confinement, which reduces its temperature but significantly shortens its lifetime.[51]

Figure 3 illustrates the interaction of the pulsed laser with the solid flat graphite target, displaying the evolution of the electron temperature and plume formation at different stages of plasma evolution. The snapshots cover both the active laser phase (5–10 ns) and the post-laser phase (30–1000 ns) under a CO_2 ambient pressure of 6 mbar, with a focal spot size of 100 μm. These images provide a clear depiction of how the plasma evolves over time, showcasing key temperature variations and structural changes in different regions of the plume.

Pressure Effect for Different Spot Sizes

Figure 4 shows the electron and ion temperatures, electron and ion number densities, and fluid velocity of the simulated graphite plasma for different spot sizes (100, 168, and 420 μm) under varying CO_2 pressures of 3–9 mbar on Mars

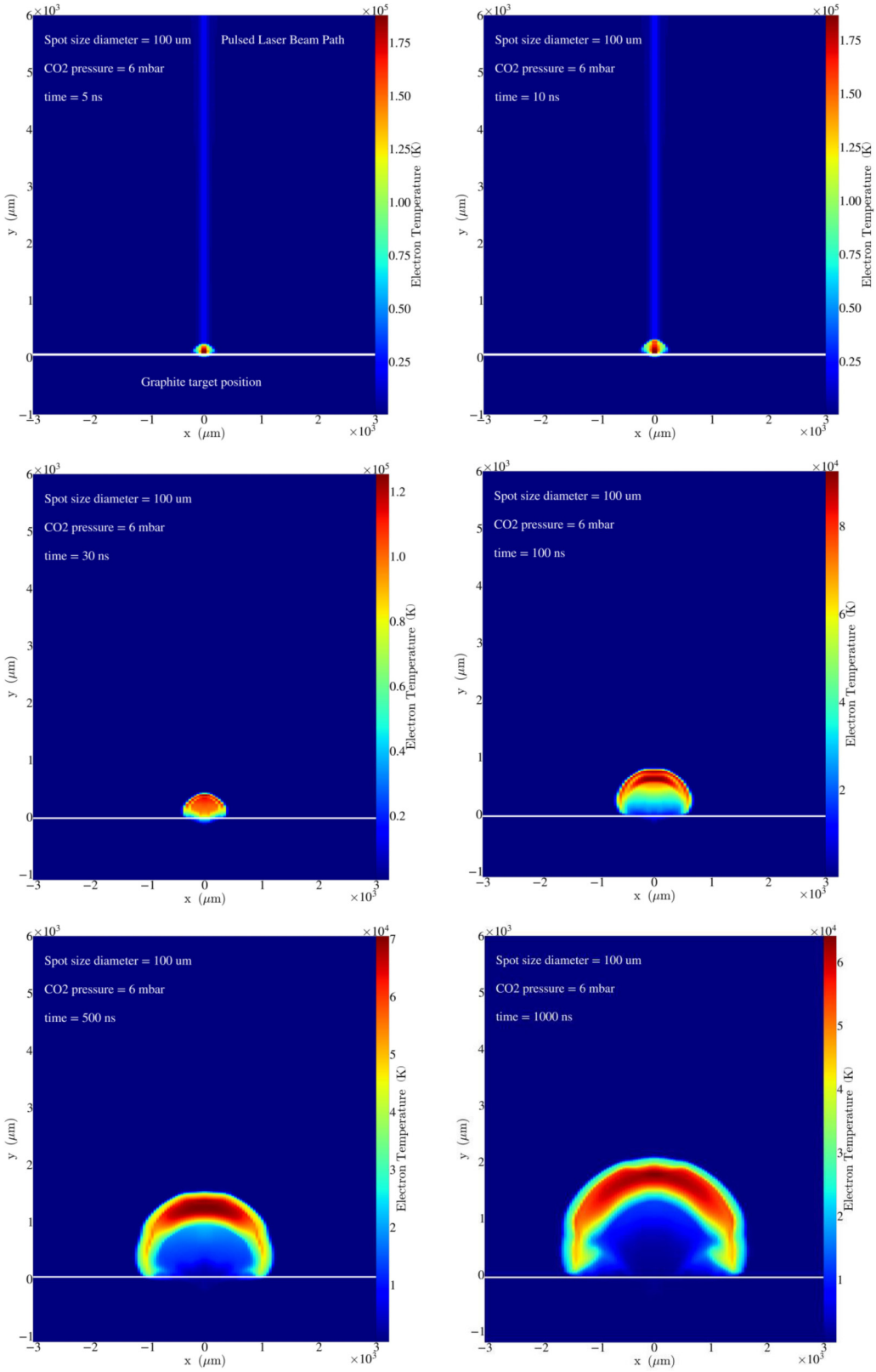

Figure 3. Plasma electron temperature distribution and plume expansion evolution at 5, 10, 30, 100, 500, and 1000 ns of simulation time for a spot size diameter of 100 μm under 6 mbar CO_2 pressure.

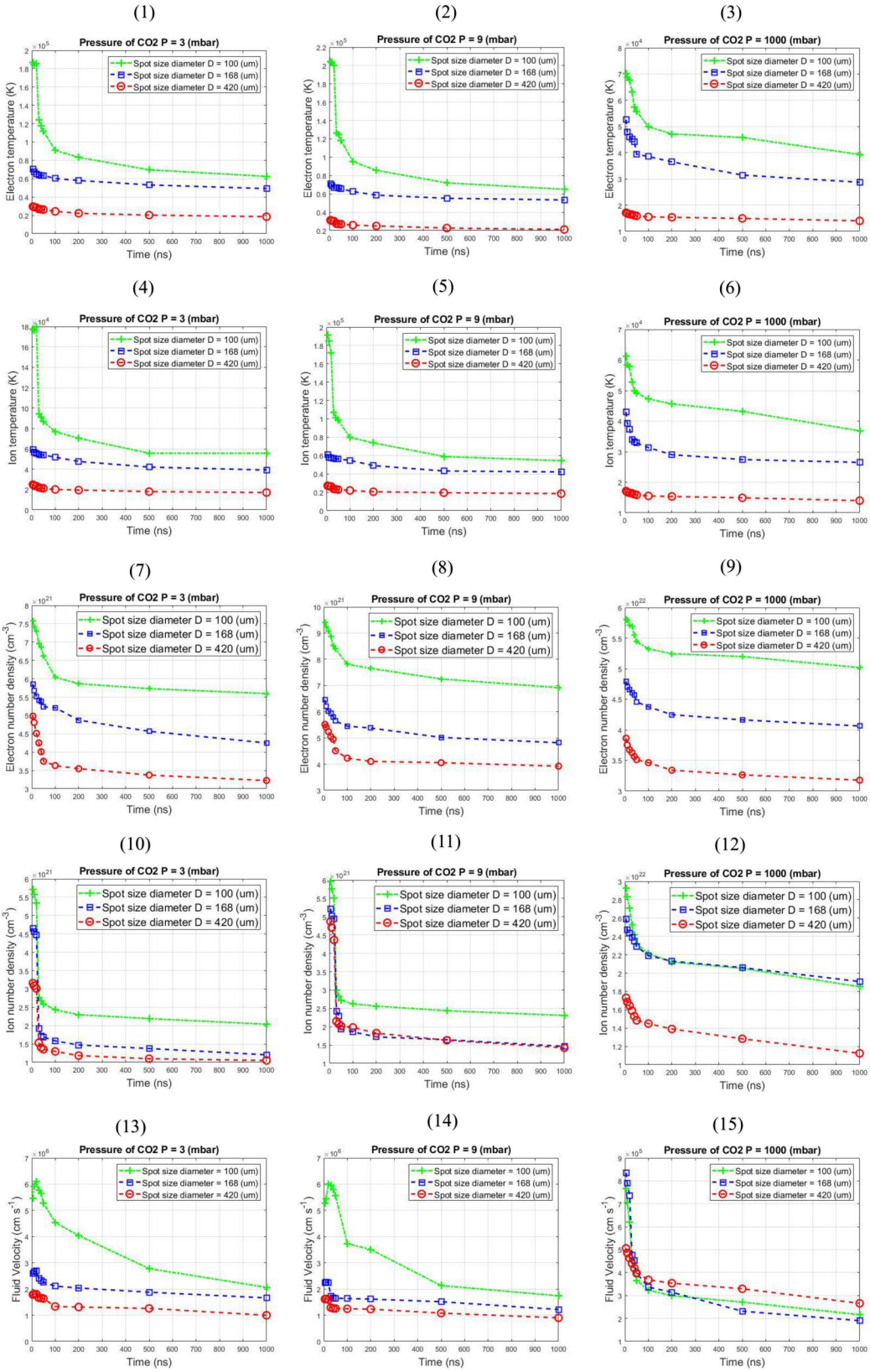

Figure 4. Variation of the electron temperature (first row), ion temperature (second row), electron density (third row), ion density (fourth row), and fluid velocity (fifth row) with time, calculated for different focusing diameters: 100 μm (green line), 168 μm (blue line), and 420 μm (red line) for three CO_2 pressures: 3 mbar (first column), 9 mbar (second column), and 1000 mbar (third column). Subpanels 1–15 represent individual cases.

and 1000 mbar on Earth. The evolution of the simulated plasma was monitored at intervals of 5 ns, from 10 to 50 ns in 10 ns steps, and then at 100, 200, 500, and 1000 ns, respectively. Each column details the results for a specific CO_2 pressure (3, 9, and 1000 mbar) across different laser irradiances: 25 GW cm^{-2} for a spot size of 100 μm, 9 GW cm^{-2} for a spot size of 168 μm, and 1.45 GW cm^{-2} for a spot size of 420 μm.

Electron and Ion Temperatures. Figure 4, subpanels 1–6, shows the variation of both electron and ion temperature distributions as a function of laser spot size and CO_2 pressure. For a fixed spot size, both electron and ion temperatures increase slightly at low pressure (a few mbar), whereas at high pressure (≥ 1000 mbar), a sharp decrease in electron and ion temperatures is observed at all simulation times. The high pressure of the ambient gas, leading to the confinement of the plasma, exerts greater resistance against the movement of plasma particles,[52] thus influencing their temperature.

For a spot size of 100 μm, the peak electron temperature when the laser pulse is activated (5–10 ns) varies from 186 676.8 K at 3 mbar to 204 475.8 K and 70 230.6 K at 9 and 1000 mbar, respectively. The peak ion temperature at 5 ns varies from 177 396.9 K at 3 mbar to 191 592.0 K and 61 210.7 K at 9 and 1000 mbar. After the laser is turned off (>20 ns), both electron and ion temperatures decrease exponentially over time due to the cooling process,[53] which is a critical aspect of graphite plasma dynamics.

When the laser spot size increases, we observe a decrease in both electron and ion temperatures, with an average decrease of ∼ 0.36 and ∼ 0.15 for spot sizes of 168 and 420 μm, respectively, at low pressure. At high pressure, the average decrease is ∼ 0.75 and ∼ 0.24 for spot sizes of 168 μm and 420 μm, respectively. As the spot diameter grows, the laser irradiance is reduced, implying less energy being delivered per unit area to the plasma particles,[54,55] leading to a decrease in particle temperatures.

The change in temperature with pressure varies based on the spot size on the target and the duration of plasma evolution. It is important to note that the temperature values we obtained are higher compared to those reported by references.[56,57] The reason is that in our simulation, we take into account the mixing between the graphite plasma formation and ambient CO_2 molecules under NLTE conditions. This implies that CO_2 molecules adhere to the surface of the target due to pressure effects, leading to a high collision rate.

These collisions result in a significant portion of energy being converted into plasma species, thereby increasing the temperature of both electrons and ions, as well as radiation emission.[58–60] Additionally, our simulations show that an increased ionization state of carbon and oxygen enhances the plasma's ability to emit and absorb radiation. This phenomenon contributes to the formation of localized regions of elevated temperatures within the plasma species.[50,61] By analyzing the temperature distribution and ionization dynamics, we observed that areas with higher ionization levels correspond to peaks in temperature, indicating a direct correlation between ionization and thermal behavior in the plasma.

Electron and Ion Densities. In Figure 4, subpanels 7–12 offer a comprehensive analysis of the electron and ion number densities measured at various time intervals, ranging from 5 to 1000 ns. The ambient gas pressure has a more significant impact on the electron and ion number densities compared to laser spot sizes.

The electron number density peaks when the laser pulse is activated at 5–10 ns. For low pressures (3–9 mbar), the electron number density ($\times 10^{21}$ cm^{-3}) rises slightly, from approximately 7.57 at 3 mbar to 9.42 at 9 mbar. At high pressure (1000 mbar), there is a sharp rise to 5.8 ($\times 10^{22}$ cm^{-3}) for a spot size of 100 μm. For spot sizes of 168 and 420 μm, the electron densities decrease by 0.77 and 0.65 folds for 3 mbar, 0.68 and 0.58 folds for 9 mbar, and 0.82 and 0.66 folds for 1000 mbar, respectively. For a spot size of 100 μm at 5 ns, the ion number density ($\times 10^{21}$ cm^{-3}) is approximately 5.71 at 3 mbar, 5.96 at 9 mbar, and 2.93 ($\times 10^{22}$ cm^{-3}) at 1000 mbar. With a spot size diameter of 168 μm, the ion number density at 5 ns decreases by 0.81, 0.88, and 0.89 folds for 3, 9, and 1000 mbar, respectively. Similarly, for a spot size of 420 μm, the ion number density decreases by 0.55, 0.82, and 0.67 folds for 3, 9, and 1000 mbar, respectively.

At the lower pressure of the Martian atmosphere, the impact of pressure on the ion number density is less significant compared to its effect on electron number density.[62] For Earth's atmosphere, both electron and ion number densities significantly increase due to the high ionization process in the plasma, generating additional free electrons and ions.[63] Upon deactivation of the laser at 20 ns, a significant exponential decrease in electron number density is observed. This decline is marked by a rapid reduction in the number of electrons within the system. As the simulation progresses, the density gradually diminishes, reaching its minimum values at later time points, specifically at 500 and 1000 ns.

Fluid Velocity. In Figure 4, subpanels 13–15 show the variation in plasma velocity with different laser spot sizes (100, 168, and 420 μm) under various CO_2 pressures ranging from 3 to 9 mbar and at 1000 mbar. Measurements were taken at intervals from 5 to 1000 ns. The results indicate a compelling correlation between fluid velocity and spot size during the initial laser activation (5–10 ns). Notably, as the spot size decreases, the fluid velocity increases, with maximum values achieved at these specific activation times.

The average velocity of plasma expansion in CO_2 peaks when the ambient pressure is 3 mbar at 10 ns. At this pressure, there is a significant rise in velocity from approximately 1.8×10^6 cm s^{-1} for a spot size of 420 μm to 2.69×10^6 cm s^{-1} and 6.1×10^6 cm

s^{-1} for spot sizes of 168 μm and 100 μm, respectively. When the ambient pressure increases to 9 mbar, the velocity increases by factors of 1.40 for a spot size of 168 μm and 3.76 for a spot size of 100 μm.

The decrease in laser spot size results in increased laser irradiance, which facilitates a more efficient transfer of energy to the plasma particles. This interaction enhances the plasma's thermal and ionization properties while also influencing its expansion dynamics. This behavior aligns with experimental observations of aluminum plasmas in the air at low ambient pressures,[64,65] and can be attributed to the deceleration of the expanding plume due to increased interactions with surrounding gas molecules.

Furthermore, at high pressure (1000 mbar), we observe a significant decrease in plasma velocity to approximately 0.14, 0.30, and 0.27 for spot sizes of 100, 168, and 420 μm, respectively. This effect is particularly evident in confined plasma by ambient gas situations, where increased pressure restricts the plasma's ability to flow at higher speeds. Upon the laser pulse turn-off (≥20 ns), the fluid velocity experiences a quasi-exponential decrease. Over time, the velocity gradually diminishes, ultimately reaching its minimum at the later time intervals of 500 and 1000 ns.

Effect of Ambiant Gases: He Versus CO_2

The surrounding gas plays a crucial role in the interaction between laser pulses and solid targets, especially in plasma formation. This section explores the influence of ambient gas composition on the evolution of graphite plasma under NLTE conditions. Simulations were conducted using He and CO_2 at the same pressure conditions. Figure 5 compares the plasma parameters, including electron and ion temperatures, densities, and fluid velocity, for both gases at pressures of 6 mbar (Mars-like) and 1000 mbar (Earth-like).

The simulations were performed for laser spot sizes of 100 μm with a laser irradiance of 25 GW cm^{-2} and 420 μm with a laser irradiance of 1.5 GW cm^{-2}. Our results were recorded at various simulation times: 5 ns and 10 ns during laser pulse activation, as well as 20–50 ns in 10 ns increments, and at 100, 200, 500, and 1000 ns after laser pulse deactivation. Each column in the figures details the results for both He and CO_2 gases under pressures of 6 and 1000 mbar for the two distinct spot sizes, 100 and 420 μm.

In Figure 5, subpanels 1–6 compare the effect of ambient gas composition (He and CO_2) on the variation of electron and ion temperature distributions at two different pressures, 6 and 1000 mbar, over time delays ranging from 5 to 1000 ns, with laser spot sizes of 100 and 420 μm, respectively. At both pressures, CO_2 has a more significant impact on the temperatures compared to He throughout all the simulation time steps refer to its ability to better confine and retain heat within the plasma due to its higher molecular mass and greater collision cross-section compared to He. Specifically, CO_2 molecules are more effective at colliding with plasma particles, transferring energy, and slowing down the expansion of the plasma plume. This results in higher temperatures being maintained for a longer duration, as the energy dissipation process is slower in CO_2.

Both electron and ion temperatures reach their peaks during the 5–10 ns laser pulse activation. At low pressure (6 mbar), the electron temperature varies from 187 821.6 K (under CO_2) and 98,153 K (under He) for a spot size of 100 μm to 30 260 K (under CO_2) and 22 181.3 K (under He) for a spot size of 420 μm. At high pressure (1000 mbar), the decrease factors are 1.5 and 1.8 for CO_2 and He, respectively, for a spot size of 100 μm. Similarly, the ion temperature varies from 185,120.7 K (under CO_2) and 96 335.4 K (under He) for a spot size of 100 μm to 25 897.3 K (under CO_2) and 20 538 K (under He) for a spot size of 420 μm at low pressure. At high pressure (1000 mbar), the electron and ion temperatures are nearly twofold lower in He than in CO_2. The primary reason is that CO_2 is denser, has a greater mass, and possesses a higher ionization potential compared to a He atmosphere.[66] It is important to note that CO_2 is denser only under the condition of equal pressure. This higher density leads to increased interactions with plasma particles, influencing the energy transfer and confinement within the plasma.

Additionally, the thermal characteristics of the ambient gas and the degrees of freedom associated with the diatomic molecules also play a significant role.[67] Furthermore, at an early delay time of 20 ns (after the laser is turned off), both the electron and ion temperatures continue to decrease exponentially over time, reaching a minimum at delay time steps of 500 and 1000 ns due to plasma expansion and the cooling effect of the background gas.

In both low (6 mbar) and high (1000 mbar) pressures, the electron and ion number densities are higher in a CO_2 atmosphere compared to a He atmosphere, as shown in Figure 5, subpanels 7–12. These results are attributed to the higher mass density and ionization potential of CO_2 ambient gas compared to He.[68] It is evident that there is a mixture between the graphite target and ambient atmospheres of CO_2 and He. The electron and ion number densities peak at 5 ns, reaching 9.2×10^{20} cm^{-3} and 2.7×10^{20} cm^{-3} under ambient He gas and 8.6×10^{21} cm^{-3} and 5.8×10^{21} cm^{-3} under CO_2 gas, for a laser spot size of 100 μm and pressure of 6 mbar. For a spot size of 420 μm, both electron and ion densities decrease by a factor of approximately 3 and 2 under He and CO_2 background gases, respectively.

This corresponds to roughly a fivefold increase at a pressure of 1000 mbar for both electron and ion number densities due to the higher number of collisions with background gases and reduced mean free path.[69] The densities exhibit an exponential decrease over time (>10 ns) due to cooling from background gases and plasma confinement.

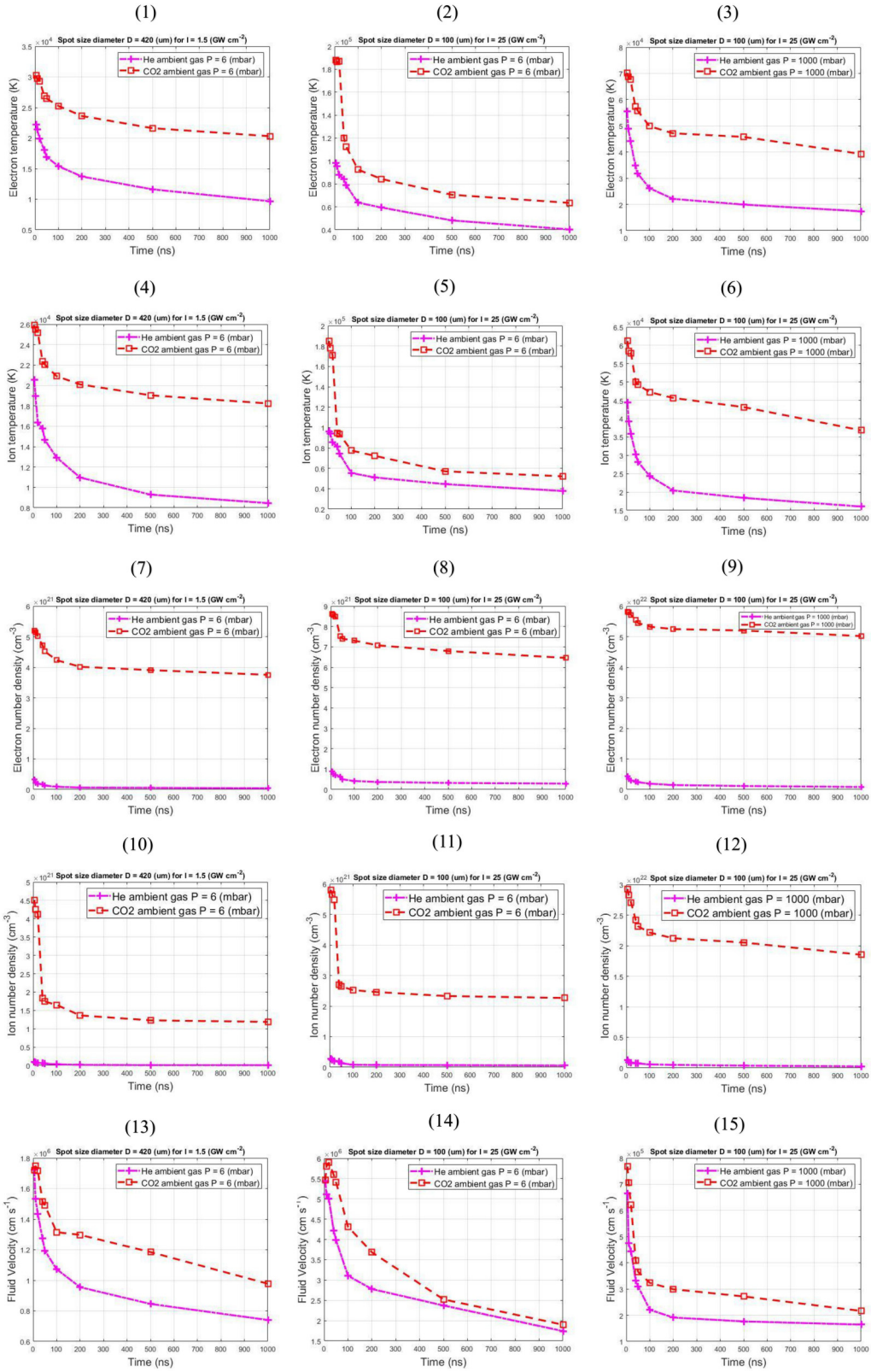

Figure 5. Variation of the electron temperature (first row), ion temperature (second row), electron density (third row), ion density (fourth row), and fluid velocity (fifth row) with time and spot sizes (100 and 420 μm). Calculations are for different ambient gas compositions: He (magenta line) and CO_2 (red line) under two pressures, 6 mbar (1st and 2nd columns) and 1000 mbar (third column). Subpanels 1–15 represent individual cases.

Intriguingly, in our simulation, the dynamic motion of fluid within the plasma is meticulously scrutinized, allowing us to extract insights into fluid velocity patterns under different ambient gases, He and CO_2, as shown in Figure 5, subpanels 13–15. These patterns underline the essence of plasma motion. Overall, the fluid velocity under a He atmosphere is lower compared to a CO_2 atmosphere, especially in the early time frame (5–10 ns). This can be attributed to the slowing down of the expanding plasma plume by the increased ambient species in CO_2 compared to He.[70] The maximum velocity at the 10 ns time step for both laser spot sizes (100 and 420 μm) increases slightly from 5.4×10^6 cm s^{-1} and 1.7×10^6 cm s^{-1} under low He pressure to 5.8×10^6 cm s^{-1} and 1.75×10^6 cm s^{-1} under low CO_2 pressure, followed by a quasi-exponential decrease after the laser is deactivated (>10 ns), reaching a minimum at delay times of 500 and 1000 ns. Increasing the background gas pressure to 1000 mbar leads to an overall decrease in velocity by a factor of 7 due to the confinement effect of the plasma.

Effect of Focusing Diameter for Fixed Laser Irradiance

In planetary LIBS applications, constant irradiance is a rare scenario, as laser irradiance typically varies due to factors such as changes in distance, atmospheric conditions, and target surface irregularities. In this study, we investigate the constant irradiance condition to isolate the effects of focusing diameter on plasma formation and dynamics. By controlling irradiance, we can focus on how variations in spot size affect energy deposition and plasma behavior, particularly in a CO_2 rich environment such as Mars. The interaction between the laser waist structure and the resulting plasma plume, influencing energy absorption, plasma confinement, and expansion, offers insights into optimizing LIBS measurements under planetary conditions.

The plasma parameters produced by a nanosecond laser are significantly influenced by laser irradiance and focusing diameter on a graphite target. Increasing the focusing diameter enhances energy transfer to the target, resulting in plasma expansion toward the incident radiation due to additional heating effects from the nanosecond lasers.[71,72] Figures 6 to 8 demonstrate the variations in electron and ion temperatures, number densities, and fluid velocity distributions in response to laser irradiances of 25 and 9 GW cm^{-2} across different focusing diameters (100, 168, and 420 μm) at both low and high CO_2 pressures.

The evolution of the simulated plasma was monitored at intervals of 5–10 ns (laser-activated) to 20–1000 ns (laser deactivated). Each row details the results for a specific laser irradiance (9 and 25 GW cm^{-2}) across different laser spot sizes (100, 168, and 420 μm) under CO_2 pressures of 3, 9, and 1000 mbar.

Electron and Ion Temperatures. At both irradiance levels of 9 and 25 GW cm^{-2}, the electron and ion temperatures increase significantly with expanding spot size, as shown in Figure 6, subpanels (1–12). For 9 GW cm^{-2} at low pressures (3–9 mbar) and during the laser's active phase (5–10 ns), electron and ion temperatures rise from approximately 5.0×10^4 K and 4.7×10^5 K for a 100 μm spot size to 9.0×10^5 K and 8.0×10^5 K for a 420 μm spot size. At 25 GW cm^{-2} with a 100 μm spot size, the temperatures reach 1.87×10^5 K and 1.86×10^5 K, increasing by factors of 1.4 and 1.7 for spot sizes of 168 and 420 μm, respectively. At high pressure (1000 mbar), both temperatures decrease by factors of approximately 3.7 and 3.9 for all spot sizes.

As the laser irradiance increases, the electrons and ions absorb more energy from the laser photons,[73] leading to an increase in their kinetic energy and, consequently, higher temperatures. Following the cessation of laser activity, typically at 20 ns, there is a marked exponential decline in these temperatures at delay times of 500 and 1000 ns in the plasma evolution.

Electron and Ion Densities. In Figure 7, subpanels 1–12 display the distributions of electron and ion number densities in the plume over time. At constant laser irradiance, significant increases in densities are observed with larger spot sizes, particularly during the active laser phase (5–10 ns). For a laser irradiance of 9 GW cm^{-2} at 5 ns, maximum electron and ion densities range from approximately 4×10^{21} cm^{-3} and 3×10^{21} cm^{-3} for a 100 μm spot size to 8×10^{22} cm^{-3} and 6×10^{22} cm^{-3} for a 420 μm spot size. When the irradiance increases to 25 GW cm^{-2} with a 100 μm spot size, the densities reach around 8×10^{21} cm^{-3} and 6×10^{21} cm^{-3}, increasing by factors of 2.9 and 4.2 for 168 μm and 420 μm spot sizes, respectively, at low pressure.

At higher pressures (1000 mbar), the number densities at the three spot sizes increase by factors of approximately 10 for electrons and 15 for ions. Larger spot sizes can lead to greater energy absorption by the graphite target, which in turn leads to more energy being transformed into plasma particles through ionization and recombination processes,[74] thereby contributing to higher number densities of electrons in the system. As time progresses in the simulation, the density gradually diminishes exponentially, eventually reaching its minimum value at the delay time points of the simulation, specifically at 500 and 1000 ns.

Fluid Velocity. The fluid velocity distribution as a function of laser irradiance and spot size is shown in Figure 8, subpanels (1–6). The results indicate a compelling correlation between fluid velocity and spot size during the laser activation at 5–10 ns. Notably, at low pressure, as the spot size increases, the fluid velocity clearly increases from 2.3, 2.6, to 3.5 (x10^{6}cm s^{-1}) for spot sizes of 100, 168, and 420 μm, respectively, at a laser irradiance of 9 GW cm^{-2}. As the laser irradiance rises to 25 GW cm^{-2}, the velocity is 5.4 (×10^6 cm s^{-1}), increasing

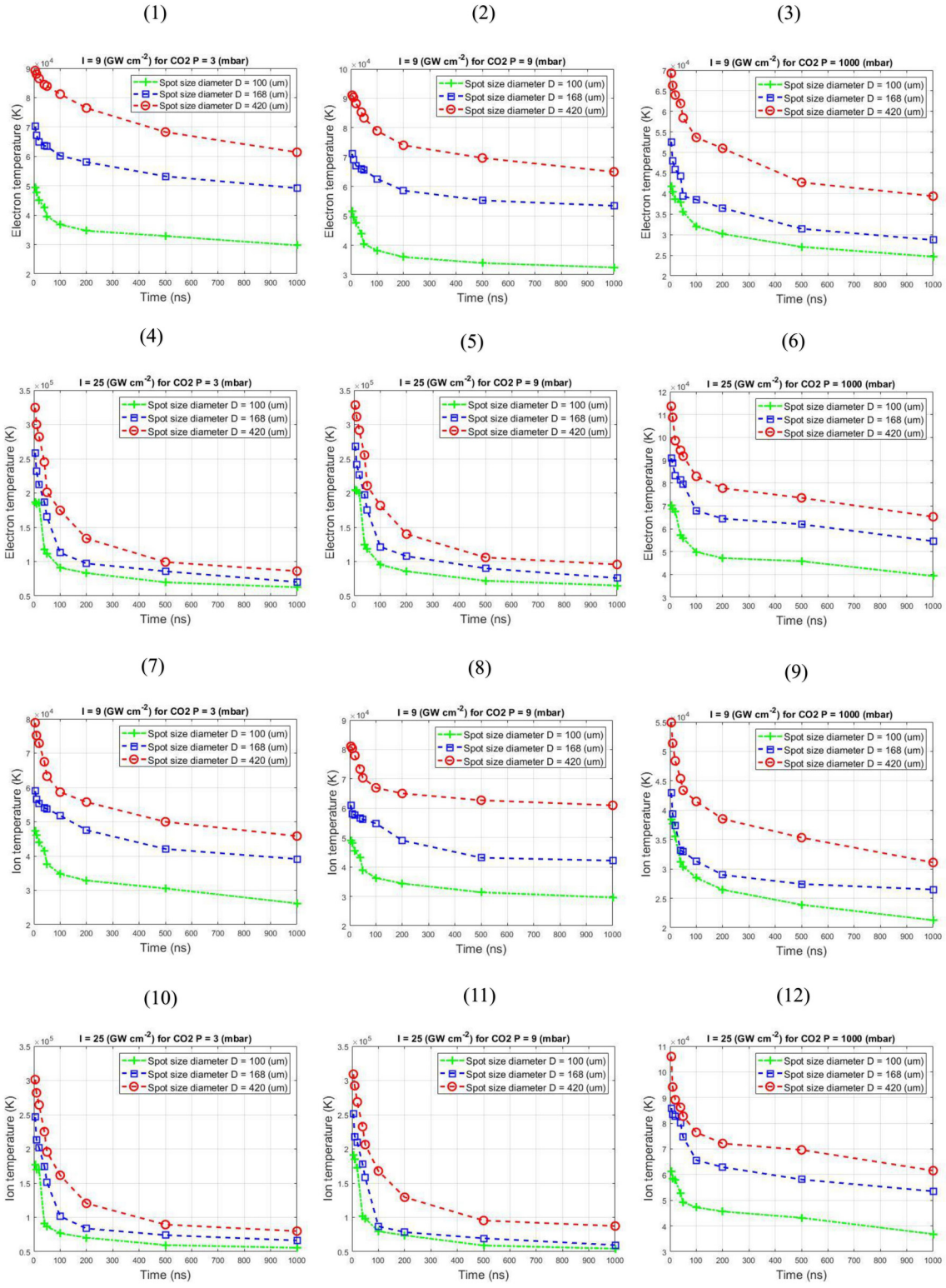

Figure 6. Variation of the electron temperature (first and second rows) and ion temperature (third and fourth rows) with time and laser irradiances 9 GW cm^{-2} (first and third rows) and 25 GW cm^{-2} (second and fourth rows). Calculated for different focusing diameters: 100 μm (green line), 168 μm (blue line), and 420 μm (red line) under three CO_2 pressures: 3 mbar (first column), 9 mbar (second column), and 1000 mbar (third column). Subpanels 1–12 represent individual cases.

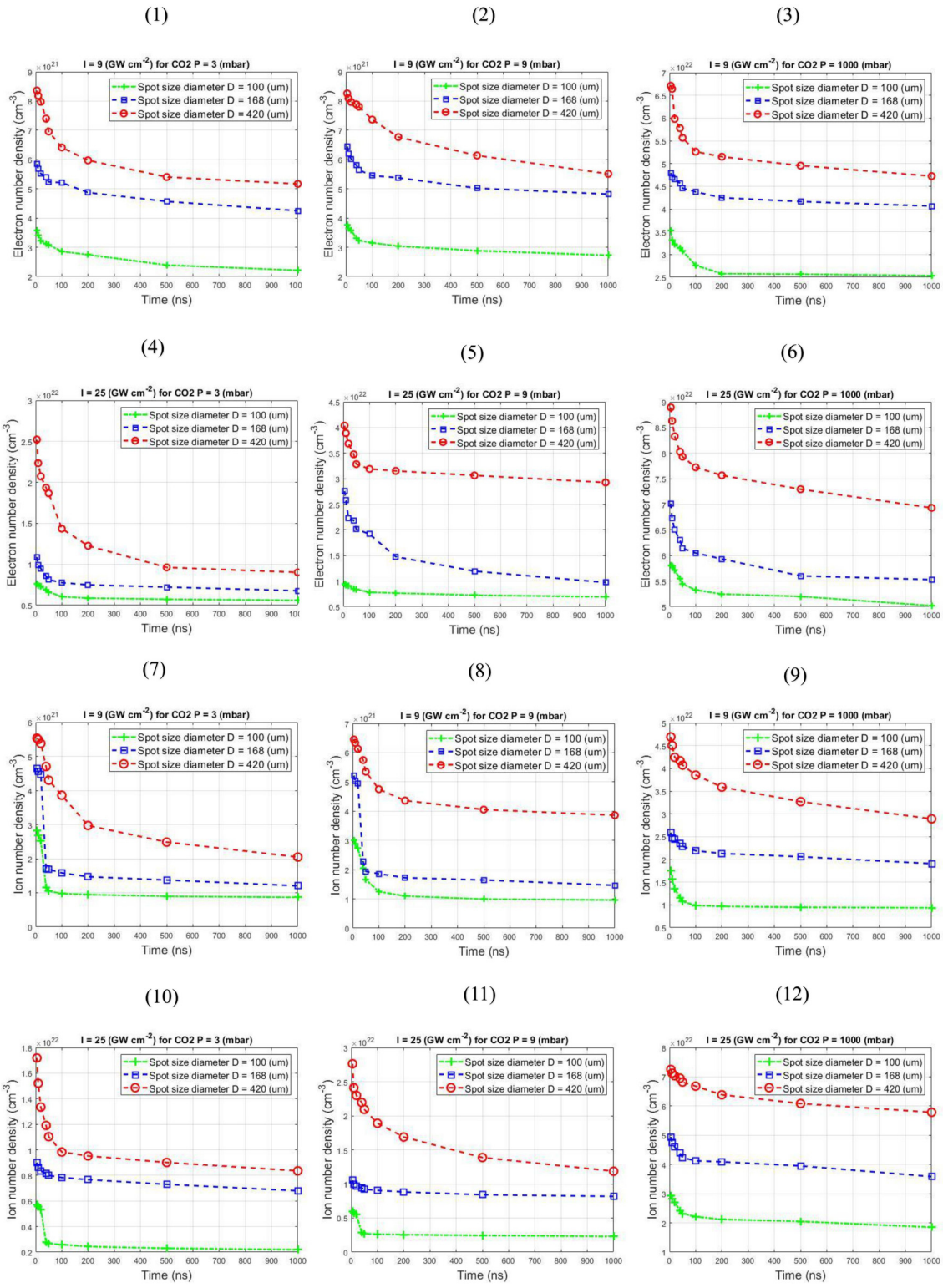

Figure 7. Variation of the electron number density (first and second rows) and ion number density (third and fourth rows) with time and laser irradiances 9 GW cm^{-2} (first and third rows) and 25 GW cm^{-2} (second and fourth rows). Calculated for different focusing diameters: 100 μm (green line), 168 μm (blue line), and 420 μm (red line) under three CO_2 pressures: 3 mbar (first column), 9 mbar (second column), and 1000 mbar (third column). Subpanels 1–12 represent individual cases.

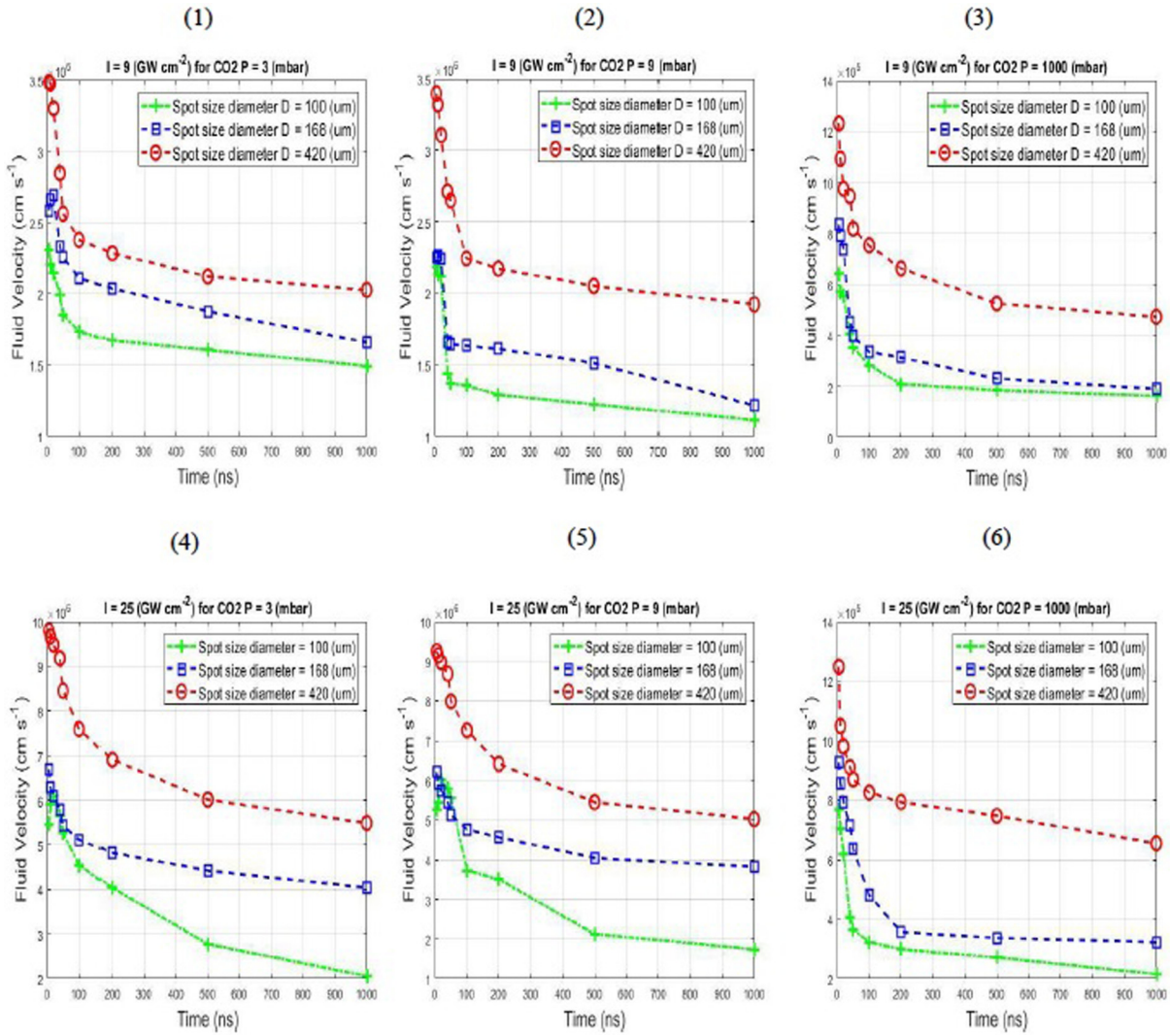

Figure 8. Variation of the fluid velocity (fifth and sixth rows) with time and laser irradiances 9 GW cm^{-2} (fifth row) and 25 GW cm^{-2} (six row). Calculated for different focusing diameters: 100 μm (green line), 168 μm (blue line), and 420 μm (red line) under three CO_2 pressures: 3 mbar (first column), 9 mbar (second column), and 1000 mbar (third column). Subpanels 1–6 represent individual cases.

by factors of 1.24 and 1.82 for spot sizes of 168 and 420 μm, respectively.

This occurs because a larger spot size typically results in more energy being absorbed by the plasma, which can enhance the acceleration of plasma species and lead to higher velocities. At high pressure (1000 mbar), the velocities at 10 ns (laser activation phase) decrease by factors of approximately fourfold (9 GW cm^{-2}) and sixfold (25 GW cm^{-2}) for spot sizes of 100, 168, and 420 μm, respectively. This is because ambient high-pressure gas can decelerate the rapid movement of plasma species. Upon the first 20 ns after the laser pulse, the fluid velocity experiences a quasi-exponential decrease. Over time, for all laser spot sizes, the velocity gradually diminishes, ultimately reaching its minimum at early time intervals of 500 and 1000 ns due to equilibration processes where the plasma loses energy to the surrounding gas.

Our results demonstrate that varying laser focusing conditions significantly influence the fundamental LIBS plasma properties for graphite targets. Focusing lenses with different focal numbers create distinct energy density distributions at the sample surface, which, in turn, determine the intensity and characteristics of the spectral lines. These findings align with the work of Surmick et al.,[16] who explored the impact of geometric factors on LIBS plasma formation for various metals under both Earth and simulated Martian conditions. Their results revealed notable differences in the spatial distribution of ionic and atomic peak emissions based on the lens-to-sample distance.

Our research extends these insights to the behavior of graphite in He and CO_2 atmospheres at various pressures, examining both the early and later stages of plasma evolution. Specifically, we investigate how the composition of the

ambient gas affects plasma plume expansion, finding that the plume is more pronounced in low-density He compared to high-density CO_2 as the background gas.[51] The emission intensity is significantly enhanced in CO_2 as the ambient gas compared to He. This enhancement is attributed to CO_2 relatively low ionization potential, higher mass density, and active chemical reactions.[75,76] Furthermore, we found that a deeper laser focus in CO_2 creates a high-temperature and high-density region in the plasma, leading to stronger atomic emissions, while a shallower focus promotes more pronounced ionic emissions. Additionally, the spectral lines may exhibit less broadening due to reduced electron densities compared to those observed with a deeper focus.

To provide a more comprehensive analysis of LIBS under Martian conditions, we explored the effects of varying ambient gas pressures. Our findings indicate that focusing effects have a greater impact on the qualitative aspects of plume expansion dynamics than ambient pressure, particularly when the laser is activated. This influence is primarily on the spatial profile and initial energy distribution in the plasma, rather than the absolute magnitudes of plasma parameters such as electron and ion densities. While pressure variations lead to more significant quantitative changes in these densities, variations in focal spot size indirectly shape plume morphology and overall plasma expansion effects that are especially pronounced in low-density environments such as Mars.

These distinctions are highly relevant to in situ LIBS elemental analysis on Mars, where both focusing and ambient gas composition are crucial in shaping LIBS signals. Mars predominantly CO_2 atmosphere affects plasma formation and signal strength, as its composition and pressure impact electron and ion interactions, thereby influencing spectral emission lines. This dual influence of focusing and pressure forms a basis for optimizing LIBS analyses on Mars by adjusting focal settings to account for its unique atmosphere, yielding more accurate and consistent spectral signatures.

Conclusion

We investigated the focusing effect on the laser-induced breakdown of graphite under both He and CO_2 ambient conditions using a three-temperature Eulerian radiation model with an NLTE approach to simulate LIBS plasma parameters. Our simulations encompassed all relevant physical processes, including laser ablation, plasma formation, shockwave propagation within the surrounding gas, and subsequent plasma cooling. We accounted for the interactions between the plasma and the ambient gases, including radiation emission and absorption. Our study explored the effects of Martian (3 to 9 mbar) and Earth-like (1000 mbar) pressures, as well as ambient gas composition, on plasma parameters. We also examined how variations in laser waist sizes and irradiances impact electron and ion temperatures and densities.

Our findings indicate that the dynamics and properties of LIBS-generated graphite plasma are highly sensitive to changes in laser focusing conditions, which significantly impact electron and ion temperatures as well as fluid velocity. Furthermore, increasing the environmental pressure in CO_2 gas, compared to He gas, results in higher electron and ion densities and reduced temperatures. Under these high-pressure CO_2 conditions, the plasma exhibits enhanced confinement, which significantly modifies the intensity and shape of the spectral peaks, thereby affecting the accuracy of plasma composition analysis.

However, it is essential to note that our simulations are constrained by certain limitations, such as the use of a single laser pulse and the relatively short simulation times for analyzing plasma evolution (up to 1 *upmus*). This limitation presents a challenge when considering real LIBS instruments, where the integration time is typically greater than 1 ms, allowing the plasma to continue evolving over longer periods. The implication for actual LIBS observations is that plasma parameters such as temperature and density, presented in our simulations, may change significantly beyond the timeframe we considered. As the plasma evolves beyond the first few microseconds, processes such as further cooling, expansion, and spectral shifts continue, which were not fully captured in our model. Expanding this limitation in future work would be beneficial to better align simulation results with experimental LIBS data, especially under planetary conditions.

Despite these limitations, the simulation approach adopted in this study provides valuable insights for optimizing LIBS analysis on Mars, where atmospheric conditions differ significantly from those on Earth. Our findings suggest specific strategies for improving the precision of elemental analysis using instruments such as ChemCam and SuperCam by selecting optimal focusing conditions and understanding the gas–plasma interactions that influence spectral emissions under Martian-like environments.

Declaration of Conflicting Interests

The authors declared no potential conflicts of interest with respect to the research, authorship, and/or publication of this article.

Funding

The authors received no financial support for the research, authorship, and/or publication of this article.

ORCID iDs

Kouider Benbaier https://orcid.org/0000-0001-8862-9353
Zeyneb Bedrane https://orcid.org/0000-0002-8375-4232
Noureddine Melikechi https://orcid.org/0000-0001-5392-9225

References

1. R. Noll, R. Noll. Handbook of Laser-Induced Breakdown Spectroscopy. Berlin: Springer, 2012.

2. D.W. Hahn, N. Omenetto. "Laser-Induced Breakdown Spectroscopy (LIBS), Part II: Review of Instrumental and Methodological Approaches to Material Analysis and Applications to Different Fields". Appl. Spectrosc. 2012. 66 (4): 347–419.
3. Y. Markushin, P. Sivakumar, D. Connolly, N. Melikechi. "Tag-Femtosecond Laser-Induced Breakdown Spectroscopy for the Sensitive Detection of Cancer Antigen 125 in Blood Plasma". Anal. Bioanal. Chem. 2015. 407: 1849–1855. 10.1007/s00216-014-8433-0
4. N. Melikechi, Y. Markushin, D.C. Connolly, J. Lasue, E. Ewusi-Annan, et al. "Age-Specific Discrimination of Blood Plasma Samples of Healthy and Ovarian Cancer Prone Mice Using Laser-Induced Breakdown Spectroscopy". Spectrochim. Acta, Part B. 2016. 123: 33–41.
5. P. Pořízka, P. Modlitbová, N. Melikechi, J. Kaiser. "Laser-Ablation Spectroscopy for Imaging of Tumor Markers and Nanoparticle Labels". In: Optical Spectroscopy and Imaging for Cancer Diagnostics: Fundamentals, Progress, and Challenges. N. Melikechi, editors. New Jersey: World Scientific Publishing, 2023. Pp. 181–206. 10.1142/9789811258961_0007.
6. S.J. Rehse, H. Salimnia, A.W. Miziolek. "Laser-Induced Breakdown Spectroscopy (LIBS): An Overview of Recent Progress and Future Potential for Biomedical Applications". J. Med. Eng. Technol. 2012. 36(2): 77–89. 10.3109/03091902.2011.645946
7. Limbeck A., L. Brunnbauer, H. Lohninger, P. Pořízka, P. Modlitbová, et al. "Methodology and Applications of Elemental Mapping by Laser-Induced Breakdown Spectroscopy". Anal. Chim. Acta. 2021. 1147: 72–98.
8. Markiewicz-Keszycka M., X. Cama-Moncunill, M.P. Casado-Gavalda, Y. Dixit et al. "Laser-Induced Breakdown Spectroscopy (LIBS) for Food Analysis: A Review". Trends Food Sci. Technol. 2017. 65: 80–93. 10.1016/j.tifs.2017.05.005
9. H.B. Andrews, M.Z. Martin, A.M. Wymore, U.C. Kalluri. "Rapid In Situ Nutrient Element Distribution in Plants and Soils Using Laser-Induced Breakdown Spectroscopy (LIBS)". Plant Soil. 2023. 495(2): 1–10. 10.1007/s11104-023-05988-7
10. D. Díaz, D.W. Hahn, A. Molina. "Evaluation of Laser-Induced Breakdown Spectroscopy (LIBS) as a Measurement Technique for Evaluation of Total Elemental Concentration in Soils". Appl. Spectrosc. 2012. 66(1): 99–106. 10.1366/11-06349
11. P. Paris, J. Butikova, M. Laan, M. Aints, et al. "Detection of Deuterium Retention by LIBS at Different Background Pressures". Phys. Scr. 2017. 2017: 014003. 10.1088/0031-8949/2017/T170/014003
12. Y. Markushin, A. Marcano, S. Rock, N. Melikechi. "Determination of Protein Hydrogen Composition by Laser-Induced Breakdown Spectroscopy". J. Anal. At. Spectrom. 2010. 25(2): 148–149.
13. R.C. Wiens, X. Wan, J. Lasue, S. Maurice. "Laser-Induced Breakdown Spectroscopy in Planetary Science". In: J.P. Singh, S.N. Thakur, editors. Laser-Induced Breakdown Spectroscopy. Amsterdam: Elsevier, 2020. Chap. 20, Pp. 441–471.
14. B. Sallé, D.A. Cremers, S. Maurice, R.C. Wiens. "Laser-Induced Breakdown Spectroscopy for Space Exploration Applications: Influence of the Ambient Pressure on the Calibration Curves Prepared From Soil and Clay Samples". Spectrochim. Acta, Part B. 2005. 60(4): 479–490. 10.1016/j.sab.2005.02.009
15. J. Wang, X. Li, H. Li, X. Li, Z. Li. "Lens-to-Sample Distance Effect on the Quantitative Analysis of Steel by Laser-Induced Breakdown Spectroscopy". J. Phys. D: Appl. Phys. 2020. 53 (25): 255203. 10.1088/1361-6463/ab7f74
16. D.M. Surmick, L. Taleh, N. Melikechi. "Effects of Laser Beam Focusing Characteristics on Laser-Induced Breakdown Spectra". Appl. Spectrosc. 2021. 75(2): 127–136.
17. H. Hou, Y. Li, Y. Tian, Z. Yu, R. Zheng. "Plasma Condensation Effect Induced by Ambient Pressure in Laser-Induced Breakdown Spectroscopy". Appl. Phys. Express. 2014. 7(3): 032402. 10.7567/APEX.7.032402
18. R.C. Wiens, S. Maurice, B. Barraclough, M. Saccoccio, et al. "The ChemCam Instrument Suite on the Mars Science Laboratory (MSL) Rover: Body Unit and Combined System Tests". Space Sci. Rev. 2012. 170(1): 167–227.
19. R.C. Wiens, S. Maurice, S.H. Robinson, A.E. Nelson, et al. "The SuperCam Instrument Suite on the NASA Mars 2020 Rover: Body Unit and Combined System Tests". Space Sci. Rev. 2021. 217: 4. 10.1007/s11214-020-00777
20. N. Melikechi, A. Mezzacappa, A. Cousin, N.L. Lanza, et al. "Correcting for Variable Laser–Target Distances of Laser-Induced Breakdown Spectroscopy Measurements With ChemCam Using Emission Lines of Martian Dust Spectra". Spectrochim. Acta B. 2014. 96: 51–60. 10.1016/j.sab.2014.04.004
21. Mezzacappa A., N. Melikechi, A. Cousin, R.C. Wiens, et al. "Application of Distance Correction to ChemCam Laser-Induced Breakdown Spectroscopy Measurements". Spectrochim. Acta, Part B. 2016. 120: 19–29. 10.1016/j.sab.2016.03.009
22. J. Lasue, A. Cousin, P.-Y. Meslin, N. Mangold, et al. "Martian Eolian Dust Probed by ChemCam". Geophys. Res. Lett. 2018. 45(20): 10,968–10,977. 10.1029/2018GL079210
23. R.C. Wiens, A.J. Blazon-Brown, N. Melikechi, J. Frydenvang, et al. "Improving ChemCam LIBS Long-Distance Elemental Compositions Using Empirical Abundance Trends". Spectrochim. Acta, Part B. 2021. 182: 106247. 10.1016/j.sab.2021.106247
24. E. Ewusi-Annan, D.M. Surmick, N. Melikechi, R.C. Wiens. "Simulated Laser-Induced Breakdown Spectra of Graphite and Synthetic Shergottite Glass Under Martian Conditions". Spectrochim. Acta, Part B. 2018. 148: 31–43. 10.1016/j.sab.2018.06.006
25. F. Liang, J. Wang, X. Fu, H. Wang. "Characteristics of Laser-Induced Steel Plasmas Generated With Different Focusing Conditions". Appl. Opt. 2023. 62: 6350–6357.
26. Q. Wang, A. Chen, Y. Liu, S. Li, M. Jin. "Comparison of Emission Signals for Femtosecond and Nanosecond Laser-Ablated Cu Plasmas by Changing the Distance from Focusing Lens to Target Surface at Different Target Temperatures". Spectrochim. Acta, Part B. 2021. 185: 106302.
27. P.B. Hansen, S. Schröder, S. Kubitza, K. Rammelkamp, et al. "Modeling of Time-Resolved LIBS Spectra Obtained in Martian Atmospheric Conditions with a Stationary Plasma Approach". Spectrochim. Acta, Part B. 2021. 178: 106115.
28. G. Cristoforetti, A. De Giacomo, M. Dell'Aglio, S. Legnaioli, et al. "Local Thermodynamic Equilibrium in Laser-Induced

Breakdown Spectroscopy: Beyond the McWhirter Criterion". Spectrochim. Acta, Part B. 2010. 65(1): 86–95.
29. A. Alberti, C. Munafò, M. Koll, M. Nishihara, et al. "Laser-Induced Non-Equilibrium Plasma Kernel Dynamics". J. Phys. D: Appl. Phys. 2020. 53(2): 025201. 10.1088/1361-6463/ab5409
30. Glumac N.G., G.S. Elliott. "The Effect of Ambient Pressure on Laser-Induced Plasmas in Air". Opt. Lasers Eng. 2007. 45: 27–35.
31. Z. Chen, Z. Chen, W. Jiang, L. Guo, et al. "Line Intensity Calculation of Laser-Induced Breakdown Spectroscopy During Plasma Expansion in Nonlocal Thermodynamic Equilibrium". Opt. Lett. 2023. 48(12): 3227–3230. 10.1364/OL.488250.
32. J.J. Macfarlane, I. Golovkin, P. Woodruff. "HELIOS-CR – A 1-D Radiation-Magnetohydrodynamics Code with Inline Atomic Kinetics Modeling". J. Quant. Spectrosc. Radiat. Transf. 2006. 99(1–3): 381–397.
33. D. Mihalas, B.W. Mihalas. Foundations of Radiation Hydrodynamics. New York: Oxford University Press, 1984.
34. J.I. Castor. Radiation Hydrodynamics. Cambridge: Cambridge University Press, 2004.
35. F. Rezaei, S.H. Tavassoli. "Numerical and Experimental Investigation of Laser Induced Plasma Spectrum of Aluminum in the Presence of a Noble Gas". Spectrochim. Acta, Part B. 2012. 78: 29–36.
36. S.S. Harilal, G.V. Miloshevsky, P.K. Diwakar, N.L. LaHaye, et al. "Experimental and Computational Study of Complex Shockwave Dynamics in Laser Ablation Plumes in Argon Atmosphere". Phys. Plasmas. 2012. 19: 083504.
37. The Flash Center for Computational Science. "FLASH User's Guide Version-4.6.2". New York: University of Rochester, 2019.
38. C. Orban, M. Fatenejad, S. Chawla, S. Wilks, et al. "A Radiation-Hydrodynamics Code Comparison for Laser-Produced Plasmas: FLASH Versus HYDRA and the Results of Validation Experiments". ArXiv. 2013. 7: 636375 10.48550/arXiv.1306.1584
39. D. Lee. "A Solution Accurate, Efficient and Stable Unsplit Staggered Mesh Scheme for Three Dimensional Magnetohydrodynamics". J. Comput. Phys. 2013. 243: 269.
40. S. Li. "An HLLC Riemann Solver for Magneto-Hydrodynamics". J. Comput. Phys. 2005. 203: 344. 10.1016/j.jcp.2004.08.020
41. T.B. Kaiser. "Laser Ray Tracing and Power Deposition on an Unstructured Three-Dimensional Grid". Phys. Rev. E. 2000. 61: 895–905.
42. M.J. Turk, B.D. Smith, J.S. Oishi, S. Skory, et al. "yt: A Multi-Code Analysis Toolkit for Astrophysical Simulation Data". Astrophys. J. Suppl. Ser. 2011. 192: 9. http://yt.enzotools.org/ [accessed Dec 20 2024].
43. MacFarlane J.J.. "IONMIX: A Code for Computing the Equation of State and Radiative Properties of LTE and Non-LTE Plasmas". Comput. Phys. Commun. 1989. 56: 259–278.
44. P. Tzeferacos, M. Fatenejad, N. Flocke, C. Graziani, et al. "FLASH MHD Simulations of Experiments that Study Shock-Generated Magnetic Fields". High Energy Density Phys. 2015. 17(Part A): 24.
45. A. Kramida, Yu. Ralchenko, J. Reader, NIST ASD Team. "NIST Atomic Spectra Database (ver. 5.9)". https://www.nist.gov/pml/atomic-spectra-database [accessed Oct 30 2021].
46. A. Cousin, O. Forni, S. Maurice, O. Gasnault, et al. "Laser Induced Breakdown Spectroscopy Library for the Martian Environment". Spectrochim. Acta, Part B. 2011. 66(11–12): 805–814.
47. S. Schröder, S.G. Pavlov, I. Rauschenbach, E.K. Jessberger, et al. "Detection and Identification of Salts and Frozen Salt Solutions Combining Laser-Induced Breakdown Spectroscopy and Multivariate Analysis Methods: A Study for Future Martian Exploration". Icarus. 2013. 223(1): 61–73. 10.1016/j.icarus.2012.11.011
48. P. Tzeferacos, M. Fatenejad, N. Flocke, G. Gregori, et al. "FLASH Magnetohydrodynamic Simulations of Shock-Generated Magnetic Field Experiments". High Energy Density Phys. 2012. 8: 322–328.
49. W. Fu, E.P. Liang, M. Fatenejad, D.Q. Lamb, et al. "Increase of the Density, Temperature and Velocity of Plasma Jets Driven by a Ring of High Energy Laser Beams". High Energy Density Phys. 2013. 9: 336–340.
50. M. Masnavi, H. Parchamy. "Calculation of the Extreme-Ultraviolet Radiation Conversion Efficiency for a Laser-Produced Tin Plasma Source". Phys. Open. 2019. 1: 100003. 10.1016/j.physo.2019.100003
51. S.S. Harilal, C.V. Bindhu, M.S. Tillack, F. Najmabadi, et al. "Internal Structure and Expansion Dynamics of Laser Ablation Plumes Into Ambient Gases". J. Appl. Phys. 2003. 93: 2380. 10.1063/1.1544070
52. H.C. Le, D.E. Zeitoun, J.D. Parisse. "Modeling of Gas Dynamics for a Laser-Generated Plasma: Propagation into Low-Pressure Gases". Phys. Rev. E. 2000. 62: 4152. 10.1103/PhysRevE.62.4152
53. M.S. Dawood, J. Margot. "Effect of Ambient Gas Pressure and Nature on the Temporal Evolution of Aluminum Laser-Induced Plasmas". AIP Adv. 2014. 4: 037111. 10.1063/1.4869076
54. E. Vors, C. Gallou, L. Salmon. "Laser-Induced Breakdown Spectroscopy of Carbon in Helium and Nitrogen at High Pressure". Spectrochim. Acta, Part A. 2008. 63(10): 1198–1204.
55. S.S. Harilal, C.V. Bindhu, R.C. Issac, V.P.N. Nampoori, et al. "Electron Density and Temperature Measurements in a Laser Produced Carbon Plasma". J. Appl. Phys. 1997. 82: 2140.
56. J. Stetzler, S. Tang, R.C Chinni. "Plasma Temperature and Electron Density Determination Using Laser-Induced Breakdown Spectroscopy (LIBS) in Earth's and Mars's Atmospheres". Atoms. 2020. 8(3): 50. 10.3390/atoms8030050
57. P.B. Hansen, S. Schroder, S. Kubitza, K. Rammelkamp, D.S. Vogt, et al. "Modeling of Time-Resolved LIBS Spectra Obtained in Martian Atmospheric Conditions with a Stationary Plasma Approach". Spectrochim. Acta, Part B. 2021. 178: 106.
58. J. Szilagyi, H. Parchamy, M. Masnavi, M. Richardson. "Spectral Irradiance of Singly and Doubly Ionized Zinc in Low-Intensity Laser-Plasma Ultraviolet Light Sources". J. Appl. Phys. 2017. 121: 033303. 10.1063/1.4973848
59. M. Masnavi, M. Richardson. "Spectroscopic Studies of Laser-Based Far-Ultraviolet Plasma Light Source". Appl. Sci. 2021. 11(15): 6919. 10.3390/app11156919
60. A.K. Sharma, R.K. Thareja. "Plume Dynamics of Laser-Producing Aluminum Plasma in Ambient Nitrogen". Appl. Surf. Sci. 2005. 243: 68–75. 10.1016/j.apsusc.2004.09.093
61. H. Parchamy, J. John Szilagyi, M. Masnavi, M. Richardson. "Quantitative Analysis of Vacuum-Ultraviolet Radiation from Nanosecond Laser-Zinc Interaction". Opt. Laser Technol. 2018. 103: 1–7. 10.1016/j.optlastec.2018.01.006

62. Z. Chen, D. Bleiner, A. Bogaerts. "Effect of Ambient Pressure on Laser Ablation and Plume Expansion Dynamics: A Numerical Simulation". J. Appl. Phys. 2006. 99(6): 063304.
63. J. Hermann, A. Lorusso, A. Perrone, F. Strafella, et al. "Simulation of Emission Spectra from Nonuniform Reactive Laser-Induced Plasmas". Phys. Rev. E: Stat. Phys., Plasmas, Fluids, Relat. Interdiscip. Top. 2015. 92: 5.
64. T.E. Itina, J. Hermann, P. Delaporte, M. Sentis. "Laser-Generated Plasma Plume Expansion: Combined Continuous-Microscopic Modeling". Phys. Rev. E: Stat. Phys., Plasmas, Fluids, Relat. Interdiscip. Top. 2002. 66: 066406.
65. S.S. Harilal, C.V. Bindhu, M.S. Tillack, F. Najmabadi, et al. "Internal Structure and Expansion Dynamics of Laser Ablation Plumes Into Ambient Gases". J. Appl. Phys. 2003. 93: 2380. 10.1063/1.1544070
66. S. Bashir, N. Farid, K. Mahmood, M.S Rafique. "Influence of Ambient Gas and Its Pressure on the Laser-induced Breakdown Spectroscopy and the Surface Morphology of Laser Ablated Cd". Appl. Phys. A. 2012. 107: 203. 10.1007/s00339-011-6730-4
67. Y. Iida. "Effects of Atmosphere on Laser Vaporization and Excitation Processes of Solid Samples". Spectrosc. Acta, Part B. 1990. 45: 1353. 10.1016/0584-8547(90)80188-O
68. Dawood M.S., J. Margot. "Effect of Ambient Gas Pressure and Nature on the Temporal Evolution of Aluminum Laser Induced Plasmas". AIP Adv. 2014. 4: 037111. 10.1063/1.4869076
69. S.A. Irimiciuc, B.C. Hodoroaba, G. Bulaic, S. Gurlui. "Multiple Structure Formation and Molecule Dynamics in Transient Plasmas Generated by Laser Ablation of Graphite". Spectrochim. Acta, Part B. 2020. 165: 105774. 10.1016/j.sab.2020.105774
70. Harilal S.S., B. O'Shay, Y. Tao, M.S Tillack. "Ambient Gas Effects on the Dynamics of Laser-Produced Tin Plume Expansion". J. Appl. Phys. 2006. 99: 083303. 10.1063/1.2188084
71. Li X., W. Wei, J. Wu, S. Jia, A. Qiu. "The Influence of Spot Size on the Expansion Dynamics of Nanosecond-Laser-Produced Copper Plasmas in Atmosphere". J. Appl. Phys. 2013. 113: 243304.
72. Martan J., J. Kunes, N. Semmar. "Experimental Mathematical Model of Nanosecond Laser Interaction with Material". Appl. Surf. Sci. 2006. 253(7): 3525–3532. 10.1016/j.apsusc.2006.07.059
73. J.F. Ready. Effect of High Power Laser Radiation. New York: Academic Press, 1971.
74. Pietanza L., G. Colonna, A.D. Giacomo, M. Capitelli. "Kinetic Processes for Laser Induced Plasma Diagnostic: A Collisional-Radiative Model Approach". Spectrochim. Acta, Part B. 2010. 65 (8): 616–626.
75. T. Delgado, L. García-Gómez, L.M. Cabalín, J.J Laserna. "Investigation on the Origin of Molecular Emissions in Laser-Induced Breakdown Spectroscopy Under Mars-Like Atmospheric Conditions of Isotope-Labeled Compounds of Interest in Astrobiology". Spectrochim. Acta, Part B. 2021. 179: 106114. 10.1016/j.sab.2020.106114
76. Dong M., J. Lu, S. Yao, Z. Zhong, J. Li, et al. "Experimental Study on the Characteristics of Molecular Emission Spectroscopy for the Analysis of Solid Materials Containing C and N". Opt. Express. 2011. 19(18): 17021–17029. 10.1364/OE.19.017021

Abstract

This thesis focuses on modeling Laser-Induced Breakdown Spectroscopy (LIBS) plasma under Martian conditions. The theoretical framework investigates the interaction of nanosecond laser pulses with a solid organic target (graphite) in a Martian-like environment, specifically involving carbon dioxide (CO_2) and helium (He) gases. A three-temperature (3T) Eulerian radiation model incorporating non-local thermodynamic equilibrium (NLTE) conditions is employed to capture the complex plasma dynamics during LIBS, taking into account the mixing between the expanding plasma plume and the surrounding gas. The study aims to provide a detailed understanding of laser ablation and plasma formation, with particular attention to the effects of laser irradiance and ambient gas pressure. The laser parameters used in the model replicate those of the ChemCam and SuperCam instruments. The work is limited to single-pulse excitation; post-ablation cavity effects are therefore not considered. Additionally, the thesis examines the impact of laser focusing conditions and ambient pressure ranging from 3 to 9 mbar (representative of Martian conditions) and up to 1000 mbar (Earth-like conditions) on key plasma parameters. The analysis is based on high-fidelity simulations performed using the open-source radiation-hydrodynamics code FLASH, which was used to calculate electron and ion temperatures, electron and ion number densities, and fluid velocities within the plasma.

Keywords: LIBS plasma, Martian conditions, 3T-NLTE Eurlian model, focusing laser conditions, ambient gas pressure.

Résumé

Cette thèse porte sur la modélisation du plasma par spectroscopie de claquage induit par laser (LIBS) en conditions martiennes. Le cadre théorique étudie l'interaction d'impulsions laser nanosecondes avec une cible organique solide (graphite) dans un environnement martien, impliquant spécifiquement des gaz de dioxyde de carbone (CO_2) et d'hélium (He). Un modèle de rayonnement eulérien à trois températures (3T) intégrant des conditions d'équilibre thermodynamique non local (NLTE) est utilisé pour capturer la dynamique complexe du plasma pendant la LIBS, en tenant compte du mélange entre le panache de plasma en expansion et le gaz environnant. L'étude vise à fournir une compréhension détaillée de l'ablation laser et de la formation du plasma, en accordant une attention particulière aux effets de l'irradiance laser et de la pression ambiante du gaz. Les paramètres laser utilisés dans le modèle reproduisent ceux des instruments ChemCam et SuperCam. Les travaux se limitent à l'excitation par impulsion unique ; les effets de cavité post-ablation ne sont donc pas pris en compte. De plus, la thèse examine l'impact des conditions de focalisation laser et d'une pression ambiante comprise entre 3 et 9 mbar (représentatives des conditions martiennes) et jusqu'à 1 000 mbar (conditions terrestres) sur les paramètres clés du plasma. L'analyse s'appuie sur des simulations haute- précision réalisées à l'aide du code open source de radiation-hydrodynamique FLASH, qui a permis de calculer les températures et les densités électroniques et ioniques, ainsi que les vitesses des fluides dans le plasma.

Mots-clés : Plasma LIBS, conditions martiennes, modèle Eulerian 3T-NLTE, conditions de focalisation laser, pression ambiante du gaz.

ملخص

تركز هذه الرسالة على نمذجة بلازما مطيافية الانهيار المُستحث بالليزر (LIBS) في ظل ظروف المريخ. يبحث الإطار النظري في تفاعل نبضات الليزر النانو ثانية مع هدف عضوي صلب (الجرافيت) في بيئة شبيهة ببيئة المريخ، وتحديدًا في غازي ثاني أكسيد الكربون (CO_2) والهيليوم (He). يُستخدم نموذج إشعاع أويلر ثلاثي درجات الحرارة (T3) يتضمن ظروف التوازن الديناميكي الحراري غير المحلي (NLTE) لالتقاط ديناميكيات البلازما المعقدة أثناء مطيافية الانهيار المُستحث بالليزر (LIBS)، مع مراعاة الاختلاط بين عمود البلازما المتمدد والغاز المحيط. تهدف الدراسة إلى توفير فهم مُفصل للاستئصال بالليزر وتكوين البلازما، مع التركيز بشكل خاص على تأثيرات إشعاع الليزر وضغط الغاز المحيط. تُحاكي معلمات الليزر المستخدمة في النموذج معلمات جهازي ChemCam وSuperCam. يقتصر العمل على إثارة نبضة واحدة؛ وبالتالي، لم تُؤخذ تأثيرات تجويف ما بعد الاستئصال في الاعتبار. بالإضافة إلى ذلك، تدرس الرسالة تأثير ظروف تركيز الليزر والضغط المحيط الذي يتراوح بين 3 و9 ملي بار (مما يُمثل ظروف المريخ) ويصل إلى 1000 ملي بار (ظروف الأرض) على معلمات البلازما الرئيسية. ويستند التحليل إلى عمليات محاكاة عالية الدقة أُجريت باستخدام برنامج FLASH مفتوح المصدر لديناميكيات الإشعاع الهيدروديناميكي، والذي استُخدم لحساب درجات حرارة الإلكترونات والأيونات، وكثافات أعداد الإلكترونات والأيونات، وسرعات السوائل داخل البلازما..

الكلمات المفتاحية: بلازما LIBS، الظروف المريخية، نموذج أويلر3T-NLTE ، ظروف الليزر البؤري، ضغط الغاز المحيط.